Available on CMS information server **CMS NOTE 1997/096**

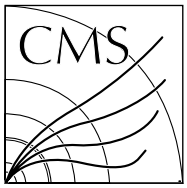

The Compact Muon Solenoid Experiment

CMS Note

Mailing address: CMS CERN, CH-1211 GENEVA 23, Switzerland

November 21, 1997

Muon Trigger of the CMS detector for LHC

G. Wrochna

CERN, Geneva, Switzerland

Abstract

This report contains a comprehensive description of the CMS Muon Trigger System. Brief review of physics to be studied at LHC leads to a list of requirements for the muon trigger. Algorithms designed to fulfil these requirements and their hardware realisation are described. Their performance is illustrated by results of extensive simulations. The report contains also some practical information like the list of milestones, schedules, available documentation, etc.

“Efficiency should be at least as good as possible!”

from a report at one of the CMS Meetings.

Praca habilitacyjna

złożona na Wydziale Fizyki Uniwersytetu Warszawskiego

Contents

Preface **4**

1 Introduction — particle physics today and tomorrow **7**
1.1 The most important questions . . . 7
1.2 Motivation for Large Hadron Collider . . . 7
1.3 Other future colliders . . . 8

2 LHC accelerator and detectors **11**
2.1 LHC machine . . . 11
2.2 Requirements for LHC detectors . . . 11
2.3 ATLAS detector . . . 13
2.4 CMS detector . . . 14

3 LHC physics — requirements for the trigger **19**
3.1 Cross sections and rates . . . 19
3.2 Physics simulation . . . 20
3.3 Review of physics channels . . . 20
3.3.1 Standard Model higgs . . . 21
3.3.2 SUSY higgs . . . 23
3.3.3 Sparticles and particlinos . . . 25
3.3.4 Alternative models and exotica . . . 26
3.3.5 b-quark physics . . . 27
3.3.6 t-quark physics . . . 28
3.3.7 Minimum bias, QCD and Standard Model physics . . . 28
3.3.8 Heavy ion physics . . . 30

4 CMS Trigger system **31**
4.1 Physics requirements . . . 31
4.2 Technical implementation . . . 32
4.3 Calorimeter Trigger . . . 33
4.3.1 Segmentation . . . 33
4.3.2 Trigger primitives . . . 33
4.3.3 Electron/photon trigger . . . 34
4.3.4 The b-electron trigger . . . 35
4.3.5 Jet trigger . . . 35
4.3.6 Missing transverse energy trigger . . . 35
4.3.7 Total transverse energy trigger . . . 35
4.3.8 The τ trigger . . . 35
4.3.9 Calorimeter Trigger performance . . . 36

5 CMS Muon Trigger design issues **37**
5.1 Requirements . . . 37
5.2 Background . . . 38
5.2.1 Introduction . . . 38
5.2.2 Muons . . . 40
5.2.3 Hadrons . . . 44
5.2.4 Uncorrelated electrons from neutrons . . . 47
5.2.5 Electrons correlated with muons . . . 49
5.2.6 Conclusions . . . 51
5.3 Track bending in the magnetic field . . . 54
5.4 Implementation of algorithms . . . 57
5.4.1 Technical limitations . . . 57
5.4.2 Choice of approach — calculus machine or coincidence logic . . . 57

6 Muon Trigger detectors **58**
6.1 Resistive Plate Chambers . . . 58
6.1.1 Required Detector Granularity . . . 59
6.1.2 Requirements on the RPC Performance . . . 61
6.1.3 Geometrical Layout of the RPC System . . . 63
6.1.4 Connection to the trigger . . . 65
6.2 Drift Tubes with bunch crossing recognition capability (DTBX) . . . 66
6.3 Cathode Strip Chambers . . . 67

7 Muon Trigger algorithms and their implementation **69**
7.1 Introduction . . . 69
7.2 RPC based Pattern Comparator Trigger (PACT) . . . 70
7.2.1 Front End Board (FEB) . . . 71
7.2.2 Link Board (LB) . . . 72
7.2.3 Trigger Board (TB) . . . 72
7.3 Drift Tube trigger . . . 74
7.3.1 Bunch and Track Identifier (BTI) . . . 75
7.3.2 Track Correlator (TRACO) . . . 75
7.3.3 Trigger Server (TS) . . . 77
7.4 Cathode Strip Chamber trigger . . . 78
7.4.1 Cathode Front End Board (strip card) . . . 78
7.4.2 Anode Front End Board (wire card) . . . 80
7.4.3 Motherboard . . . 81
7.4.4 Port Card . . . 82
7.5 Track Finder . . . 82
7.5.1 Extrapolator . . . 83
7.5.2 Track Assembler . . . 83
7.5.3 Track Router . . . 84
7.5.4 Assignment Units . . . 84
7.5.5 Barrel/endcap corner . . . 84
7.6 Muon Sorter . . . 85
7.6.1 RPC PACT sorting tree . . . 85
7.6.2 DT/CSC sorting tree . . . 85
7.6.3 RPC PACT Ghost Buster . . . 87
7.7 Global Muon Trigger . . . 87
7.7.1 Final muon sorting . . . 87
7.7.2 Preprocessing . . . 87
7.7.3 Matching RPC and DT/CSC information . . . 88
7.7.4 Isolated muon trigger . . . 88
7.7.5 Multimuon and other triggers . . . 88

8 Beam tests of trigger processor prototypes **90**
8.1 Drift Tubes . . . 90
8.2 Cathode Strip Chambers . . . 91
8.3 Resistive Plate Chambers . . . 92

9 Simulated trigger performance **95**
9.1 Simulation software . . . 95
9.1.1 Event generation . . . 95
9.1.2 Detector simulation . . . 95
9.1.3 Geometry definition . . . 95
9.1.4 Particle tracking . . . 96
9.1.5 Detector response . . . 96
9.1.6 Trigger algorithms — current status . . . 96
9.2 Geometrical acceptance and low momentum cutoff . . . 97
9.3 Overall performance of trigger subsystems . . . 100
9.3.1 Drift Tubes . . . 100
9.3.2 Cathode Strip Chambers . . . 102
9.3.3 Track Finder . . . 103
9.3.4 Resistive Plate Chambers and Pattern Comparator Trigger . . . 104
9.3.5 Global Muon Trigger . . . 111
9.4 Muon and calorimetric trigger thresholds and rates . . . 112

10 Organisational issues **115**
10.1 Scale of the project . . . 115
10.2 Participating institutes . . . 115
10.3 World Wide Web services . . . 116

A Milestones and schedule **127**

B Momentum scale **132**

C Useful numbers and formulae **133**

D Dictionary of acronyms **134**

Preface

The purpose of this report

The purpose of this report is three-fold. First, it is intended to be a handbook for CMS people whose work is concerned with the muon trigger. Therefore, it contains many tables and plots defining various parameters of the system and it provides a lot of practical information like the list of milestones, WWW resources, available documentation, etc. The first two chapters can serve as an introduction for newcomers.

Second, it has its special place in the chain of documents reviewing the muon trigger system design and development. It contains the updated version of specifications of the baseline trigger algorithms [83]. It also forms a base for some chapters of the *Muon Technical Design Report (TDR)* to be released in December 1997 and the future *Trigger and Data Acquisition TDR.*

Last, but not least this report is my *Habilitation Thesis* submitted to *Faculty of Physics, Warsaw University* in order to obtain a *D. Sc.* degree. As such, it should be a general review of the subject. At the same time it should also document the work I have done in the field, both coordinating the work of the CMS Muon Trigger Group, and making the design and simulation of various aspects of the muon trigger myself.

My personal contribution

What is my personal contribution can be traced following the bibliography given at the end of this report. I started my work in the field in March 1991 joining the RD5 experiment [152, 153] which was a pilot project to CMS, designed to study various aspects of muon detection. At the same time, I began to participate in writing of the CMS software, and simulating its muon system. I also took part in the design and simulation of the Resistive Plate Chamber (RPC) based muon trigger. The scope of my work was extended when Drift Tube and Cathode Strip Chamber (CSC) triggers were proposed in 92 and 93/94 respectively. I studied complementarity and integration issues of these muon trigger subsystems. In 1994 I was appointed as the CMS Muon Trigger Coordinator. Perhaps 90% of the content of this report is concerned with my work on this position.

The challenging subject

One of the major difficulties writing this report was an iterative character of the design process of the Muon Trigger. In the real life, after setting basic physics goals, the rough ideas of trigger algorithms were considered, and studied by simulation. Further improvements were proposed. These ideas have been confronted with technical possibilities and financial constraints. The design, which emerged, was then again checked by simulation. This in turn led to a refined design, and so on. This iteration circle is very difficult to describe in a linear document. Certain assumptions or proposed solutions may give the first impression that they are introduced *ad hoc*, without enough justification. The justification is sometimes placed in later chapters, because it requires e.g. rather detailed description of a given part of the system.

Another difficulty was the speed of changes in the status of the design. The process of implementing the algorithms into electronics is perhaps at its highest derivative right now. Therefore, Chapters 7-10 can be considered as the snapshots of the design taken in autumn 1997, where some details are subject to change. Chapters 1-6 contain more general information which is rather stable. With all these reservations in mind I still hope that the paper gives an overall picture of the Muon Trigger system which is not too much distorted.

A reader might be surprised that this paper, intended to be a *Habilitation thesis* in the field of experimental particle physics, does not contain any experimental results in this field. Indeed, the first physics results of the discussed project will hopefully be available only in about 10 years today. This is the reality of the contemporary

particle physics — the projects are extended over more than one generation[1]. However, the impression that the report is nothing but a technical description of an electronics system would be very shallow. There is rich physics in all chapters, except maybe 6, 7, and 10. Dozens of physics channels mentioned in Chapter 3 are just the top of an ice mountain. Behind each table row there are sometimes months of work of many people. Describing each channel, even with a couple of sentences, would blow up the paper. Instead, the references are given, where an interested reader can find all the details about channels of his interest. Chapter 5 is also imbued with physics. It is true that it is mainly the physics of background, which rarely excites audience of large conferences. Nevertheless, it is a physics which we have to master, if we want to discover highs or neutralino.

The outline of this report

The outline of this report is based on the following scheme —
(corresponding chapter numbers are given below each item)

physics	→	requirements	→	design	→	performance verification	→	actual realisation
1, 2, 3		4, 5		6, 7		8, 9		10, A

The first three chapters are devoted to physics to be studied at the LHC. The current situation of particle physics is sketched and a motivation for the Large Hadron Collider is given in Chapter 1. The LHC machine and its detectors are briefly described in Chapter 2. Chapter 3 contains a tabular overview of physics to be studied in CMS and short discussion of expected cross sections and rates.

The goal of the next two chapters is to discuss all ingredients needed to design a trigger. General requirements on the Trigger and Data Acquisition System (DAS), derived from the information presented in Chapters 1-3, are described in Chapter 4. An overview of the Trigger and DAS is also given in this chapter. Specific requirements for the Muon Trigger are presented in Chapter 5. This chapter contains also an extensive discussion of the experimental environment (background, magnetic field, etc.) and technical limitations. I consider this chapter as the most important one in this report in the sense that it has the highest intellectual content. It contains original results of research in the field of particle interactions with matter.

The actual Muon Trigger design is presented in the following two chapters. Muon detectors are described in Chapter 6, whereas the trigger algorithms and their electronics realisation are described in Chapter 7. The design has been verified by prototype tests and extensive simulations which is discussed in Chapters 8 and 9 respectively. Chapter 10 and Appendix A are dealing with the actual realisation of the project. They describe how the work is organised in practice.

Acknowledgements

This report, although it is edited by one person, contains results obtained by many of my colleagues. Some of them made designs or performed calculations which I directly quote in the paper. Others supported me by various means. It is impossible to recall all the names. However, I would like to mention at least some of them.

Janusz Zakrzewski was the first one who showed me the beauty of experimental high energy physics and helped me to take off in this field.

Roman Szwed who was my *M.Sc.* thesis supervisor, taught me how to do physics in practice. I shall never forget his tutelage and help.

I owe my most sincere thanks to Andrzej K. Wróblewski, who helped me to go at large, supervising my *Ph.D.* thesis, assisting in my first publications and promoting my first appearances at international conferences.

I continue to be grateful to Jan Królikowski, who displayed wonderful perspectives of the LHC physics, introducing me to RD5 and CMS experiments. His support was invaluable to me. I would like to thank him and other colleagues from the Warsaw Group for a very fruitful collaboration within CMS. Brain storming discussions with them, especially with Maciek Kudła, were always a great inspiration to me.

I would like to express my thanks to all colleagues from RD5 and CMS collaborations. I am grateful to Michel Della Negra, who as the RD5 and CMS spokesman and the CERN group leader, was always very supportive for me, even I was rather troublesome subordinate. Friendly atmosphere which he created in the group made my work there a pleasure. Ernst Radermacher, the RD5 co-spokesman and CMS Technical coordinator, was always able to

[1] My son, who was born on the day of CMS EoI presentation, 5 March 1992, still has a chance to make a *Ph.D.* on the CMS data analysis.

find some time in his busy day to discuss with me various details of the CMS design. Daniel Denegri, the unique physics guru, is always open to all brilliant and crazy ideas. Most of my knowledge of the LHC physics is due to him.

The unforgotten adventure in my life were the early days of RD5. Since then I owe a debt of gratitude to Fritz Szoncso and Gyorgy Bencze. I could not have done much without them.

Another interesting adventure was the initial development of the CMS software. I would like to mention gratefully the excellent collaboration, especially with Veikko Karimäki and Marcin Konecki. This was possible thanks to Martti Pimiä, whose coordination and encouragement were always very helpful indeed.

I would like to express my gratitude to my current supervisors: Jim Virdee (new CERN Group Leader), Fabrizio Gasparini (Muon Project Manager), Sergio Cittolin (TriDAS Project Manager), and Wesley Smith (Trigger Coordinator) for very effective and friendly collaboration.

Today the CMS Collaboration has over 1500 members and many of them contributed in some way to this report. Among them are: Carmen Albajar, Alberto Benvenuti, Rob Bergman, Richard Breedon, Giacomo Bruno, David Chrisman, Mikołaj Ćwiok, Marco Dallavalle, Wojtek Dominik, Umberto Dosselli, Andrzej Fengler, Yuri Fisyak, Marco De Giorgi, Igor Golutvin, Maciej Górski, Jay Hauser, Mika Huhtinen, Giuseppe Iaselli, Vladimir Karjavin, Alexander Kluge, Winston Ko, Roberto Martinelli, Anna Meneguzzo, Guenakh Mitselmakher, Petr Moissenz, Norbert Neumeister, Paul Padley, Jacek Pliszka, Krzysztof Poźniak, Antonio Ranieri, Hans Reithler, Herbert Rohringer, Jeff Rowe, Claudia-Elisabeth Wulz, Torsten Wildschek, Anton Taurok, Piotr Zalewski, and Pierluigi Zotto. Many thanks to all of you!

Writing this report I have got a lot of help from Jan Królikowski. Without his criticism this paper would be undoubtly much worse. I am also grateful to Michel Della Negra, Ryszard Gokieli, Wesley Smith, and Andrzej Wróblewski for their comments to the draft.

I wish to express special thanks to my wife Małgorzata. Her understanding, patience and spiritual support are make my work possible.

Finally, I would like to thank God, who created such a magnificent world. I am so grateful to him that he allowed me to study the crumbs of his Wisdom and admire the reflections of his Beauty.

Grzegorz Wrochna

Chapter 1

Introduction — particle physics today and tomorrow

1.1 The most important questions

At the fall of the 20th century particle physics reached a very dramatic point. After unification of electromagnetic and weak forces in seventies, the Standard Model of fundamental interactions was developed. It provides a consistent description of all known phenomena involving electroweak and strong interactions. It was confirmed with high precision by many experiments, and no deviations from its predictions were found till today. Recent measurements at Large Electron-Positron collider (LEP) confirmed many Standard Model predictions with accuracy of one per mill. However, the Standard Model has several important drawbacks. First of all, it has about 20 parameters which values are not determined within the model. They just have to be measured experimentally. Among them are the masses of elementary fermions. In the Standard Model fermions acquire their masses due to spontaneous symmetry breaking by the Higgs mechanism. This mechanism, however, is put into the model "by hand". It requires existence of a Higgs particle — a neutral scalar boson which has not yet been discovered.

There are other questions not answered by the Standard Model.

- The origin of masses
  - Is it really Higgs mechanism?
  - Why the masses (or higgs couplings) have particular values?
- Why the fermions exist in three generations?
- Why they are mixed?
- What is the origin of CP violation?
- How to treat "soft" phenomena by the Standard Model, which relays on perturbative calculus?
- How to incorporate gravity?

The last but not least question is whether the Standard Model is at all a valid description of fundamental phenomena. The regular structure and symmetry of the Standard Model suggests that there is a deeper and more general theory behind it, the Standard Model is only a kind of effective theory. In some sense, the situation is similar to one in chemistry after Mendeleyev invented his table of elements. The regular pattern of columns and rows imposed, in a very elegant way, order in the properties of elements and their reactions, but its origin remained mysterious and unexplained until the electron structure of atom was understood.

1.2 Motivation for Large Hadron Collider

Above list of questions suggests the following strategy for future experiments

- find Higgs particle(s), or exclude its existence in the range predicted by theory (up to $\approx$ 1 TeV),
- look for possible deviations from the Standard Model predictions,
- search for exotic particles.

These three possibilities have been already exploited without a success by present colliders — LEP at CERN (Geneva), HERA at DESY (Hamburg) and Tevatron at FNAL (near Chicago). Standard Model higgs has not been found. New limits have been set on masses of particles predicted by Minimal Supersymmetric Standard Model (MSSM) which is an extension of the SM, the most favourable by many theorists. No evidence for more exotic objects, like leptoquarks, was observed. Current limits on masses of those particles are given in Table 1.1.

Table 1.1: Results of new particle searches — 95% exclusion limits. Values for future colliders are only approximate. The data are taken from [157, 158, 159, 160]. Some entries for SUSY particles, especially for MSSM higgses, are empty because the mass reach depends significantly on parameters of the model. They will be discussed in more detail in Chapter 3.

particle		mass limit [GeV]					comment
		present	LEP192	TeV II	TeV 33	LHC	
SM higgs	H	77.1	95	80-100	120	1000	
MSSM higgs	h, A	64.5					for any $\tan\beta$
	$H^{\pm}$	54.5					
chargino	$\chi^{\pm}$	91	94	210	250		for $m_{\chi^{\pm}} \Leftrightarrow m_{\chi^0} > 10$ GeV
LSP[1]	χ^0	14		210	250	350	within SUGRA
sleptons	$\tilde{e}$, $\tilde{\mu}$, $\tilde{\tau}$	80, 73, 55	83 - 88	100		400	
stop	$\tilde{t}$	48	75 - 90		120		
squark, gluino	$\tilde{q}$, $\tilde{g}$	260	85	390	450	2000	for $m_{\tilde{q}} = m_{\tilde{g}}$
leptoquarks[2]	LQ	240		300	385	2200	vector, $\kappa = 1$
		200		250	330	1800	vector, $\kappa > 0.25$
				150	250	1400	scalar

[1] The Lightest Supersymmetric Particle.

[2] The first generation leptoquarks are considered.

The κ is a parameter characterising an anomalous coupling of vector leptoquarks to gluons. In many realistic gauge theories $\kappa = 1$.

Several upgrades of todays accelerators are foreseen in coming years. They are summarised in Table 1.2, together with future new accelerators. The LEP will reach $\sqrt{s} = 192$ GeV in the year 1998. Tevatron energy will be increased from 1.8 TeV to 2.0 TeV and its luminosity will be multiplied by factor a 10 before the year 1999. Yet another Tevatron upgrade around the year 2004 is being considered, which may increase the luminosity up to $10^{33}\mathrm{cm}^{-2}\mathrm{s}^{-1}$. The increase of available mass limits is given in Table 1.1.

However, a new machine is needed in order to push the limits significantly. This is because the expected cross sections are very low (sometimes as low as several femtobarns). Relatively high masses (100-1000 GeV) of searched particles call for experiments being able to observe 10^{16}-10^{17} particle collisions with energy in multi-TeV range. These were the main goals for the design of the Large Hadron Collider — an accelerator to be build at European Laboratory for Particle Physics CERN in Geneva. One can see from Table 1.1, that concerning its discovery potential, it is incomparable to upgrades of present colliders.

1.3 Other future colliders

The main drawback of all hadron colliders, including the LHC, is the fact that only a small fraction (typically $\sim$10%) of the beam energy is carried by colliding partons. On the other hand this is, however, a great advantage, because a wide energy range can be scanned without changing parameters of the beam. Another advantage of the LHC are high couplings of proton constituents — quarks and gluons — to new predicted particles. These two facts make the LHC a very good machine for making discoveries. However, once a new particle is discovered, one would like to produce it copiously in a clean environment in order to study its property. For this lepton colliders are better. A good example is the LEP which produces millions of Z^0's after this boson was discovered in Super Proton-Antiproton Collider. In the case of the LHC, discovering a higgs does not necessarily settle whether

Table 1.2: Present and future accelerators.

accelerator name	colliding particles	$\sqrt{s}$ [TeV]	luminosity $[10^{33}\mathrm{cm}^{-2}\mathrm{s}^{-1}]$	date of start	date of end
LEP 1	e^+e^-	0.091	0.024	1989	1994
LEP 2	e^+e^-	0.130 - 0.192	0.045	1995	1999 (2000)
HERA	$e^\pm p$	0.3	0.016	1992	?
Tevatron I	$p\bar{p}$	1.8	0.02	1987	1997
Tevatron II	$p\bar{p}$	2.0	0.2	1999	?
TeV 33	$p\bar{p}$	2.0	1	2004	?
LHC	pp	14.0	10	2005	?
LEP×LHC	e^-p	1.3	0.1	?	?
NLC	e^+e^-	0.5 - 1.5	5 - 20	2008?	?
Muon Collider	$\mu^+\mu^-$	0.5	0.7 - 5	?	?
VLHC	pp	60 - 200	10	?	?
NNLC	e^+e^-	5.0	100	?	?
Next MC	$\mu^+\mu^-$	4.0	100	?	?

the Standard Model is correct. One needs to measure precisely its properties. Two lepton colliders are being considered for this purpose — the Next Linear Collider (NLC) of e^+e^- pairs and the First Muon Collider. Their parameters are also given Table 1.2. Feasibility study of the NLC are already well advanced and they are no major technical difficulties in building such a machine. The Muon Collider is technically more challenging, but it can probe different couplings than the NLC. Especially the couplings of higgs to muons are much higher than those to electrons, which could make the Muon Collider a real "higgs factory".

The discovery potential of future accelerator is illustrated in Fig. 1.1. The mass reach for a new heavy boson Z' is shown according to expectations of various models. In the case of the LHC it extends to 4-5 TeV.

Let us close this chapter with some ideas for future accelerators for our grandsons (see Table 1.2). Very Large Hadron Collider (VLHC), Next to Next Linear Collider (NNLC) or Next Muon Collider (NMC) look like a fiction, but this is already a science. Simulation and design study are already going on. For example, the proceedings of workshop *New directions in high energy physics* (Snowmass, Colorado, 1996) contain 25 articles (in total over 100 pages) devoted to the VLHC. It seems that the LHC is not the Last Hadron Collider.

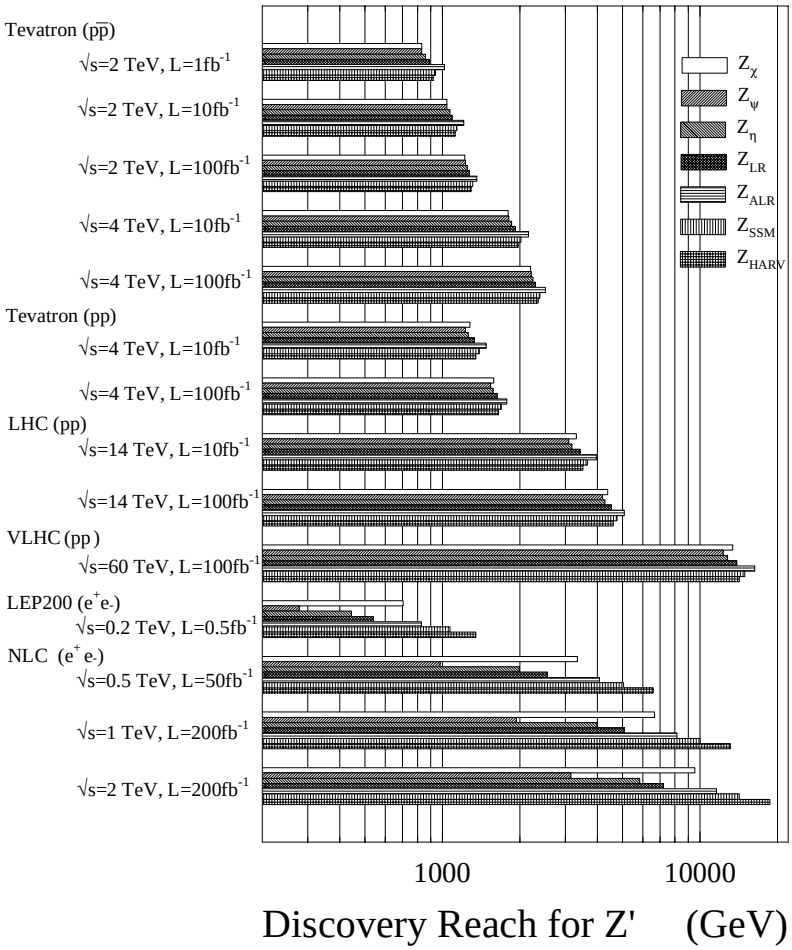

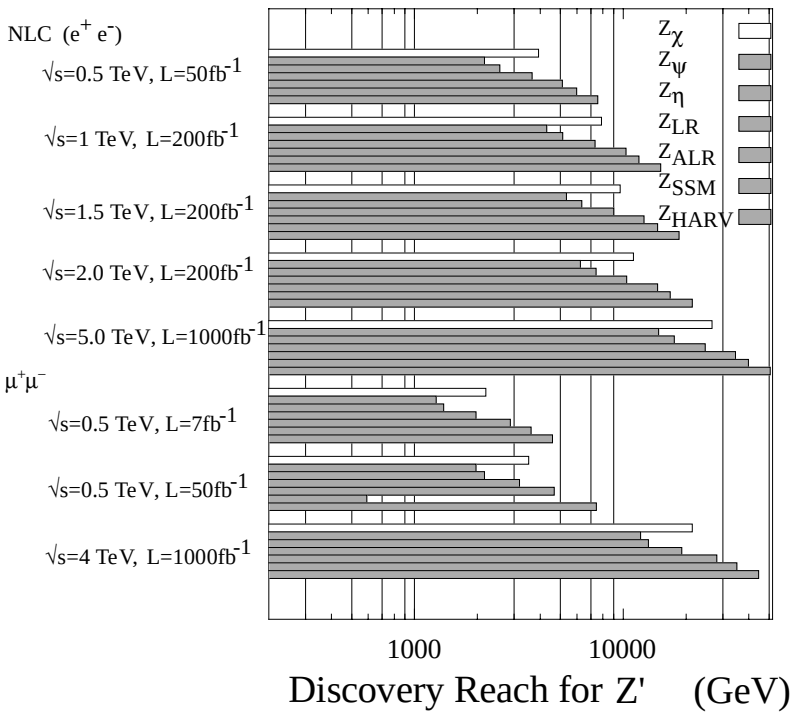

Figure 1.1: Z’ discovery potential of future accelerators, assuming different theoretical models [161, 162].

Chapter 2

LHC accelerator and detectors

2.1 LHC machine

Large Hadron Collider is a circular accelerator of proton and heavy ion (up to Pb) beams. It will be placed in the tunnel of currently running Large Electron-Positron accelerator (LEP). Its commissioning is planned for the year 2005. It will provide proton-proton collisions with the center of mass energy $\sqrt{s} = 14$ TeV. The designed luminosity of $10^{34}\mathrm{cm}^{-2}\mathrm{s}^{-1}$ will be obtained by colliding proton bunches with a frequency of 40 MHz, with about 20 pp collisions per bunch crossing (b.x.). Main parameters of the machine are summarised in Table 2.1.

Table 2.1: Basic parameters of the LHC accelerator in the pp mode.

Collision energy	7+7 TeV
Relativistic factor γ	7461
Circumference	27 km
Dipole field	8.4 T
Crossing points	4
Luminosity	$10^{34}\mathrm{cm}^{-2}\mathrm{s}^{-1}$
Number of bunches	2835
Bunch spacing	25 ns $\Leftrightarrow$ 7.48 m
Particles per bunch	10^{11}
Bunch crossing frequency	40 MHz
pp collisions per b.x.	~ 20
Beam current	2×0.536 A
Stored energy	2×334 MJ
Beam size in arc	$0.303 \times 0.303\ \mathrm{mm}^2$
Beam size at inter. point	$15.9 \times 15.9\ \mu\mathrm{m}^2$
RMS bunch length	0.257 ns $\Leftrightarrow$ 7.7 cm
Luminosity life time	~ 10 hours

2.2 Requirements for LHC detectors

Collisions in LHC will be observed by 4 detectors: ALICE, ATLAS, CMS, and LHC-B (see Fig. 2.1). ALICE and LHC-B are designed to study heavy ion collisions and b-quark physics respectively. ATLAS and CMS are general purpose detectors. In this paper we discuss in detail only the CMS detector and we just briefly describe ATLAS for comparison.

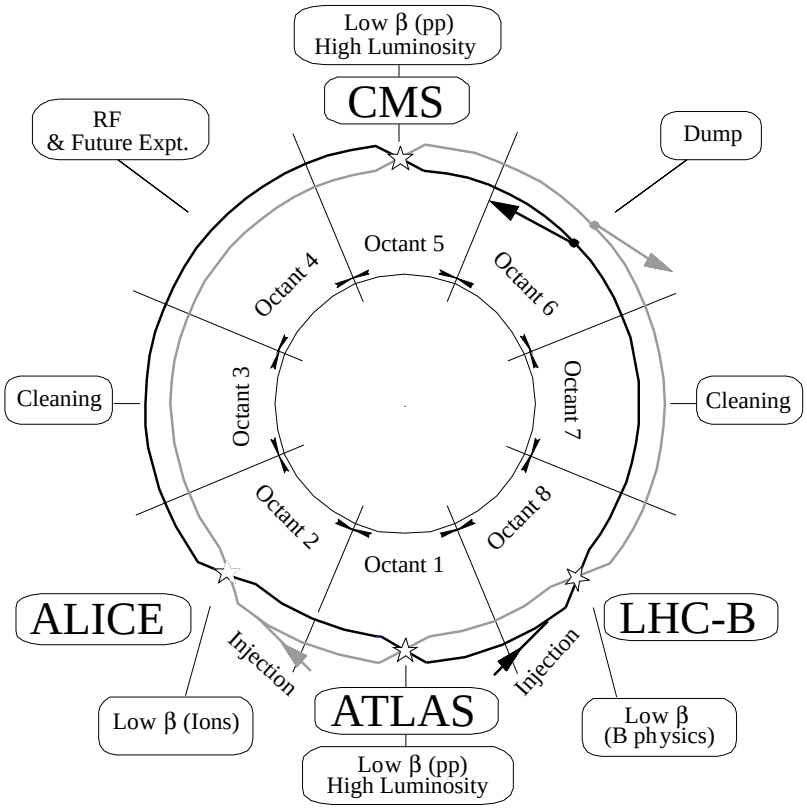

Figure 2.1: Layout of the Large Hadron Collider.

Interesting physics in modern high energy experiments can be studied mainly by measuring properties of three types of objects

- charged, long lived leptons — muons and electrons,
- photons,
- jets and missing energy.

At the LHC energy jets are produced in most of the pp collisions. They results from fragmentation of quarks and gluons. Jets with the high transverse energy E_t are signatures of interesting physics channels. In order to measure jet energy a calorimetric detector is needed. It should be thick enough (typically 10 nuclear interaction lengths λ) to fully contain hadronic showers.

Unbalanced E_t observed in an event, i.e. missing energy $\not\!\!E_t$, means that there was at least one particle which escaped detection. This could be either a neutrino or yet unknown stable neutral particle, like supersymmetric neutralino. Therefore the calorimeter should be as hermetic as possible to avoid fake $\not\!\!E_t$ due to cracks.

Photons at LHC have a special importance. This is because they offer the best possibility to discover Higgs particle lighter than $\sim$ 130 GeV through the decay H$\rightarrow \gamma\gamma$. Both energy and angle between the photons should be measured with high precision to suppress enormous background from $\pi^0 \rightarrow \gamma\gamma$ decays. Therefore, the electromagnetic part of the calorimeter should have very good energy and angular resolution. High granularity of the electromagnetic calorimeter also helps to suppress the background, by imposing the photons isolation from any jets.

Electromagnetic calorimeter will be also used to identify electrons, and measure their energy. To distinguish them from photons one has to make use of the fact that they are charged particles and can be observed with ionisation detectors. Tracking in a magnetic field enables independent measurement of electron transverse momentum p_t which should match the calorimetric measurement of E_t. It also allows us to apply an additional isolation criteria requesting no other tracks near by, thus excluding particles originating from jets.

Muons can be relatively easily distinguished from other charged particles because of their ability to penetrate dense materials. They are practically the only particles which can be detected beyond the calorimeters. There is a certain probability that some other particles emerging from the tail fluctuations of hadronic shower will exit the calorimeter, but tracking in magnetic field outside the calorimeter can effectively suppress this background.

Isolation is a very important tool not only in the case of electrons and photons. Muons from decays of Z, W or heavier particles can also be recognised this way. Lepton τ produces isolated electron, muon or hadrons. Hadrons from the τ decay can be recognised as a narrow, isolated jet.

2.3 ATLAS detector

The name "ATLAS" was coined as an abbreviation of "**A T**oroida**L A**paratu**S** [154], which underlines the central role played in this detector by large toroidal magnets (Fig. 2.2) located on the outside of the detector. The magnets create a magnetic field of $\sim$0.6 T used to bend muon tracks. Precise muon measurement is done with pressurised Monitored Drift Tubes (MDT) in the barrel and with Cathode Strip Chambers (CSC) in the endcaps. Triggering is done with Resistive Plate Chambers (RPC) in the barrel and Thin Gap Chambers (TGC) in the endcaps.

Both electromagnetic and hadronic calorimeters use liquid argon technology. An exception is barrel hadronic calorimeter which is an iron/scintillator sandwich.

The Inner Detector is enclosed in a 7 m long solenoidal magnet with a diameter of 2.3 m. It produces an axial magnetic field of 2 T. The outer part of the tracker consists of straw tubes. This part of the tracker has transition radiation capability. Going inwards, tracks are measured by silicon tracker and pixel detector.

The overall layout of the ATLAS detector is shown in Fig. 2.2. Basic parameters are listed in Table 2.2

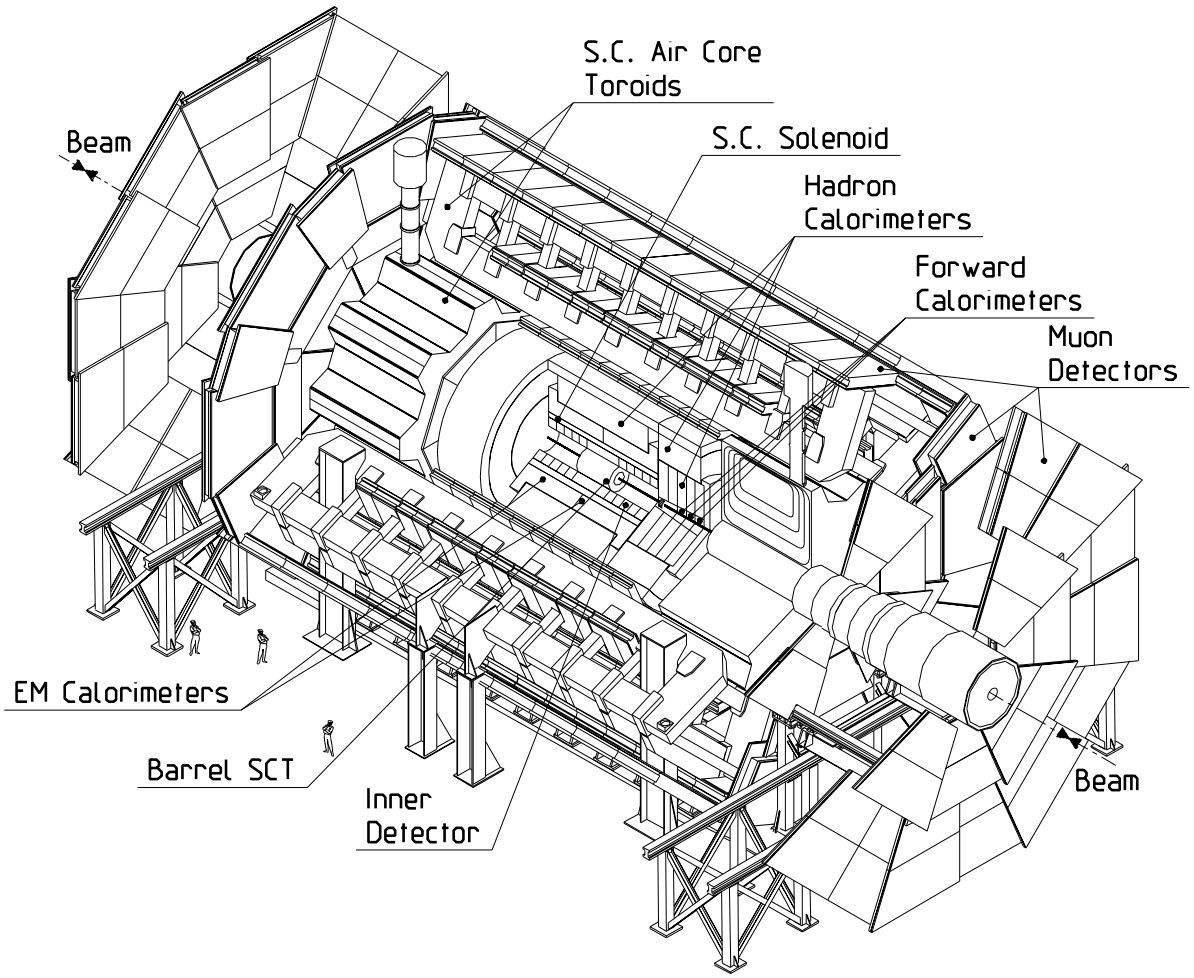

Figure 2.2: Layout of the ATLAS detector.

Table 2.2: Basic characteristics of the ATLAS detector.

detector component	measurement resolution	η coverage measurement	η coverage trigger
inner detector	$\frac{\Delta p}{p} = 20\%$ at $\|\eta\| < 1.7$, p_t = 500 GeV $\frac{\Delta p}{p} = 50\%$ at $\|\eta\| = 2.5$, p_t = 500 GeV	± 2.5	—
muon detector	$\frac{\Delta p}{p} = 11\%$ at p_t = 1 TeV	± 2.7	± 2.4
e.m. calorimeter	$\frac{\sigma}{E} = \frac{10\%}{\sqrt{E}} \oplus 0.7\%$	± 3.2	± 2.5
hadron calorimeter:			
barrel and endcap	$\frac{\sigma}{E} = \frac{50\%}{\sqrt{E}} \oplus 3\%$	± 3.2	± 3.2
forward	$\frac{\sigma}{E} = \frac{100\%}{\sqrt{E}} \oplus 10\%$	$3.2 < \|\eta\| < 4.9$	$3.2 < \|\eta\| < 4.9$

2.4 CMS detector

The abbreviation "CMS" stands for **C**ompact **M**uon **S**olenoid [156]. Its main parts are an inner tracker, calorimeters and a muon system. They are shown in a perspective view in Fig. 2.3 and in XY and RZ cross sections in Figures 2.4, 2.5. Open view of the detector is shown in Figure 2.6. The experimental hall is drawn in Figure 2.7.

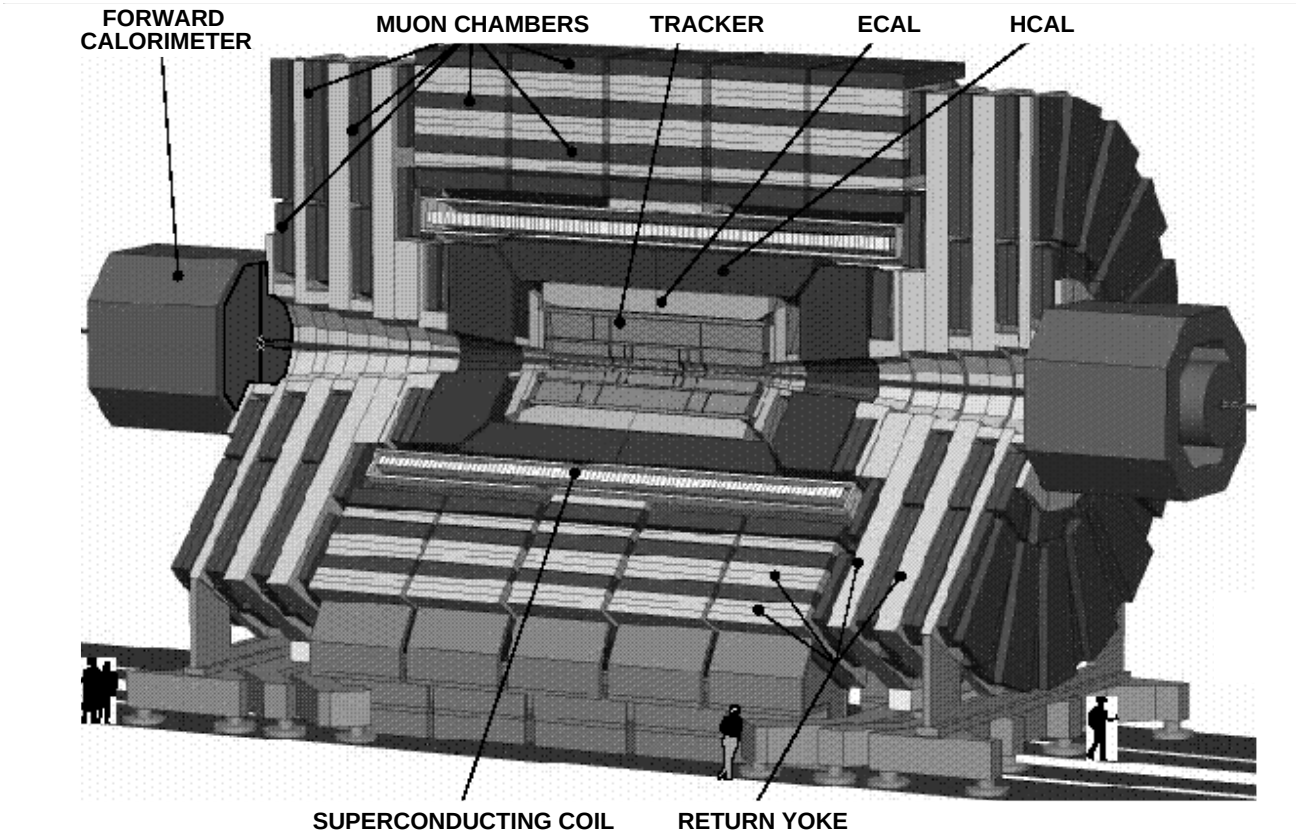

Figure 2.3: Layout of the CMS detector.

The inner tracker consists of silicon pixel, silicon microstrips detectors and MicroStrip Gas Chambers (MSGC). The electromagnetic calorimeter is a matrix of $PbWO_4$ crystals. The hadronic calorimeter is a copper/scintillator sandwich up to $|\eta| = 3$. At higher $|\eta|$ it is completed with a very forward calorimeter made of iron with quartz fibers as sensitive elements. The characteristic feature of the CMS detector is that the inner tracker and both calorimeters are contained within the large superconductive solenoid, 6 m in diameter and 13 m long. The coil creates 4 T magnetic field. Outside the coil the magnetic flux is returned by an iron yoke. The yoke is interleaved with 4 muon stations. Each barrel muon station consists of Drift Tubes (DT) and RPC's. Endcap muon stations are equipped with Cathode Strip Chambers (CSC) and RPC's as well.

Basic performance of the CMS detector is summarised in Tables 2.3 and 2.4. Some of the parameters vary significantly with η and ϕ. Parametrisation of their behaviour is provided by Fortran routines listed in the third column of Table 2.4. The routines are described in technical notes quoted at the bottom of the table.

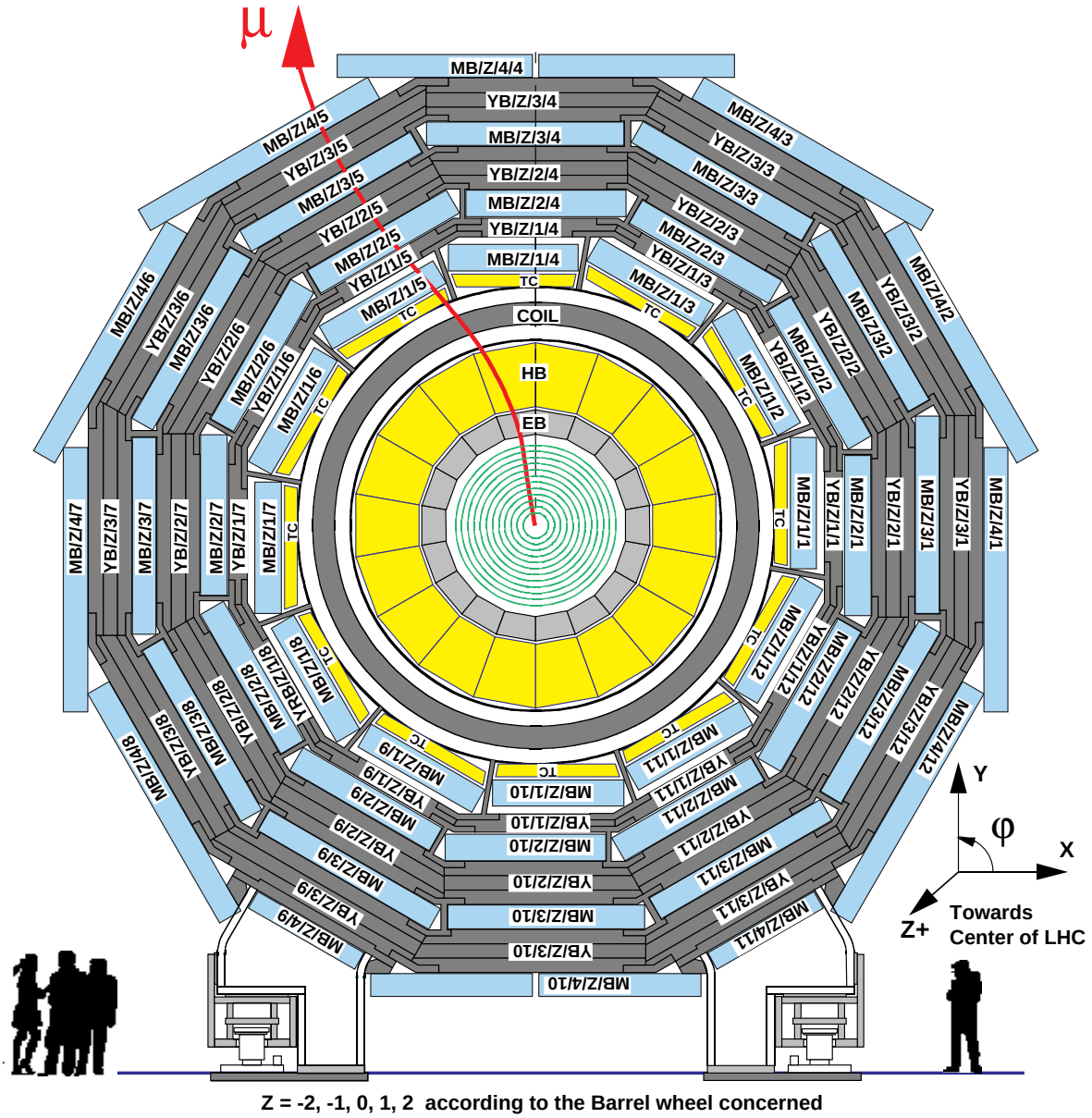

Figure 2.4: XY cross section of the CMS detector.

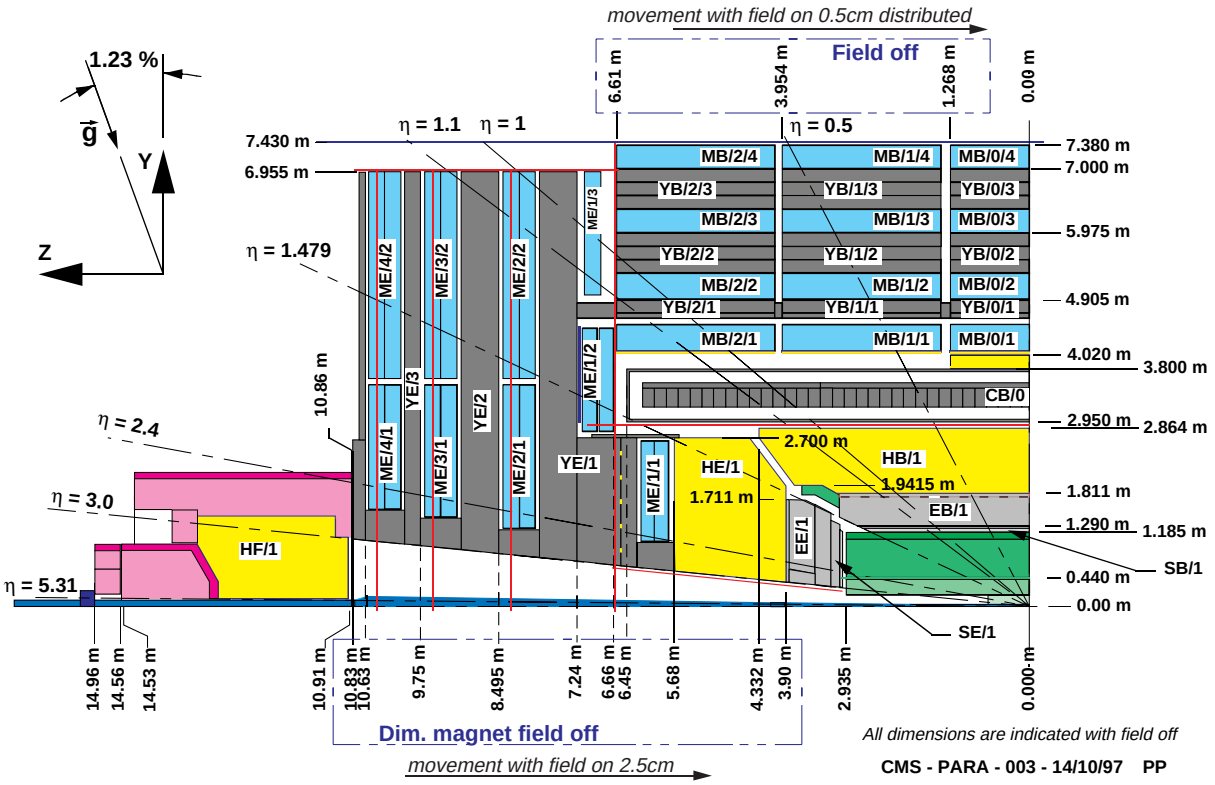

Figure 2.5: RZ cross section of the CMS detector.

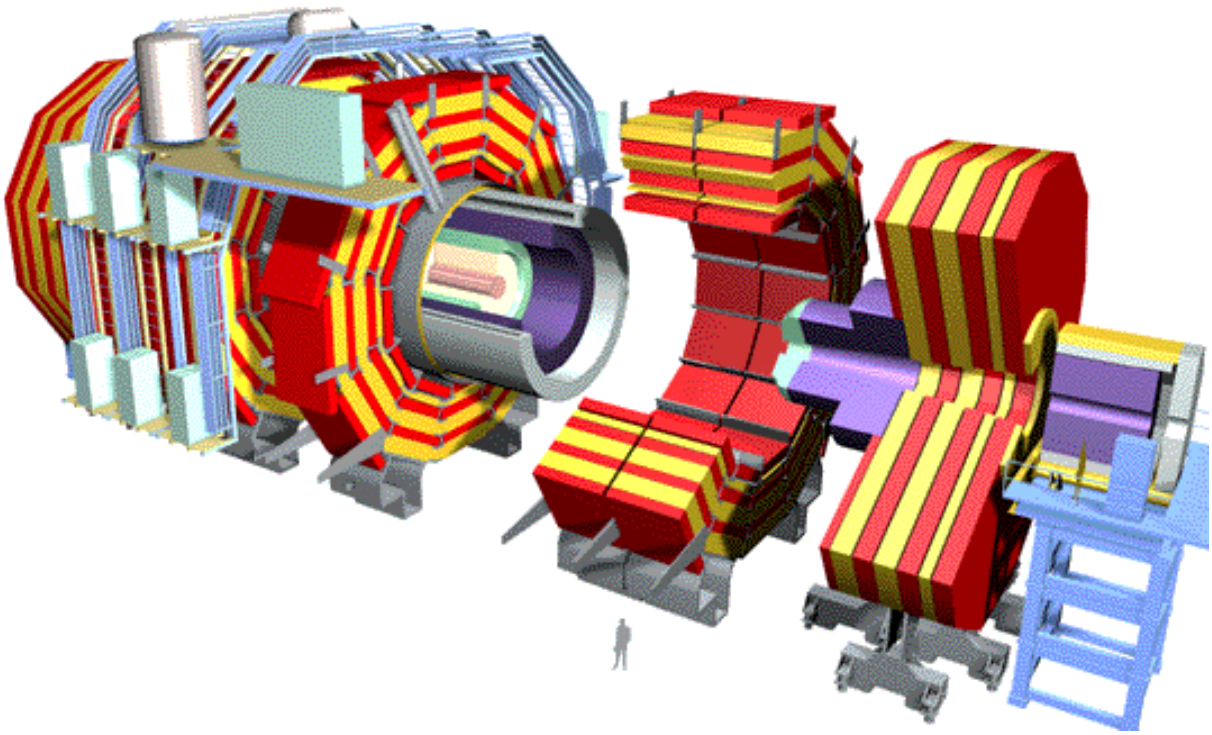

Figure 2.6: Open view of the CMS detector.

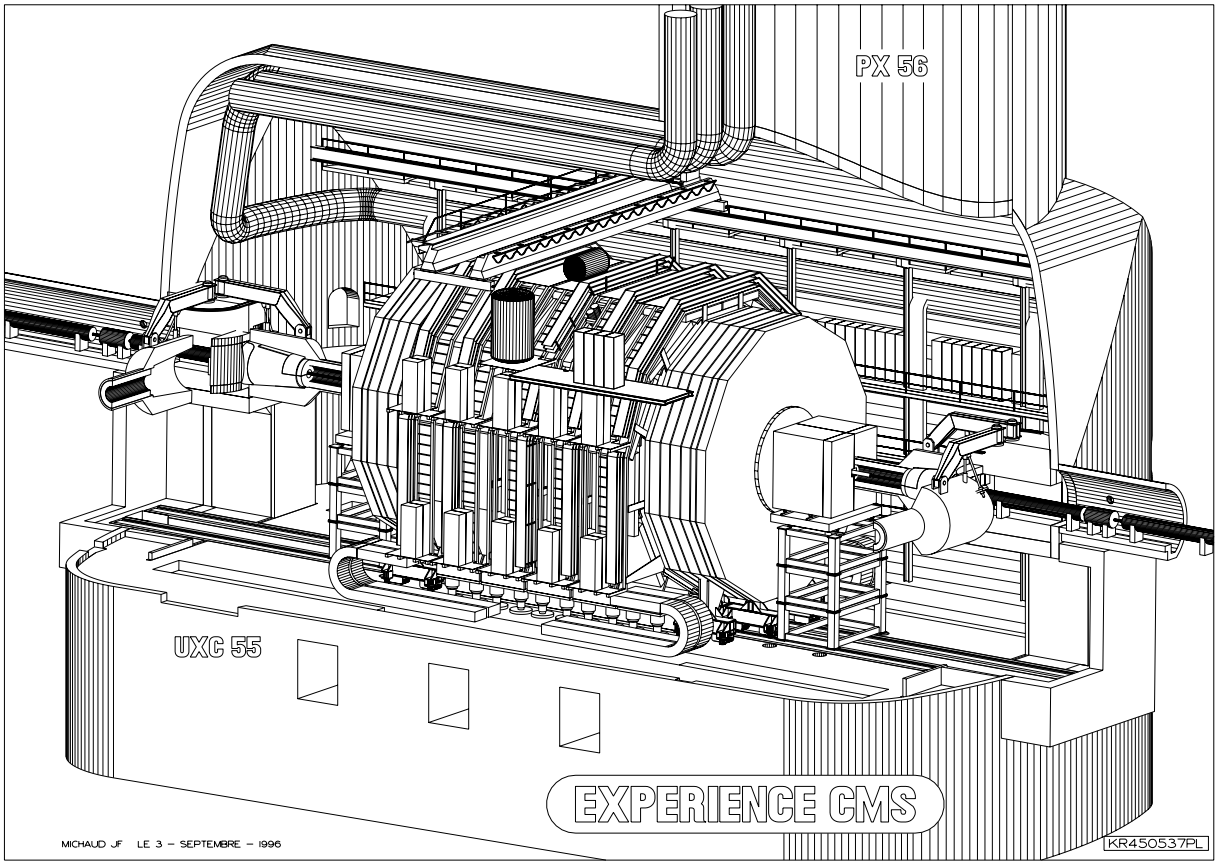

Figure 2.7: CMS detector in the experimental hall.

Table 2.3: Basic characteristics of the CMS calorimetry.

parameter	average value
geometrical coverage	ECAL $\|\eta\| < 2.6$, HCAL: $\|\eta\| < 3$ forward calorimeter (HF): $3 < \|\eta\| < 5$
e,γ energy resolution (noise term given for $\mathcal{L} = 10^{33} \rightarrow 10^{34}$)	barrel: $\frac{\sigma}{E} = \frac{2.7\%}{\sqrt{E}} \oplus 0.55\% \oplus \frac{0.155 \rightarrow 0.205}{E}$ endcap: $\frac{\sigma}{E} = \frac{5.7\%}{\sqrt{E}} \oplus 0.55\% \oplus \frac{0.220 \rightarrow 0.245}{E}$
π^0 rejection efficiency (requiring γ efficiency = 90%)	40-60% for p_t^π = 20-100 GeV
γ conversions (all / not recovered)	barrel: 24% / 5%, endcap: 35% / 9%
γ direction resolution	40 mrad / $\sqrt{E}$
single hadron energy resolution	barrel: $\frac{\sigma}{E} = \frac{65\%}{\sqrt{E}} \oplus 5\%$ endcap: $\frac{\sigma}{E} = \frac{83\%}{\sqrt{E}} \oplus 5\%$ HF: $\frac{\sigma}{E} = \frac{100\%}{\sqrt{E}} \oplus 5\%$
dijet effective mass resolution	17% for $m_{jj} = m_Z, 50 < p_t^{jet} < 60$ GeV 10% for $m_{jj} = m_Z, 500 < p_t^{jet} < 600$ GeV 5.6% for $3 < m_{jj} < 4$ TeV

Energy E is expressed in GeV.

Table 2.4: Basic characteristics of the CMS tracking and muon detector.

parameter	average value	routines
μ geometrical acceptance	$\sim$95%, $\|\eta\| < 2.4$	ACCMRPC
μ reconstruction threshold	barrel: $p_t > 4$ GeV endcap: $p > 8$ GeV	
dp/p for μ (p in TeV)	barrel: $\frac{\Delta p}{p}\% = 4\%\sqrt{p}$ endcap: $\frac{\Delta p}{p}\% = 0.9\%$ for $p < 0.05$ TeV $\frac{\Delta p}{p}\% = 4\%\sqrt{p}$ for $0.05 < p < 2$ TeV $\frac{\Delta p}{p}\% \approx p$ for $p > 2$ TeV	MDPOVP, MSMEARP
dp/p for other particles with vertex constraint (p_t in GeV)	1.5% $p_t \oplus$ 0.5% for $\|\eta\| = 0$ 2.0% $p_t \oplus$ 0.7% for $\|\eta\| = 1.8$ 4.5% $p_t \oplus$ 0.9% for $\|\eta\| = 2.25$	TDPOVP, TSMEARP
dp/p for other particles without vertex constraint (p_t in GeV)	1.7% $p_t \oplus$ 0.5% for $\|\eta\| = 0$ 2.4% $p_t \oplus$ 0.7% for $\|\eta\| = 1.8$ 6.0% $p_t \oplus$ 0.9% for $\|\eta\| = 2.25$	TDPOVP, TSMEARP
impact parameter resolution	(see [156] Fig.11.4)	TDIMPAC, TSMEARI
primary vertex resolution (p_t in GeV)	$\sigma_{r\phi}[\mu m] = 7 + 940/\Sigma\|p_t\|$ $\sigma_z[\mu m] = 16 + 1940/\Sigma\|p_t\|$	
secondary vertex resolution	6-8% of the B_S^0 flight path	
b-tagging efficiency (for various cuts)	signal: 20, 31, 40, 53% background: 1.2, 2.7, 7.1, 13%	
τ-tagging efficiency	signal: 50%, background: 3%	
K_S^0 reconstruction efficiency	$\sim$35%	(see [156] Fig.11.7)
μ trigger efficiency	$\sim$95% for high p_t μ, $\|\eta\| < 2.4$	EFFMRPC
lowest p_t μ trigger threshold	4 GeV for $\|\eta\| < 1.5$ 2.5 GeV for $1.5 < \|\eta\| < 2.0$ 2 GeV for $2.0 < \|\eta\| < 2.4$	ACCMRPC, EFFMRPC
μ reconstruction and matching efficiency	$\sim$98%	

Barrel/endcap division of the muon system is at $|\eta| \approx 1.5$.
Note the difference between p and p_t in some formulae.

Routines MDPOVP, MSMEARP are in http://ucdheg.ucdavis.edu/cms100/car/mufpar.car.
They are documented in CMS TN/95-026.

Routines TDPOVP, TSMEARP, TDIMPAC, TSMEARI
are in //TRAK/TRUTIL directory of /afs/cern.ch/cms/cmsim/cms103/cmz/trak.cmz.
They are documented in CMS TN/94-275.

Routines ACCMRPC, EFFMRPC are available at
/afs/cern.ch/user/k/konec/public/html/rpcpar/ or http://cmsdoc.cern.ch/~konec/rpcpar/.
They are documented in CMS TN/96-104.

Routines containing "SMEAR" in their names provide resolution smearing. They change a value of a given variable by a random number generated according to parametrised distribution.

Chapter 3

LHC physics — requirements for the trigger

3.1 Cross sections and rates

Cross sections of phenomena to be studied at LHC span many orders of magnitude. This is illustrated in Fig. 3.1 where other accelerators are also shown for comparison.

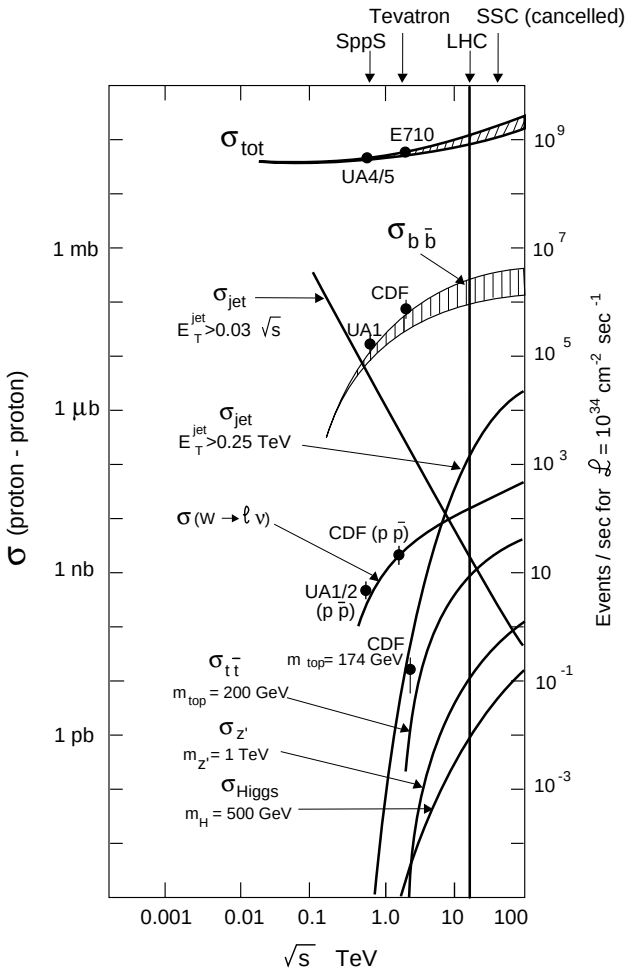

Figure 3.1: Inclusive proton-(anti)proton cross sections σ for basic physics processes. Interaction rates for the nominal luminosity are given on the right scale.

The enormous range of the cross sections makes the triggering at LHC a very challenging task. The trigger system has to select efficiently a few interesting events among millions of background ones. Note the relatively high cross section for b-quarks. The physics of b-quarks is very interesting in itself, because of quark mixing and CP violation phenomena. On the other hand it is one of the main sources of muons which constitute huge background for other processes. Similar example is the top quark. It was discovered just recently and it will be studied in detail for the first time at LHC. However, it is a very severe background to more exotic physics, because it has signatures very similar to many new expected particles.

In the following sections of this chapter we are going to review basic physics channels to be studied at LHC. Since there is a vast literature on the subject we do it here only in a brief, tabular form. Our goal is to derive requirements for the trigger.

3.2 Physics simulation

Most of the physics studies for CMS, including those discussed in this paper, were done with event generators, like PYTHIA [134], ISAJET [135], or their supersymmetric extensions. Some results were obtained on the particle level, without simulating the detector. More advanced studies were performed with the CMSIM program [136], which simulates in detail the detector response. For more information concerning the simulation of physics processes discussed in this chapter we refer the reader to the quoted papers. Simulation more directly connected to the trigger is discussed in Section 9.1.

3.3 Review of physics channels

In this section we review the physics channels to be studied at LHC, looking for possible ways of triggering. We refer to CMS documents quoting cuts applied in Monte Carlo analysis. Trigger threshold on corresponding objects should never be lower. The following trigger objects are considered:

- μ — muon (any),
- μ_i — isolated muon (no jet around),
- e — electron/photon (isolated),
- e_b — b-electron (from b-quark decay),
- jet — local energy concentration in the calorimeter,
- τ — tau trigger (a kind of narrow jet),
- $\not{E}_t$ — missing transverse energy,
- 2μ, 2e, eμ, 2 jets, 3 jets, etc. — multi-object triggers.

Only isolated electrons and photons are considered because otherwise one cannot stand the background from QCD jets. This is not satisfactory for b-quark physics and therefore a dedicated, so called b-electron trigger is required. Possible implementation of those triggers will be discussed in Section 4.3 and Chapter 7.

Whenever we consider a multi-muon trigger for a given channel, the efficiency will be complemented with corresponding single object triggers. For example some dimuon events may escape a 10 GeV two-muon trigger if one of the muons is beyond the trigger acceptance. However, those among them which have one muon of $p_t > 20$ GeV can be recovered by a single μ trigger set at 20 GeV. In this sense we can say that the two-muon μ trigger implies the use of a single muon trigger, which can be denoted shortly: $\boxed{2\mu} \triangleright \boxed{\mu}$. This means that wherever in the tables of this chapter we quote the two-muon trigger $\boxed{2\mu}$, the single muon one $\boxed{\mu}$ is also applicable. The complete set of this kind of dependencies is given below:

- $\boxed{\mu_i} \triangleright \boxed{\mu}$
- $\boxed{\mathrm{e}_b} \triangleright \boxed{\mathrm{e}}$
- $\boxed{\text{4 jets}} \triangleright \boxed{\text{3 jets}} \triangleright \boxed{\text{2 jets}} \triangleright \boxed{\text{1 jet}}$
- $\boxed{\text{any multi-object trigger}} \triangleright \boxed{\text{all corresponding single object triggers}}$

Channels having low value of the (cross section $\times$ branching ratio) product require high luminosity to collect reasonable statistics. Some others can be better studied at low luminosities because e.g. pileup of several pp interactions, typical for high luminosity, can spoil vertex finding, etc. We denote this in the following way:

- H — high luminosity: $\mathcal{L} = 10^{34}\mathrm{cm}^{-2}\mathrm{s}^{-1}$
- L — low luminosity: $\mathcal{L} = 10^{33}\mathrm{cm}^{-2}\mathrm{s}^{-1}$
- VL — very low luminosity: $\mathcal{L} = 10^{32}\mathrm{cm}^{-2}\mathrm{s}^{-1}$

References in the tables are given in the following convention:

- **x.y.z** — chapters of the *CMS Technical Proposal* [156]
- **LOI x.y.z** — chapters of the *CMS Letter Of Intent* [155]
- **yy-xxx** — CMS Technical Note **CMS TN/yy-xxx**
- **yy/xxx** — CMS Internal Note **CMS IN yy/xxx**
- **Nyy/xxx** — CMS Note **CMS NOTE yy/xxx**
- **CRyy/xxx** — CMS Conference Report **CMS CR yy/xxx**

Empty cells correspond to the areas where study have not yet been done or the information is not available. Notation $p_t > 0$ means that no trigger threshold is required; it is enough to observe the muon in the detector.

3.3.1 Standard Model higgs

The quest for the Higgs particle is a major goal of LHC. Many physics channels were envisaged to cover the entire range of possible higgs mass — from todays limit of 77 GeV up to almost 1 TeV. The expected observability is shown in Fig. 3.2 in terms of *significance* S. It is defined as $N_S/\sqrt{N_B}$ or $N_S/\sqrt{N_S + N_B}$, where N_S and N_B stand for number of signal and background events respectively. The threshold of S=5 can be considered as a discovery limit. It corresponds to the signal being 5 standard deviations σ over the background.

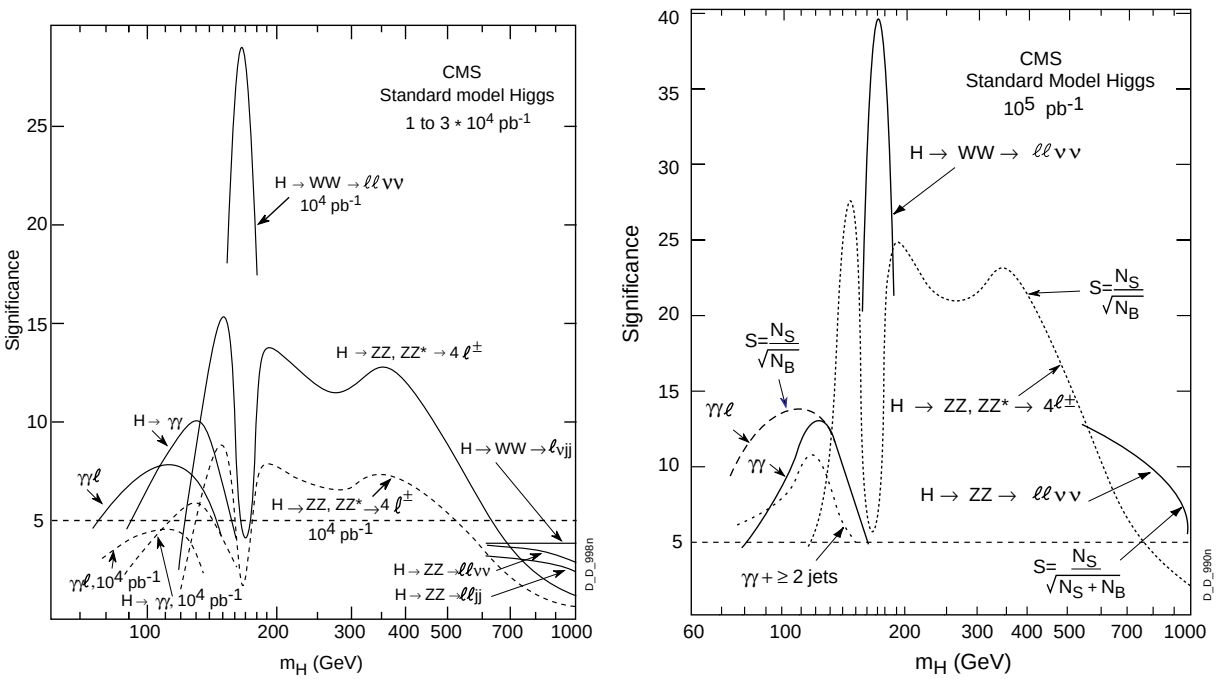

Figure 3.2: Expected observability of Standard Model higgs in CMS with integrated luminosity of $10^4\,\mathrm{pb}^{-1}$ (left plot, dashed line), $3 \cdot 10^4\,\mathrm{pb}^{-1}$ (left plot, solid line), and $10^5\,\mathrm{pb}^{-1}$ (right plot) [163].

Possible ways of triggering are reviewed in Table 3.1. It is already known from present experiments, that higgs cannot be too light. triggering should not be very difficult, because relatively high thresholds can provide high acceptance.

Table 3.1: Search for Standard Model higgs

physics channel	references	$\mathcal{L}$	offline cut (GeV)	trigger
$H \to \gamma\gamma$	12.1.2, 93-75, 94-289 94-290, CR97/6	H	$p_t(\gamma) > 40, 25$	2e
$H \to \gamma\gamma$ $+WH$ or $t\bar{t}H$	12.1.4, 93-86 94-247	H	$p_t(\gamma) > 40, 20$ $p_t(\ell) > 20$	2e eμ_i
$H \to \gamma\gamma$ je		H		2e, jet
$H \to ZZ^* \to 4\ell$	12.1.5, 93-85 94-214, 95-18	L	$p_t(e) > 20, 15, 10, 10$ $p_t(\mu)$ >10-20, 5-10, 5, 5	2e,2μ_i eμ_i
	95-19, 95-59, 95-101 96-100, N97/43	H	$p_t(e) > 20, 15, 10, 10$ $p_t(\mu) > 20, 10, 5, 5$	2e,2μ_i eμ_i
$H \to ZZ \to 4\ell$	12.1.6, 93-79 93-101, 95-11	L	$p_t(e) > 20, 15, 10, 10$ $p_t(\mu) > 10, 5, 5, 5$	2e,2μ_i eμ_i
	95-18, 95-19 95-76, 96-92	H	$p_t(e) > 20, 15, 10, 10$ $p_t(\mu) > 20, 10, 5, 5$	2e,2μ_i eμ_i
$H \to ZZ \to \ell\ell\nu\nu$	12.1.7 93-87 95-75	L	$\not{E}_t$> 100 $p_t(\ell) > 20, 20$ $p_t(Z \to \ell\ell) > 60$	$\not{E}_t$ 2e,2μ_i
	12.1.7, 92-49 94-179 95-75	H	$\not{E}_t$> 100 $p_t(\ell) > 20, 20$ $p_t(Z \to \ell\ell) > 200$	$\not{E}_t$ 2e,2μ_i
$H \to ZZ \to \ell\ell jj$	12.1.8, 93-88 95-75	L	$p_t(\ell) > 20$ $p_t(Z \to jj) > 100$	e μ
	12.1.8, 92-49 94-178, 95-75	H	$p_t(\ell) > 50$ $p_t(Z \to jj) > 150$	e μ
$H \to WW \to \ell\nu jj$	12.1.8 93-88	L	$\not{E}_t$> 100 $p_t(\ell) > 20$ $p_t(W \to jj) > 150$	$\not{E}_t$ e μ
	12.1.8, 92-49 94-178 95-154	H	$\not{E}_t$> 150 $p_t(\ell) > 150$ $p_t(W \to jj) > 300$	$\not{E}_t$ e μ
$H \to WW \to \ell^+\nu\,\ell^-\bar{\nu}$	N97/83	L,H	$p_t(\ell) > 25, 10$	2e,2μ_i,eμ_i

See also general reports: N97/57, N97/80.

Let us consider in detail the following channels:

- H (80 GeV) $\to \gamma\gamma$
- H (120 GeV) $\to ZZ^* \to 4\ell$
- H (500 GeV) $\to ZZ \to \ell\ell\nu\nu$
- H (800 GeV) $\to ZZ \to \ell\ell jj$

Figures 3.3-3.6 show how trigger acceptance depends on the thresholds. It is seen that the full acceptance is preserved for a single lepton cut at ∼20 GeV and two-lepton cut at ∼10-15 GeV. The highest single lepton threshold one can consider is ∼40-50 GeV for the light higgs (80-120 GeV) and ∼100-150 GeV for the heavy one (500-800 GeV). Beyond that the trigger acceptance is seriously degraded. These numbers will be used in the next chapter to derive requirement for the trigger and data acquisition.

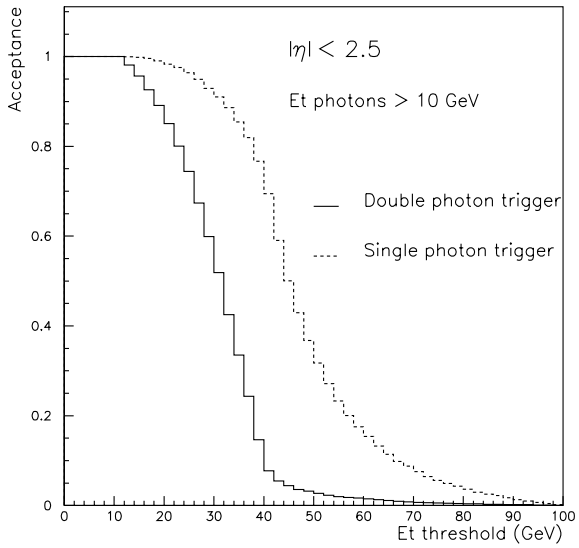

Figure 3.3: Acceptance of the single and double photon trigger for $H \rightarrow \gamma\gamma$ (m_H=80 GeV) [103].

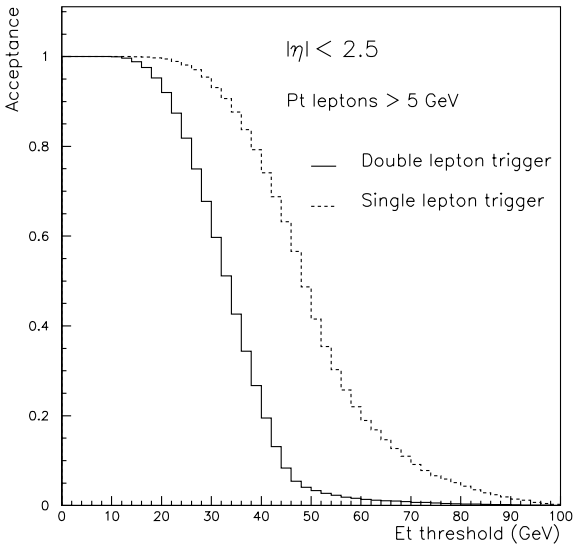

Figure 3.4: Acceptance of the single and double lepton trigger for $H \rightarrow ZZ^* \rightarrow 4\ell$ (m_H=120 GeV) [103].

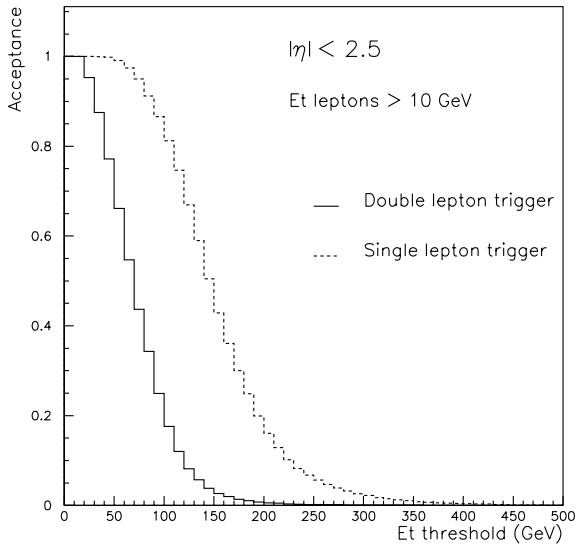

Figure 3.5: Acceptance of the single and double photon trigger for $H \rightarrow ZZ \rightarrow \ell\ell\nu\nu$ (m_H=500 GeV) [103].

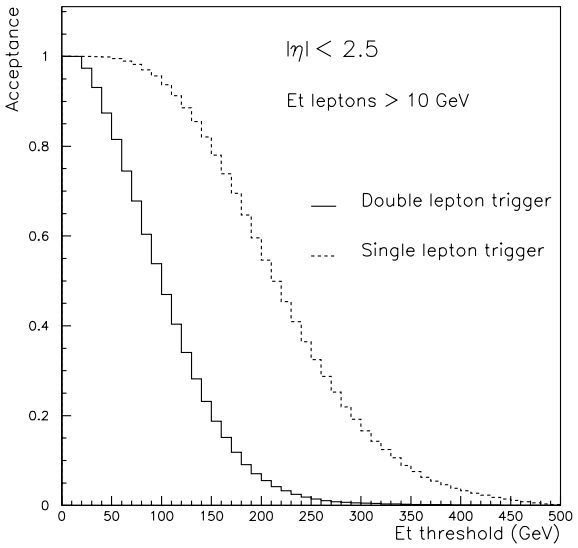

Figure 3.6: Acceptance of the single and double lepton trigger for $H \rightarrow ZZ \rightarrow \ell\ell jj$ (m_H=800 GeV) [103].

3.3.2 SUSY higgs

The case of Minimal Supersymmetric Standard Model (MSSM) is more complicated than the SM because there are two Higgs doublets. The masses of different higgses are related through the ratio of of the expectation values v_1/v_2 usually denoted as $\tan\beta$. The observability of MSSM higgses in CMS is shown in Fig. 3.7 in terms of 5σ significance contours. The triggering is not more difficult than in the SM case, as it can be seen from Table 3.2.

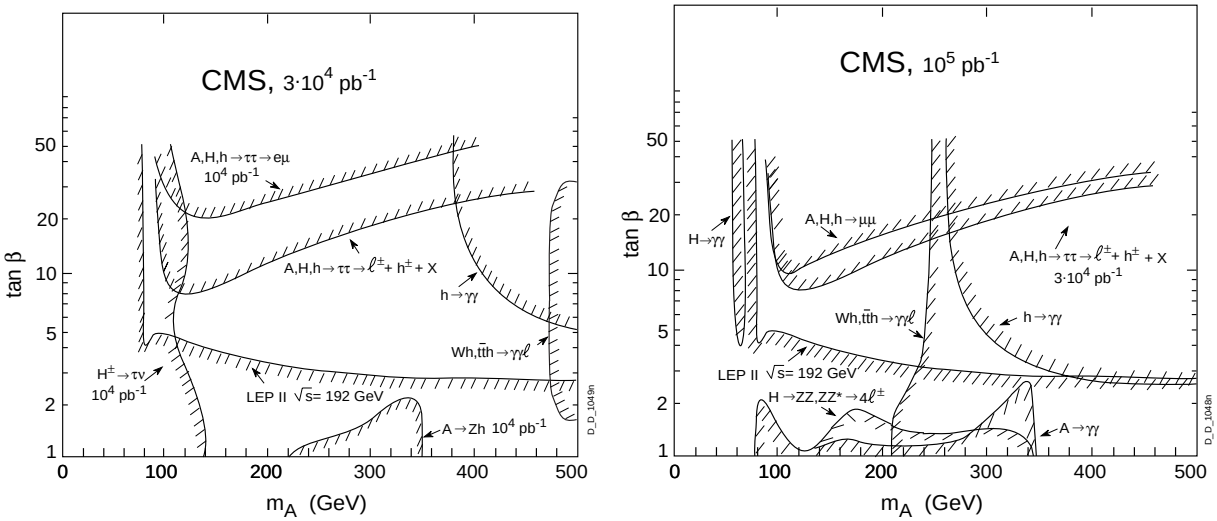

Figure 3.7: Expected observability of MSSM higgses in CMS with integrated luminosity of $3 \cdot 10^4$ pb^{-1} (left plot), and 10^5 pb^{-1} (right plot). The lines represents 5σ significance contours. Basic assumptions — $m_{top} = 175$ GeV, $m_{SUSY} = 1$ TeV, no stop mixing [163].

Table 3.2: Search for SUSY higgs

physics channel	references	$\mathcal{L}$	offline cut (GeV)	trigger
$h, H \to \gamma\gamma$	see SM $H \to \gamma\gamma$ + 96-102	H	$p_t(\gamma) > 40, 40$	
$h \to ZZ^*$	see SM $H \to ZZ^*$ + 96-96			
$h, H \to ZZ$	see SM $H \to ZZ$ + 96-96			
$h, A, H \to \tau\tau \to$ τ-jet τ-jet X		L		2τ
$h, A, H \to \tau\tau \to \ell^{\pm}$ τ-jet X	12.2.4, 93-98 93-103, 96-29 N97/2	L	$p_t(\ell) >$ 10-40, isol. $\not{E}_t >$ 20-30 $E_t^{jet} >$ 40-80	e,μ_i, τ
$h, A, H \to \tau\tau \to e\mu X$	12.2.4, 93-84	L,H	$p_t(e) > 20$ $p_t(\mu) > 20$	e,μ_i eμ_i
$t \to H^{\pm} b, \quad H^{\pm} \to \tau\nu$	12.2.5, 92-48 94-233	L	$p_t(\ell) > 20$, isol. $p_t(\mu) > 7$, b-tag	e,μ_i 2μ,eμ, τ
$h, A, H \to \mu\mu$	12.2.6-7, 94-182	L,H	$p_t(\mu) > 10, 10$	2μ_i
$A \to Zh \to \ell\ell b\bar{b}$	(12.2.8) 96-49	L	$p_t(e) > 20, 20$ $p_t(\mu) > (5,5)$ 10, 10 $E_t^{jet} > 20$	2e,2μ_i eμ
$Wh, Zh, Hh \to (\ell)\ell b\bar{b}$	12.2.9		W, Z, t	2e,2μ_i,eμ
$H \to WW \to \ell^+\nu\,\ell^-\bar{\nu}$	see SM H			

See also general reports: 93-122, N97/57.

3.3.3 Sparticles and particlinos

If the supersymmetry is indeed realised in our world, the ZOO of many new particle species will keep us busy for many years, discovering them one by one, and studying their properties. The results of those studies will have also cosmological implications, as the lightest SUSY particle can constitute a significant fraction of the dark matter in the universe. The expected observability of SUSY is shown in Figs 3.8 and 3.9 as 5σ significance contours in the $(m_0, m_{1/2})$ plane, m_0 being a common scalar mass, $m_{1/2}$ — the mass of gaugino.

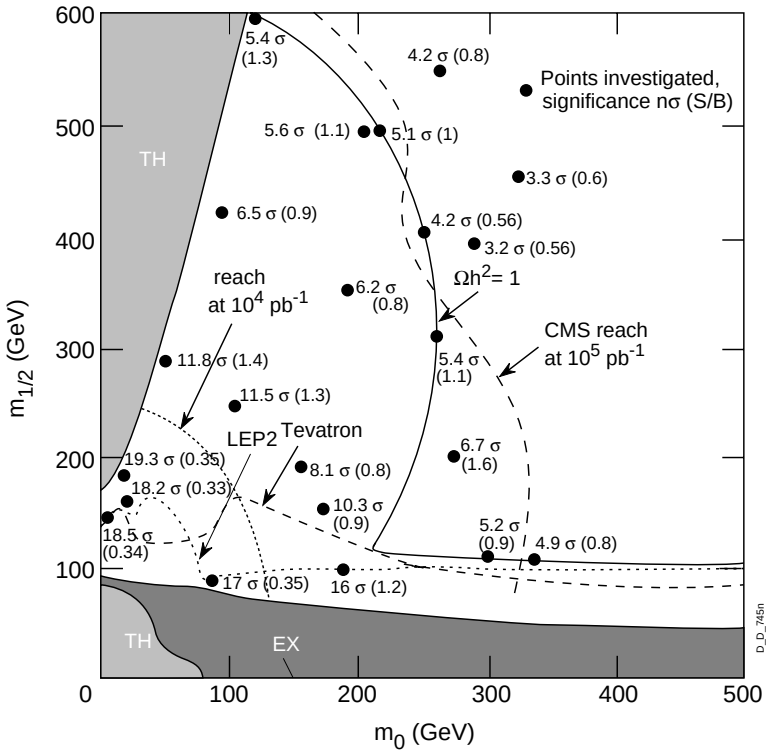

Figure 3.8: Expected observability of sleptons in 2 lepton final state in SUGRA MSSM with $\tan\beta$=2, A_0=0, $\mu<0$ [164]. The dashed lines represents 5σ significance contours. The solid line represents cosmological Ωh^2=1 boundary. Shaded areas are excluded by theory (TH) or by previous experiments (EX).

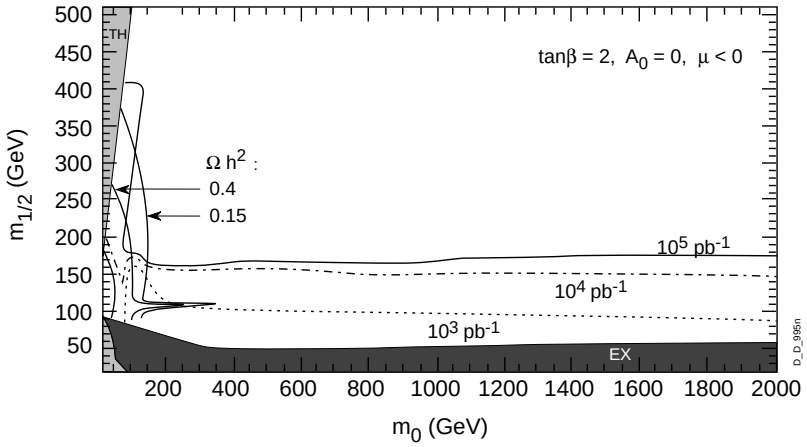

Figure 3.9: Expected observability of chargino and neutralino in $\tilde{\chi}_i^{\pm}\tilde{\chi}_j^0 \rightarrow 3\ell + \not{E}_t$+ no jets [165]. The lines represents 5σ significance contours for different integrated luminosities. Relic neutralino matter density Ωh^2 contours are also given. Shaded areas are excluded by theory (TH) or by previous experiments (EX).

The channels already studied by simulation in CMS are listed in Table 3.3. Complicated cascade decays will create many hard leptons, very useful for triggering. Squarks will produce numerous jets. Neutralinos and gravitino might be detected by missing energy $\not{E}_t$.

Table 3.3: Search for SUSY partners

physics channel	references	$\mathcal{L}$	offline cut (GeV)	trigger
$\tilde{g}\tilde{g}$, $\tilde{q}\tilde{q}$ $\rightarrow$ 1-4 ℓ χ_1^0 2jets	95-90, 95-91, 94-318 96-22, 96-95, 96-103 N97/15, N97/16	L,H	$p_t(\ell) > 10$-20 $\not{E}_t > 100$ $E_t^{jet} > 40$	2e, $2\mu_i$, eμ
$\tilde{q}\tilde{q}$ $\rightarrow$ 4 jets	N97/67	L,H	$E_t^{jet} > 100, 100, 100, 100$	E_t^{jet}
$\tilde{q}\tilde{g}$ $\rightarrow$ χ_i^0 $\rightarrow$ χ_j^0h h $\rightarrow$ b$\bar{\text{b}}$	N97/70	L,H	$\not{E}_t > 100$ $E_t^{jet} > 20, 20, 20, 20$	$\not{E}_t$
$\tilde{\ell}\tilde{\ell}$ $\rightarrow$ 2-3 ℓ χ_1^0's	96-59	L,H	$p_t(\ell) > 20$ $\not{E}_t > 50$	2e, $2\mu_i$, eμ
$\chi_2^0\chi_1^\pm$ $\rightarrow$ $\ell\ell$ χ_1^0 $\ell'\nu\chi_1^0$	N97/7, N97/65 N97/69, N97/94	L,H	$p_t(\ell) > 15$	2e, $2\mu_i$, eμ
$\chi_1^0\chi_1^0$ $\rightarrow$ $\tilde{\text{G}}\gamma$ $\tilde{\text{G}}\gamma$	N97/79	L,H	$p_t(\gamma) > 40, 40$ $\not{E}_t > 100$	2e, $\not{E}_t$

See also general reports: 93-125, 95-66, 96-58, 96-65, CR97/9, CR97/12, CR97/19.

3.3.4 Alternative models and exotica

Higgs mechanism is not the only possibility of explaining the masses of fundamental fermions. Alternative models often predict new particles, like additional gauge bosons W' and Z'. A few examples are given in Table 3.4. The new particles are expected to be as heavy as several hundred GeV and they produce very hard leptons, easy to trigger.

Table 3.4: Search for exotic particles

physics channel	references	$\mathcal{L}$	offline cut (GeV)	trigger
VV scattering	12.1.9, 94-276	H	$p_t(W, Z) > 300$	2e, $2\mu_i$, eμ
$W' \rightarrow \mu\nu$	LOI 8.1.3	H		μ_i
$W' \rightarrow WZ \rightarrow \mu^\pm\nu\mu^+\mu^-$	LOI 8.1.3, 93-57	H	$p_t(\mu) > 100, 100, 100$	$2\mu_i$
$Z' \rightarrow \mu\mu$	LOI 8.1.3, 93-107	L,H	$p_t(\mu) > 20, 20$	$2\mu_i$
leptoquarks LQ (scalar, $\sim$1.5 TeV)	CR96/3	H	$p_t(\mu) > 200, 200$ $E_t^{jet} > 200, 200$	$2\mu_i$ $2\mu_i$
compositness ($Z \rightarrow \gamma\gamma\gamma$)	94-188	H	$p_t(\gamma) > 20, 20, 10$	2e
technicolor ρ_T, ω_T		H		

3.3.5 b-quark physics

The b-quark physics seems to be the most challenging task for the muon trigger. Muons from b decays are very soft and their spectrum is rapidly falling down with p_t. Therefore the trigger thresholds should be as low as possible to preserve relatively high acceptance. This is well seen in Table 3.5.

Table 3.5: Study of the b-quark physics

physics channel	references	$\mathcal{L}$	offline cut (GeV)	trigger
$B_d^0 \to J/\psi\, K_s^0 \to \ell^+\ell^-\pi^+\pi^-$ $b \to \mu_{tag}$ or $b \to$e$_{tag}$	12.4.2, 12.4.4, 93-69 94-193, 96-105 96-116, 96-117	L	$p_t(\mu) >$ 2-4, 2-4, 0 p_t(e) $> 5, 5, 2$	2μ e$_b\mu$
$B_d^0 \to J/\psi\, K_s^0 \to \ell^+\ell^-\pi^+\pi^-$ with self-tagging or b-jet tagging	95-39	L	$p_t(\mu) >$ 2-4, 2-4 p_t(e) $> 5, 5$	
$B_d^0 \to J/\psi\, K_s^0 \to \ell^+\ell^-\pi^+\pi^-$ with Λ tagging	94-189	L	$p_t(\mu) >$ 2-4, 2-4 p_t(e) $> 5, 5$	
$B^\pm \to J/\psi\, K^\pm,\ b \to \mu_{tag}$	12.4.5	L	$p_t(\mu) >$ 2-4, 2-4, 0	2μ
$B_d^0 \to J/\psi\, K^{*0},\ b \to \mu_{tag}$	94-237, 96-105	L	$p_t(\mu) >$ 2-4, 2-4, 0	2μ
$B_s^0 \to J/\psi\, \phi,\ b \to \mu_{tag}$	N97/72	L	$p_t(\mu) >$ 2-4, 2-4, 0	2μ
$B_d^0 \to \pi^+\pi^-$ $b \to \mu_{tag}$ or $b \to$e$_{tag}$	12.4.3-4, 94-114 94-328	L	$p_t(\mu) > 6.5$ p_t(e) > 10 $p_t(\pi) > 5$	μ e$_b$
$B_s^0 \to D_s^{(*)\pm}\mu X$	12.4.5	L	$p_t(\mu) > 10$	μ
$B_d^0 \to D^{*\pm}\mu X$	94-184	L	$p_t(\mu) > 10$	μ
$B_s^0/\bar{B}_s^0 \to D_s^\mp,\ D_s^\mp \to \phi\pi^\mp$ $\phi \to K^+K^-,\ b \to \mu_{tag}$	12.4.6, 93-117 94-183, 94-184	L	$p_t(\mu) > 10$	μ
$B_s^0 \to \mu^+\mu^-$	12.4.7, 94-186	L	$p_t(\mu) > 4.3, 4.3$	2μ
$\Lambda_b \to J/\psi\, \Lambda$	94-227	L	$p_t(\mu) >$ 2-4, 2-4	
$\Xi_b \to J/\psi\, \Xi$				
$\Lambda_b \to \Lambda_c^+\pi^- \to p\, K^+\pi^-\ \pi^-$	94-227	L		
$\Lambda_b \to \Lambda_c^+\pi^- \to p\, K^0\ \pi^-$				

See also general reports: 94-229, 95-10, 95-178, 96-139, CR96/2, CR96/5.

3.3.6 t-quark physics

The LHC is a real top quark factory. Even at the initial luminosity of $10^{33}\mathrm{cm}^{-2}\mathrm{s}^{-1}$ the $t\bar{t}$ pairs will be produced copiously at the speed of one per minute. The rates of muons from top events are shown in Figs 3.10 and 3.11 as diamonds. One can see from Table 3.6 that the triggering is rather easy. An interesting case is the last channel in the table. It offers the most precise measurement of the top mass, because of the J/ψ constraint. However, muons from J/ψ are very soft and the trigger threshold should be as low as possible. In fact this is the only channel which may require three muon trigger.

Table 3.6: Study of the top quark

physics channel	references	$\mathcal{L}$	offline cut (GeV)	trigger
$t\bar{t} \rightarrow W^{\pm}_{\rightarrow \mu\nu}\, W^{\mp}_{\rightarrow X}$	LOI 8.1.4	VL	$p_t(\mu) > 50$ $E_t^{jet} > 50$	μ_i
$t\bar{t} \rightarrow W^{\pm}_{\rightarrow \mu\nu}\, W^{\mp}_{\rightarrow X}\, b/\bar{b}_{\rightarrow \mu}$	92-34	L	$p_t(\mu) > 40, 15$ $E_t^{jet} > 30$	2μ,μ_i
$t\bar{t} \rightarrow W^{\pm}_{\rightarrow \mu\nu}\, W^{\mp}_{\rightarrow X}\, b_{\rightarrow \mu}\, \bar{b}_{\rightarrow \mu}$	93-73	L	$p_t(\mu) > 30, 4, 4$ $E_t^{jet} > 30$	2μ,μ_i
$t\bar{t} \rightarrow W^{\pm}_{\rightarrow \mu\nu}\, W^{\mp}_{\rightarrow X}\, b/\bar{b}_{\rightarrow J\psi \rightarrow \mu\mu}$	93-118	L,H	$p_t(\mu) > 30, 4, 4$ $E_t^{jet} > 30$	2μ,μ_i
$t\bar{t} \rightarrow W^{\pm}_{\rightarrow \mu\nu}\, W^{\mp}_{\rightarrow X}\, \bar{b}_{\rightarrow \mu}\, b/\bar{b}_{\rightarrow J\psi \rightarrow \mu\mu}$		H	$p_t(\mu) > 15, 4, 4, 4$ $E_t^{jet} > 30$	3μ,μ_i

3.3.7 Minimum bias, QCD and Standard Model physics

Table 3.7: Study of minimum bias, QCD and Standard Model physics

physics channel	references	$\mathcal{L}$	offline cut (GeV)	trigger
SM tests: $WZ, W\gamma$				2e, $2\mu_i$, eμ
"soft physics"		L	min. bias	min. bias
inclusive W		L,H		e, μ_i
inclusive Z		L,H		2e, $2\mu_i$

Many new expected particles decay to W or Z bosons. Therefore the inclusive W and Z production can be considered as bench mark processes for the trigger. The rates muons from W and Z events are shown in Figs 3.10 and 3.11 as triangles. They should be compared to "minimum bias" rates, indicated by squares. By "minimum bias" muon rates we understand here the rate of muons created by decays of u, d, s, c, and b quarks.

There are several important observations to be done on Figures 3.10 and 3.11. First, the p_t^{cut} dependence of the rate is very strong. Therefore, changing the p_t cut can be a very effective tool of controlling the trigger rate. Second, the double muon rate is two orders of magnitude lower than the single muon rate for the same threshold. Thus, the trigger p_t threshold can be much lower for the processes producing more than one muon. Third, the muon rate below $p_t = 10$ GeV is dominated by "minimum bias" physics. All these observations have an important impact on the design of the muon trigger, which will be described in the next chapters.

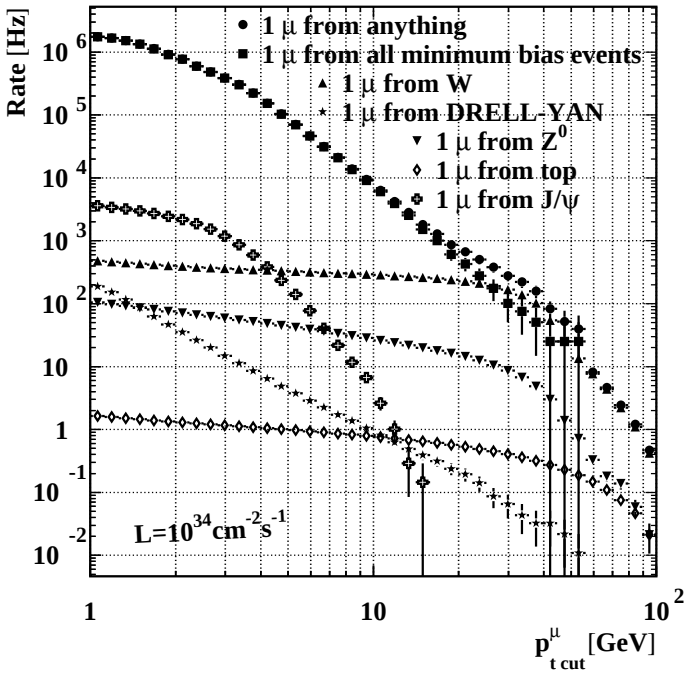

Figure 3.10: Single muon rates ($|\eta| < 2.4$) [80]. The rate is defined as a number of events with at least one muon with transverse momentum p_t^μ above a given threshold p_{tcut}^μ.

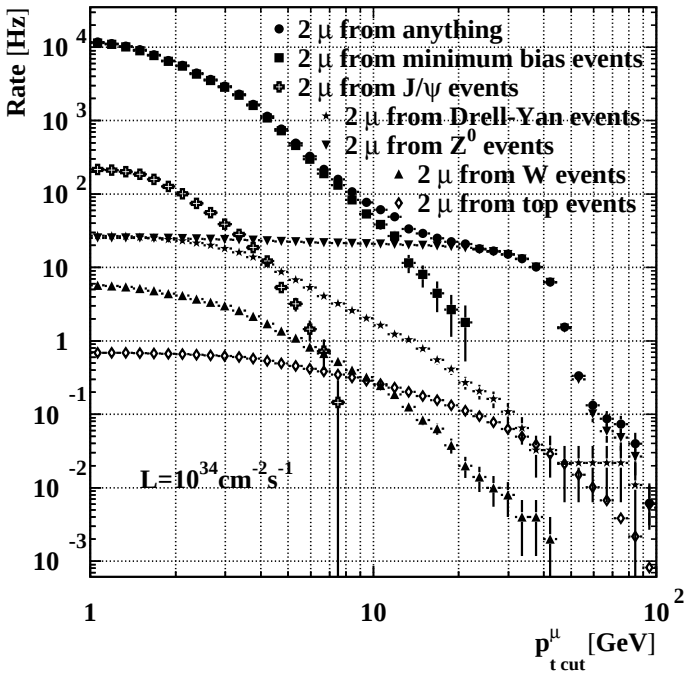

Figure 3.11: Double muon rates ($|\eta| < 2.4$) [80]. The rate is defined as a number of events with at least two muon with transverse momentum p_t^μ above a given threshold p_{tcut}^μ. Notation "*2 μ from top events*" means that at least one muon in each event comes from t or $\bar{t}$ decay. The second one may come from another source, e.g. π or K decay.

3.3.8 Heavy ion physics

Heavy ion physics is the very special case. Let us concentrate here on the extreme example of Pb-Pb collisions. They will occur with luminosity as low as $10^{27}\mathrm{cm}^{-2}\mathrm{s}^{-1}$, but the density of particles in each event will be about 1000 times higher than in a single pp collision. On the other hand the particle spectra are very soft which requires low trigger thresholds. The requirements for the muon trigger are very different from those for pp collisions and we refer the interested reader to a dedicated study [77].

Table 3.8: Study of heavy ion physics

physics channel	references	$\mathcal{L}$	offline cut (GeV)	trigger
heavy ions: $\Upsilon \rightarrow \mu^+\mu^-$	12.5.1, N97/89, N97/95	–	$p_t(\mu) >$ 2-4, 0	μ
heavy ions: $Pb\,Pb \rightarrow jets$	12.5.2	–	$E_t^{jet} > 50$	2 jets

See also general reports: CR97/15, IN97/32.

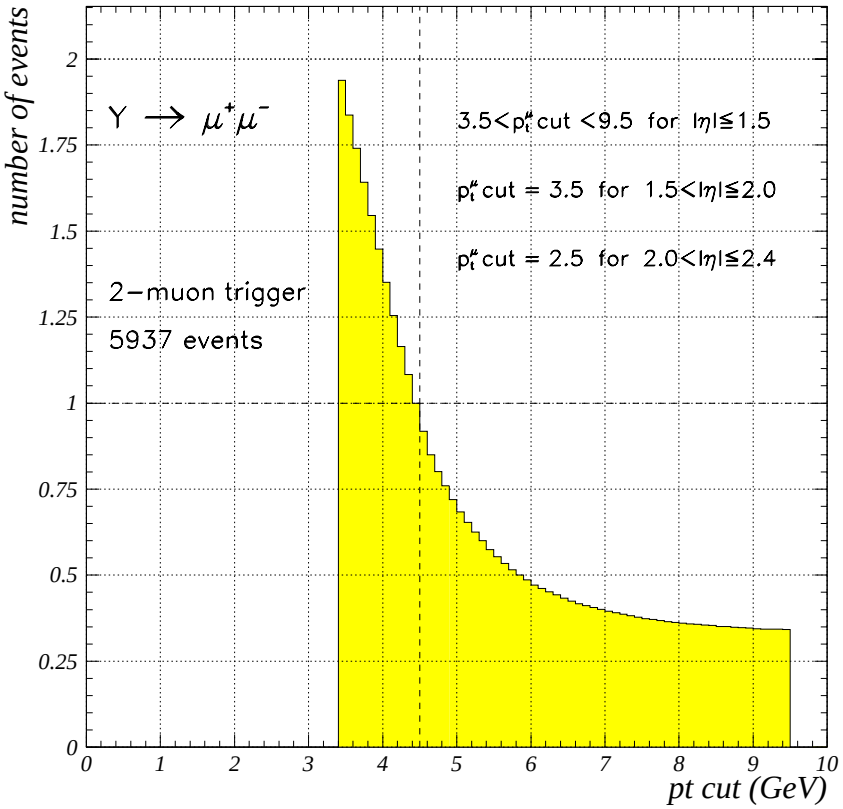

Figure 3.12: Acceptance for $\Upsilon \rightarrow \mu^+\mu^-$ as a function of muon trigger threshold p_t^{cut}, normalised to $p_t^{cut} = 4.5$ GeV.

Chapter 4

CMS Trigger system

4.1 Physics requirements

Particles discussed in the previous chapter can be divided into three classes, as shown in Table 4.1. Each class has different requirements for the trigger.

Table 4.1: Particles to be studied at LHC.

	light	medium	heavy
mass	$\ll 100$ GeV	~ 100 GeV	$\gg 100$ GeV
particle	b-quark	t, W, Z, light higgs	heavy higgs, Z′, W′, SUSY particles
luminosity	$10^{33}\mathrm{cm}^{-2}\mathrm{s}^{-1}$	$10^{33}\mathrm{cm}^{-2}\mathrm{s}^{-1}$, $10^{34}\mathrm{cm}^{-2}\mathrm{s}^{-1}$	$10^{34}\mathrm{cm}^{-2}\mathrm{s}^{-1}$

From the tables of the previous chapter one can see that most of the interesting physics processes produce at least two trigger objects. Only a very few channels require single-object triggers *per se*. Those are:

- $h, A, H \to \tau\tau \to \ell^{\pm}\tau$-jet$X$
- $B_d^0 \to \pi^+\pi^-$ with $b \to \mu_{tag}$ or $b \to \mathrm{e}_{tag}$
- $B_s^0/\bar{B}_s^0 \to D_s^{\mp}$, $D_s^{\mp} \to \phi\pi^{\mp}$, $\phi \to K^+K^-$, $b \to \mu_{tag}$
- inclusive W

In the first two channels one can still try to apply multi-object triggers looking at the τ-jet or treating the $\pi^+\pi^-$ pair as a kind of narrow jet.

The fact that multi-object triggers are of primary importance at LHC has very substantial implications for the principle of the trigger operation. Different combination of objects may require different trigger thresholds. Therefore one should not perform any cut on single objects on the level of muon or calorimeter trigger.[1] These triggers can only recognise objects, estimate their p_t or E_t and send them to the Global Trigger. The Global Trigger is the only place when the objects are combined and the cuts are applied depending on a given combination.

It has been shown [103] that medium and heavy particles (see Table 4.1) can be effectively recognised applying a logical OR of the following conditions:

- single $\ell^{\pm}$ or γ with $p_t > 60$ GeV,
- two $\ell^{\pm}$ or γ with $p_t > 15$ GeV,
- $\not{E}_t > 150$ GeV.

The rate of processes selected by these criteria is dominated by standard physics background (Table 4.2), and it does not exceed 100 Hz. This does not include instrumental background and therefore the First Level Trigger (LV1) rate can be much higher. However, the instrumental background should be eliminated by higher trigger levels, and one can consider the rate of 100 Hz as a first estimate of needed mass storage (e.g. tape drives) capacity.

Single-object triggers are used mainly to recover the multi-object events which were not recognised by the multi-object triggers, because of incomplete acceptance. Therefore, the criteria on their thresholds are not very

[1] There are some instrumental limitations on detecting very soft particles, e.g. curling of the tracks of $p_t < 0.7$ GeV, etc.

Table 4.2: Standard physics background at LHC for $\mathcal{L} = 10^{34}\mathrm{cm}^{-2}\mathrm{s}^{-1}$.

condition	process	rate
1γ of $E_t > 60$ GeV	$\pi^0 \to \gamma\gamma$	10 Hz
2γ of $E_t > 15$ GeV	$\pi^0 \to \gamma\gamma$	10 Hz
$1\ell^{\pm}$ of $p_t > 60$ GeV	$W \to \ell$, jet$\to \ell$	10 Hz
$2\ell^{\pm}$ of $p_t > 15$ GeV	$Z \to \ell^+\ell^-$	20 Hz
$\not{E}_t > 150$ GeV	QCD jets	10 Hz

strict. The actual working point should be chosen as a result of the trade off between the efficiency and the rate. A reasonable upper limit is about 100 GeV. Beyond this point efficiency for various heavy objects is significantly degraded (see Chapter 3). The useful lower limit for μ/e/γ at $\mathcal{L} = 10^{34}\mathrm{cm}^{-2}\mathrm{s}^{-1}$ is about 20 GeV. Below this value one cannot further improve the efficiency for objects like W, Z or heavier, whereas the rate is dominated by leptons from quark decays (except the top quark). At this point, the rate of every single object is of the order of a kHz (see e.g. Fig. 3.10). Adding all the channels together and leaving some room for an instrumental background one can expect the total LV1 of the order of 10^4 Hz. Thus, in order to have some safety margin, the Second Level Trigger (LV2) should be able to receive $\sim 10^5$ Hz of events.

One can conclude this section with the following list of requirements:

- mass storage should be able to accept 100 Hz of events;
- input of the LV2 should be able to accept 100 kHz of events;
- muon and calorimeter LV1 recognise objects and estimate their p_t or E_t; cuts are applied by the Global LV1;
- expected thresholds for photons, electrons and muons are as shown in Table 4.3

Table 4.3: Expected LV1 thresholds [GeV].

	e/γ	2 e/γ	e$_b$	2 e$_b$	μ	2 μ
$\mathcal{L} = 10^{33}\mathrm{cm}^{-2}\mathrm{s}^{-1}$	15-40	10	10	5	10	5
$\mathcal{L} = 10^{34}\mathrm{cm}^{-2}\mathrm{s}^{-1}$	20-100	15	—	—	20-100	10

4.2 Technical implementation

Bunch crossings occur at the LHC every 25 ns. The LV1 has to be able to analyse each crossing. The time of 25 ns is by far not enough to recognise a trigger object and measure its p_t or E_t. Therefore the CMS LV1 trigger utilises pipeline processor technique. Any trigger algorithm is divided in steps. Each step is performed in 25 ns time by a trigger processor unit. The result is latched, and at the end of a 25 ns period it is sent to the next processor unit and the data from the new bunch crossing are taken. This way the trigger decision is delivered at the end of the chain every 25 ns, regardless of the chain length.

Detector data must wait for the LV1 trigger decision in pipeline memories. The data from a given bunch crossing are shifted to the next memory unit every 25 ns. At the end of the pipeline they have to meet the trigger decision and they are either read out or discarded. Thus the length of the readout pipeline must be equal to the total LV1 latency.

Different detectors use either digital or analog pipeline memories. There are technical limitations on the length of analog pipeline memories. At present memories as long as 120-150 bunch crossings are feasible. This implies that the total LV1 latency should not be longer than 3 μs.

The LV1 trigger scheme described above is common for ATLAS and CMS. The two experiments differ in the implementation of higher level triggers (Fig. 4.1). In the case of ATLAS the division between the LV2 and LV3 is fixed. The LV3 consists of commercial processors performing standard physics analysis. The LV2 is a custom build hardware device consisting of a number of dedicated DSP-like processors. The LV2 processors analyse data only from a *Region of Interest* (RoI) — fraction of the detector indicated by the Fist Level Trigger.

In the case of CMS the LV2/LV3 division is flexible. One can even imagine higher number of levels, depending on actual needs. This is because all higher level triggering is performed by a powerful farm of commercial processors called *Event Filter Farm*.

Description of the Event Filter Farm exceeds the scope of this report. In the next section we briefly describe the calorimeter LV1. The rest of the paper is devoted to the detailed description of the muon LV1.

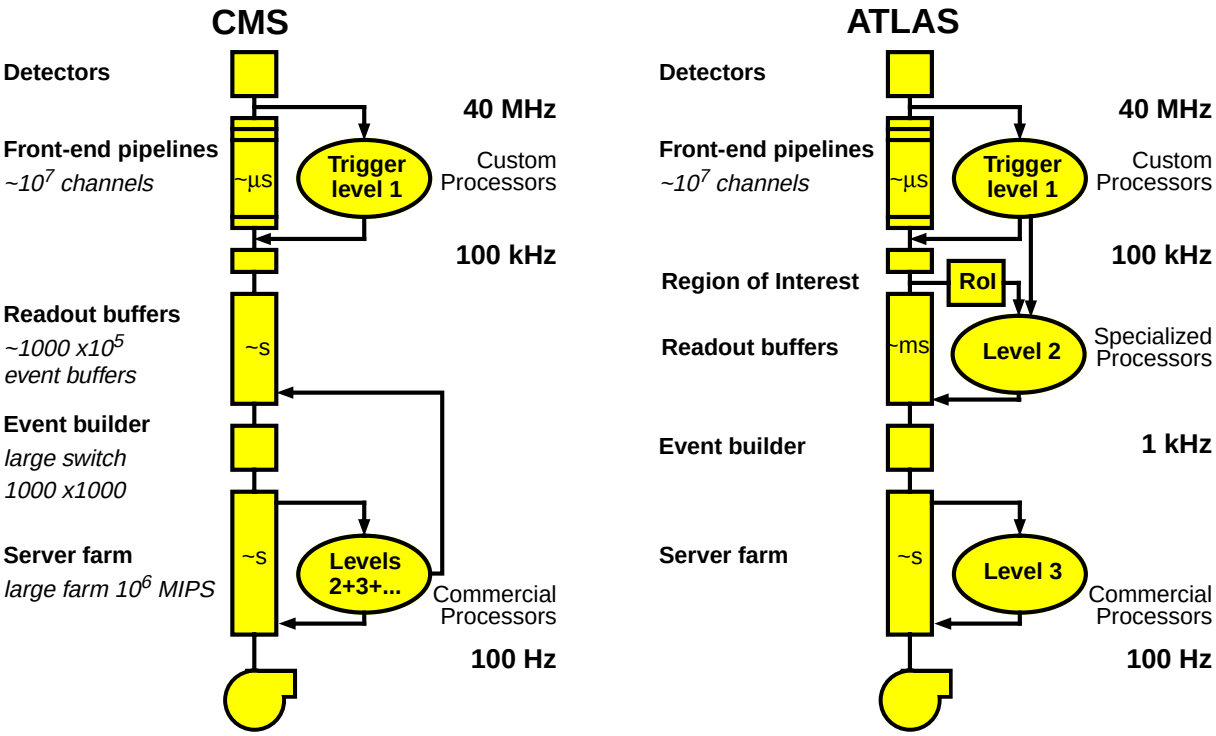

Figure 4.1: Trigger and DAQ scheme of CMS (left) and ATLAS (right).

4.3 Calorimeter Trigger

4.3.1 Segmentation

Calorimeter trigger is based on three kind of detectors: electromagnetic calorimeter ECAL (pseudorapidity $|\eta| < 3.0$), hadronic calorimeter HCAL ($|\eta| < 3.0$), and very forward calorimeter HF ($2.6 < |\eta| < 5.0$).

HCAL is designed as a copper/scintillator sandwich. Its readout is arranged in towers of $\Delta\eta \times \Delta\phi = 0.087 \times 0.087$. This size defines *calorimeter trigger cell*.

ECAL is made out of $PbWO_4$ crystals. Each crystal in the barrel has a size of $\Delta\eta \times \Delta\phi = 0.0145 \times 0.0145$, thus each trigger cell contains 6×6 crystals (see Fig. 4.2). Each cell is divided into 6 *strips* of $\Delta\eta \times \Delta\phi = 0.0145 \times 0.087$ i.e. 1×6 crystals. In the endcaps the number of crystals per cell depends on pseudorapidity.

Proposed HF segmentation is about $\Delta\eta \times \Delta\phi = 0.035 \times 0.035$ for $2.6 < |\eta| < 4.0$ and 1.0×0.7 for $4.0 < |\eta| < 5.0$. It is still being optimised.

4.3.2 Trigger primitives

The following *trigger primitives* are generated by the calorimeter front-end electronics:

- transverse energy G_t inside an ECAL cell, $G_t = G_{\text{cell}} \cdot \sin\theta$
- fine grain local isolation bit LI,
- transverse energy H_t inside an HCAL cell, $H_t = H_{\text{cell}} \cdot \sin\theta$
- MIP bit – energy deposit compatible with minimum ionising particle.

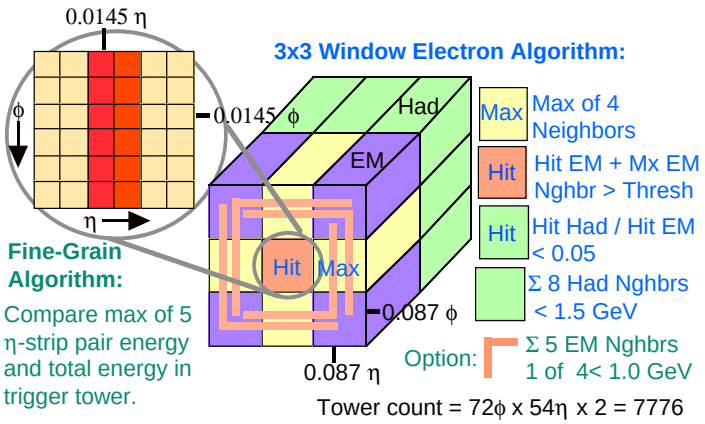

Figure 4.2: Calorimeter trigger primitives and cuts. The cuts are denoted here in a symbolic way only, and they are described in detail in the text.

The local isolation bit LI for each cell is computed in the following way. For each pair i of adjacent strips in the 6×6 ECAL cell a sum L_t^i of transverse energy deposits is calculated. The largest one L_t^{max} is found. The ratio $R = L_t^{max}/G_t$ is compared to a programmable threshold R^{thres}. If $R > R^{thres}$ the LI bit is set.

4.3.3 Electron/photon trigger

Let us introduce the following symbols for calorimeter cells and transverse energy deposited in them (see Fig. 4.2)

- G_t^{hit} — the ECAL cell containing most of the energy (denoted "Hit" in the figure)
- G_t^{max} — cell with maximal G_t of four G_t^{hit} neighbours (denoted "Max" in the figure)
- H_t^{hit} — the HCAL cell behind the G_t^{hit}
- Σ_8^H — sum of H_t of 8 HCAL cells around H_t^{hit}
- Σ_5^G — sum of G_t of 5 ECAL cells (L-shaped "corner") around G_t^{hit}
- E_t^{thres} — the transverse energy threshold

An electron/photon candidate has to fulfil the following requirements:

1. $G_t^{hit} + G_t^{max} > E_t^{thres}$ (transverse energy threshold)
2. $R = L_t^{max}/G_t^{hit} > 0.89$ (lateral shower profile – "cluster shape")
3. $H_t^{hit}/G_t^{hit} < 0.05$ (longitudinal shower profile)
4. $\Sigma_8^H < 1.5$ GeV (hadronic isolation)
5. At least one of four $\Sigma_5^G < 1.0$ GeV (electromagnetic isolation)

The first condition is a simple transverse energy threshold. An electromagnetic energy contained within two calorimeter cells is considered.

The second condition makes use of the fact that electromagnetic shower caused by a single electron is relatively narrow and at least of 89% of its energy is contained within an area of $\Delta\eta \times \Delta\phi = 2 \times 6$ strips.

The third condition is designed to get rid of charged hadrons. A shower caused by an electron should be contained within the electromagnetic calorimeter. Only up to 5% of energy is allowed to leak into the hadronic compartment.

The last two conditions are needed to suppress the π^0 background. Two photons coming from a π^0 decay are very difficult to distinguish from an electron. However, π^0 are mostly produced within jets, whereas electrons from decays of interesting particles are well isolated. The forth condition imposes a hadronic isolation. The total energy contained in 8 hadronic cells surrounding the impact point of electron should be smaller than 1.5 GeV. The

fifth condition is an electromagnetic isolation. It is required that the energy surrounding the 4 cells containing an electron is lower than 1 GeV.

The conditions are designed in such a way that the data flow from the calorimeter to the trigger processors and number of interconnections are minimised. The actual values of the cuts are results of complicated optimisation. They are designed to suppress significantly the background maintaining high efficiency for electrons. Brief discussion on this subject one can find in Section 4.3.9. For more details we refer the reader to the original papers [141]-[151].

4.3.4 The b-electron trigger

In order to reduce the E_t^{thres} for electrons from b-quark decays an additional requirement should be imposed. One can make use of the fact that a b-electron is slightly separated from the remnants of other decay products. This kind of isolation can be achieved by tightening the cut on the R parameter. Normal hadronic and electromagnetic isolation should not be, however used. Thus the b-electron is selected as follows

1. $G_t^{hit} + G_t^{max} > E_t^{thres}$ (transverse energy threshold)
2. $R = L_t^{max}/G_t^{hit} > 0.95$ (lateral shower profile)
3. $H_t^{hit}/G_t^{hit} < 0.05$ (longitudinal shower profile)

4.3.5 Jet trigger

Jet trigger is the simplest one and it consist of only one condition. The transverse energy contained within one calorimeter region (4×4 cells) should be higher than threshold:

$$\sum_{4\times 4}(G_t + H_t) > E_t^{thres}$$

4.3.6 Missing transverse energy trigger

Let us define for each calorimeter cell two energy components:

$$E_x = (G_t + H_t) \cdot \cos\phi$$

$$E_y = (G_t + H_t) \cdot \sin\phi$$

where ϕ is the azimuthal position of the cell. Missing transverse energy $\not{E}_t$is defined as

$$\not{E}_t = \sqrt{\left(\sum_{|\eta|<5} E_x\right)^2 + \left(\sum_{|\eta|<5} E_y\right)^2}$$

Thus the missing transverse energy is a vector sum of E_t deposits in all calorimeter cells. The missing energy trigger requires the $\not{E}_t$value to be above the threshold.

4.3.7 Total transverse energy trigger

The total E_t trigger requires the scalar sum of E_t deposits in all calorimeter cells to be above the threshold:

$$E_t^{tot} = \sum_{|\eta|<5} (G_t + H_t) > E_t^{thres}$$

4.3.8 The τ trigger

The τ trigger is similar to the jet trigger with additional requirement that the size of the jet should be limited. Details of the algorithm are still under optimisation and the reader is referred to current technical notes on the subject (see e.g. [140]).

4.3.9 Calorimeter Trigger performance

For a detailed discussion of the Calorimeter Trigger performance we refer the reader to the specialised papers [141]-[151]. Here we would like to present only a few examples. We have chosen the triggers related to an electron. The single and double electron/gamma trigger rates are shown in Figures 4.3 and 4.4 respectively. The raw trigger rate is subsequently reduced by adding new requirements. The usefulness of all requirements is clearly seen, as each one reduces the trigger rate by factor 2-4.

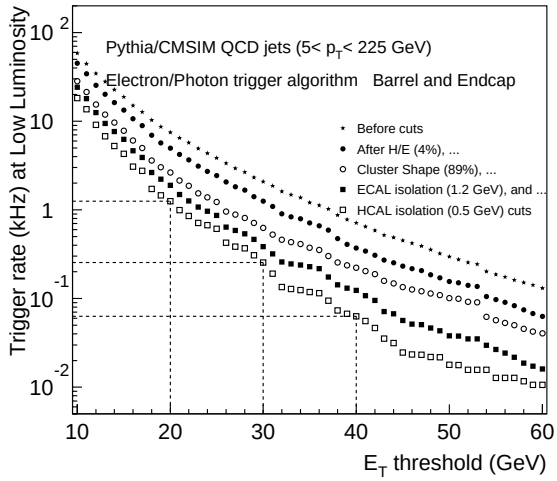

Figure 4.3: Single e/γ trigger rate [145]

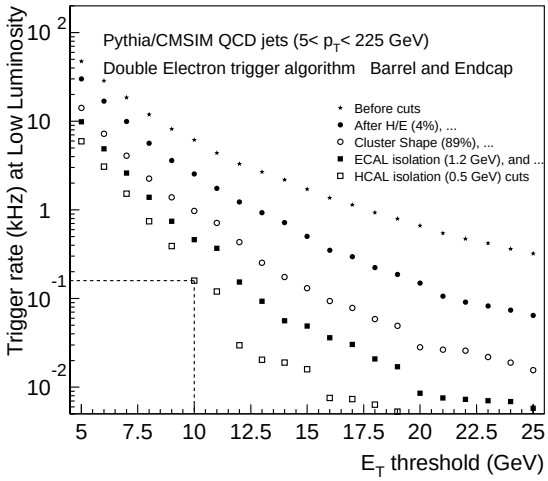

Figure 4.4: Double e/γ trigger rate [145]

As described in Sec. 4.3.4, different set of requirements was found to be useful for electrons from b-quark decays. It is illustrated in Figures 4.5 and 4.6. The effect of the cut on the lateral shower profile (fine grained algorithm) is shown in Fig. 4.5 for two different thresholds. Changing this threshold, one can exploit the trade off between efficiency and rate in order to optimise the signal/background ratio.

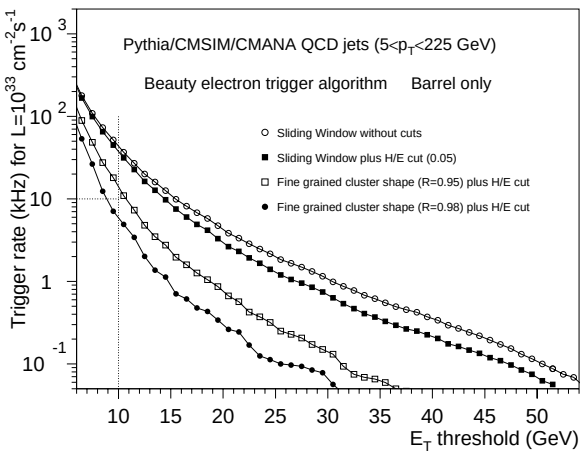

Figure 4.5: Single b-electron trigger rate [144]

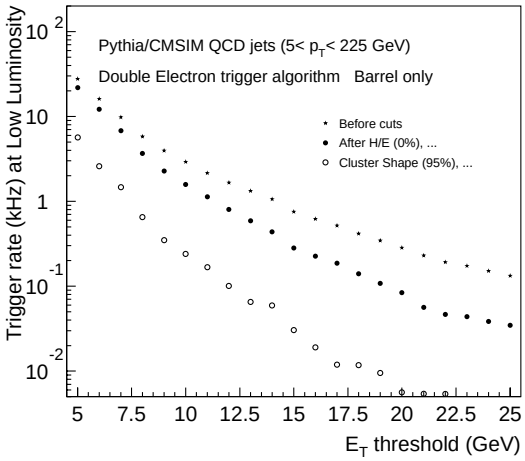

Figure 4.6: Double b-electron trigger rate [145]

Chapter 5

CMS Muon Trigger design issues

5.1 Requirements

General requirements described in the previous chapter can be defined much more precisely for the specific case of the muon trigger. They are listed below together with brief justifications. More detail discussion will follow in subsequent chapters.

The basic tasks of the CMS Muon Trigger are:

- **muon identification,**
- **transverse momentum measurement,**
- **bunch crossing identification.**

It has to fulfil the following requirements.

Geometrical coverage: up to $|\eta| = 2.4$, in order to cover the entire area of the muon system.

Latency: $< 3.2\mu$s. Total trigger processing, including 2×120 m optical fibres (1.2 μs) to the control room, should stay within the length of the tracker pipelines equal to 128 bunch crossings. This implies that the trigger algorithms cannot be too complicated.

Trigger dead time: not allowed. Every bunch crossing has to be processed in order to maintain high efficiency crucial for many physics channels with low cross section.

Maximal output rate: 15 kHz for luminosities $\leq 10^{34}\mathrm{cm}^{-2}\mathrm{s}^{-1}$. Maximal second level input rate is 100 kHz. Uncertainty in estimates of cross sections and luminosity variations during a single run requires a large safety margin. By design, the average first level output rate should not exceed 30 kHz, shared between muon and calorimeter triggers. About 5-10 kHz is assigned for the single muon trigger. This implies a rejection factor of $\sim 10^{-5}$ at the highest luminosity.

Low p_t reach: should be limited only by muon energy loss in the calorimeters. It is equal to about 4 GeV in the barrel and it decreases with $|\eta|$ down to ~ 2.5 GeV. This is required mainly for b-quark physics at $\mathcal{L} = 10^{33}\mathrm{cm}^{-2}\mathrm{s}^{-1}$.

The highest possible p_t cut: ~50-100 GeV. Expected threshold needed to restrict the single muon trigger rate to 5-10 kHz at $\mathcal{L} = 10^{34}\mathrm{cm}^{-2}\mathrm{s}^{-1}$ is 15-20 GeV. Uncertainty in estimates of cross sections and background levels requires a large safety margin. Increasing the threshold from 15-20 GeV to 50-100 GeV reduces the rate by an order of magnitude.

Background rejection: single muon trigger rate due to background should not exceed the rate of prompt muons from heavy quark decays at the nominal threshold (15-20 GeV). This is necessary to maintain the rejection factor stated above. The prompt muon rate is irreducible except for channels where the isolation criterion can be applied (see below).

Isolation: transverse energy E_t deposited in each calorimeter region of $\Delta\eta \times \Delta\phi = 0.35 \times 0.35$ around a muon is compared with a threshold. This function is needed to suppress the rate of background and prompt muons form heavy quark decays when triggering on muons not accompanied by jets. This is particularly useful in channels like h,A,H $\rightarrow \mu\mu$, h,A,H $\rightarrow \tau\tau$, $\mathrm{t\bar{t}} \rightarrow$ WW, and gluino decays.

Output to the Global Trigger: up to 4 highest p_t muons in each event. In principle only 3 muons are necessary for the Global Trigger to perform single- and multi-object cuts including the three-muon trigger. The 4-muon output introduces some safety margin. For example, from physics point of view, a low p_t isolated muon

might be preferable over a higher p_t non isolated muon. Delivering 4 muons we reduce the probability that a low p_t isolated muon will not be selected because of the presence of higher p_t non isolated muons. This way we also reduce the probability of accepting ghosts instead of real muons.

5.2 Background

5.2.1 Introduction

Background classification

The task of the muon trigger is especially difficult because of the presence of severe background. In fact this is the major challenge of the design. There are three main sources of background:

- proton-proton interactions themselves
- beam losses because of the limited LHC aperture (p-nucleus collision with energy of 7 TeV in the laboratory system)
- cosmic rays

These sources produce various effects in the detectors. We group them into four classes depending on how they can influence the trigger:

track — a set of aligned track segments from several muon stations
track segment — a set of aligned hits within one muon station
correlated hit — caused by a real muon or its secondaries
uncorrelated hit — caused by phenomenon not related to a given muon

Dominant sources of each class of background are given in Table 5.1. They will be discussed one by one in the consecutive sections.

Table 5.1: Background classification

detected objects	caused by	dominant source
tracks	muons	b- and c-quark decays, π and K decays
track segments	hadrons	punchthrough and backsplashes
correlated hits	electrons	muon bremsstrahlung, δ-rays, e^+e^- production
uncorrelated hits	electrons	thermal neutrons $\rightarrow \gamma \rightarrow$ e

Distribution of absorbers

Background rates depend crucially on the distribution of absorbers in the experiment. From the point of view of the muon trigger two issues are especially important:

- material thickness in front of muon station
- shielding of highly illuminated elements

The amount of absorber in front of muon system determines the background rates due to punchthrough of hadronic showers. Therefore it is sensible to express it in terms of nuclear interaction lengths λ. The total material thickness in front of each muon station is given in Fig. 5.1.

The most exposed elements in the experimental hall are

- Forward Calorimeter (HF)
- LHC beam collimators, made of copper
- quadrupole magnets

They are shown together with their shielding in Fig. 5.2. Heavy elements of the shielding like iron and concrete are designed to stop energetic hadrons. Light organic materials like polyethylene are intended to capture neutrons, with the additives such as magnetite or boron to increase the neutron capture cross section.

Presented shielding design is a result of a long optimisation process which is not yet finished. The reader interested in this subject is referred to [110]-[127].

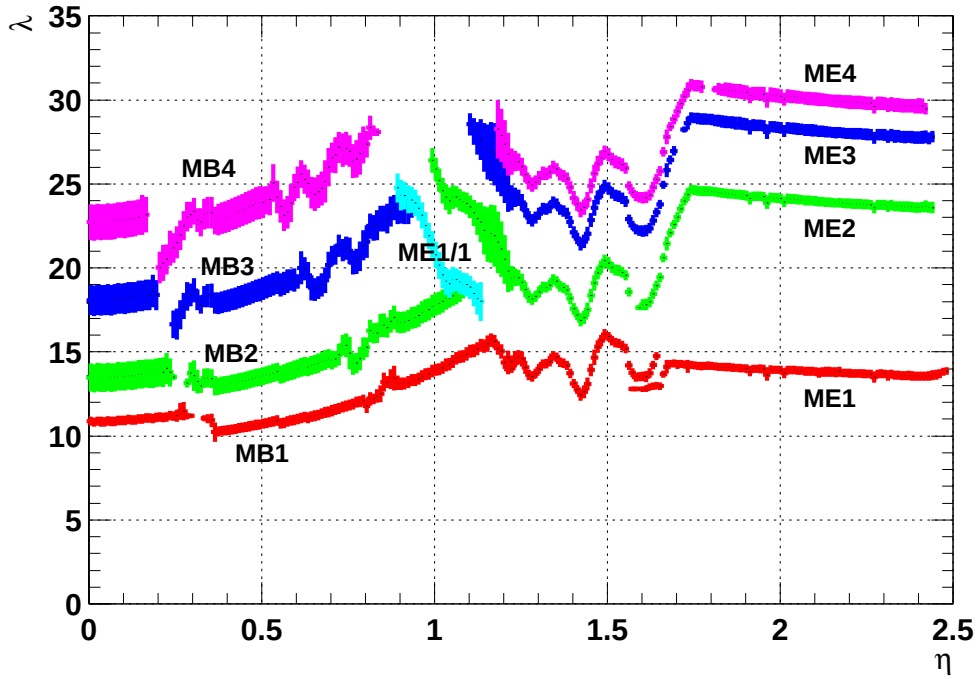

Figure 5.1: Material thickness in front of muon stations expressed in nuclear interaction lengths λ. The width of the bands reflects the non-cylindrical geometry of CMS.

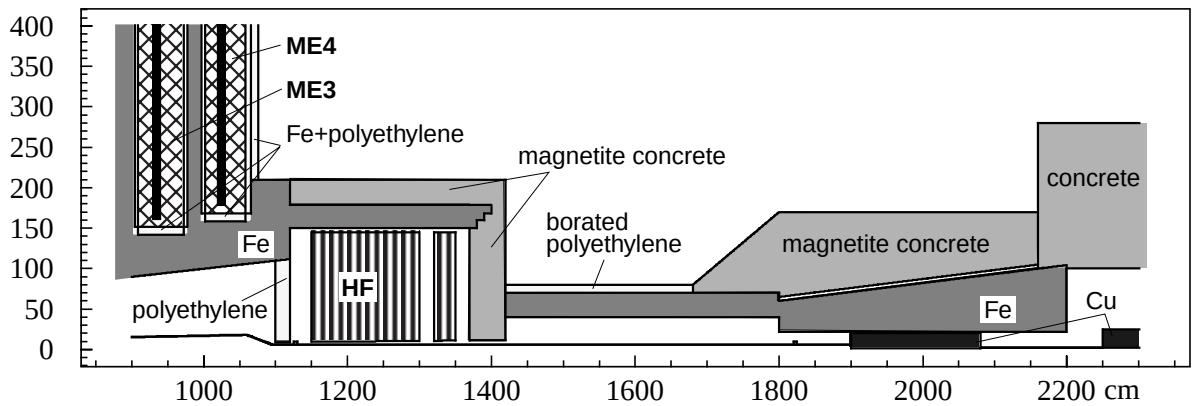

Figure 5.2: CMS shielding.

RD5 experiment

The challenge of background reduction in the LHC environment was recognised at the very early stage of the project. Already in 1991 a dedicated experiment, called RD5 [152], was build at CERN to study different aspects of muon detection in the presence of various backgrounds. We describe it briefly here, because its results will be discussed in subsequent sections of this paper. They are crucial for understanding of many phenomena related to muon detection at LHC.

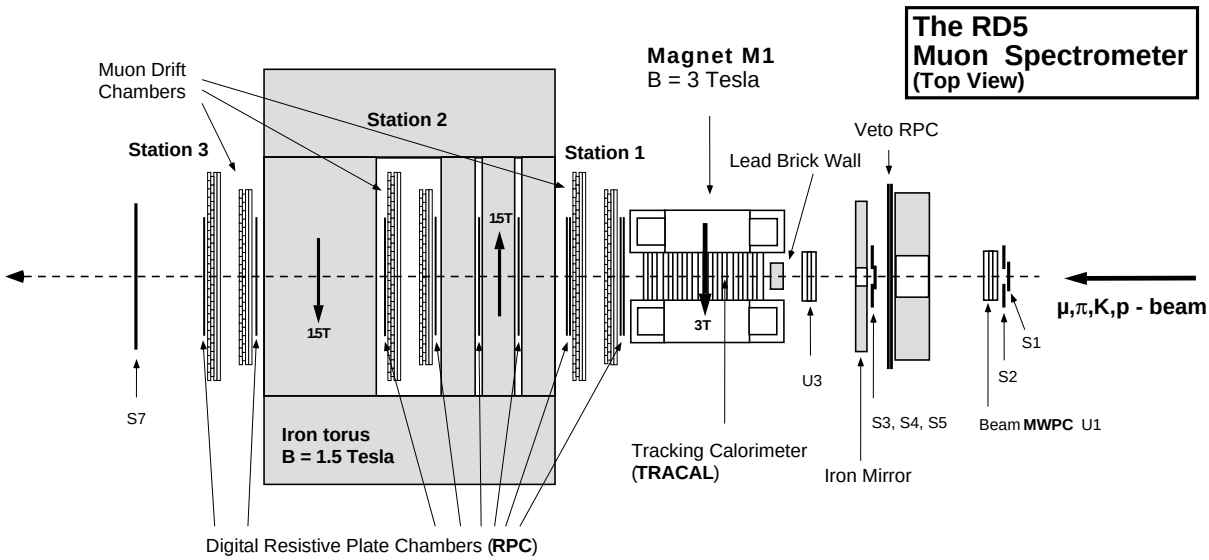

Figure 5.3: RD5 experimental setup.

The RD5 setup is shown in Fig. 5.3. Functionally, it resembles the basic structure of the CMS detector with its magnet, return yoke, calorimeter and muon system. Its main two parts are magnets: a 3 T superconducting solenoid playing the role of CMS magnet, and a 1.5 T warm toroid which first part simulates the CMS return yoke. Using both parts of the toroid one has a structure similar to ATLAS.

The magnets are interleaved with muon stations equipped with various kind of muon chambers. Inside the solenoid there is a calorimeter called TRACAL because of its tracking capabilities. In front of the magnets there are multiwire chambers and the silicon tracker used for beam monitoring. The setup is completed by trigger scintillators.

The RD5 setup was used to test various types of muon chambers planned for LHC and several entire muon trigger systems. Main physics results are the measurements of hadronic shower punchthrough through different absorber thickness and radiation of high energy muons. They are discussed in the following sections.

5.2.2 Muons

Muons in CMS can come from several sources:

1. proton-proton interactions
   (a) decays of heavy objects like W, Z, top, higgs, etc.
   (b) b- and c- quark decays
   (c) decays of hadrons composed with quarks u, d and s (mainly π and K)
   (d) punchthrough of hadronic showers
2. beam losses because of the limited LHC aperture (sometimes called *beam halo muons*)
3. cosmic rays

Muons of 1a and 1b together are often called *prompt muons*, because they are produced very close to the pp vertex. Life time of longest living b-mesons, expressed as $c\tau$ is no longer than 500 μm. Even taking into account the relativistic dilatation most of the particles containing b or c quark will decay within 1 cm from the vertex.

The division between 1c and 1d is somewhat arbitrary. This is because muons in hadronic showers are also coming from hadron decays. The only difference is that in the first case the mother hadron was created in the

primary pp interaction whereas in the second one it is a product of strong interactions in the hadronic cascade. However the two cases cannot be easily distinguished experimentally if a primary hadron decayed inside the calorimeter volume before any strong interaction. Therefore in this paper we follow the commonly used naming convention which is better defined from the experimental point of view. We call decay muon a product of hadron decay which took place before the calorimeter. The name punchthrough muon we use for muons from hadron decays within the calorimeter, regardless what was the origin of the hadron.

On the other hand it is sometimes difficult to distinguish soft punchthrough muons from other charged particles produced in hadronic showers. Therefore we will discuss them together with hadrons in the section devoted to punchthrough.

Prompt muons

This class of muons we consider as a signal and we will use it as a reference to all kind of backgrounds. The rate of prompt muons is dominated by b- and c-quark decays up to p_t ~20 GeV; above 20 GeV the W decays take over (see Fig. 3.10 page 29, where b and c decays are included in the "minimum bias" set [80]). It does not show any significant dependence on η. The p_t dependence can be parametrised with the following formula [84]:

$$\frac{dN}{d\eta\, dp_t} = a \exp\left[\Leftrightarrow \frac{(x \Leftrightarrow \mu)^2}{2\sigma^2} \right]$$

where

$$x = \log_{10}\ p_t\ [\mathrm{GeV}], \quad a = 1.3084 \cdot 10^6,\ \mu = \Leftrightarrow 0.7250,\ \sigma = 0.4333\ .$$

The distribution is given in $[\mathrm{GeV}^{-1}\cdot\mathrm{s}^{-1}]$.

Muons from hadron decays

The rate of primary hadrons also does not depend significantly on η and can be parametrised as a function of p_t:

$$\frac{dN}{d\eta\, dp_t} = a\ \left({p_t}^{\alpha} + b\right)^{\beta}$$

where

$$a = 1.1429 \cdot 10^{10},\ b = 0.8251,\ \alpha = 1.306,\ \beta = \Leftrightarrow 3.781\ .$$

In order to calculate the rate of decay muons one has to convolute the above formula with the decay probability, which depends on the particle type, η and p. The result it shown in Fig. 5.4a together with rates of muon from b- and c-quark decays. These are the rates of muons entering the calorimeter. Soft muons cannot penetrate the calorimeter and therefore the rate of muons reaching the muon system is reduced at low p_t. This is shown in Fig. 5.4b. The rate dependence on η is given in Fig. 5.5. It is seen that the rate of muons in the forward region is much higher than in the barrel. The local rate per cm^2 in different muon stations is shown in Fig. 5.6.

Cosmic muons

A typical rate of cosmic muons on the ground level is about 10 $\mathrm{Hz/m}^2$. One can expect a reduction factor of approximately one hundred with respect to ground level cosmic rate. Hence the local rate is $\sim 10^{-5}$ $\mathrm{Hz/cm}^2$ and it is completely negligible compared to other sources.

Since the detector cross section has roughly 22×15 m^2 the total rate of muons crossing it is about 30 Hz. This is already well below the rates from other sources, discussed above. Moreover, only very few of the cosmic muons will have a chance to give a trigger because it requires the tracks to be pointing to the vertex.

There is another side of the coin — it will be very difficult to make any trigger test with cosmic muons.

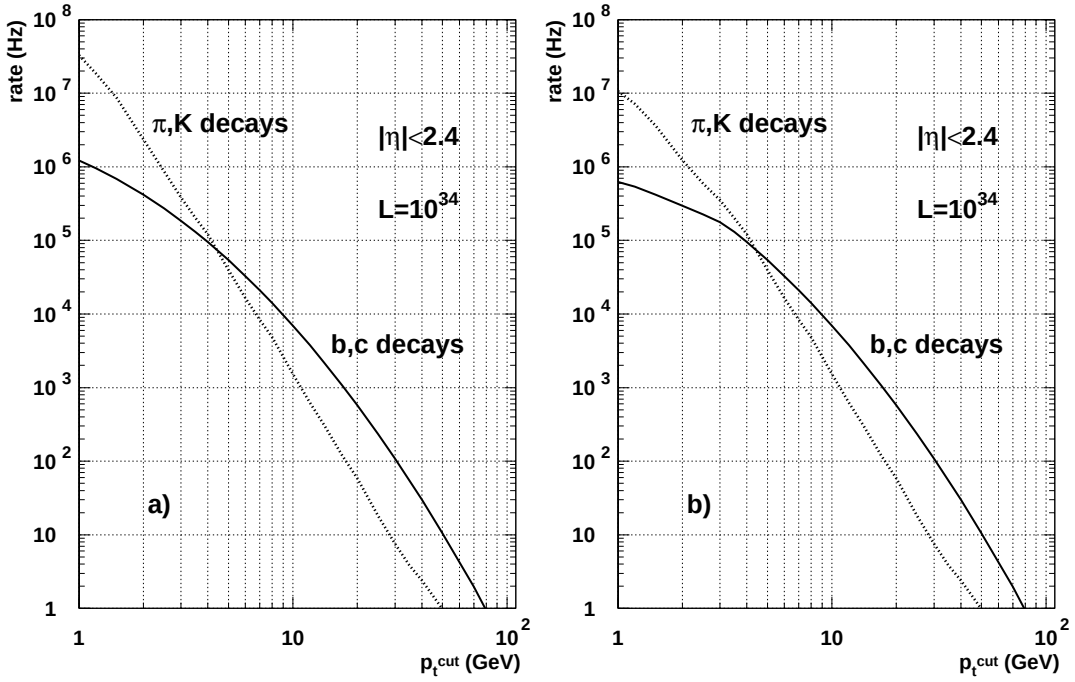

Figure 5.4: Integrated muon rates: a) before and b) after calorimeters.

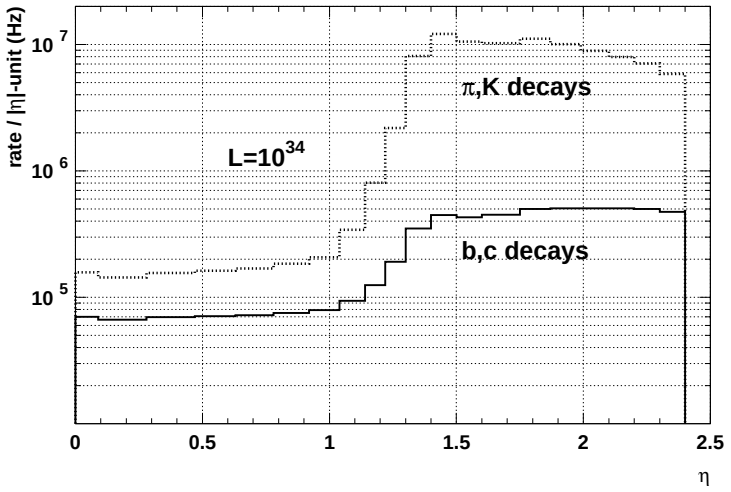

Figure 5.5: Muon rates after calorimeters.

Beam halo muons

The limited aperture of the LHC causes some beam losses. Particles deviating from the beam center will interact with machine elements producing many secondaries. Most dangerous of them are energetic muons because of their ability to penetrate matter. They will enter the experimental hall and traverse the detector almost parallel to the beam. They have a very small probability to cause the trigger because they do not point to the vertex. In the endcap chambers, however, they might be seen as local track segments.

Estimated rate of halo muons is shown in Fig. 5.6 together with muon rates from the pp interactions. In the barrel, the two rates cannot be compared directly. This is because the halo muons are entering barrel chambers from the side and the rate is expressed per cm^2 of the side surface.

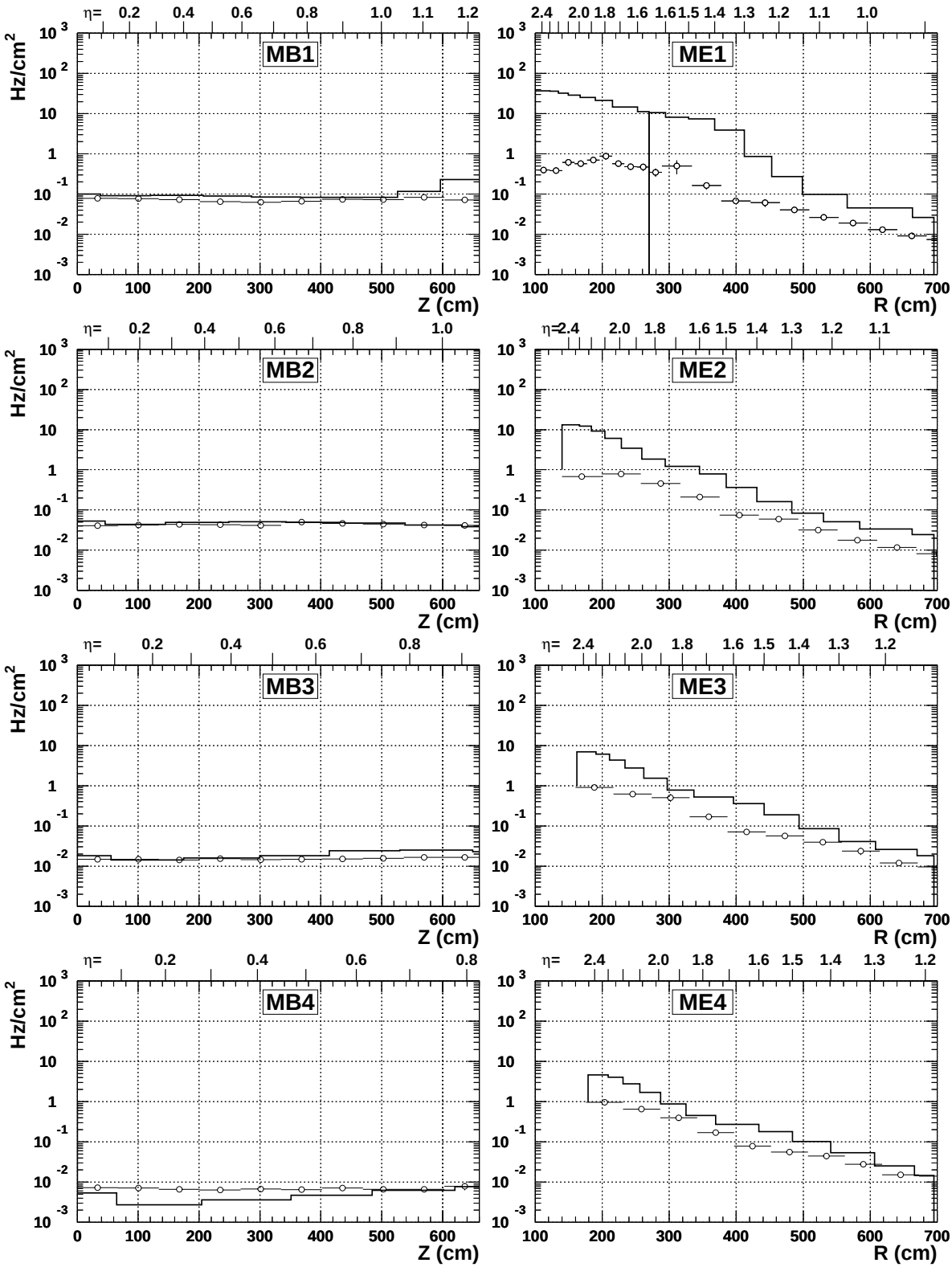

Figure 5.6: Muon rates in the barrel muon stations (MB1-4) as a function of Z coordinate and in the endcap muon stations (ME1-4) as a function of R coordinate, from pp interactions (solid line) [84, 4] and from the beam halo (open circles) [114].

5.2.3 Hadrons

Hadronic punchthrough

Hadronic punchthrough can affect the muon trigger in two ways:

- increasing occupancy in muon chambers;
- creating track segments in muon stations.

These two effects are illustrated if Figs 5.7 and 5.8 respectively, which shows "event display" pictures from the RD5 experiment. In the first case, the interaction of incoming pion occurred close to the end of the calorimeter. Thus a significant part of the hadronic shower evolved inside the muon station. In the second case, one of the hadrons from the cascade has decayed into a muon which then penetrated the iron, reaching the second muon station.

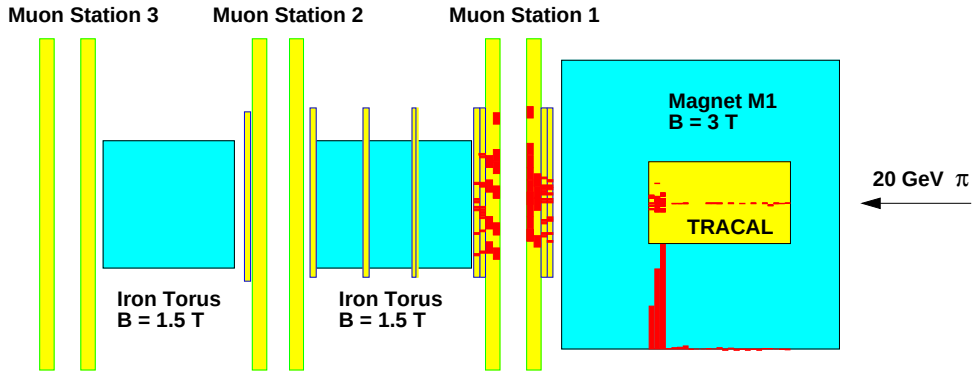

Figure 5.7: High occupancy in the muon station caused by a punchthrough from a 20 GeV π — event observed in RD5 experiment.

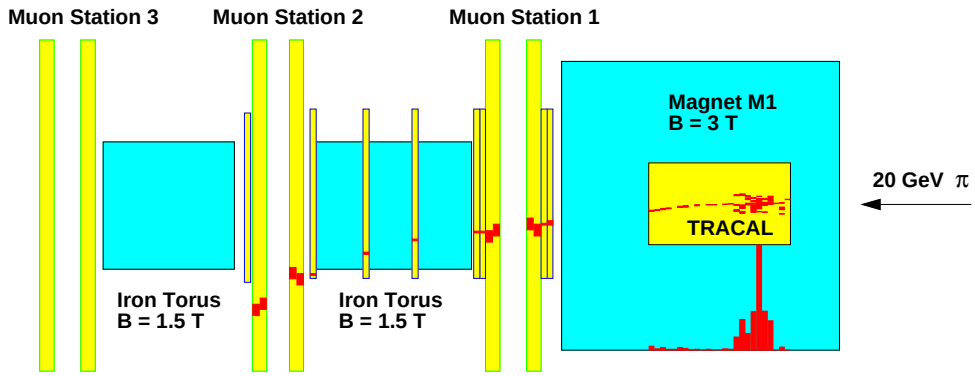

Figure 5.8: Punchthrough muon from a 20 GeV π — event observed in RD5 experiment.

Punchthrough effect was studied very extensively in the RD5 experiment. Total punchthrough probability (Fig. 5.9), multiplicity, spatial, angular and momentum (Fig. 5.10) distributions of punchthrough particles were measured for various incident particle types and momenta, with and without the magnetic field. It has been shown that the punchthrough effect is well reproduced by GEANT [128] with its both hadronic shower versions, FLUKA [129] and GHEISHA [130]. An exception is low momentum data ($\sim$10 GeV) which are not very well described by GHEISHA (see Fig. 5.9).

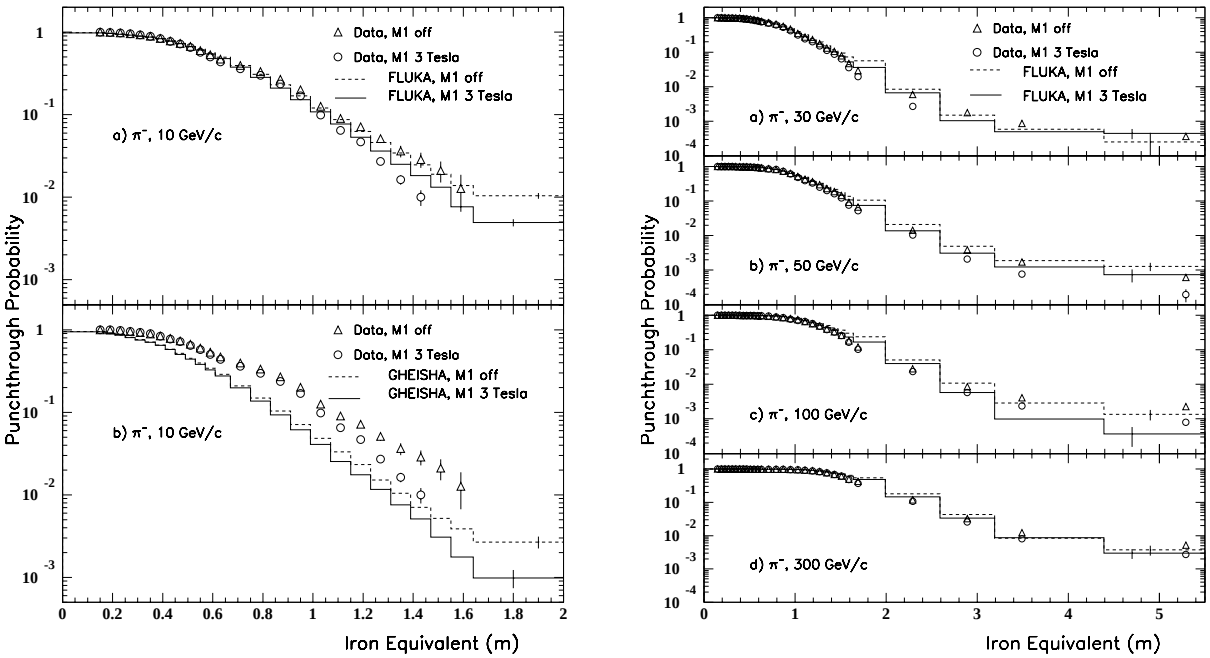

Figure 5.9: Punchthrough probability as a function of the material thickness.

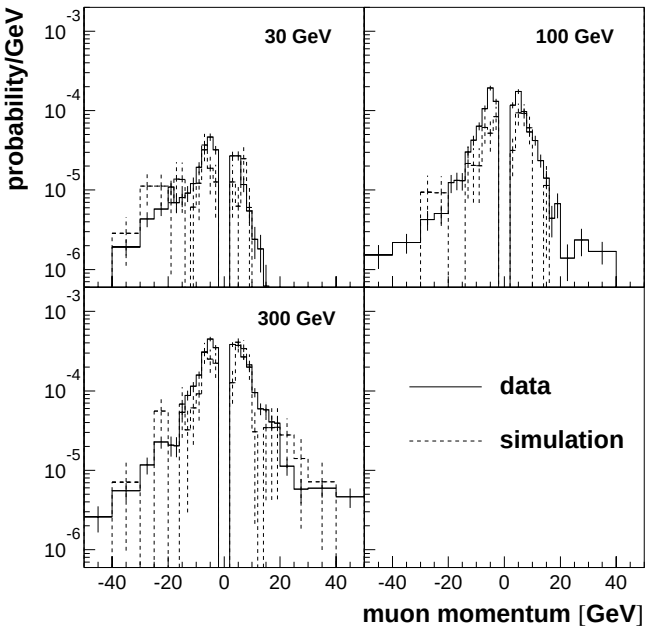

Figure 5.10: Momentum distribution of punchthrough particles for different energies of a primary hadron: 30, 100 and 300 GeV.

Backsplash from forward calorimeter and beam collimators

When highly energetic hadron hits one of the forward detector elements some products of the hadronic shower can be emitted at large angles and travel towards muon chambers. This effect is often called a *backsplash*, although it has very similar nature to punchthrough and the division is somewhat artificial. The total rate of charged hadrons due to punchthrough and backsplashes of particles from pp interactions is shown in Fig. 5.11 together with hadron rates due to beam halo.

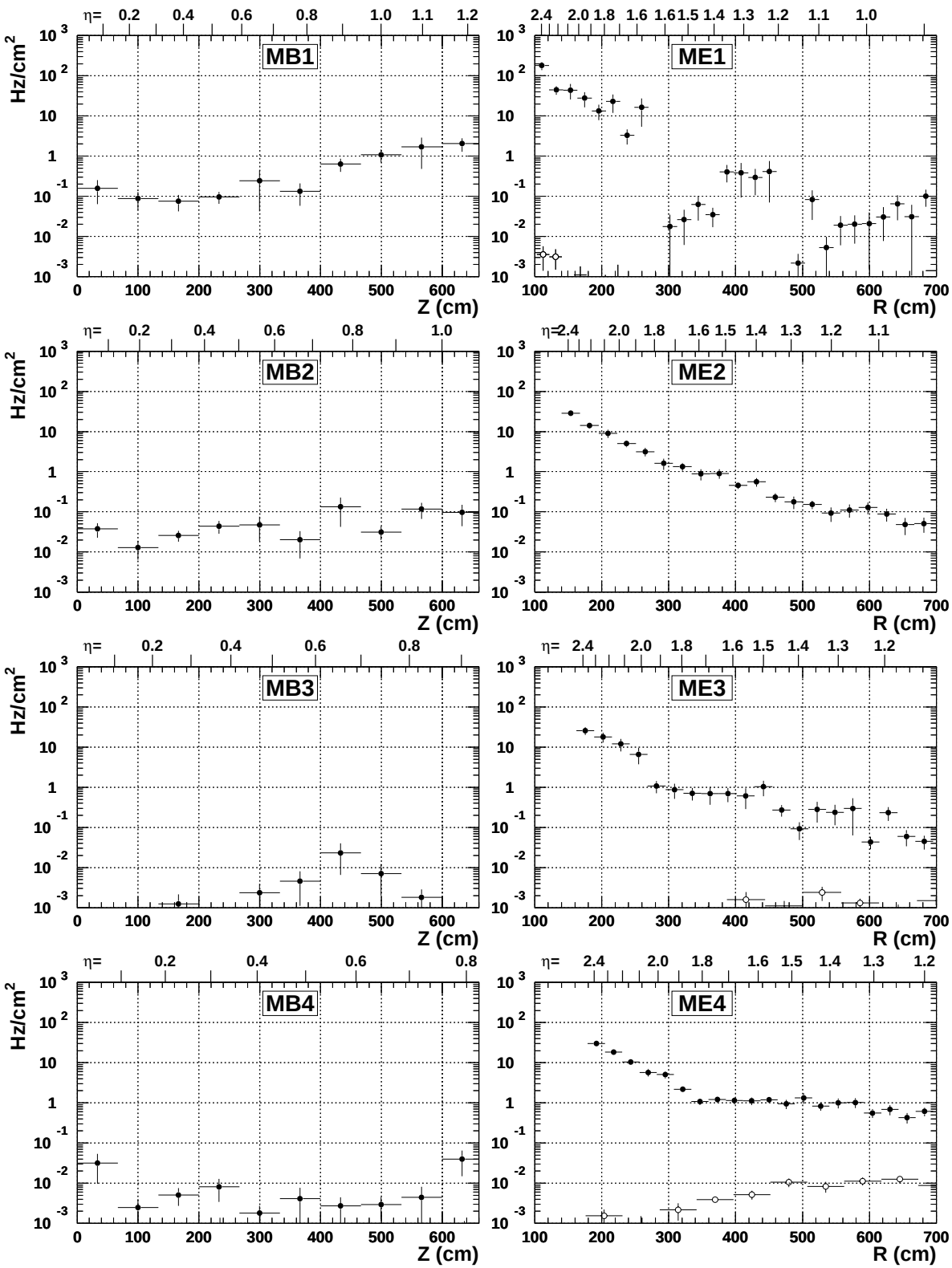

Figure 5.11: Charged hadron rates in the muon stations due to punchthrough and backsplashes of particles from pp interactions (full circles) [108] and from the beam halo (open circles) [114].

5.2.4 Uncorrelated electrons from neutrons

The very last product of hadronic showers are thermal neutrons. They cannot cause hits in detectors by themselves. However, they can be captured by nuclei and produce photons by deexcitation. Such a photon can in turn create an e^+e^- pair eventually causing hits in detectors. If the capture happens in iron or hydrogen the photons have energy of 2-8 MeV which may result in electrons penetrating several chamber layers. For rough estimates, one can assume that the flux of electrons causing hits is $\sim$100 times lower than the photon flux, which is in turn $\sim$10 times lower than the flux of neutrons. The thermal neutrons behave like a gas filling all the experimental hall. They can travel long distances even in dense matter and therefore it is difficult to shield them out. The most effective way to stop them is addition of ^{10}B which has the capture cross section several orders of magnitude higher than iron or hydrogen. Moreover the resulting photons have only 200 keV energy and they cannot produce e^+e^- pairs.

There is another mechanism through which neutrons can produce detector hits. Elastic neutron-proton collision can give some kinetic energy to the proton which can be then registered by the detector. It has been shown [118], however, that the hit rate due to this effect is negligible compared to the n$\rightarrow\gamma\rightarrow$e mechanism.

Simulation of thermal neutrons is extremally difficult and time consuming because one needs to track neutrons with energies as low as single electronovolts. The results are very sensitive to details of the simulated geometry, especially of the shielding and of the chambers themselves. In order to gain confidence in the results three different programs are used by the CMS Radiation Working Group: FLUKA [129], GCALOR [131], and MARS [132], each with its own advantages and drawbacks. Comparison of their results is given in Fig. 5.12 which shows the rates of hits due to thermal neutrons in various muon stations. They have been calculated as photon rates multiplied by 0.01 probability of causing a hit. Agreement between FLUKA and GCALOR is remarkable. MARS results, although they suffer from low statistics, are systematically higher than others. Before drawing any conclusion from this fact one has to make sure that the simulated geometries are compatible. Each program introduce geometry in a different way which is in fact the major problem in any comparison between them.

Comparison of rates due to neutrons from different sources is given in Fig. 5.13. For the pp collisions the electrons are simulated explicitly in contrast to Fig. 5.12, where the simulation was terminated at the level of photons. This give more direct estimate for the price of $\sim$100 times lower statistics.

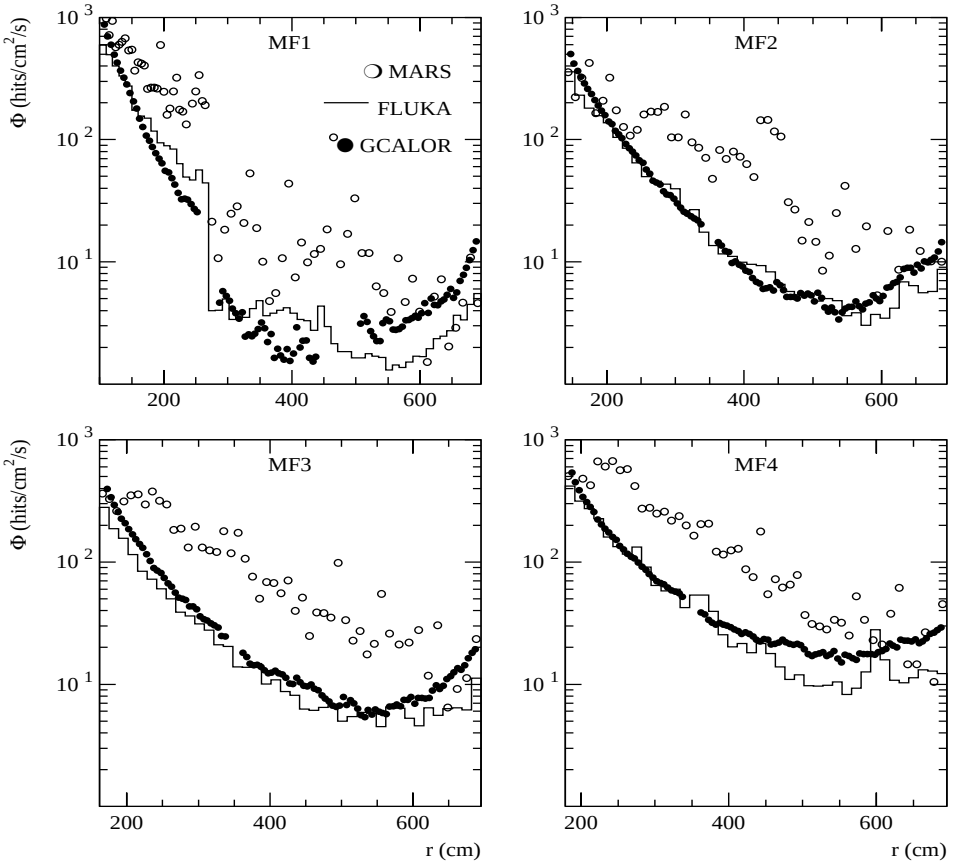

Figure 5.12: Thermal neutron originated (n$\rightarrow\gamma\rightarrow$e) rates in muon chambers [109].

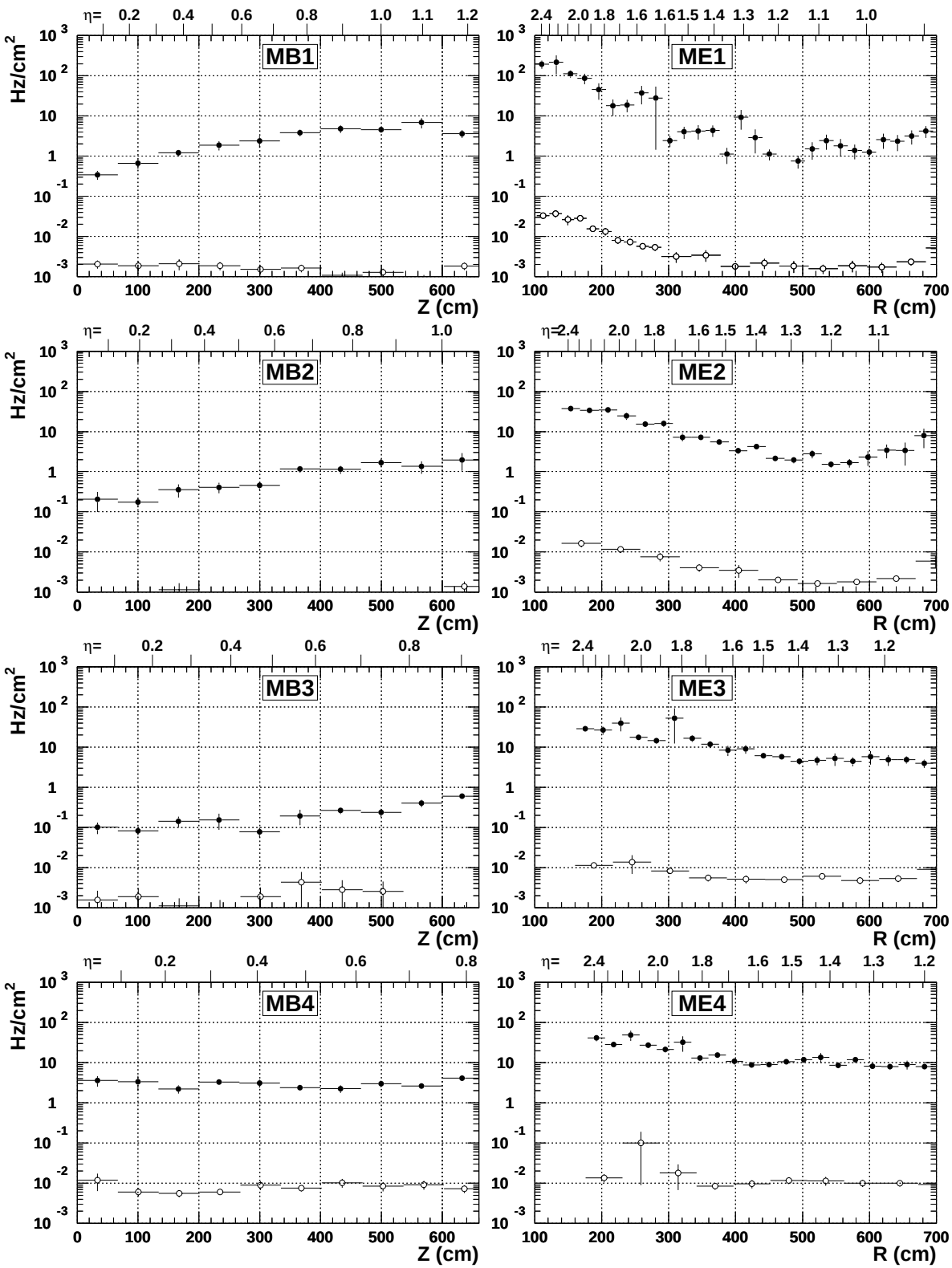

Figure 5.13: Thermal neutron originated (n→ γ →e) rates in muon chambers: from pp interactions (full circles) [108] and from the beam halo (open circles) [114].

5.2.5 Electrons correlated with muons

Muon traversing matter can lose its energy by four processes

- ionisation (including delta ray production)
- bremsstrahlung, i.e. photon emission,
- direct e^+e^- pair production,
- nuclear interactions.

Probability of the last one can be neglected[1] compared to others. Probability of the first three processes is given in Fig. 5.14 as a function of muon momentum and energy of secondaries. The most probable effect is an emission of a soft delta ray. The most hurting one, however, is emission of hard electron or photon (> 1 GeV), which can develop entire electromagnetic shower. An example is shown in Fig. 5.15 which is an "event display" from the RD5 experiment. Second muon station is full of hits and thus useless for a measurement. A similar example is shown in Fig. 5.16, this time the muon radiation is simulated by GEANT [128].

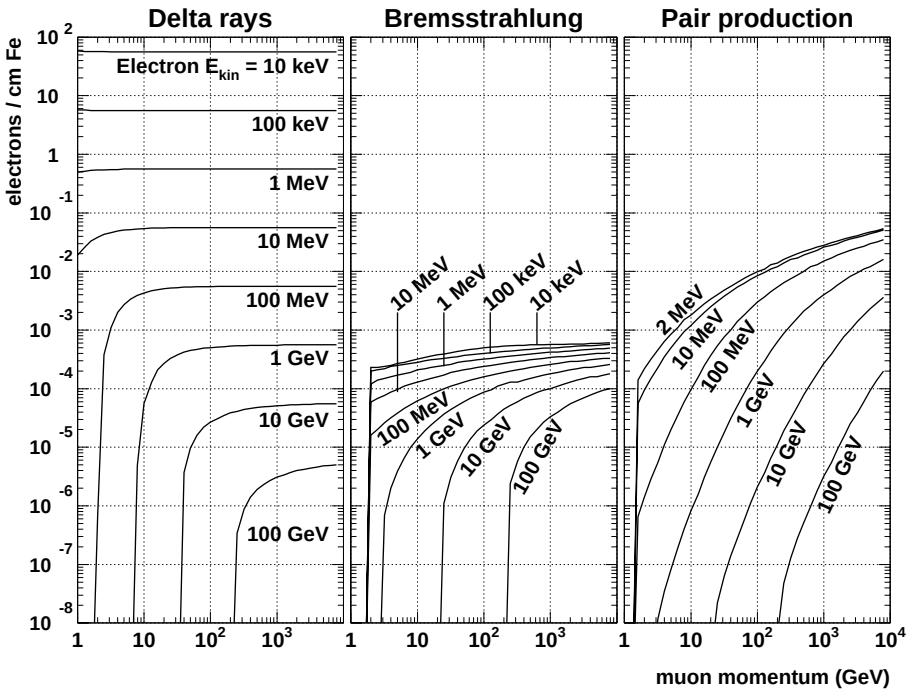

Figure 5.14: Production of electrons by muons traversing matter.

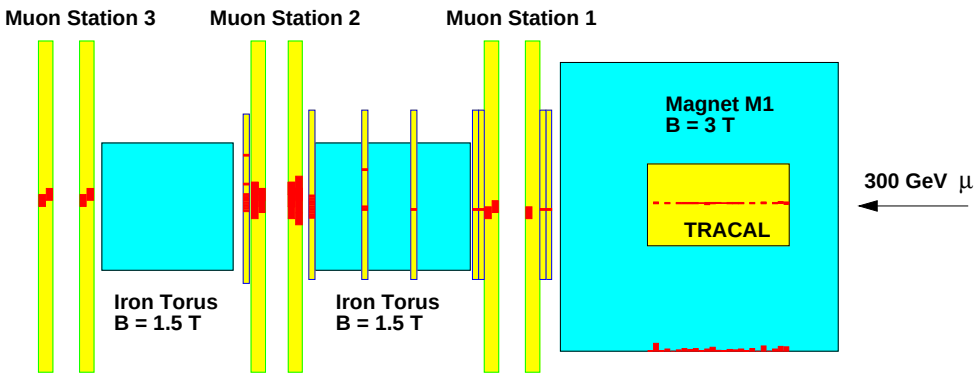

Figure 5.15: Electromagnetic shower from 300 GeV μ — event observed in RD5 experiment.

[1]The energy loss dE/dx due to nuclear interactions is an order of magnitude lower than due to bremsstrahlung and pair production.

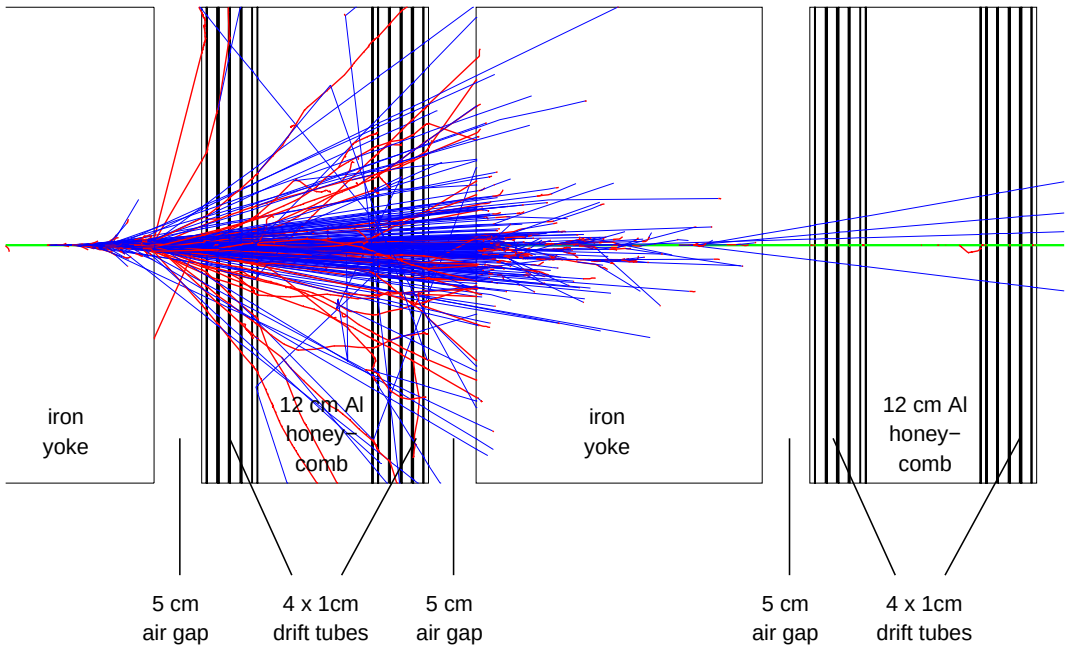

Figure 5.16: Electromagnetic shower produced by 22 GeV photon emitted by 1 TeV muon (GEANT simulation).

Emission of secondaries by muons was studied in detail in the RD5 experiments. Microscopic study were performed with a silicon microstrip detector. Results are shown in Fig. 5.17. The data are well reproduced by GEANT simulation. The phenomenon of muon radiation was also studied with various kinds of muon chambers. Chamber response, however, depends crucially on the details of chamber construction and operation. Therefore, we will come back to this problem after describing the muon chambers and trigger algorithms.

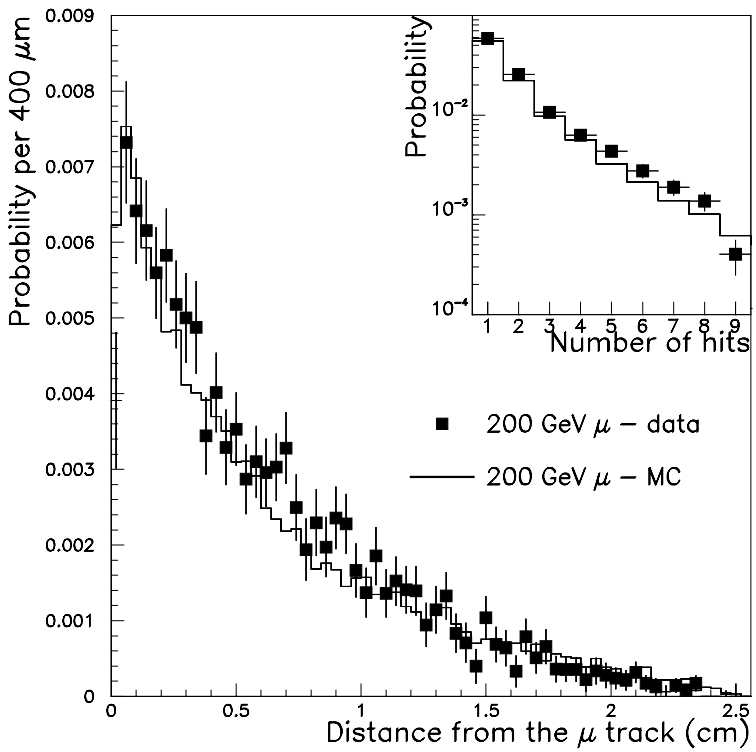

Figure 5.17: Secondaries emitted by muon traversing iron, measured 4.7 cm from the iron surface.

5.2.6 Conclusions

Let us summarise background considerations according to the way they can influence the trigger.

Tracks

The tracks are coming mainly from muons. The total rate above 5 GeV is dominated by prompt muons which we consider as signal. Therefore we do not expect major problems for trigger in this domain.

Track segments

These are coming mainly from punchthrough and backsplashes, however halo muons cannot be neglected. Designing the trigger one should provide bandwidth high enough to transmit detected track segments including background. One should also impose rather strict requirements on matching several track segments into full tracks in order to suppress random coincidences of several background track segments. These issues are discussed in the next chapters.

Correlated hits

Hits correlated with muons are characteristic for muons of energy 100 GeV and above. They can disturb measured hit position and track segment angle which may lead to problems with matching of different track segments and muon momentum estimate. The only way to fight this background is redundancy: several muon station in the detector, several detector layers per station. In the next chapter it will be shown that this rule is applied thoroughly in the design.

Uncorrelated hits

Local background rates from different sources are compared in Fig. 5.18. In major part of the detector the rate is dominated by uncorrelated electrons. The total rate is given in Fig. 5.19. The highest rates are in the inner ring of endcap chambers: ME1/1, ME2/1, ME3/1, and ME4/1. They amount for a few hundred Hz/cm^2 approaching 1 kHz/cm^2 at the very bottom of ME1/1. Elsewhere the rates stay around 10 Hz/cm^2 and they never exceed 100 Hz/cm^2. The maximal rates of hits in different muon stations are summarised in Tab. 5.2.

Table 5.2: Maximal rate of hits (Hz/cm^2) in different muon stations.

muon station	1	2	3	4
barrel	10	3	1	5
outer endcap	20	20	20	20
$\|\eta\| < 2.1$	250	70	100	80
$\|\eta\| < 2.4$	500	100	100	100

This kind of background is probably the most difficult because of its intensity. It may affect the trigger in several ways:

- spoil functioning of the detectors (efficiency drop, etc.);
- saturate data bandwidth of various connections;
- disturb position and time measurement by overlapping real muons;
- cause fake track segments by random coincidence of several hits.

In order to suppress those effects one should take the following measures:

- optimal detector and shielding layout, proper materials;
- high granularity of detectors;
- fast signal shaping, short gates, etc.;
- strict requirements on matching hits into track segments and segments into full track;
- redundancy everywhere.

Concrete implementation of these measures in the CMS Muon Trigger design will be shown in next chapters.

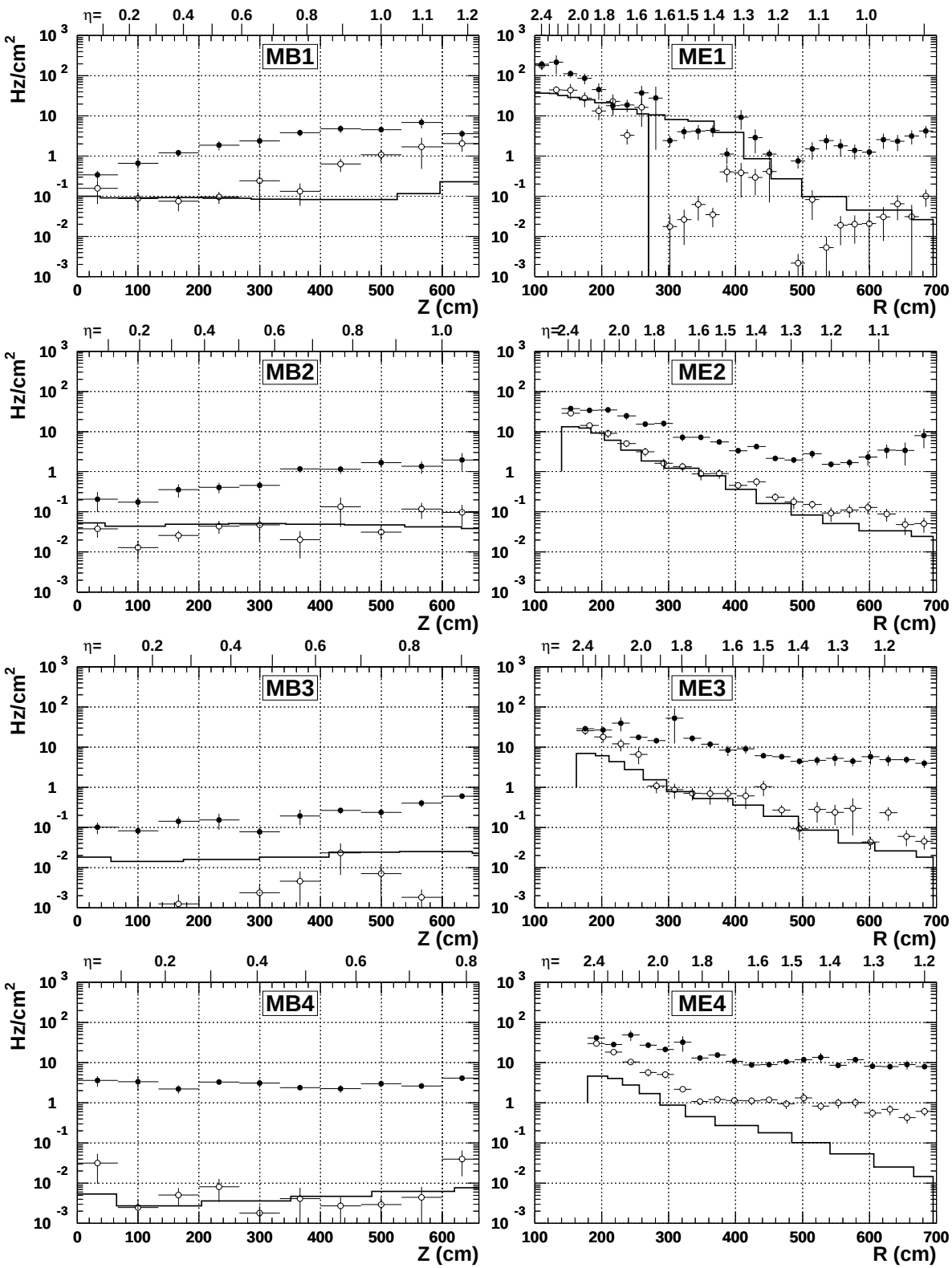

Figure 5.18: Background rates in muon chambers: muons (solid line), charged hadrons (open circles), electrons (full circles). The data from different sources shown in Figures 5.6, 5.11, and 5.13 are summed together.

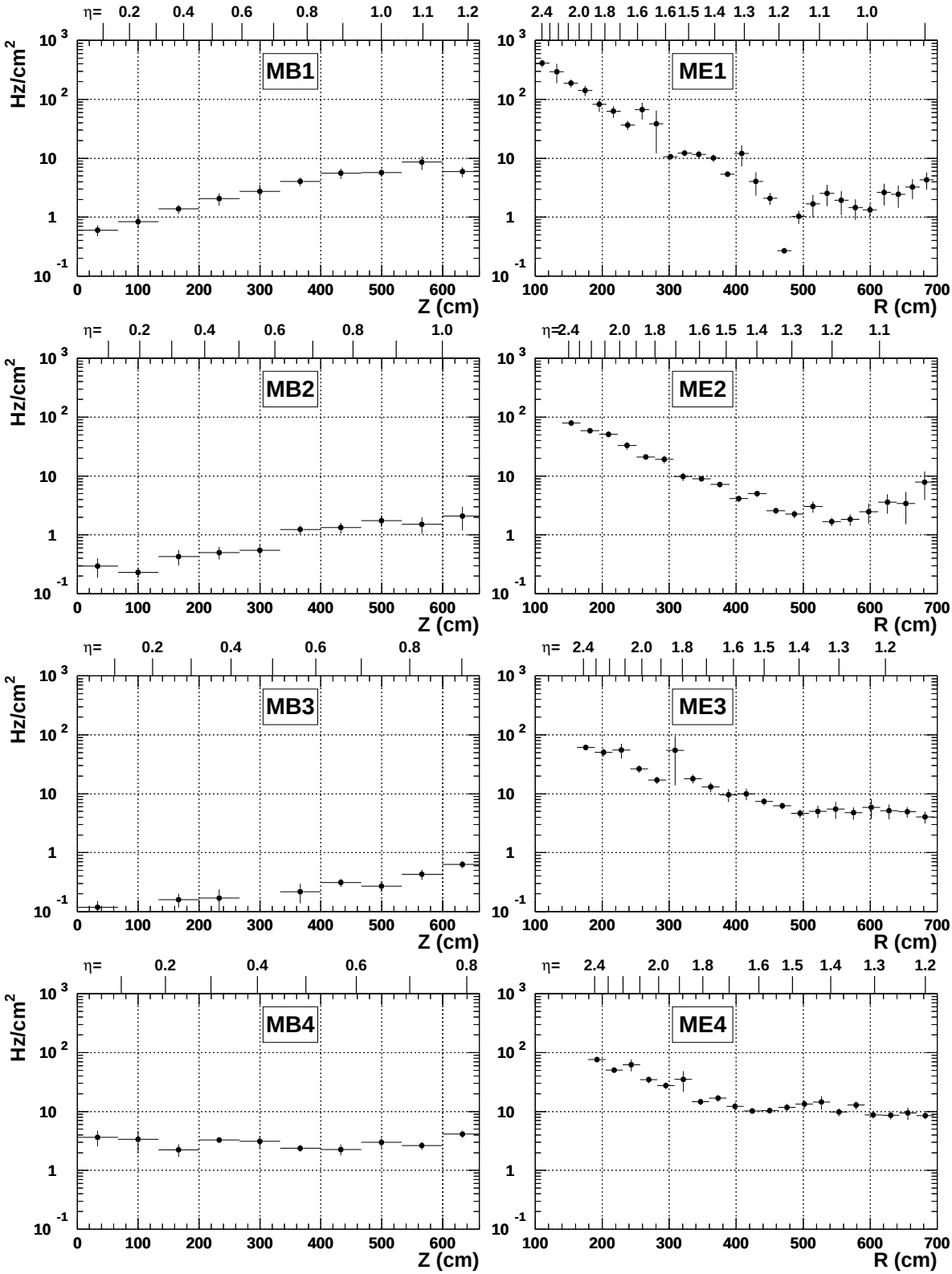

Figure 5.19: Total rate in muon chambers. Contributions of different kind of particles shown in Fig. 5.18 are summed together.

5.3 Track bending in the magnetic field

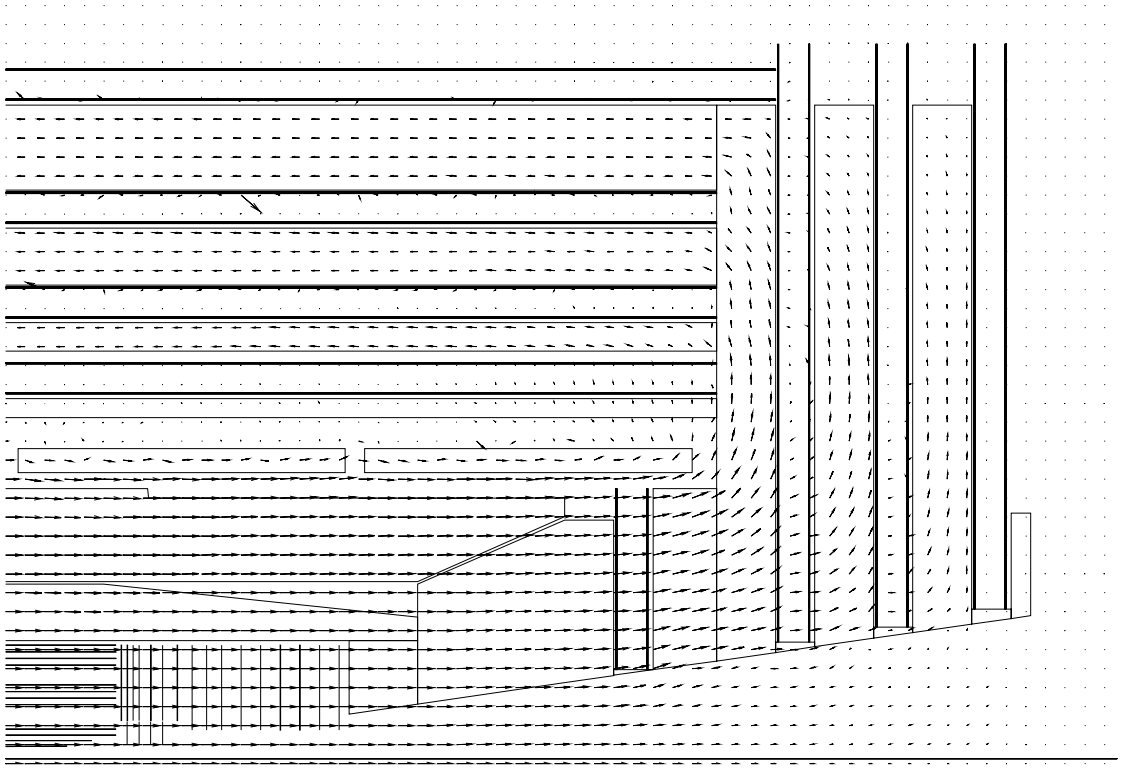

Figure 5.20: Magnetic field map of CMS

Measurement of the muon transverse momentum p_t is based on track bending in the magnetic field. The magnetic field in the CMS detector is created by a long superconducting solenoid (Fig. 5.20). Since the dominant component of the $\boldsymbol{B}$ field is along the beam direction, tracks are primarily bent in the $r\phi$ plane (perpendicular to the beam direction). Thus, tracks in rz projection are approximately straight lines, i.e. they keep almost constant η value along the path. The presence of a radial field component $\boldsymbol{B_r}$, especially in the forward part of the detector, slightly modifies this picture. A track bent by the $\boldsymbol{p_t} \times \boldsymbol{B}$ force gets some tangential component $\boldsymbol{p_\phi}$. Then the $\boldsymbol{p_\phi} \times \boldsymbol{B_r}$ produces the z component of the Lorentz force. As a result, the track's η changes along its path. This deflection in η is rather small because the p_ϕ component is small in comparison to the total p value. Even for the softest tracks reaching the muon stations, the change in η typically does not exceed 0.15 (see Fig. 5.21). Thus, in order to measure the transverse momentum of the track, it is enough to observe the dominant bending in the $r\phi$ plane. A few examples of simulated muon tracks are shown in Fig. 5.22.

Bending angle of the track is given by the integral of the $\boldsymbol{B} \times \boldsymbol{dl}$ product, where $\boldsymbol{dl}$ is an infinitesimal vector along the track. Fig. 5.23 shows this value as a function of R in the barrel, and as a function of Z in the forward part of the CMS detector. It grows linearly until the track reaches the coil and then it falls down in the return yoke due to the change of the sign of $\boldsymbol{B} \times \boldsymbol{dl}$.

If the detectors are optimally placed, one can make use of the whole integrated absolute value of the $\boldsymbol{B} \times \boldsymbol{dl}$ product. This value is shown in the right part of Fig. 5.23. One can see that in the barrel it is almost constant and approximately equal to 17 Tm. In the forward region it decreases with pseudorapidity η but even at the edge of the acceptance of the muon system it remains as large as 6 Tm. Such a big value causes the track bending to be larger than multiple scattering effect (see Fig. 5.24) and thus allows to disentangle various momenta even for the highest η and the lowest p_t values within the acceptance of the muon system.

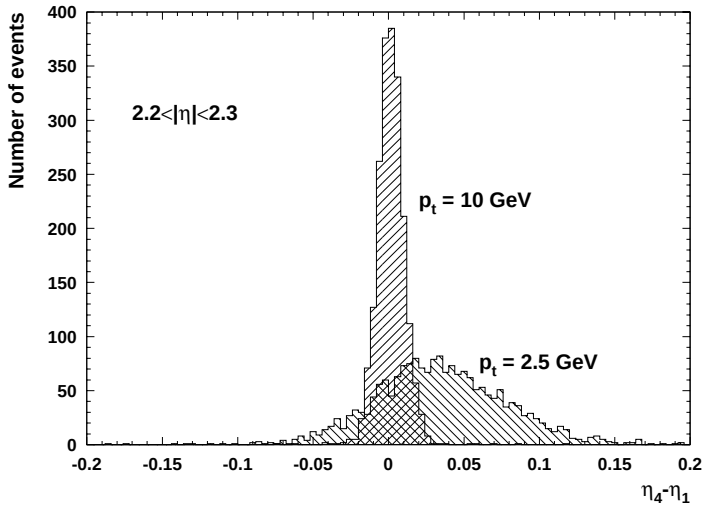

Figure 5.21: Track deflection in η between stations ME1 and ME4

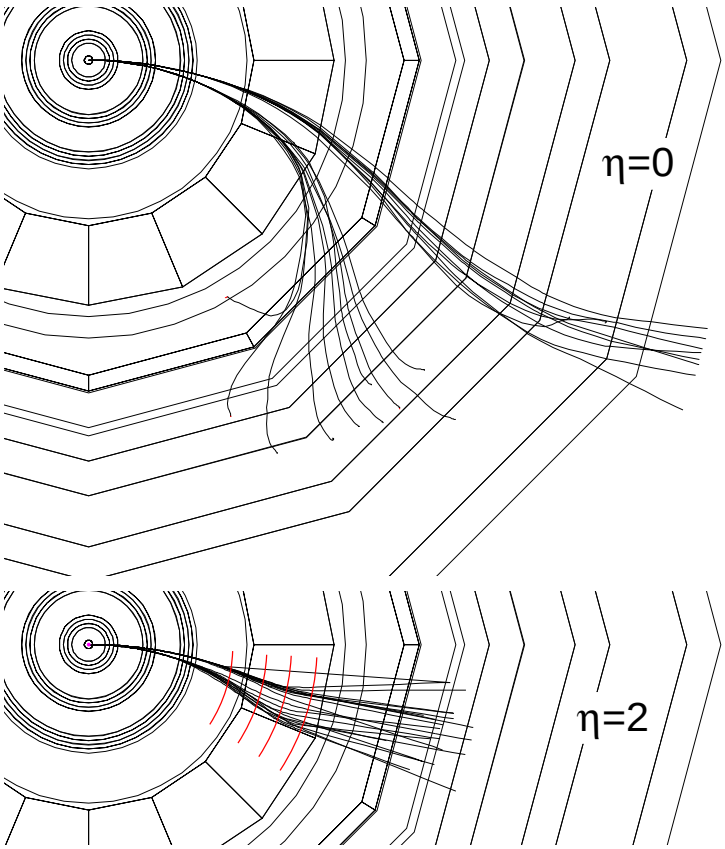

Figure 5.22: Simulated muon tracks with p_t = 4 and 6 GeV. In the second figure the places where the tracks cross the forward muon stations are indicated by four arcs.

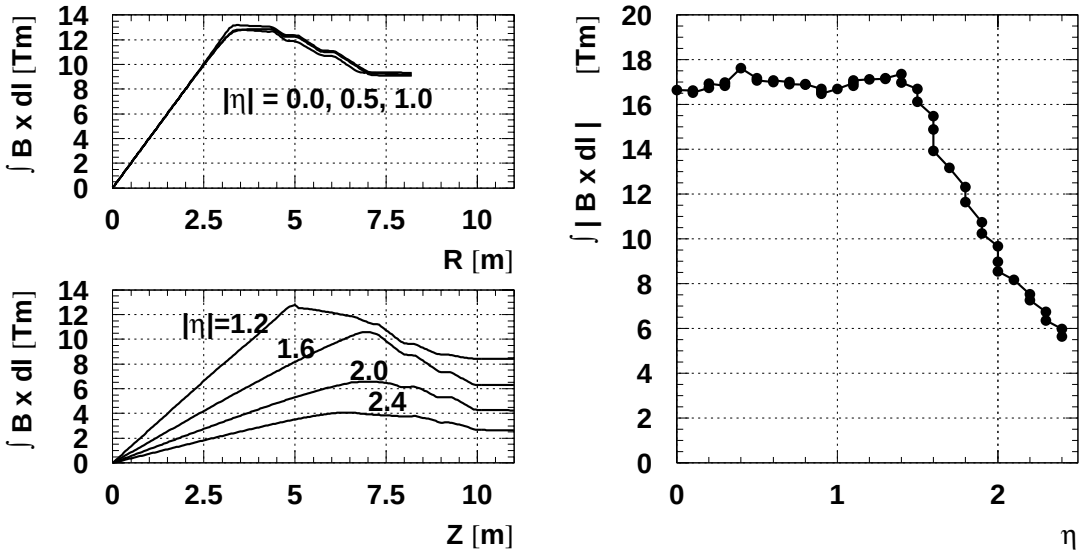

Figure 5.23: CMS bending power

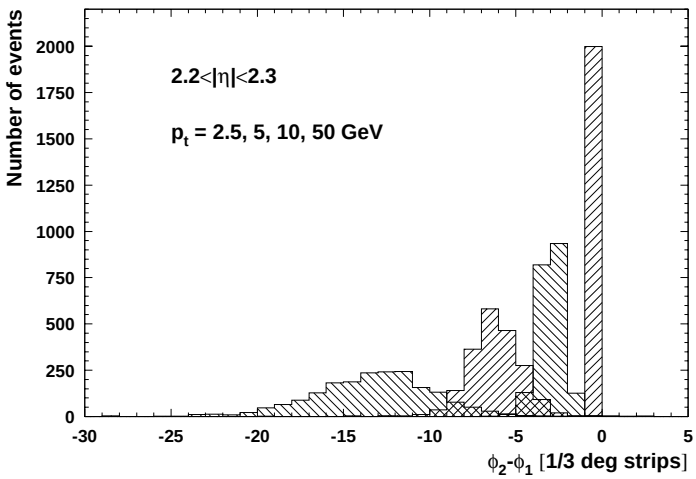

Figure 5.24: Track bending measured by stations ME1 and ME2 equipped with readout elements of $\Delta\phi = \frac{1}{3}^{\circ}$.

5.4 Implementation of algorithms

5.4.1 Technical limitations

Basic tasks of the Muon Trigger should be performed by algorithms having detector information (hits) as an input. In principle high precision and large number of hits along a muon track should lead to more reliable muon recognition and better momentum measurement. In practice, however, there are technical limitations which put important constrains on the performance of algorithms.

Processing time

Out of $\sim 3\,\mu$s of total trigger latency, roughly 2/3 is used to transfer the information from the detector to the control room and back. Thus only approximately 40 b.x. is available for the data processing. Among them a fair fraction is used for synchronisation and local data transfer between chips, boards and crates. Finally only 10-30 b.x. remains for actual trigger algorithm. Keeping in mind that modern electronics can perform only a few basic logical operations (like AND, OR, etc.) per b.x. (25 ns), the algorithms must be relatively simple.

Data transfer

- **Within a chip** — usually, only a fraction (typically 40-80 %) of resources potentially available in a chip can be used, because of routing problems. This is especially important in the case of FPGA[2] devices.
- **Between chips** — very often the actual limitation on a chip functionality comes not from its content but from the number of pins. Size and price of a chip depend strongly on its package.
- **Between boards** — standard crate backplane buses (like VME) are often not fast enough to ensure needed data sharing between different boards. Technically challenging and expensive custom backplanes are required.
- **Between crates** — standard cables (e.g. flat twisted pair) cannot be used to connect much more than 1000 signals to one crate. One can approach 10 kilobits/b.x. rate serialising the signals and sending them through a high speed link.
- **Between detectors and the control room** — in this case only high speed ($>$ 1 Gbit/s) optical links are feasible. Their cost constitute a substantial fraction of the total cost of the system.

5.4.2 Choice of approach — calculus machine or coincidence logic

One possible approach to the pattern recognition and momentum fit is a calculus machine. Addresses of hit detector elements can be converted into coordinates. Track saggita or bending angle can be calculated and converted into p_t. Main advantage of this method is possibility of exploiting high precision detector information with relatively small data flow. Parameters of the algorithm can be easily reprogrammed. The main drawback is low speed. Therefore only a limited number of track candidates can be considered, which might be a problem in case of high background rate.

An alternative method is to "hardwire" the calculations. That means finding a track by direct coincidences of signals from hit detector elements and assigning p_t by e.g. look-up tables, or similar technique. This method is fast, but requires a lot of hardware. In the case of low occupancy, a large number of processors most of the time do nothing but compare zeros with zeros. Therefore, it can be used only for a system with relatively small number of channels and limited precision. However, once the system is build, it is bottle-neck free. No matter what the rate is, all the information will be processed and there is no risk of efficiency loss. The only run-time limitation is the output rate which should not exceed the second level trigger capabilities.

The two methods are complementary, each one having its own advantages and drawbacks. Both are used in different places of the CMS Muon Trigger System (see Sec. 7).

[2] Field Programmable Gate Array — chip with programmable functionality

Chapter 6

Muon Trigger detectors

Muons stations should be equipped with detectors enabling triggering as well as precise momentum measurement. The momentum measurement requires position determination with accuracy $\approx 200\ \mu m$ per measuring plane in the barrel and $\approx 50 \Leftrightarrow 100\ \mu m$ in the endcaps.

In the barrel the expected occupancies and rates are rather low (< 10 Hz/cm^2, see Sec. 5.2.6, p. 51). Therefore, drift tubes (DT) [137] are natural candidates for muon chambers in this region. They cannot stand high magnetic field, but the field in the barrel is confined to the iron yoke and the muon stations are almost free of the field.

Situation is more difficult in the endcaps. Here the muon stations are in the strong (up to 4T) and very nonuniform (see Fig. 5.20, p. 54) magnetic field. Moreover, the occupancies and the rates are substantially higher (10-1000 Hz/cm^2) than in the barrel. These conditions exclude drift tubes. The solution chosen by CMS is Cathode Strip Chambers (CSC) [138].

Both DT and CSC can be used for the trigger. Their excellent spatial precision ensures sharp momentum threshold. However, having a long drift time ($\sim$400 ns for DT and $\sim$40 ns for CSC), they require rather complicated electronics to make correct bunch crossing assignment (see Section 7.3 and 7.4). Another drawback of CSC's and DT's is that the two spatial coordinates are given by long strips or wires. This may cause ambiguities in case of several tracks going through one chamber.

These drawbacks can be compensated by superior features of dedicated trigger detectors. Such detectors must be characterised by the excellent timing ($\sigma \sim 2$ ns) and high granularity. Strategy of using both precise muon chambers and fast dedicated detectors for the triggering purposes is commonly applied by experiments running currently on hadronic beams, like CDF, D0, H1, and ZEUS. These experiments use scintillating counters as dedicated trigger detectors. Segmentation required at LHC (see the next section) makes this solution unpracticable because of technical and financial reasons. Therefore both LHC experiments ATLAS and CMS envisage Resistive Plate Chambers (RPC) [139] in this place (in addition ATLAS uses Thin Gap Chambers in the endcaps).

In the next sections we are going to describe briefly RPC, DT and CSC designed for CMS. We put emphasis on their use for the trigger. Requirements for DT and CSC are driven mainly by precise momentum measurement, and we are not going to discuss them here. In contrast we spend a lot of time discussing requirements for RPC.

6.1 Resistive Plate Chambers

A typical RPC [139] consists of two parallel plates, made out of resistive material (with resistivity $10^9 \Leftrightarrow 10^{12}$ $\Omega \times$cm), e.g. bakelite (Fig. 6.1). The plates are separated by a gas gap of a few mm thickness. The outer surfaces of the resistive material are coated with conductive graphite paint to form the HV and ground electrodes. The readout is done by metal cathode strips, placed on outside of the separate plastic foil glued over the conducting surface of the cathode. One chamber can consist of more than one gas gaps separated by resistive plates and having a common readout in order to improve the efficiency. The whole structure is made gas tight and encased in a Faraday cage of thin metal foil.

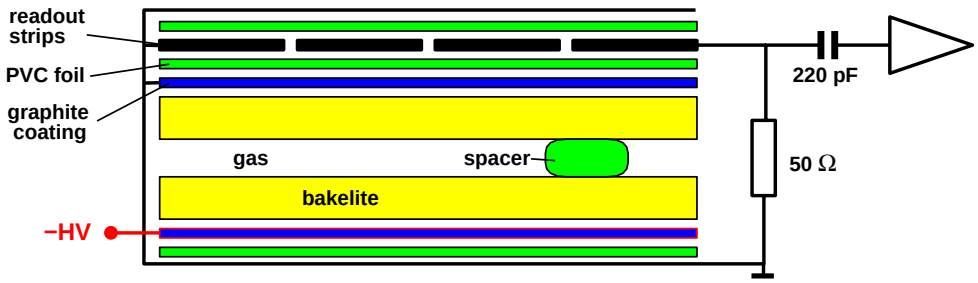

Figure 6.1: Single gap Resistive Plate Chamber.

6.1.1 Required Detector Granularity

Since in CMS the precision in ϕ determines momentum resolution, RPC are equipped with strips running parallel to the beam (along z) in the barrel and radially in the endcaps. The crucial point in the design of the RPC system is the choice of detector granularity. Possible factors to be considered are listed in Tab. 6.1. Dominant upper and lower limits are marked with $\Downarrow$ and $\Uparrow$ respectively.

Table 6.1: Determination of the RPC granularity

Strip width ($\Delta\phi$)	
track bending (required momentum resolution)	$\Downarrow$
multiple scattering and energy losses	
cluster size	
Strip length ($\Delta\eta$)	
signal propagation time along the strip (bunch cross. assign.)	$\Downarrow$ *barrel*
change of the bending with η	$\Downarrow$ *endcaps*
change of η due to the non-$r\phi$ bending	
Strip area (number of strips)	
number of channels (cost)	
complexity of the trigger processor (feasibility)	$\Uparrow$
number of interconnections (feasibility)	$\Uparrow$
capacitance	
occupancy	
probability of random coincidences of background hits	$\Downarrow$ *endcaps*
mechanics of the chamber	

Let us discuss the dominant factors one by one.

Track Bending and Strip Width

In order to maintain the single muon trigger rate at the level of a few kHz for luminosity of $10^{34}\text{cm}^{-2}\text{s}^{-1}$ one should apply $p_t^{cut} \approx$ 15-20 GeV (see Sec. 5.1). Having in mind necessary safety margin one can require that the highest possible p_t^{cut} should be somewhere between 50 and 100 GeV. It has been found that this is possible with with strips $\Delta\phi \approx 1/3^\circ$ which corresponds roughly to 2-3 cm in the inner muon stations (MB1 and MB2) of the barrel. This can be seen from the formulas collected in Fig. 6.2.

The obtained $\sigma_{1/p_t} \approx 1/100$ GeV means that a 50 GeV track is measured by two stations with precision $^{+50}_{-17}$ GeV and a 100 GeV one with $^{+\infty}_{-50}$ GeV. This is confirmed by a detailed GEANT simulation as shown in Fig. 6.3. It shows the track bending measured by $\Delta\phi$ expressed in one strip units. It is seen that the 50 GeV tracks are concentrated mainly in bin "-1". This means that they can be distinguished from the straight (infinite p_t) tracks, which would occupy bin "0". The 100 GeV tracks are distributed in bins "0" and "-1", i.e. they can be

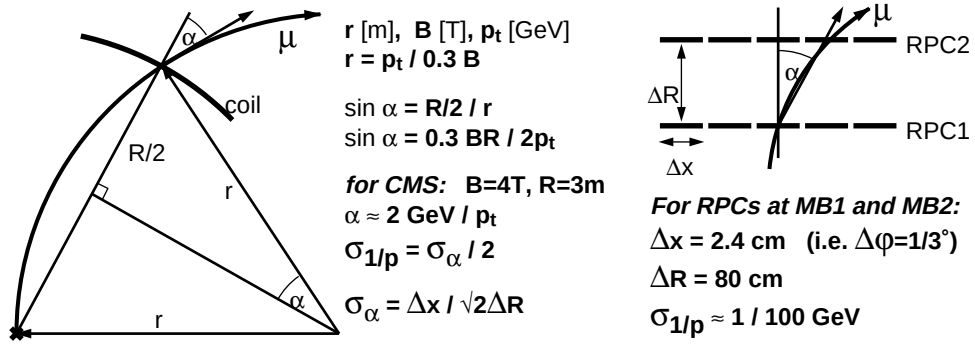

Figure 6.2: Momentum measurement in the solenoidal field of CMS.

distinguished neither from 50 GeV nor from infinite p_t tracks. This can be improved by using more muon stations. One can use the overlap of 50 and 100 GeV distributions as a measure of this improvements. It is plotted in Fig. 6.4 which shows that it saturates above 5 planes. On the other hand one should watch the complication of the trigger logic. It can be expressed in terms of the number of possible combinations (or patterns) of hits caused by a track crossing given strip. This number grows exponentially with the number of measuring planes, which is shown in Fig. 6.5. The two figures justify that the actual choice of 4 RPC planes used for the CMS trigger is reasonable.

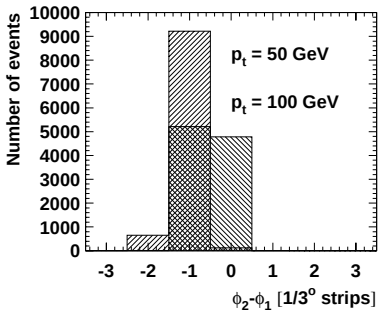

Figure 6.3: Bending angle measured by the first two muon stations.

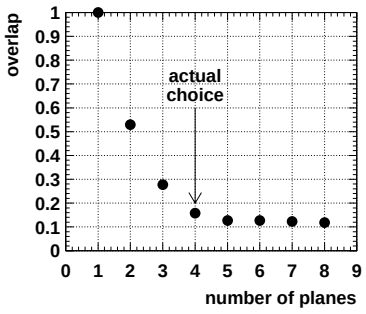

Figure 6.4: p_t resolution expressed as an overlap of 50 and 100 GeV distributions.

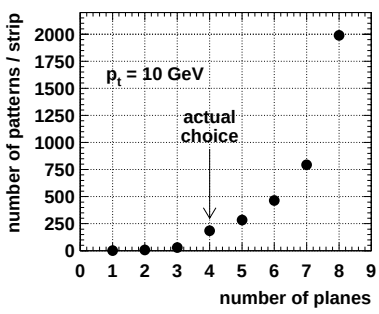

Figure 6.5: Complication of trigger logic presented as a number of patterns per strip.

The above reasoning should not be understood as a precise optimisation algorithm giving exactly number 4 as an output. Triggering with 3 stations is also possible, although with worse resolution. One should also keep in mind a need for some redundancy. One station can be lost from the measurement because of dead areas, electromagnetic showers caused by radiating muons or punchthrough from hadronic showers, as discussed in Sec. 5.2. In fact the RPC trigger algorithm (described in detail in Sec. 7.2) requires hits in at least 3 out of 4 muon stations. In the events where hits in all 4 stations are available, the p_t estimate is more precise.

Track Bending and Strip Length

As shown in Sec. 5.3 the bending power $\int |B \times dl|$ of the CMS magnet in the barrel is constant and equal 17 Tm. In the endcap however it decreases down to 8 Tm at $|\eta|$=2.0 and to 6 Tm at $|\eta|$=2.4 . Therefore particles of a given p_t are bent differently at different $|\eta|$. This is shown in Fig. 6.6 where the bending measured by $\Delta\phi$ between the first two stations is expressed in one strip units. The bending angle $\Delta\phi$ significantly depends on $|\eta|$. Thus one has to know $|\eta|$ in order to determine p_t from the $\Delta\phi$ measurement. From Fig. 6.6 one can see that precision of the order of 0.1 η-unit is needed, which determines the maximal length of the strips.

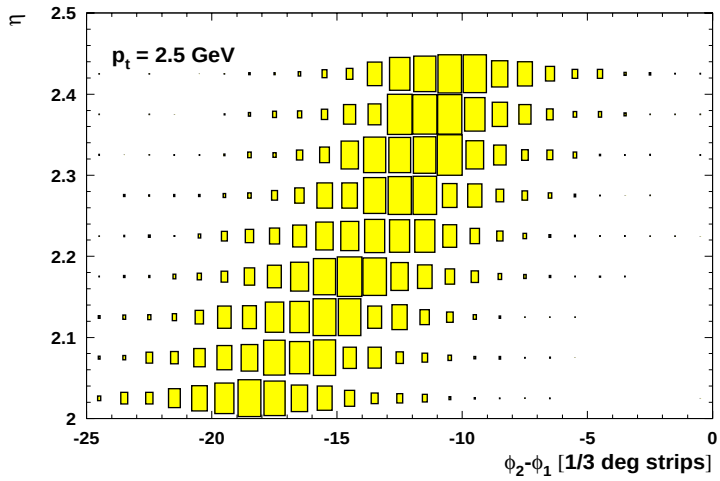

Figure 6.6: In the endcaps the track bending $\Delta\phi$ depends on $|\eta|$.

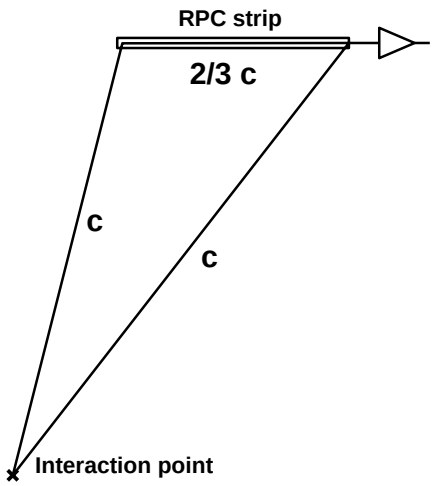

Figure 6.7: Uncertainty due to the time of flight and the signal propagation along the strip.

Time of Flight and Signal Propagation

Muons emitted at different η cross a given RPC strip at different positions. Therefore they have different time of flight and different time is needed for signals to propagate along the strip to an amplifier. Fig. 6.7 shows two extreme cases. Let us denote the radial position of the strip by R and the position of its two ends along the beam by Z_1 and Z_2. The shortest time is in the case where the muon hit the strip next to the amplifier:

$$t_2 = c\sqrt{R^2 + Z_2^2}$$

The longest one is when the muon hit the opposite end, so the signal must propagate along the entire strip with a speed v, typically close to $\frac{2}{3}c$:

$$t_1 = c\sqrt{R^2 + Z_1^2} + v(Z_2 \Leftrightarrow Z_1)$$

If we require this time spread $\Delta t = t_1 \Leftrightarrow t_2$ not to dominate the bunch crossing assignment precision it should not be much longer than 5 ns. This means, that the strip length should be of the order of 1 m or shorter.

Random Coincidences of Background Hits

The single hit rate in CMS muon stations was discussed in Sec. 5.2. In the barrel it stays at the level of 1-50 Hz/cm^2 and it should not cause any problems. In the endcaps it is quite uniformly distributed if expressed in $\eta\phi$ coordinates [24]. Therefore projective geometry has an advantage that the rate per one RPC strip is roughly constant. For strips of $\Delta\phi = 1/3^\circ$ and $\Delta\eta = 0.1$ it is about 6000 Hz per strip [21]. This corresponds to $\sim$ 30 hits per bunch crossing in the whole detector at high luminosity.

Those hits can affect the trigger rates in two ways. Random coincidence of several such hits in different stations can cause false trigger if they are by chance aligned along a possible muon track. A coincidence of a single background hit with hits of low p_t, curved muon track can look like more straight track and thus increase the apparent muon momentum. These two phenomena will be discussed in detail in Sec. 9.3.4.

6.1.2 Requirements on the RPC Performance

Chamber Efficiency

Since the trigger relay on coincidence of several RPC planes, each of them must be very efficient. We set our target at **98%**. This can be ensured e.g. by use of double gap chambers with staggered spacers.

Timing

Unambiguous bunch crossing identification requires trigger gates to be open for less then 25 ns. Leaving some margin for electronics set up time etc. one can assume 20 ns for this length. Another 5 ns should be subtracted for the signal propagation discussed above. Thus only 15 ns is left for the intrinsic RPC jitter. The precise requirement may be that: **98% of events should stay within 15 ns wide window**. In practice it corresponds roughly to $\sigma \approx 2$ ns, but the tails are important. This must include any time-walk, e.g. due to rate variations, because it is impossible or impractical to correct for it.

Clusters

It is a characteristic of RPC that a single minimum ionising particle often causes signals from several adjacent strips to pass a discriminator threshold (see Fig. 9.18, p. 104). This leads to deterioration of the momentum measurement. Therefore, one should require that **the average cluster size is not bigger than 2 strips** and that **the fraction of events with clusters having more than 4 strips does not exceed 1%**.

Rate Capability

Hit rates expected in CMS have been discussed in Sec. 5.2. Experience with simulating different shieldings by various programs suggests that we cannot trust their predictions with accuracy better than factor 2. It is not related to the quality of the programs. It rather reflects the fact that the background rates are very sensitive to the details of the detector and shielding geometry.

Another factor 2 is required to account for unknown cross sections. It has been shown [84] that PYTHIA 5.7 [134], used for trigger studies, cannot reproduce rates measured by UA1, CDF and D0 with better accuracy. Thus, in order to stay on the safe side we need to apply a safety factor of at least 4. The derived requirements on the rate capability are summarised in Tab. 6.2.

Table 6.2: Expected and required RPC hit rates

muon station		expected rate (Hz/cm^2)	required rate (Hz/cm^2)
MB 1-4		10	50
ME 1-4	outer ring	20	100
ME 2-4	$\|\eta\| < 2.4$	100	500
ME 1	$\|\eta\| < 2.1$	250	1000
ME 1	$\|\eta\| < 2.4$	500	2000

Assuming uniform technology for the entire CMS one should aim for the most demanding conditions, i.e. those at the inner part of the endcap. However, it should be investigated whether using different technology for the endcap and staying with more relaxed requirements for the barrel, may result in significant cost savings and/or a more robust design. The limit for $|\eta|$ <2.4 is to remind us that the eventual upgrade requires better performing detectors.

Conclusions

Main requirements discussed above are summarised in Fig. 6.8. One can ask how rigid are the particular values we have chosen. For example the requirement of 98% efficiency was not precisely justified. In fact one can only justify this kind of requirements only when they are taken together. This is done in Table 6.3 which shows the efficiency of the trigger which can be achieved requiring coincidence of at least 3 RPC planes.

The first column of the table shows that assuming our baseline requirements one can achieve the overall single muon trigger efficiency of 99% and the two-muon one of 98%. Unfortunately, it is already known that the average geometrical acceptance for coincidence of 3 planes in the barrel is 95% rather than 100% (see Fig. 9.2, p. 98). This reduces the single μ trigger efficiency down to 95% and the two-muon one down to 90%. If we achieve the detector and timing efficiency only 95% instead of 98% the trigger efficiency degrades down to 91% and 83%

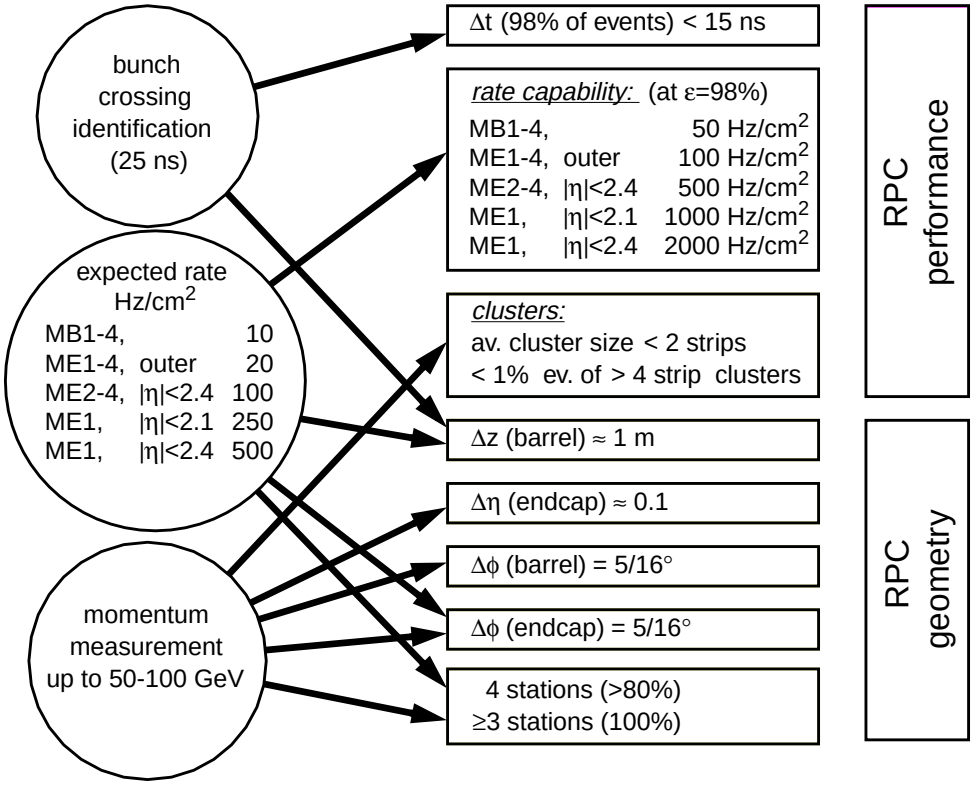

Figure 6.8: Driving requirements on the RPC system for CMS.

Table 6.3: Efficiency of the trigger based on coincidence of at least 3 RPC planes for various RPC parameters.

$\Delta t < 15$ ns	(single spot)	98%	98%	95%	90%
RPC efficiency	(one chamber)	98%	98%	95%	90%
geometrical acceptance	(≥ 3 planes)	100%	95%	95%	95%
1 μ trigger efficiency	(≥ 3 planes)	99%	95%	91%	81%
2 μ trigger efficiency	(≥ 3 planes)	98%	90%	83%	65%

for single and two-muon triggers respectively. This should be considered as an absolute lower limit on required efficiencies, because any further reduction dramatically jeopardise the trigger, which can be seen from the last column of Table 6.3.

6.1.3 Geometrical Layout of the RPC System

As a result of the above optimisation the following geometry was chosen. Each muon station will be equipped with one RPC plane except two innermost barrel stations MB1 and MB2 which will contain two RPC planes. This is because low momentum muons ($p_t < 5$-6 GeV) cannot reach the outer stations, for which a special low p_t trigger is foreseen. Those additional planes will be referred to as MB1′ and MB2′. Such additional planes are not necessary in the endcaps where the same p_t corresponds to much higher total momentum. Finally, the low p_t reach of the CMS muon trigger will be about 4 GeV in the barrel and 2.0-3.5 GeV in the endcaps.

The physical segmentation of RPC strips in the barrel is projective in ϕ and constant in z. The CMS barrel consists of 5 wheels (see Fig. 2.3, p. 14) containing 4 muon stations each. RPC in each wheel are divided in 2 along z. An exception is the inner layer of MB2 which is used as a reference plane for the trigger defining its segmentation (see the next Section). In this layer each of 5 wheels is divided in 3, thus the barrel is divided in 15 *rolls* numbered from $\Leftrightarrow$7 to 7. Correspondence between the roll number and the z coordinate is given in Tab. 6.4. Above we argued for the strip width of $\Delta\phi = 1/3°$, which would result in having 90 strips per chamber. It was

decided to have 96 strip, i.e. $\Delta\phi = 5/16^\circ$ instead, in order to facilitate the design of digital electronics. The strips are numbered around CMS from 0 to 1151 following the ϕ coordinate. Precise dimensions of the chambers as well as single strips are given in Fig. 6.9.

Table 6.4: Physical segmentation of RPC strips in the reference plane (dimensions in cm).

roll	0	1	2	3	4	5	6	7
z_{min} (MB2)	-43	43	148	233	318	415	500	585
z_{max} (MB2)	43	128	233	318	403	500	585	671
η_{min} (MB2)	-0.09	0.09	0.28	0.47	0.63	0.78	0.92	1.04
η_{max} (MB2)	0.09	0.28	0.47	0.63	0.78	0.92	1.04	1.14
roll	8	9	10	11	12	13	14	15
r_{max}	695	595	540	492	438	392	351	299
r_{min}	595	540	492	438	392	351	299	264
η_{min} (ME2)		1.14	1.22	1.30	1.40	1.50	1.60	1.75
η_{max} (ME2)		1.22	1.30	1.40	1.50	1.60	1.75	1.87
roll	16	17	18	19	20	21	22	23
r_{max}	264	233	208	187	169	154	141	128
r_{min}	233	208	187	169	154	141	128	116
η_{min} (ME2)	1.87	1.99	2.10	2.20	2.30			
η_{max} (ME2)	1.99	2.10	2.20	2.30	2.40			

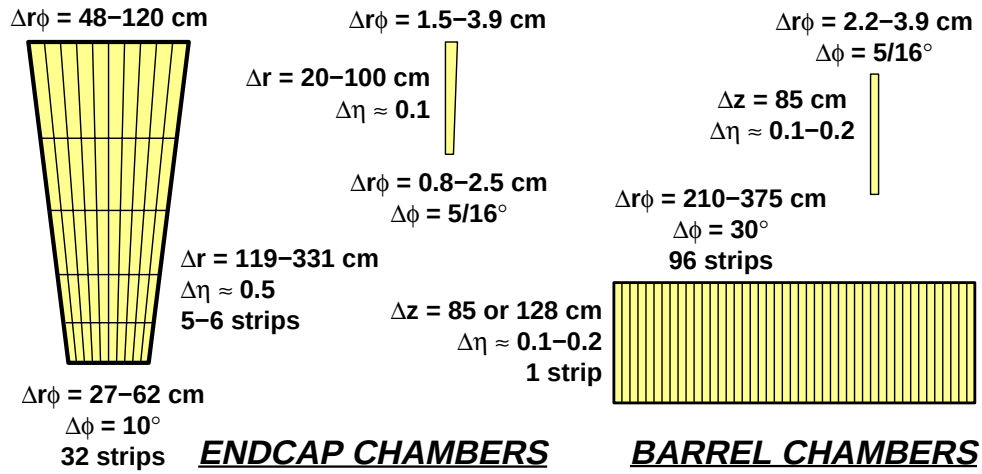

Figure 6.9: Dimensions of RPC chambers and strips. For each dimension its lowest and highest value is given.

The RPC segmentation in the endcaps it is projective in ϕ and constant in r, i.e. the strip division lines are parallel to the beam. Hence each endcap roll is a set of strips contained by a cylinder of inner radius r_{min} and outer radius r_{max}, as defined in Tab. 6.4. The forward endcap rolls are numbered from 8 to 23 and backward endcap rolls — from $\Leftrightarrow$23 to $\Leftrightarrow$8. This strip geometry can be realised in various ways. One example is shown in Fig. 6.9. In this solution one chamber covers $\Delta\eta \times \Delta\phi = \sim 0.5 \times 10^\circ = 5 \Leftrightarrow 6 \times 32$ strips. Recently another option is under study: $\Delta\eta \times \Delta\phi = \sim 0.2 \times 30^\circ = 2 \times 96$ strips.

In total there will be 1656 RPC's in CMS covering the area of 3400 m^2. They will be read out by about 200 000 electronics channels. Detail breakdown of the number of channels is given in Tab. 6.5.

Table 6.5: Number of RPC channels for various muon stations.

muon	MB				ME								
station	1	2	3	4	1/1	1/2	1/3	2/1	2/2	3/1	3/2	4/1	4/2
η div.	2+2	3+2	2	2	5(+3)	3	3	4(+3)	6	3(+3)	6	3(+3)	6
subtotal	13				39(+12)								
channels	13×5 wheels × ×12 sectors ×96 strips				39(+12)×2 endcaps × ×12 sectors ×96 strips								
total	74 880				89 856 (+ 27 648)								
grand total	164 736 (+ 27 648 = 192 384)												

6.1.4 Connection to the trigger

The RPC strips are connected to *Pattern Comparator Trigger* (PACT) described in detail in Sec. 7.2. The logical segmentation of the PACT trigger is projective in ϕ and η. It is defined by the strips in MB2 and ME2 chosen as the reference planes. The logical ϕ segmentation just follows the physical one. One *trigger segment* is based on 8 reference strips, hence segments are numbered from 0 to 143. The η segment boundaries are given in Tab. 6.4. The segments in η form 39 *rings* (also called *towers*) which are numbered from $\Leftrightarrow$19 to 19 as shown in Fig. 6.10.

In every ring 4 RPC planes are chosen to be connected to the segment processors. The chosen planes are indicated in Fig. 6.10. In the barrel there are additional low p_t (> 5 GeV) processors receiving signals from MB1, MB1′, MB2 and MB2′ planes.

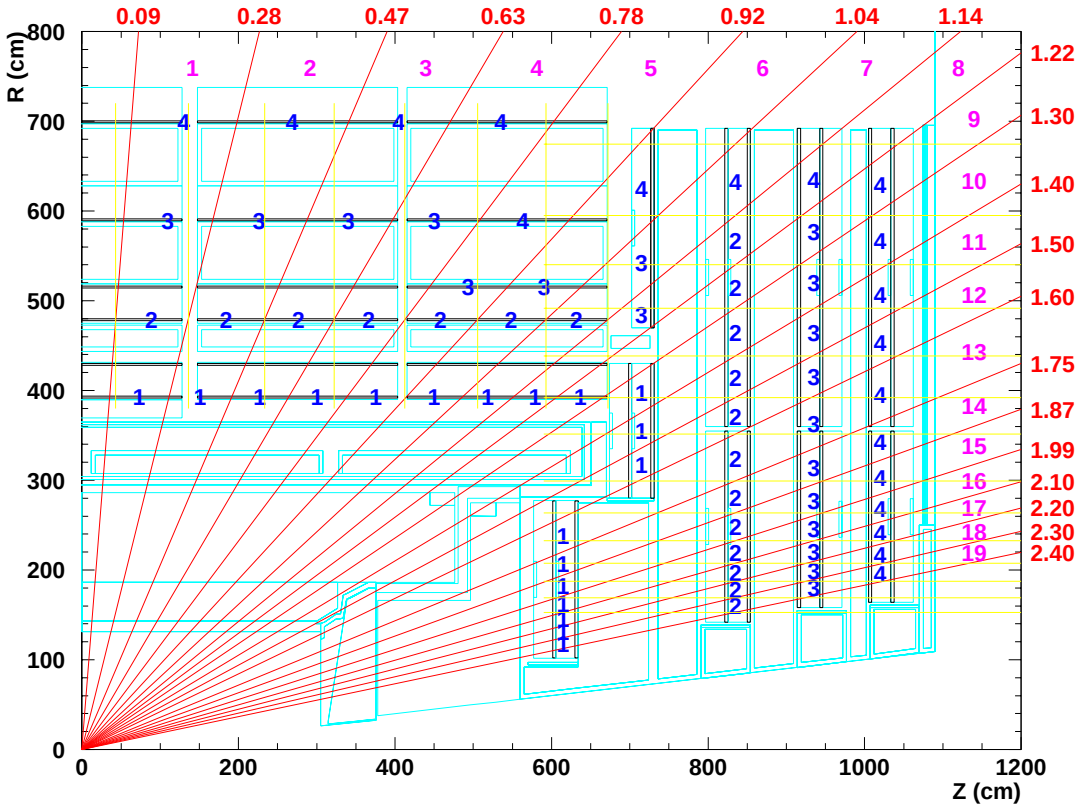

Figure 6.10: Physical segmentation of RPC chambers and logical segmentation of PACT.

6.2 Drift Tubes with bunch crossing recognition capability (DTBX)

Each of 4 muon stations in the barrel is equipped with a DTBX chamber [137] which consists of 12 layers of drift tubes (see Fig. 6.11). The layers are arranged in 3 quartets called *superlayers* (SL). Two of the superlayers measure the $r\phi$ coordinate, one measures η. The superlayers are fixed to a thick aluminium honeycomb which ensures the stiffness of the chamber and provides a lever arm between the two $r\phi$-superlayers. The chambers are 2.54 m long and 2-4 m wide, depending on the station.

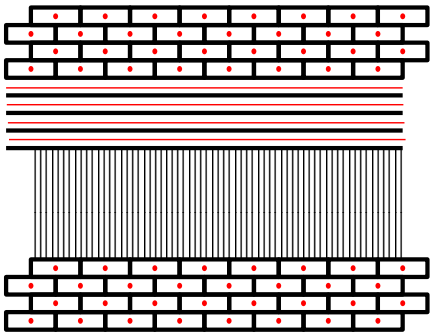

Figure 6.11: Schematic cross section of DTBX chamber.

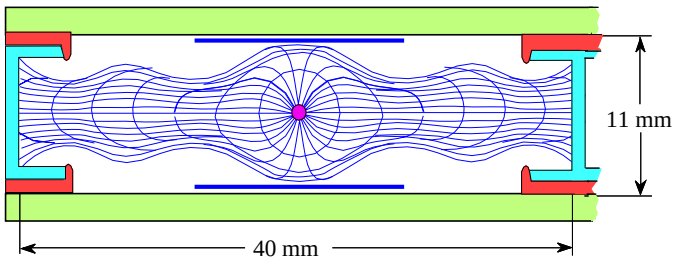

Figure 6.12: DTBX drift cell.

Each chamber is made out of 2 mm thick aluminium plates, separated by aluminium I-beams forming independent drift cells. The electrostatic cell layout is shown in Fig. 6.12. The I-beams acts as cathodes, therefore they are insulated from the plates which are grounded. Anode wires are made of stainless steel and they have diameter of 50 μm. Two additional electrodes in the middle of the cell improve the shape of the field.

A single tube is 40 mm wide (drift direction) and the distance between planes of tubes is 13 mm. The maximal drift time with a drift velocity of 50 μm/ns is about 400 ns. The chamber is designed to be operated in proportional mode with a non-flammable gas mixture (Ar/CO_2). Basic parameters of the DTBX system are summarised in Table 6.6.

Table 6.6: DTBX system.

Chamber length (z)	256 cm
MB1 width ($r\phi$)	209 cm
MB2 width ($r\phi$)	254 cm
MB3 width ($r\phi$)	311 cm
MB4 width ($r\phi$)	406 cm
Cell size	40×11 mm^2
Number of channels	194 880
Number of chambers	250
Total area of chamber planes	1730 m^2

Most of the requirements on the Drift Tubes are driven by the spatial precision needed for the off-line momentum measurement. However, there is one important feature required for triggering — linearity of the relation between the drift time and position. In order to keep low trigger latency one cannot afford complicated calculations. Therefore the algorithm described in Section 7.3 relies on this linearity. The complicated electrostatic layout of the chamber ensures that the linearity is maintained in a magnetic field up to 0.5 T with a deviation of <5 ns.

6.3 Cathode Strip Chambers

Endcap muon stations are equipped with Cathode Strip Chambers [138]. CSC are multiwire proportional chambers with segmented cathode readout. High precision coordinate along the wire is obtained by extrapolation of charges induced on several adjacent cathode strips. In CMS the strip width varies from 3.2 to 16 mm. Obtained resolution is in the range between 80 and 450 μm for one layer. For the trigger purposes, however, resolution of $\sim \frac{1}{2}$ of strip is good enough.

CMS chambers have trapezoidal shape (Fig. 6.13). One chamber consists of six detecting layers (Fig. 6.14). The layers are separated by 16 mm thick polycarbonate plastic honeycomb panels which make the chamber stiff and provide a lever arm necessary to measure angle of the tracks. In each layer the strips are running radially. In angular units the strip width $\Delta\phi$ varies from 2.0 to 4.3 mrad and the length $\Delta\eta$ from 0.35 to 0.60 η units. Combined resolution of six layers approaches $\sim 50\mu$m.

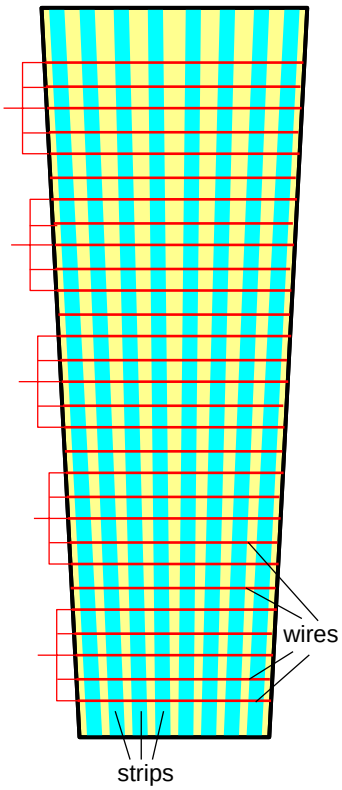

Figure 6.13: Schematic layout of Cathode Strip Chamber.

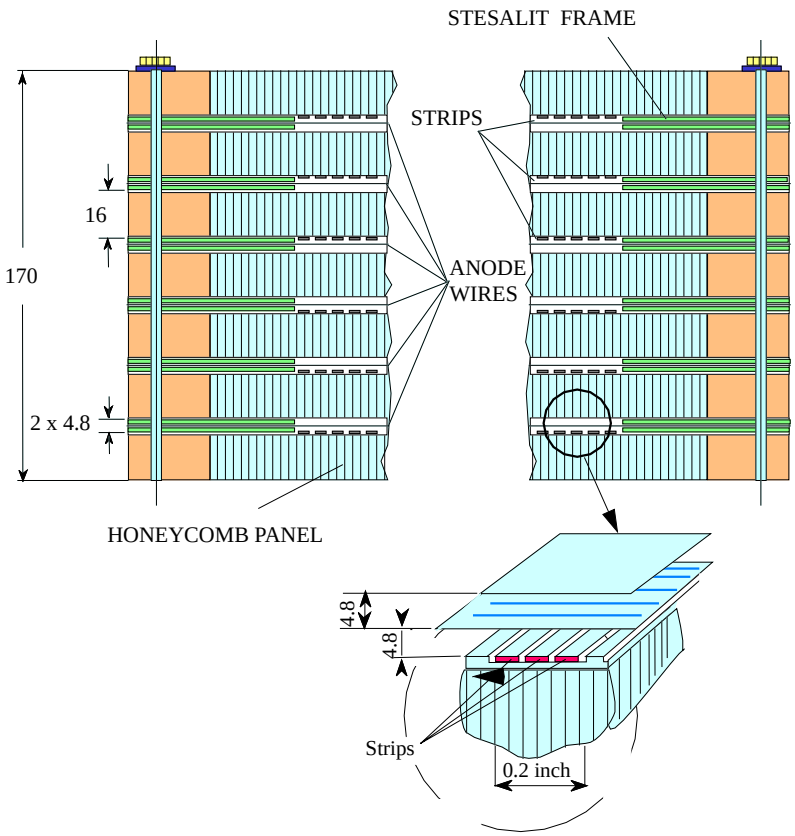

Figure 6.14: CSC cross section.

The wires are perpendicular to the strips, except ME1/1 where the wires are tilted by 25°. This is to compensate the Lorentz effect in high magnetic field (almost 4T) to which the chamber is exposed. The wires have 50μm diameter and they are spaced by 2.5 or 3.175 mm. Groups of 5-17 wires are readout together providing the spatial resolution of $\Delta r \approx$16-54 mm, i.e. $\Delta\eta \approx$ 0.01-0.04.

Because of the complicated geometry of the endcaps the chambers have different dimensions. They are listed in Tab. 6.7. Parameters of the whole system are summarised in Tab. 6.8.

Table 6.7: Cathode Strip Chambers (dimensions in mm).

Chamber type	1/1	1/2	1/3	2/1	2/2	3/1	3/2	4/1	4/2
Chambers in ϕ	36	36	36	18	36	18	36	18	36
Inner radius R_1	1002	2800	4835	1391	3550	1620	3550	1790	3550
Outer radius R_2	2700	4300	6955	3450	6955	3450	6955	3450	6955
Chamber length L	1698	1500	2120	2059	3405	1830	3405	1660	3405
Top width W_2	663	1011	1197	1508	1507	1508	1507	1508	1507
Bottom width W_1	340	731	826	732	871	818	871	882	871
Left dead zone ΔL	75	104	104	104	104	104	104	104	104
Top dead zone ΔT	65	69	69	69	69	69	69	69	69
Right dead zone ΔR	75	104	104	104	104	104	104	104	104
Bottom dead zone ΔB	65	69	69	69	69	69	69	69	69
Bottom strip length	383	–	–	524	–	606	–	668	–
Top strip length	1185	1362	1982	1397	3267	1086	3267	855	3267
Number of strips in ϕ	64	80	64	80	80	80	80	80	80
Top strip width	7.8	9.8	15.2	15.7	16.0	15.7	16.0	15.7	16.0
Bottom strip width	3.2	6.7	10.9	6.8	8.4	7.9	8.4	8.7	8.4
Number of anode groups	64	48	48	112	64	112	64	112	64
Wire spacing	2.500	3.175	3.175	3.175	3.175	3.175	3.175	3.175	3.175
Wires per group	11	9	14	6	17	5	17	5	17
Anode group width	27.5	28.6	44.5	19.0	54.0	15.9	54.0	15.9	54.0

Table 6.8: Cathode Strip Chamber system.

	ME1/1	others	total
Number of 6-plane chambers	72	468	540
Number of anode channel	27648	196992	224640
Number of cathode channels	55296	269568	324864
Number of wires (millions)	0.27	2.14	2.41
Total area of chamber planes (m^2)	368	8122	8490

Chapter 7

Muon Trigger algorithms and their implementation

7.1 Introduction

The First Level Muon Trigger of CMS uses all three kinds of muon detectors: Drift Tubes (DT), Cathode Strip Chambers (CSC) and Resistive Plate Chambers (RPC). An excellent spatial precision of DT and CSC ensures sharp momentum threshold. Their multilayer structure provides a possibility of effective background rejection. RPC are dedicated trigger detectors. Their superior time resolution ensures unambiguous bunch crossing identification. High granularity makes possible to work in high rate environment. Time information and both spatial coordinates of a detected particle are carried by the same signal, which eliminates ambiguities typical for wire detectors.

Complementary features of muon chambers (DT/CSC) and dedicated trigger detectors (RPC) allows us to build two trigger subsystems which deliver independent information about detected particles to the Global Muon Trigger. Advantages of having two such subsystems are numerous. The muon chambers and the dedicated trigger detectors deliver different information about particle tracks. They behave differently in difficult cases and they respond in different ways to various backgrounds. Properly combining the information from both systems results in high efficiency and powerful background rejection. Two extreme cases of such combinations are the logical OR, which is optimised for efficiency, and the logical AND, optimised for background rejection. However, neither of these operations results in full use of the complementary functions of the muon trigger components and more sophisticated algorithm should be used. This is possible, because both the muon chambers and the dedicated trigger detectors deliver an information about the quality of detected muon candidates.

Another important advantage of the two component system is a possibility of crosschecks and crosscalibration. Trigger data from the two components collected by the DAQ can be compared online. This enables the quick discovery of possible problems and gives a possibility of immediate action. When studying cross sections, asymmetries etc., it is very important to know the trigger efficiency and acceptance. Usually this is done by running with thresholds much lower than the measurement range. Two component system offers a unique ability to measure these quantities in a more unbiased way.

Logically, the muon trigger system consists of the following items:

- Pattern Comparator Trigger (PACT) based on Resistive Plate Chambers (RPC)
- Drift Tube (DT) Trigger
- Cathode Strip Chamber (CSC) Trigger
- Track Finder (TF)
- Muon Sorter
- Global Muon Trigger

Functional relations between the components are shown in Fig. 7.1. Cumulative latency is given in bunch crossing units (bx). Three shaded backgrounds show the location of the electronics: at the chamber, in the experimental hall and in the control room. Optical links of 1 Gbit/s are indicated by circles. Most of the DT trigger electronics is placed in the experimental hall, but an option is being considered to mount it directly on the chambers.

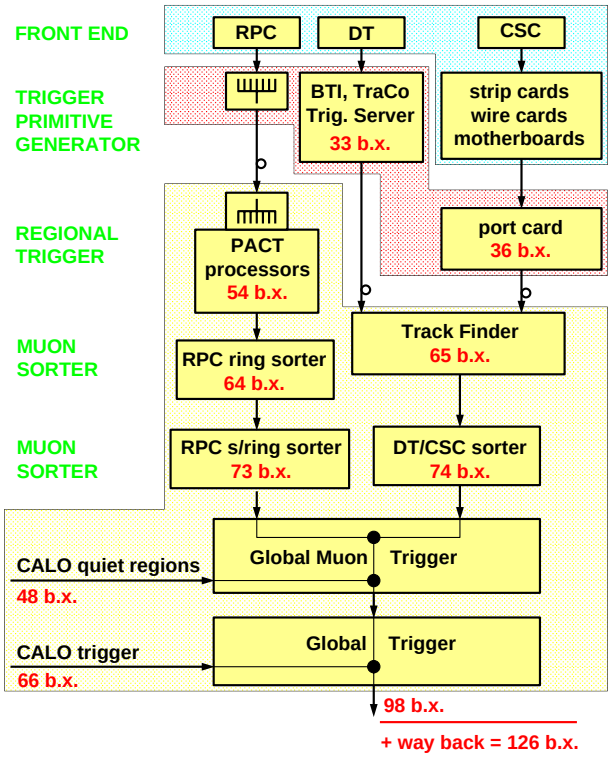

Figure 7.1: Functional scheme of the Muon Trigger.

DT and CSC electronics first process the information from each chamber locally. Therefore they are called *local triggers*. As a result one vector (position and angle) per muon station is delivered. Vectors from different stations are collected by the Track Finder which combines them to form a muon track and assign a transverse momentum value. This information is sent to the Muon Sorter. TF plays role of a *regional trigger*.

In the case of RPC there is no local processing apart from synchronisation and cluster reduction. Hits from all stations are collected by PACT logic. If they are aligned along a possible muon track, a p_t value is assigned and the information is sent to the Muon Sorter.

The Muon Sorter selects 4 highest p_t muons from each subsystem in several detector regions and sends them to the Global Muon Trigger. The Global Muon Trigger compares the information from TF (DT/CSC) and PACT (RPC). So called quiet bits delivered by the Calorimeter Trigger are used to form an isolated muon trigger. The 4 highest p_t muons in the whole event are then transmitted to the Global Trigger. Finally transverse momentum thresholds are applied by the Global Trigger for all trigger conditions.

The components of the Muon Trigger system are described in the following sections. At the beginning of each section a brief the description of the corresponding algorithm is given. It is followed by an overview of the subsystem in terms of its logical units. Each unit is then described in detail in a dedicated subsection.

7.2 RPC based Pattern Comparator Trigger (PACT)

The goal of the RPC trigger is to detect a muon traversing several muon stations, measure its direction and transverse momentum, and identify the bunch crossing in which the muon was created. The principle of the trigger is illustrated in Fig. 7.2. The solenoidal field bends tracks in the $r\phi$ plane. A pattern of hits recorded by RPC's carries the information about the bending, and can be used to determine p_t of the track. This is done by comparison with a predefined set of patterns corresponding to various p_t. Therefore we call this device Pattern Comparator Trigger (PACT) [22]. Bunch crossing is identified naturally by the arrival time of the RPC signals.

The PACT electronics is housed by four kind of boards:

- Front End Board (FEB)
- Link Board (LB)
- Trigger Board (TB)
- Readout Board (RB)

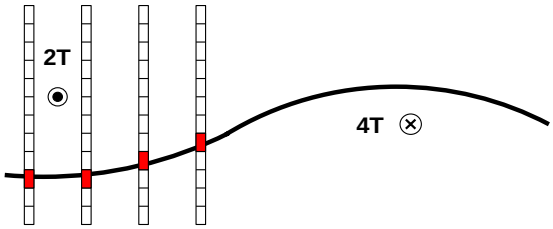

Figure 7.2: RPC Pattern Comparator Trigger principle.

Signals from RPC strips are first amplified, discriminated and synchronised with a clock on FEB. Then they are sent to LB where the data are compressed and transmitted through optical links to TB and RB. Each TB receives data from 4 RPC planes. They are combined into patterns in Pattern Comparator (PAC) ASIC's. If they match one of the predefined patterns its p_t, η and ϕ are sent to Muon Sorter for further processing.

Segmentation of the entire PACT system is given is Tab. 7.1. Ring and super-ring processors belong logically to Muon Sorter and they will be described in Section 7.6. Below we describe functionality of Front End Board, Link Board and Trigger Board. Readout Board, performing functions typical for the Data Acquisition System will not be discussed here.

Table 7.1: PACT segmentation. The quantity is given for baseline ($|\eta| < 2.1$) and upgrade ($|\eta| < 2.4$)

item	subdivision	$\Delta\phi$	$\Delta\eta$	quantity	
strip	—	5/16°	0.1-0.2	164 736	27 648
segment	8 strips / plane	2.5°	0.1-0.2	4752	864
TB	12 segments	30°	0.1-0.2	396	72
ring	12 TB's	360°	0.1-0.2	33	6
"super-ring"	3 rings	360°	∼0.35	11	2

7.2.1 Front End Board (FEB)

One RPC chamber having 96 channels is served by 4 Front End Boards, shown in Fig. 7.3. Each FEB houses 4 *Front End Chips* (FEC). Single FEC contains 6 channel preamplifier and discriminator. Each pair of FEC's is connected to a *Synchronisation Unit* (SU). Here the signals are shaped to a programmable length (<25 ns) and synchronised with the LHC clock distributed by the TTC (*Timing, Trigger and Control*) network.

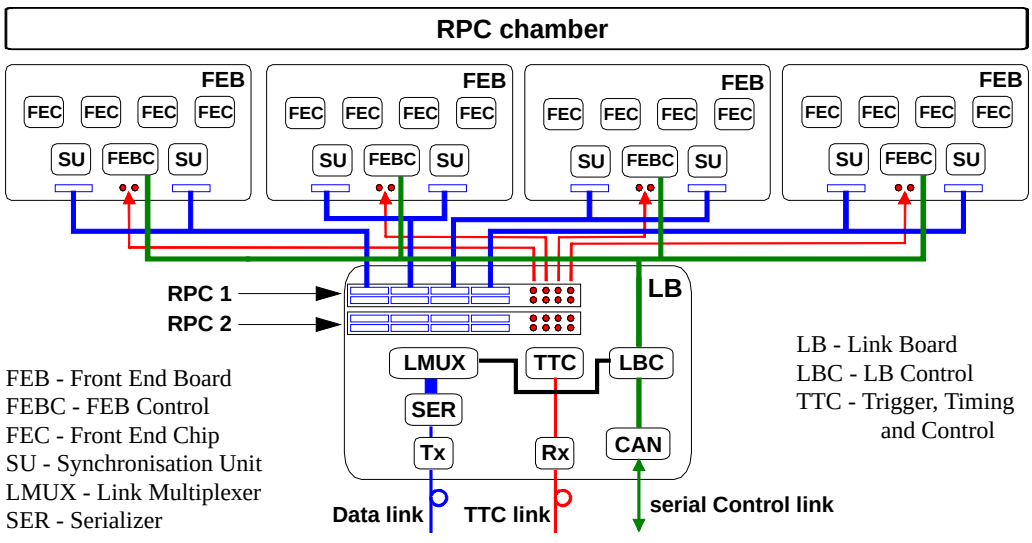

Figure 7.3: RPC front end trigger electronics.

7.2.2 Link Board (LB)

Data from two RPC's are collected by *Link Board* (LB) via short twisted-pair copper cables. The major task of LB is to transmit the RPC data to Trigger Boards and Readout Boards located in the Control Room.

Transmission of row data would require very high bandwidth: 200 000 channels $\times$ 1 bit $\times$ 40 MHz = 8 T bits/s i.e. for example 8000 optical links of 1 G bits/s. This would be very expensive solution. Fortunately the average occupancy of the system is very low. It is dominated by uncorrelated electrons originated by captured neutrons (see Sec. 5.2.6) and it amounts for about $1.5{\cdot}10^{-4}$, i.e. $\sim$30 hits/bx. One should, however, keep in mind that there are high local fluctuations. One muon accompanied by secondaries can cause hits on $\sim$10% of strips in one chamber. These characteristics leave a lot of room for optimisation of transmission algorithms. Currently the following data compression scheme is envisaged (Fig. 7.4):

- strips are grouped by 12 (or 8), i.e. one chamber is divided into 8 (or 12) sections;
- only non-empty groups are sent; it may last a few bunch crossings;
- new data arriving in the meantime are buffered to avoid dead time.

The algorithm is realised by *Link Multiplexer* (LMUX) and *Serializer* (SER). LMUX selects non-empty bunches. SER pushes them through the link in consecutive bunch crossings. Format of the data is given in Tab. 7.2.

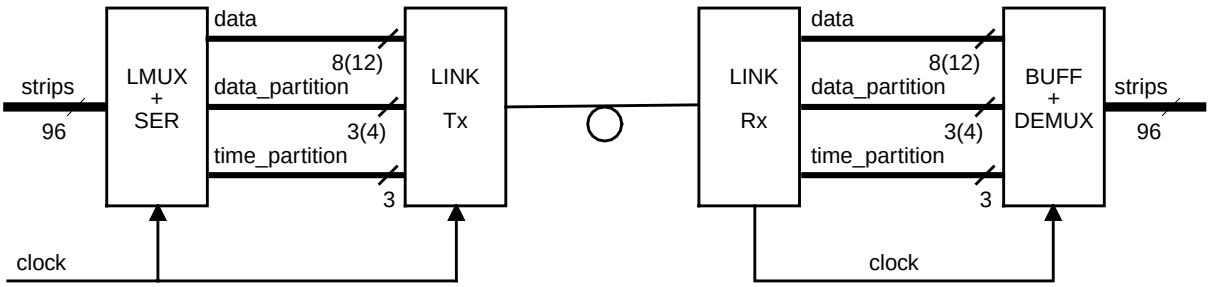

Figure 7.4: RPC data transmission from Link Board to Trigger Board.

Table 7.2: Compressed RPC data format

variable	bits	unit / precision
strip data	12 (or 8)	1 strip = 1 bit
section number	3 (or 4)	1 section = 12 (or 8) strips
chamber number	1	1 chamber = 96 strips
bunch crossing	3	modulo 8
status bit	1	–

7.2.3 Trigger Board (TB)

Data preprocessing

Trigger and Readout Board receives the compressed RPC data through an optical link. In the trigger crate the data flow is split into to streams: trigger path and DAQ path. In the trigger path the row data format is restored. This is needed for fast pattern comparison. Because signal from one muon can be shared by more than one strip, detected clusters are reduced in size by removing extreme strips. This improves momentum resolution of the system. For low p_t muons, when the resolution is limited by multiple scattering, the strips are grouped by 2 or 4, depending on the momentum. The ϕ resolution needed for given p_t depends on η. Therefore the grouping of strips into 2- and 4-folded logical OR's may be different in different rings.

Segment processor

Further processing is done in *segments*. Segment is the basic logical unit of PACT. It covers $\Delta\phi = 2.5^\circ \times \Delta\eta \approx 0.1$ rapidity unit. It is defined by 8 strips in a reference muon station. As the reference station we have chosen ME2 and the first RPC plane in MB2. Each *segment processor* is equipped with 4 Pattern Comparator (PAC) chips covering different p_t intervals. Two of them work on single strips, one on 2- and one on 4-folded logical OR's.

Pattern Comparator (PAC) ASIC

PAC compares patterns of hits from 4 RPC planes with predefined *valid patterns*. The valid patterns are first obtained from simulation and will be corrected later using real reconstructed muon tracks. Because a given pattern can be created by muons from a certain p_t range we deliberately choose to assign the upper limit of this p_t range to this pattern. The pattern must consist of at least 3 hits from different planes. If it consists of 4 different plane hits a *4/4 quality bit* is set to 1. Otherwise it is set to 0. This bit is used further to select the best muon candidates because a missing hit can cause overestimation of the muon momentum.

Practical realisation of PAC is shown schematically in Fig. 7.5. One pattern is a coincidence (an AND gate in the Fig.) of hits from different RPC planes. Patterns must be programmable, therefore each coincidence input line is in fact a multiplexer selecting one of the strips from a given plane. Patterns are then grouped in several p_t bins. Also the grouping is programmable, thus the coincidence outputs are demultiplexers selecting one of the p_t coder inputs. If more than one pattern is present the highest p_t of all observed patterns is delivered. The same rule is applied when the outputs of all PAC's in a segment are combined. Full information delivered by each segment processor is described in Tab. 7.3. This information is further processed by the Muon Sorter.

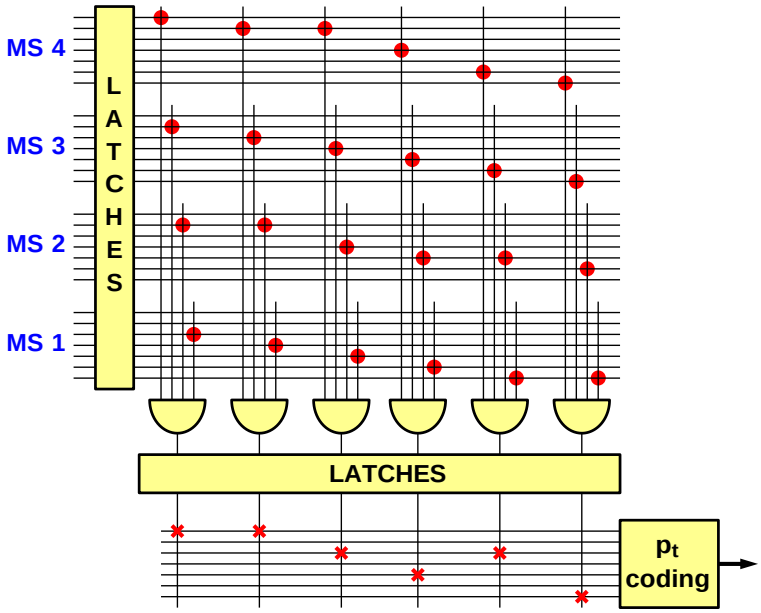

Figure 7.5: Pattern Comparator (PAC).

Table 7.3: Information delivered by PACT segment processor ($\leq$ 1 track per segment)

variable	bits	unit / precision
η	6	~ 0.1 η unit
ϕ	8	2.5°
muon sign	1	—
p_t	5	nonlinear scale
3/4 quality bit	1	—

7.3 Drift Tube trigger

The goal of the local Drift Tube trigger is to detect a charged particle crossing the chamber, measure its position and angle, and identify the bunch crossing in which the particle was created. Each chamber consists of 3 quartets (*superlayers*) of measuring planes. Two of them measure the ϕ coordinate, one measures the z. The track recognition is done in two steps — first, in each superlayer independently, then an attempt is made to combine the track segments from both ϕ-superlayers. Position, angle and time (bunch crossing number) of each track segment are calculated from drift time of hits by solving a system of linear equations. This is done using a meantimer-like technique.

Drift Tube electronics is divided into two paths — trigger and readout (see Fig. 7.6). In the readout path, the signals are digitised by TDC and sent to the DAQ system by ReadOut Server (ROS). The trigger electronics consists of three parts:

- Bunch and Track Identifier (BTI)
- Track Correlator (TRACO)
- Trigger Server (TS)

Each BTI looks for coincidence of aligned hits in 4 layers of one Drift Tube superlayer (SL). Positive coincidence is considered as a *track segment*. Its parameters (position and angle) are calculated and then sent to TRACO which tries to combine track segments from the two SL measuring the ϕ coordinate. The best combinations from all TRACO's of one chamber together with SL_η track segments are collected by TS. After final selection two of them (at most) are sent to the Track Finder.

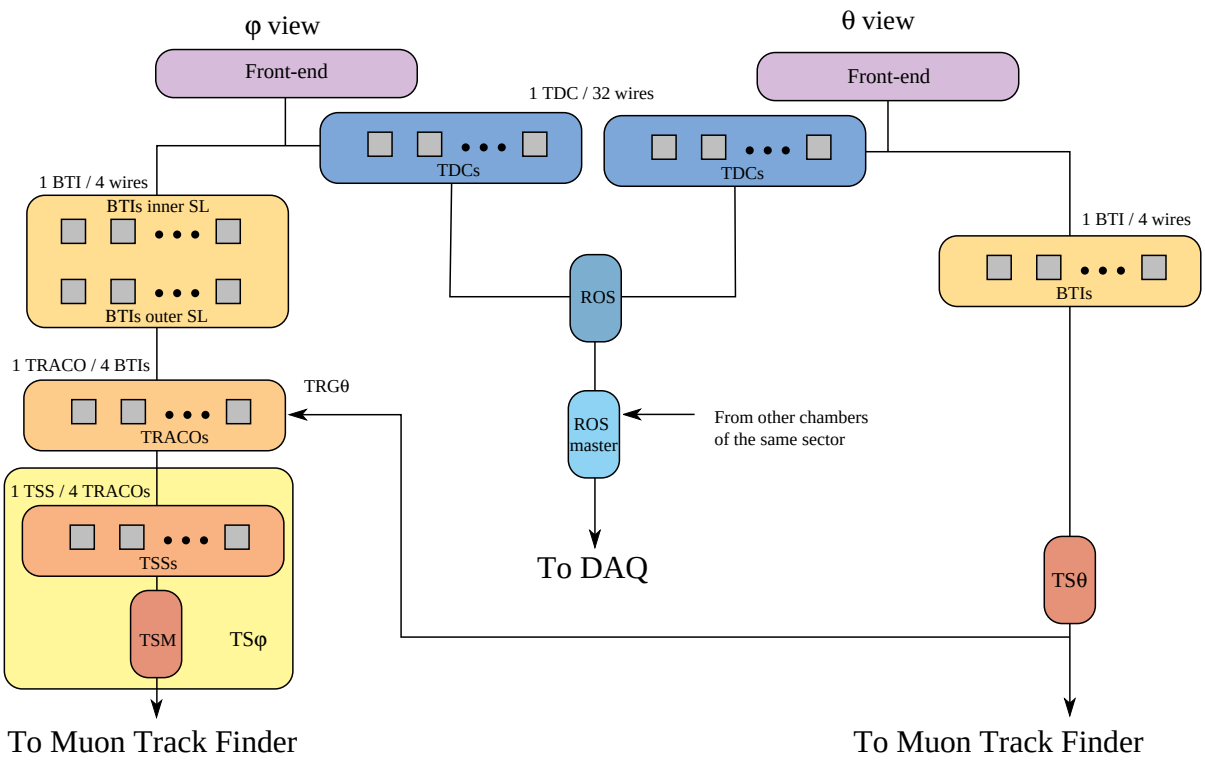

Figure 7.6: Block diagram of the Drift Tube electronics.

7.3.1 Bunch and Track Identifier (BTI)

Tracks in each superlayer SL are recognised by BTI using generalised meantimer technique (Fig. 7.7). Signals from 4 DT layers are connected to clock driven shift registers. Shifting time in the registers compensates the drift time, thus 4 signals are aligned in a fixed time after the particle passage, approximately equal to the maximal drift time. This enables bunch crossing identification. Cases when only 3 aligned hits are found are also accepted but they are called *Low Quality Triggers* (LTRG) and they set the *H/L quality bit* to 0. *High Quality Triggers* (HTRG), based on 4 aligned hits, set the H/L quality bit to 1. In case of more than 1 track candidate an arbitrary one is delivered but HTRG has preference over LTRG.

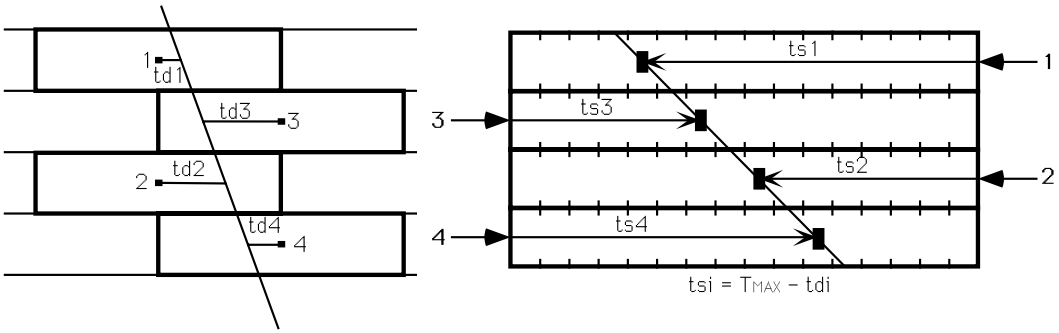

Figure 7.7: Bunch and Track Identifier (BTI).

The maximal drift time of 400 ns and the clock cycle of 25 ns determine the position measurement unit to be equal to 1.25 mm. A lever arm of at least 22 mm gives an angular precision better than 60 mrad. A single BTI unit is connected to 2+2+2+3 tubes in 4 layers respectively covering a spatial range of 80 mm and an angular range of $\pm 45.7°$. Hence 6+6 bits are needed to express the measured position+angle. The acceptance for 3 hit tracks is slightly wider than $\pm 45.7°$ but the efficiency decreases with the angle, approaching 0 at $\pm 56°$.

Table 7.4: Information delivered by DT BTI ($\leq$ 1 track per BTI)

variable	bits	unit / precision
track position x	6	1.25 mm
track angle ψ	6	60 mrad
H/L quality bit	1	—

7.3.2 Track Correlator (TRACO)

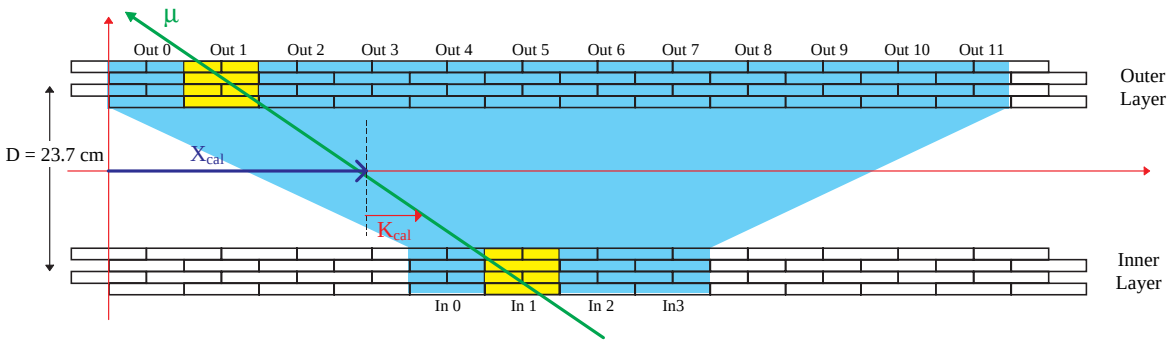

Figure 7.8: Coverage of one Track Correlator.

Track pairs from inner (SL_i) and outer (SL_o) ϕ-superlayers are combined by the *Track Correlator* (Fig. 7.8). It compares their angles, ψ_i and ψ_o, (Fig. 7.9) with the angle ψ_{cor} defined by the positions x_i and x_o with precision of 10 mrad. If the correlation is successful then ψ_{cor} and x_{cor} are transmitted and *CORR quality bit* is set to 1. Otherwise CORR=0 and HTRG is chosen. If both tracks have the same quality the one from SL_i is taken.

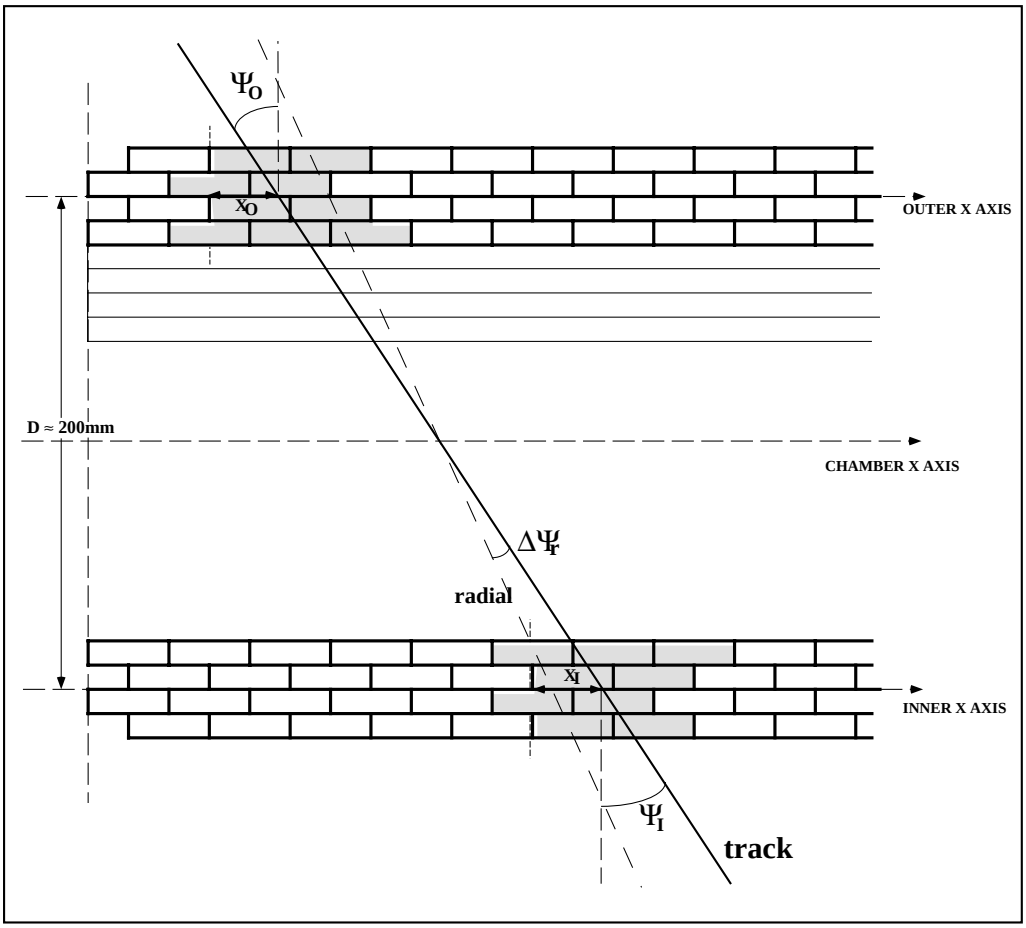

Figure 7.9: Track Correlator principle.

Each TRACO serves 5 SL_i and 15 SL_o in order to match the BTI angular acceptance. It selects up to 2 candidate BTI pairs using H/L bit and deviation from radial direction $\Delta\psi_r$ which should be smaller for higher p_t tracks. HTRG has preference over $\Delta\psi_r$ for the first candidate, and vice versa for the second one. If a second trigger comes right after the first one, only one track is transmitted and the overlap flag OVLP is set to 1. The MULT flag informs if there are other tracks to be transmitted. TRACO also receives information from the η-superlayer. It is used together with H/L bits from ϕ-superlayers to determine two trigger quality bits TRG0 and TRG1. The described algorithm flow is the standard one, but other choices are available using programmable control bits.

Table 7.5: Information delivered by TRACO ($\leq$ 2 tracks per TRACO)

variable	bits	unit / precision
track position $\phi(x)$	10	1.25 mm
track angle ψ	5	10 mrad (if CORR=1) 60 mrad (if CORR=0)
control bits: CORR, MULT, OVLP, TRG(1:0)	5	—

7.3.3 Trigger Server (TS)

TRACO outputs from one chamber (up to 28 TRACO's) are collected by *Trigger Server*. It has to select up to 2 track candidates from each bunch crossing having smallest $\Delta\psi_r$. To be compatible with the TRACO algorithm the priorities are different for the first track and for the second track. For the first one candidates with HTRG have preference over those with LTRG only. For the second one only $\Delta\psi_r$ is considered.

The TS task is complicated by the fact that TRACO can transmit two track segments serially, in 2 consecutive bunch crossings. In order to find the true second best track one has to compare the second best one of bunch 1 with the best one of bunch 2. Precise synchronisation of TRACO and TS action gives the total latency smaller than the sum of the two components. This is shown in detail in Tab. 7.6.

Table 7.6: Operational sequences of TRACO and TS

Delay w.r.t. BTI trigger	TRACO sequence	TS sequence
1 bx	• read ψ and x from BTIs • select lowest $\Delta\psi_r$: BTI_i^1 and BTI_o^1 from all BTIs, preferring HTRG	
2 bx	• send $\Delta\psi_r$ of 1^{st} track to TS_ϕ • receive TRG_η from TS_η • select lowest $\Delta\psi_r$: BTI_i^2 and BTI_o^2 from all BTIs, but BTI_i^1 and BTI_o^1	
3 bx	• send $\Delta\psi_r$ of 2^{nd} track to TS_ϕ • calculate 1^{st} track TRK_1 • set 1^{st} CORR flag	• receive $\Delta\psi_r$ of 1^{st} track from TRACO • find 1^{st} lowest $\Delta\psi_r$ • select 1^{st} TRACO
4 bx	• send TRK_1 to TS_ϕ • calculate 2^{nd} track TRK_2 • set 2^{nd} CORR flag	• receive $\Delta\psi_r$ of 2^{nd} track from TRACO • find 2^{nd} lowest $\Delta\psi_r$ • select 2^{nd} TRACO
5 bx	• send TRK_2 to TS_ϕ	• read 1^{st} track from TRACO
6 bx		• read 2^{nd} track from TRACO
7 bx		• transmit 1^{st} and 2^{nd} track to Track Finder

TS transmits two selected tracks in parallel to the Track Finder. Format of the data is given in Tab. 7.7. In addition, positions of all tracks detected by BTI in η-superlayers are coded in 32 bits with 8 cm resolution (Tab. 7.8). They are transmitted to Track Finder in parallel to the ϕ information.

Table 7.7: Information delivered by DT Trigger Server: ϕ-projection (≤ 2 track per chamber)

variable	bits	unit / precision
track position $\phi(x)$	11	1.25 mm
track angle ψ	8	10 mrad (if CORR=1) 60 mrad (if CORR=0)
quality bits: CORR, TRG(1:0)	3	—

Table 7.8: Information delivered by DT Trigger Server: η-projection (per chamber)

variable	bits	unit / precision
position of triggered BTIs	32	8 cm

Figure 7.10: CSC trigger electronics.

The first three boards are placed directly on a chamber as shown in Fig. 7.11. Signals from strips and wires are first processed independently by Cathode and Anode Front End Boards. Hits from 6 planes are combined into Local Charged Tracks (LCT). Selected LCT's are sent to the Motherboard where strip and wire LCT's are combined together. Port Card collects information from several Motherboards and sends it to the Track Finder.

7.4.1 Cathode Front End Board (strip card)

Cluster center finding

Typical cathode signal is shared by a few strips. The first task of the strip electronics is to find the center of the cluster with a half strip precision. Details of this algorithm are still under discussion. Currently two possibilities

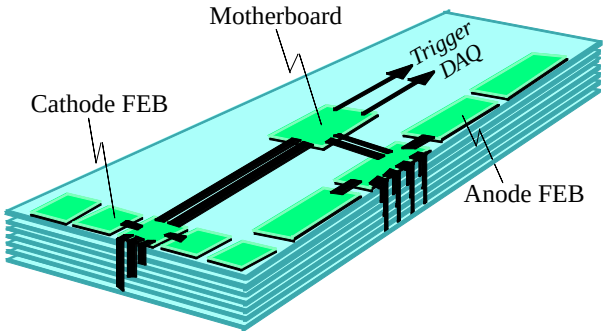

Figure 7.11: Front end electronics on CSC.

are being envisaged (Fig. 7.12):

- algorithm 1 working on discriminated signals, calculating the cluster center from strips on the cluster edge,
- algorithm 2 using a network of analog comparators (Fig. 7.13) looking for the highest signal and its neighbours.

Algorithm 1:

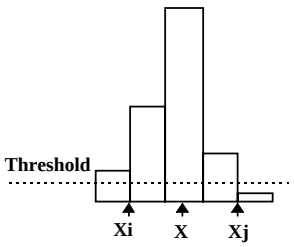

X = 1/2 (Xi + Xj).

where:
X - hit coordinate
Xi, Xj - coordinates of extreme strips in the cluster.

Algorithm 2:

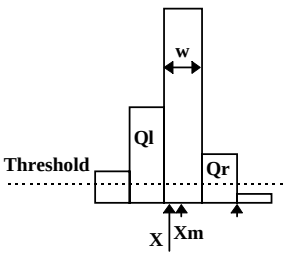

X = Xm , for one strip;
X = Xm - w/4, if Ql > Qr;
X = Xm + w/4, if Qr > Ql.

where:
Xm - strip coordinate with max. charge;
w - strip width ;
Ql, Qr - the charge on left and right strips of the cluster.

Figure 7.12: Algorithms to achieve half-strip resolution.

Pattern matching

One CSC strip card handles 16 strips $\times$ 6 layers. The strip signals are brought into coincidence within *roads* within a time bucket of 100 ns for the local strip trigger. For p_t in the range 10 - 100 GeV the road is 4 $\times$ half strip wide. For low p_t, between 2.5 and 10 GeV, the half strip signals are grouped by 4 (to the width of two strips) and the road is 4 $\times$ double strip wide. One or two missing hits in a road are allowed, i.e. 4/6 (4 out of 6) and 5/6 patterns are accepted in addition to 6/6 ones.

Priority encoding

The best pattern in a road and then the best one on a entire strip card is found by *priority encoding*. First 6/6 patterns take priority over 5/6 and 4/6, then low bend-angle (high p_t) take priority over high bend-angle (low p_t).

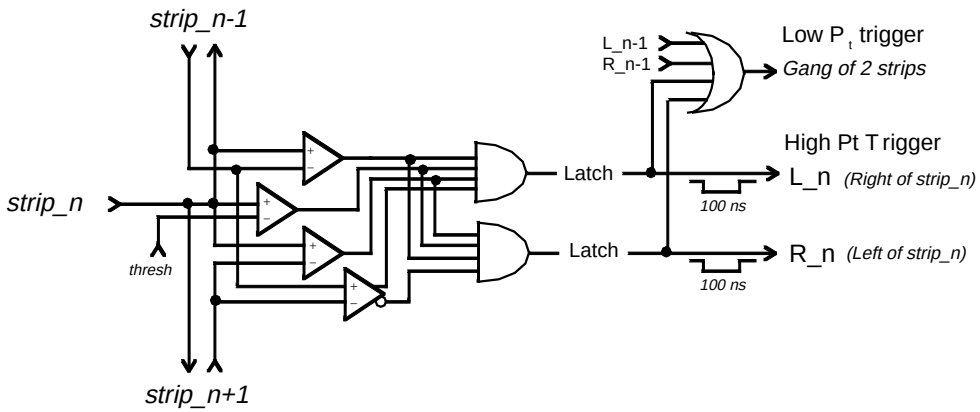

Figure 7.13: One channel of the Comparator Network.

This mechanism also enables some tuning of the system by assigning higher or lower priority to selected patterns. Local Charged Track with the highest priority pattern in a given strip card is transmitted to the Motherboard in the following format:

- LCT position (modulo half a strip)
- LCT pattern ID
- pattern coincidence level (6/6, 5/6 or 4/6)
- half-strip / double-strip flag

7.4.2 Anode Front End Board (wire card)

Bunch crossing identification and pattern matching

The main task of the wire card is to recognise the bunch crossing. It is not straightforward because signals from six layers are spread within 50 ns interval due to the drift time. A possible algorithm is shown in Fig. 7.14.

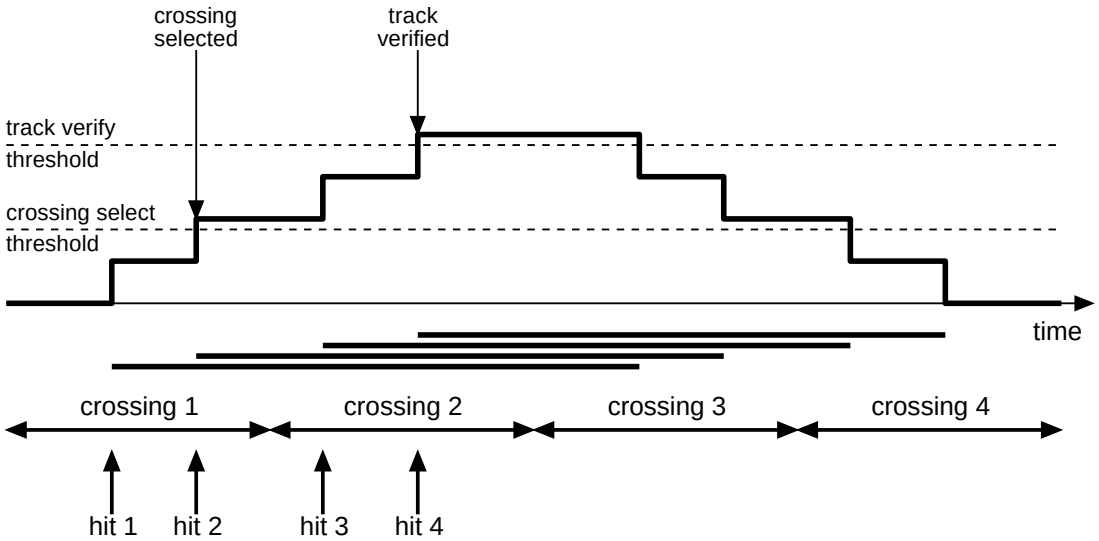

Figure 7.14: Bunch crossing assignment algorithm for CSC.

We use each hit in a CSC layer to produce a rectangular pulse. The length of the pulse t_w should be slightly larger than the maximal drift time. The pulses that are assigned to a road are added together. If a second hit is added to the first, the pulse height goes over the crossing select threshold and a candidate track in this crossing is stored. However, the existence of a track assigned to this crossing is not established until 2 more additional hits are found in this road within the t_w time window established by the earliest hit. If this occurs, the pulse height exceeds the track verification threshold and the track is confirmed and assigned to the original crossing where the crossing

select threshold was passed. Even if the verification (by passage of the 4-hit threshold) happens in the subsequent crossing to the establishment of the candidate track (by passage of the 2-hit threshold), the track is still assigned to the crossing where the candidate was originally found. The length of the time window t_w depends on parameters of the chamber+electronics. Currently chosen values are 50 ns for ME1/1 and 75 ns for ME1/2-ME4.

Priority encoding

Priority encoding for wire Local Charged Tracks is similar to that for strips. First 6/6 patterns take priority over 5/6 and 4/6, then higher priority is given to tracks better pointing to the vertex. LCT with the highest priority pattern in a given wire card is transmitted to the Motherboard in the following format:

- LCT position (modulo group of ganged wires)
- LCT pattern ID
- pattern coincidence level (6/6, 5/6 or 4/6)

7.4.3 Motherboard

LCT selection and buffering

One Motherboard receives information from 4-10 Cathode FEB's and 3-4 Anode FEB's. First, the number of strip LCT's and wire LCT's is reduced to two of each type, having the highest priority code. A wire LCT has bunch crossing identified exactly, whereas a strip LCT has it assigned with ± 1 b.x. accuracy only. Therefore the best two strip LCT's have to be buffered for another two bunch crossings. Thus, every b.x. one has to choose the best two strip LCT's among six candidates.

Matching of wire and strip LCT's

Each strip LCT should be matched with one wire LCT. Usually there should be at most one track crossing the chamber. In such a case the matching is trivial. There are, however, events where more than one muon cross the chamber, or addition LCT's are created by background. In the case of ≥ 1 strip LCT or ≥ 1 wire LCT it is difficult to decide which strip LCT should be matched with which wire LCT. Several ways of solving this ambiguity were envisaged:

- use information available at the motherboard like coincidence level (number of hits) etc.;
- make coincidence with RPC strips which are ~ 6 times shorter then those of CSC;
- make coincidence with an additional plane of CSC pads;
- replace one layer of radial strips with inclined strips (so called 5R+1U solution);
- replace 6 layers of radial strips with 3+3 stereo layers (so called U+V solution);
- solve ambiguities in the Track Finder hoping that the extrapolation of ghosts will fail;
- solve ambiguities in the Global Muon Trigger comparing with track candidates from RPC.

Current baseline solution, however, is rather simple:

- match the best (the highest priority) strip LCT with the best wire LCT,
- match the second best strip LCT with the second best wire LCT.

Transfer to the Port Card

Track segments created by matching strip LCT and wire LCT are transfered to a Port Card. Before the transfer the following functions are performed:

- overlaps with neighbour chambers in ϕ are resolved,
- strip LCT information is converted into position ϕ and bend angle ψ_ϕ,
- wire LCT information is converted into position $\eta(r)$ and incident angle ψ_η,
- alignment corrections are applied,
- quality information based on coincidence level (6/6, 5/6 or 4/6) and priority code of strip and wire LCT's is attached (precise definition of quality bits is not yet defined).

One Motherboard can be connected to more than one Port Card. Each track segment is routed to the proper Port Card depending on its coordinates.

7.4.4 Port Card

The task of the Port Card is to collect information from several Motherboards and send it to the Track Finder. CSC chambers covers 10° or 20° (see Tab. 6.7) while the Track Finder works with 30° sectors. Port Card is placed on the detector and it receives the information for Motherboards through twisted-pair copper cables. The best three track segments are selected and send to the Track Finder. Since the Track Finder is placed in the control room, the data are sent by optical links. Data format is given in Tab. 7.9.

Table 7.9: Information delivered by CSC Port Card for ϕ- and η-projection respectively (≤ 2 tracks per chamber).

variable	bits	unit / precision
track position ϕ	11	1-9 mrad
track angle ψ_ϕ	8	~10 mrad
quality information (see text)	not yet defined	—
track position $\eta(r)$	8	16-54 mm
track angle ψ_η	8	~50-100 mrad
quality information (see text)	not yet defined	—

7.5 Track Finder

The main task of the Track Finder is to combine track segments delivered by Drift Tubes and Cathode Strip Chambers from different stations into full muon tracks and assign p_t values to them. Its basic unit called *sector processor* covers $\Delta\phi = 30^\circ$ and $\Delta\eta \approx 0.2 \Leftrightarrow 0.5$. The algorithm consists of three steps (Fig. 7.15). First, track segments from different stations are matched by an extrapolation method. Then the matched pairs are combined into a full track. Finally unique values of ϕ, η and p_t are assigned to the track.

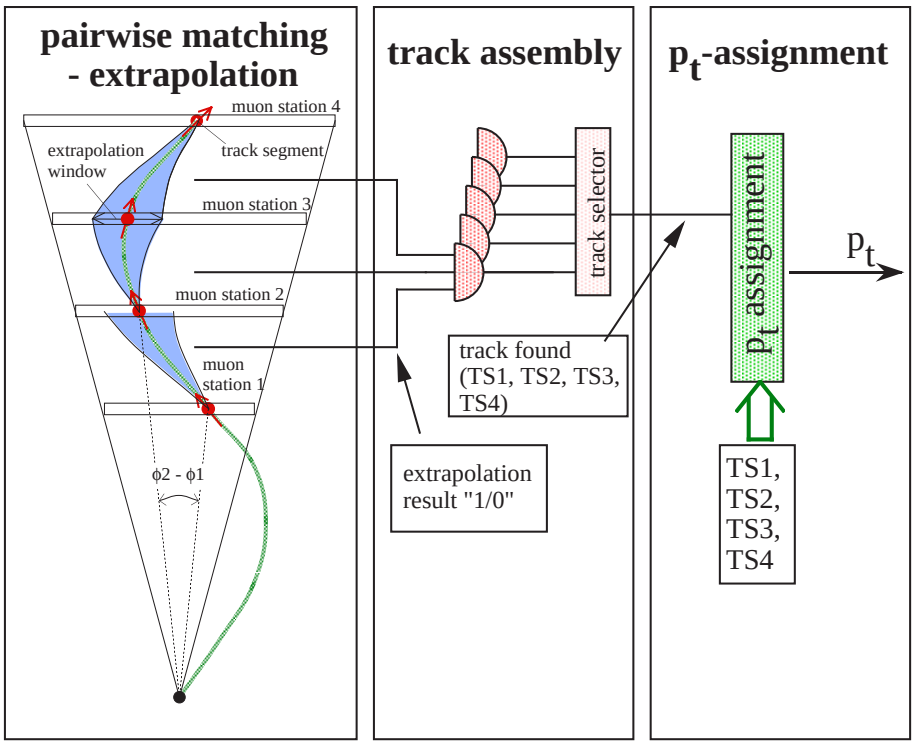

Figure 7.15: Track Finder principle.

The algorithm is performed by the following units (see Fig. 7.16):

- **Extrapolator**
  - Extrapolation Unit (EU)
  - Extrapolation Result Selector (ERS)
- **Track Assembler**
  - Track Segment Linker (TSL)
    - TSL units
    - Single Track Selector (STS)
  - Track Selector (TSel)
    - Track Cancellation Logic (TCL)
- **Track Router** (TR)
- **Assignment Units** (AU)
  - quality, η, ϕ, and p_t

Their functionality will be described in the subsequent sections.

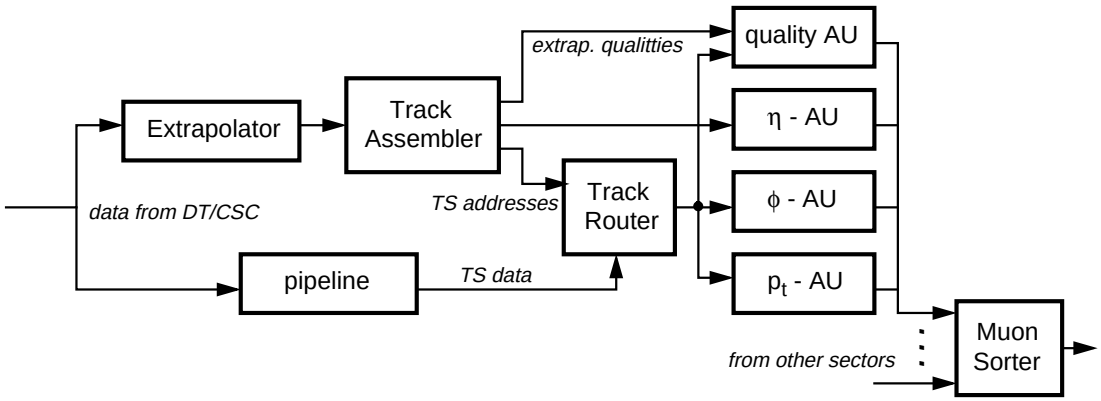

Figure 7.16: Track Finder block diagram.

7.5.1 Extrapolator

Having track segment in some of 4 muon stations, several extrapolations from one station to another are done in parallel by *Extrapolation Units* (EU). In the barrel they are: $1 \rightarrow 2$, $2 \rightarrow 3$, $4 \rightarrow 3$, $1 \rightarrow 3$, $2 \rightarrow 4$, and $1 \rightarrow 4$. The extrapolation is based on position ϕ and bend angle ψ of a track segment. The bend angle ψ is used as a starting direction and as a measure of p_t to find the track curvature. In the barrel the $p_t(\psi)$ relation is unique but in the forward region it depends also on η. A pair of track segments is considered as matched if the extrapolation of the first one coincides with the position (and possibly the angle) of the second one within a given accuracy. Two best extrapolations for each source track segment are selected by *Extrapolation Result Selector* (ERS).

7.5.2 Track Assembler

The *Track Segment Linker* (TSL) attempts to combine all matched pairs into a full track. At least two matched track segments are required. Number of possible candidates is reduced by *Single Track Selector* (STS) which selects only one candidate for each innermost source track. The selection is based on the quality of the two track segments.

Next steps are performed by the *Track Selector* (TSel). First *Track Cancellation Logic* (TCL) removes track candidates which are identical to parts of longer tracks. It also removes shorter candidates having common segments with longer ones. Finally two highest rank track candidates are selected. The rank is defined by two criteria (ordered by priority):

1. Track consisting of higher number of track segments are preferred.
2. Station 1 and 2 have preference over 3 and 4.

Track segments belonging to the selected tracks are sent to the *Assignment Unit* by *Track Router* (TR).

7.5.3 Track Router

Full information about track segments is stored in a pipeline memory during the processing time of the *Extrapolator* and the *Track Assembler*. The *Track Router* (TR) extracts from the pipline the information related to the selected track segments, combines it with the output of the *Track Assembler* and transfers it to the *Assignment Units*.

7.5.4 Assignment Units

The last step is to assign unique ϕ, η and p_t to the track. In most of the cases, the p_t is calculated as a function of the bend angle between two stations $\phi_i \Leftrightarrow \phi_j$. There are few exceptions when the local bend angle ψ of the track segment in one station is used instead. In the forward region also the η information must be used. The resulting values are then transmitted to the Muon Sorter. A single sector processor can deliver up to 2 tracks. They are selected using p_t and quality bits.

Table 7.10: Information delivered by Track Finder ($\leq$ 2 track per sector)

variable	bits	unit / precision
η	6	~ 0.1 η unit
ϕ	8	2.5°
muon sign	1	—
p_t	5	nonlinear scale
quality bits	2	—

7.5.5 Barrel/endcap corner

The presented algorithm works well in the barrel. It also works in the endcaps provided that $\eta \Leftrightarrow \phi$ ambiguities described in the previous section are solved properly by CSC trigger itself.

The most difficult situation is in the barrel/endcap transition region where some track segments come from DT and others from CSC. In this region the extrapolation from CSC to DT is ambiguous. Extrapolation from DT to CSC cannot be done, because it requires η coordinate which cannot be delivered by DT for $|\eta| > 0.85$ due to the limited BTI acceptance ($\psi_{max} = 45.7$ corresponds to $\eta_{max} = 0.86$). Several possible solutions are considered:

- use $\phi_{ME2} \Leftrightarrow \phi_{ME1}$ to get rid of the ambiguity in CSC $\rightarrow$ DT extrapolation;
- assume that the track has high p_t to get rid of the ambiguity in CSC $\rightarrow$ DT extrapolation (this degrades slightly the performance at low p_t);
- make CSC $\rightarrow$ DT extrapolation within "wide window" containing ambiguities; in case of $>$1 candidate pairs select one with better p_t match or better quality bits;
- make DT $\rightarrow$ CSC extrapolation within a "wide window" containing η-uncertainties; in case of $>$1 candidate pairs select one with better p_t match or better quality bits;
- use only DT or only CSC taking advantage that at least two stations of one kind are crossed by each track.

Yet another problem in this region is the presence of magnetic field up to ~ 0.9 T in MB1 and MB2. It causes an increase of the drift time and in consequence reduction of the ϕ-BTI efficiency below 70%.

7.6 Muon Sorter

The Muon Sorter receives the information from the Pattern Comparator Trigger or Track Finder in a form described in Tab. 7.3 and Tab. 7.10 respectively. One single sorter chip accepts up to 8 muons on the input and delivers up to 4 muons on the output, sorted according to their quality and than p_t. In the RPC PACT part a ghost suppression algorithm is applied (see below). The output data has the same format as the input (Tab. 7.11). A lack of muon is indicated by p_t=0. The sorting chips are arranged in a form of a tree sorting out the 4 highest p_t muons among all candidates in several detector regions (see Fig. 7.17). In total **1065** sorting chips are needed.

Table 7.11: Information about each muon handled by Muon Sorter ($\leq$ 8 tracks on input, $\leq$ 4 tracks on output)

variable	bits	unit / precision
η	6	$\sim 0.1\ \eta$ unit
ϕ	8	2.5°
muon sign	1	—
p_t	5	nonlinear scale
quality bits	2	—

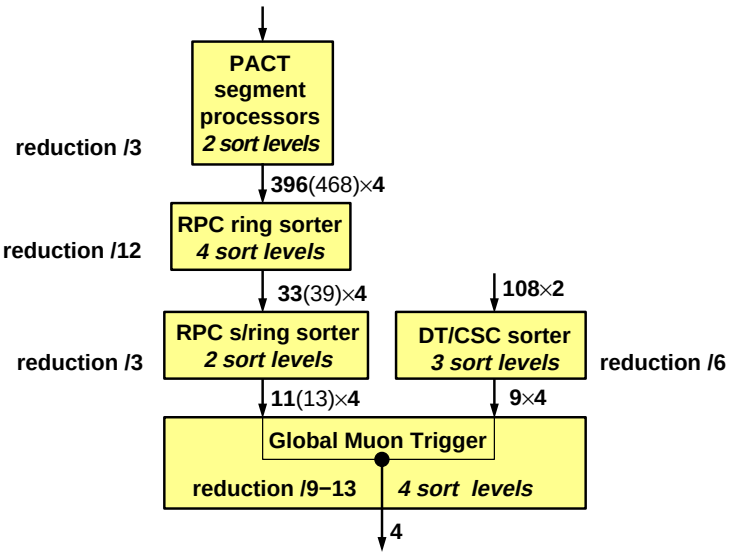

Figure 7.17: Muon Sorter tree.

7.6.1 RPC PACT sorting tree

In the case of PACT the first step of sorting is done already at *Trigger Boards* (TB) grouping 12 segment processors each. Their outputs (4 per TB) are further processed by 33 (or 39 in the case of upgrade) *ring sorters*, each covering a *ring* of $\Delta\eta \approx 0.1$ and $\Delta\phi = 360^\circ$. Then the rings are grouped by 3 into 11 (or 13) *superrings* of $\Delta\eta \approx 0.35$ and $\Delta\phi = 360^\circ$. Thus up to 11×4 (or 13×4) muons are delivered to the Global Muon Trigger. Details are given in Tab. 7.12.

7.6.2 DT/CSC sorting tree

The DT/CSC TF sectors are grouped into 9 regions of $\Delta\eta \approx 0.5$ and $\Delta\phi = 360^\circ$ (5 in the barrel and 2 in each endcap) thus providing 9×4 muons at the Muon Sorter output. This segmentation is, however, still subject to optimisation. Details of the DT/CSC sorting tree are given in Tab. 7.13.

Table 7.12: RPC PACT sorting tree for baseline ($|\eta| < 2.1$) and upgrade ($|\eta| < 2.4$).

	inputs accounting				inputs		Sorter chips	
$\|\eta\|_{max}$	2.1	2.4			2.1	2.4	2.1	2.4
Trigger and	33	+6	×12	×12	4752	+864	ϕ Ghost Buster	
Readout Board	33	+6	×12	×6	2376	+432	396	+72
	33	+6	×12	×4	1584	+288	198	+36
Ring	33	+6	×12	×2	792	+144	99	+18
Sorter	33	+6	×12		396	+72	66	+12
	33	+6	×8		264	+48	33	+6
Super-ring	33	+6	×4		132	+24	η Ghost Buster	
Sorter	33	+6	×4		132	+24	22	+4
	22	+4	×4		88	+16	11	+2
Global	11	+2	×4		44	+8	6	+1
Muon	6	+1	×4		24	+4	4	
Trigger	4		×4		16		2	
	2		×4		8		1	
Global Trigger			4		4			
Total number of Sorter chips							838	+151

Table 7.13: DT/CSC sorting tree.

	inputs accounting			inputs	Sorter chips
DT/CSC	9	×12	×2	216	36
Sorter	9	×8	×2	144	18
	9	×8		72	9
Global	9	×4		36	6
Muon	6	×4		24	4
Trigger	4	×4		16	2
	2	×4		8	1
Global Trigger		4		4	
Total number of Sorter chips					76

7.6.3 RPC PACT Ghost Buster

RPC strips in non-reference planes are seen by more than 1 PACT segment processor. Such overlap of processor domains is necessary to account for bending variations an multiple scattering. Only strips in the reference plane are assigned to segments in a unique way. Since the trigger requires coincidence of 3 out of 4 planes, the same hits in 3 non-reference planes can be recognised as a muon by different segment processors. Thus a single muon can be seen as two or more muons and cause a two-muon trigger. Such artificial additional muons are called *ghosts*.

ϕ Ghost Buster

The ϕ Ghost Buster is the first step of muon sorting tree. It has twice less outputs than inputs, i.e. at most one out of 2 segments can be selected depending on its neighbourhood.

Let us denote a given segment by A, its "right" (lower ϕ) neighbour by Z and its "left" neighbours by B and C. Let us introduce usual ordering relation using track quality q and momentum p_t:

$$A > B \;\Leftrightarrow\; q(A) > q(B) \;\texttt{OR}\; q(A) = q(B) \;\texttt{AND}\; p_t(A) > p_t(B)$$

Segment A can be selected only in the two cases:

- A is better than neighbours (local maximum): $Z < A > B$
- A is last but one segment of wider maximum: $Z \leq A = B > C$

η Ghost Buster

The η Ghost Buster has equal number of inputs and outputs. Thus it is not a level of the sorting tree in a strict sense. It is placed between two levels, after sorting in ϕ and before sorting in η. It vetoes some candidates in a way similar to ϕ Ghost Buster. The practical realisation is, however, more complicated, because it has to deal with 4 segments from each η ring, rather than with single segments. It is described in detail in Ref. [2].

7.7 Global Muon Trigger

The following sequence of actions is performed by the Global Muon Trigger.

7.7.1 Final muon sorting

The 4 highest p_t muons in the whole event are selected. From the logical point of view this is the last step of the Muon Sorter and the algorithm is as described in the previous section. It is placed in the Global Muon Trigger because it might be advantageous to perform it after the RPC and DT/CSC matching. This is because the matching can suppress some ghosts which otherwise could be selected instead of real muons. Simulation study on this subject should be done.

7.7.2 Preprocessing

There are some operations which should be performed on the data coming out of the Muon Sorter. They are specific to particular subsystems but performing them only on the selected muons can save a lot of hardware. These operations can be considered as a preparation for further Global Muon Trigger action.

The ϕ, η and p_t conversion. RPC and DT/CSC subsystems have different segmentations and therefore they can use different ϕ and η scales. The p_t scales can also be different because the performance of the two subsystems depends on p_t in different ways. The p_t coding may even depend on the detector region. Therefore the data from both subsystems should be converted by lookup tables to common scales, before they are compared to each other.

Muon sign validation. Both RPC and DT/CSC subsystems use one bit for the muon sign. However, due to limited momentum resolution, it is meaningful only up to a certain p_t value, depending on η. In case the muon sign will be used in some trigger condition, an additional bit should be created saying whether the sign information for a given muon is meaningful or not. It can be done by a lookup table having η and p_t on the input.

7.7.3 Matching RPC and DT/CSC information

The information coming from the two subsystems should be combined before the final trigger decision. At the end of the sorting tree each of them deliver up to 4 muon candidates in several detector regions with their η, ϕ, signs, p_t and quality bits. First the spatial coordinates should be checked to determine whether the two candidates can be attributed to the same physical muon. Let us consider two cases.

Candidate is seen by only one subsystem. A decision should be taken whether this candidate should be considered as a real or a fake muon. It should be based on (in order of preference):

- quality bits: if they are high a real muon case is more probable
- background level at the given detector region: in a high background region a fake muon is more probable
- p_t of the candidate: it is more harmful for physics to lose high p_t muons; probability of low p_t fake muon is much higher
- current running conditions: one should trade off efficiency against fake muon rate

Candidate is seen by both subsystems. A decision should be taken which momentum estimate should be chosen. It should be based on (in order of preference):

- quality bits: their high value indicates a more reliable estimate
- background level at the given detector region: the two subsystems have different response to background, e.g RPC are more sensitive to uncorrelated hits whereas DT/CSC can be affected by correlated background (additional tracks).
- p_t of the candidates: DT/CSC are more precise at high p_t, but they can underestimate p_t, RPC are less precise but they can only overestimate p_t.
- current status of each detector in a given region: e.g. noisy chambers can cause p_t overestimation.

In any track recognition system there is a trade-off between the track recognition efficiency and the number of accepted fake tracks. Tightening cuts one can reduce the number of fake tracks for the expense of efficiency loss. Having two different subsystems one can improve the efficiency/fakes balance. Less correlated the subsystems are, better improvement can be achieved. This is because the characteristics of fake tracks in the two subsystems are different.

The above criteria are at the moment only qualitative but they should be quantified by detailed simultaneous simulation of all the subsystems. Only then they can be turned into workable algorithms. The first attempt to design such an algorithm is shown in Fig. 7.18.

First, the distance between two muon candidates is calculated for each possible pair. The pair with the shortest distance is selected and the corresponding muons are removed from the list. Then, remaining candidates are considered and again the pair with the shortest distance is selected. The iterations continue until all pairs with a distance below a given threshold are processed. In the next step, one of the two muons in each pair is selected using a *single rank* value, which is a function of muon p_t and its quality bits. At the end a *final rank* for each muon is calculated. It depends on the single rank and on the matching quality. Muons successfully matched have higher priority than single candidates. Muons from pairs with shorter distance are preferable. Finally, the muons are sorted according to the final rank and the four best candidates are sent to the Global Trigger.

7.7.4 Isolated muon trigger

This is an additional operation of the Global Muon Trigger. The isolated muon trigger algorithm checks whether there was a significant energy deposit in a calorimeter around a given muon. So called *quiet bits* delivered by the calorimeter trigger are used for this purpose. A quiet bit is assigned to each calorimeter region of $\Delta\eta \times \Delta\phi = 0.35 \times 0.35$ and it is set if the transverse energy E_t deposited in this region is below a threshold. Details of this algorithm are currently under study. Possible use of MIP information from the calorimeter trigger is also being envisaged.

7.7.5 Multimuon and other triggers

After preparing the information about all individual objects the Global Trigger performs all foreseen cuts and selections. Among them there are a di-muon trigger, possibly three-muon trigger, muon-electron trigger and other combined triggers. The cuts might be asymmetric, e.g. two different thresholds might be required for the two muons in a pair to pass the two muon trigger. For details the reader is referred to Global Trigger documentation, e.g. [92].

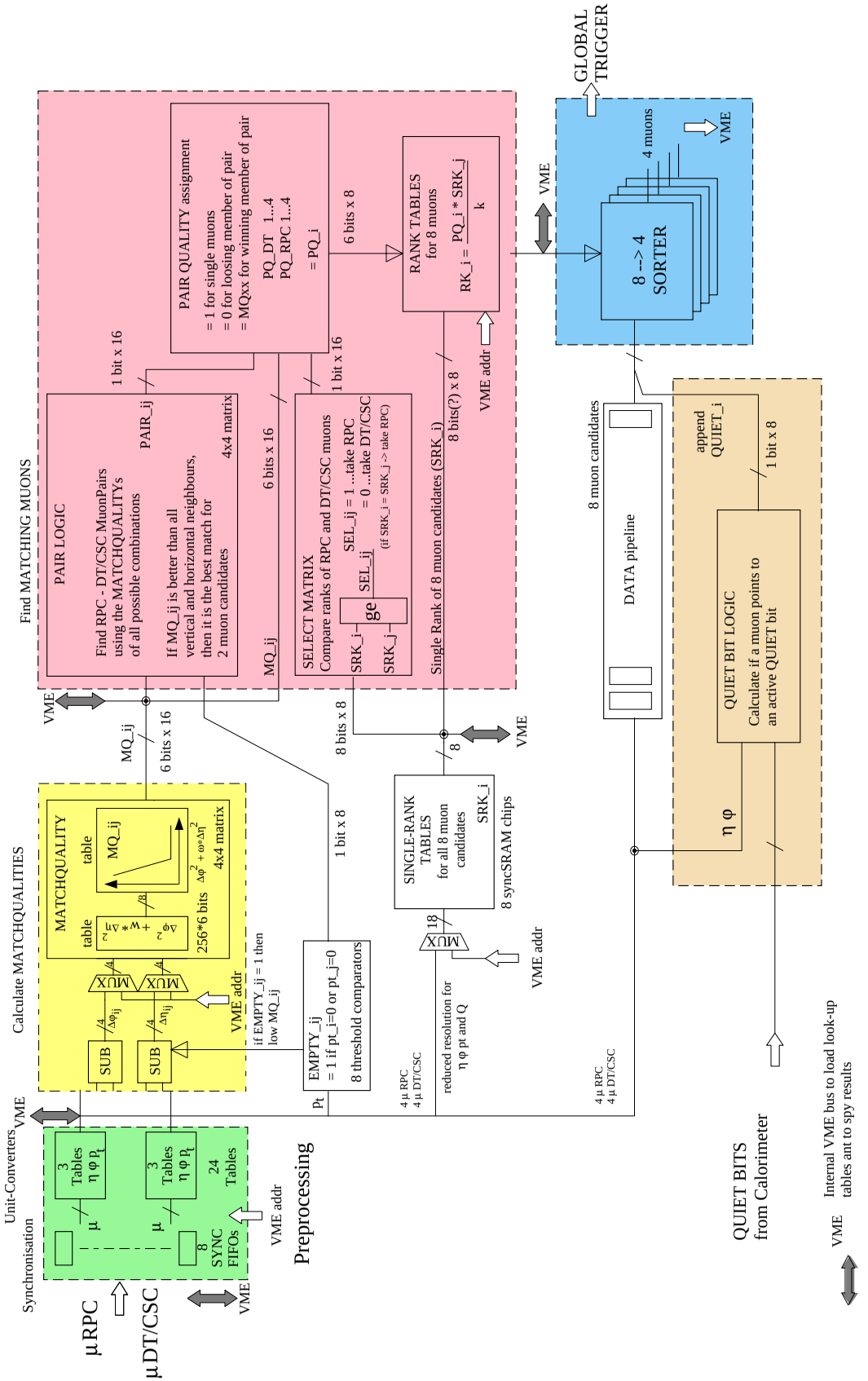

Figure 7.18: Block diagram of the Global Muon Trigger.

Chapter 8

Beam tests of trigger processor prototypes

8.1 Drift Tubes

The first prototype of Bunch and Track Identifier circuit was build in 1995 [33]-[35]. It was implemented in FPGA technology using XILINX XC4013 chip with 6 ns grade. Because of obvious limitations of FPGA technology the functionality of the prototype was reduced compared to the designed ASIC[1]. It was connected to 8, instead of 9 tubes and only a subset of all needed tube combinations was considered. Nevertheless the basic functionality, namely track recognition using generalised meantimer method was implemented.

BTI efficiency as a function of the drift time in the first layer for right incident angle is shown in Fig. 8.1a. The wavy shape of the function is due to mismatch between the programmed maximum drift time $t_{max} = 350$ ns and the actual one which turned out to be 335 ns. The drift time was not equally compensated in all the layers and the hits were not precisely aligned after t_{max}.

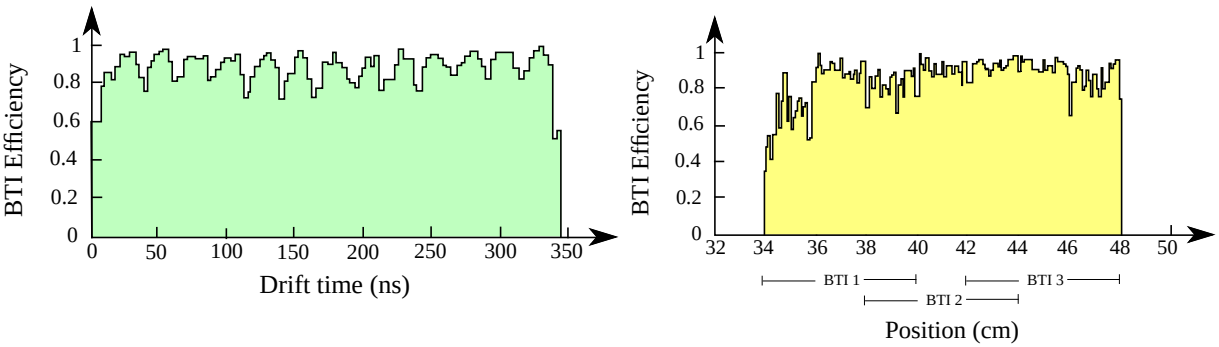

Figure 8.1: BTI prototype efficiency vs drift time and position.

BTI efficiency vs track position is shown in Fig. 8.1b for three BTI chips. Each one covers 6 cm, but only 4 cm with full efficiency. Therefore they should overlap by 2 cm. In the region of proper coverage, i.e. 36-48 cm the efficiency is rather uniform and equal to 90% on average.

One of the crucial items in all LHC trigger devices is time synchronisation. Trigger processors can work correctly only when driven by clock being in phase with incoming particles. Sensitivity of the BTI prototype to this this phase shift is shown in Fig. 8.2a. From the figure one can see that about ± 5 ns deviation is tolerable. One should stress an excellent agreement between the simulation results and the experimental data.

All the BTI characteristics discussed above were measured for right incident angle. The efficiency for different angles is shown in Fig. 8.2b. Again good agreement of measured and simulated data can be seen.

Overall conclusion of the test is that the working principle of BTI is valid. Behaviour of the prototype is fully understood and can be well simulated. Next step will be already fully functional ASIC prototype.

[1] Application Specific Integrated Circuit — custom made chip

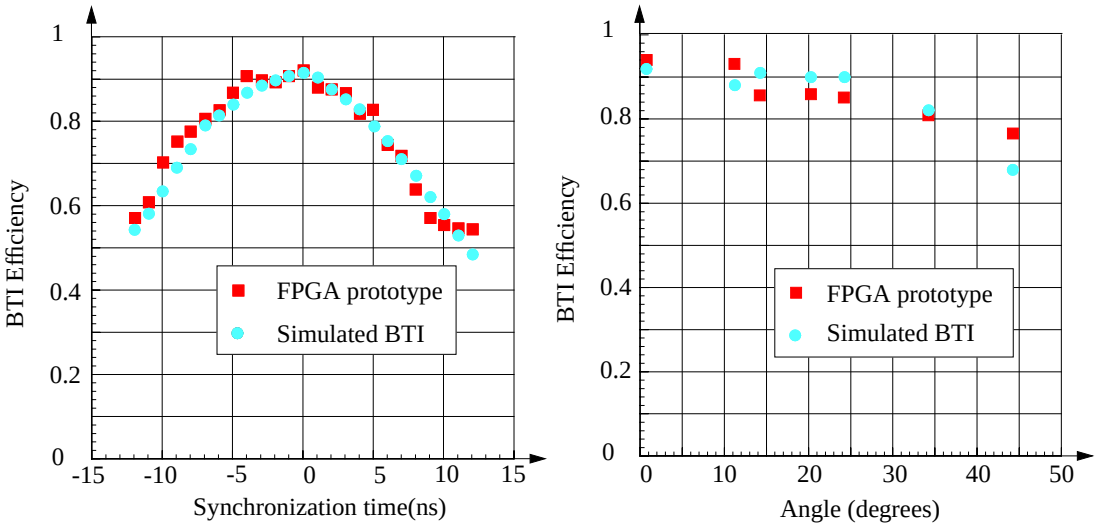

Figure 8.2: BTI prototype efficiency vs synchronisation time and muon direction.

8.2 Cathode Strip Chambers

CSC Cathode and Anode Front End Boards with trigger electronics are currently being constructed and they have not yet been tested with a beam. There were, however, several CSC prototypes tests where their properties crucial for trigger algorithms have been tested.

Fig. 8.3 shows the time distribution of anode signals from 6 layers of ME1/1 prototype. It is seen that 40-50 ns gate would be enough to include hits from all the layers. The second hit always arrives within 20 ns which makes possible an unambiguous bunch crossing assignment according to the algorithm described in Sec. 7.4.

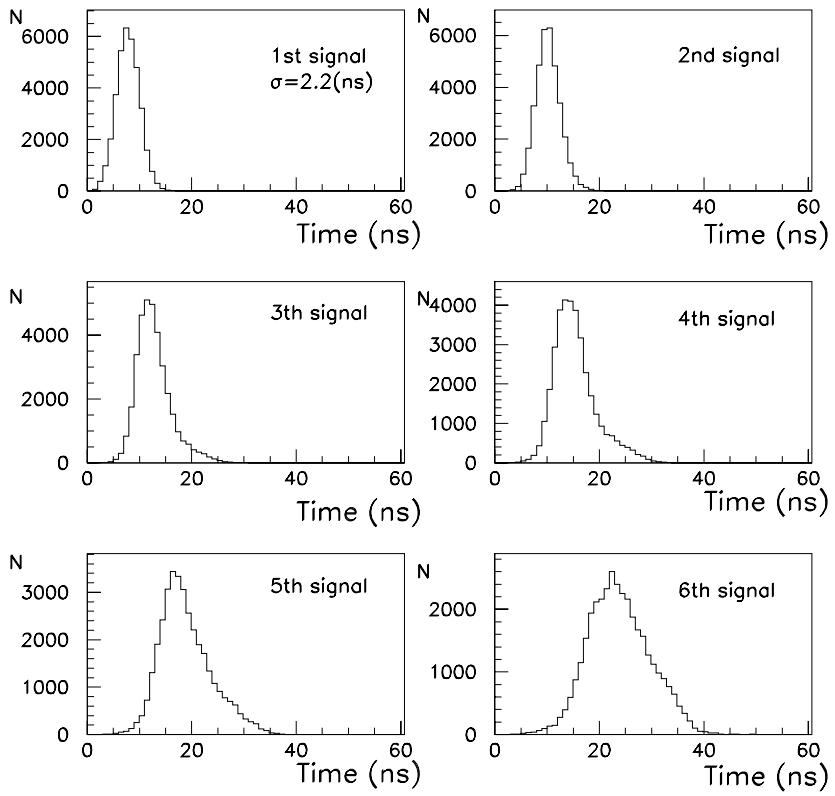

Figure 8.3: Time distribution of anode signals from 6 layer CSC prototype.

8.3 Resistive Plate Chambers

The principle of Pattern Comparator Trigger was for the first time tested in the framework of the RD5 experiment in 1993. RD5 was equipped with twelve planes of 2×2 m^2 RPC chambers with 3 cm wide horizontal strips (see Fig. 8.4). Four of them corresponding to four CMS muon stations were used in this test. The muon penetrated 144 cm of steel plates before arriving at the first RPC and then 60 cm of iron to each of the subsequent chambers. The readout by the trigger processor covered 18, 20, 24 and 30 strips from consecutive chambers which was sufficient for the current study.

The processor itself was built using three programmable ALTERA 7128 chips, each of them corresponding to a single PAC (Fig. 8.4). Two more ALTERA units were used to feed the data into the PAC's and to handle communication with the VME. The trigger processor was loaded with patterns corresponding to the different momentum intervals: 10-20, 20-30, 30-50, 50-100, and above 100 GeV. Each pattern consisted of four strip numbers from consecutive chambers. The patterns were selected in such a way as to keep at least 99% of tracks at each energy.

Fig. 8.5 shows the trigger efficiency as a function of the beam momentum for various thresholds. It can be seen that the selectivity of the trigger (i.e. the steepness of the curve) is good.

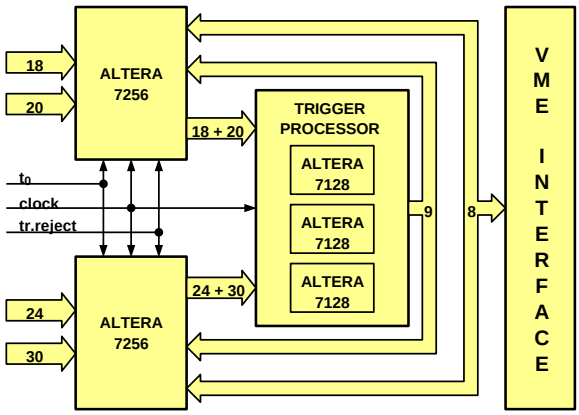

Figure 8.4: PACT prototype VME board.

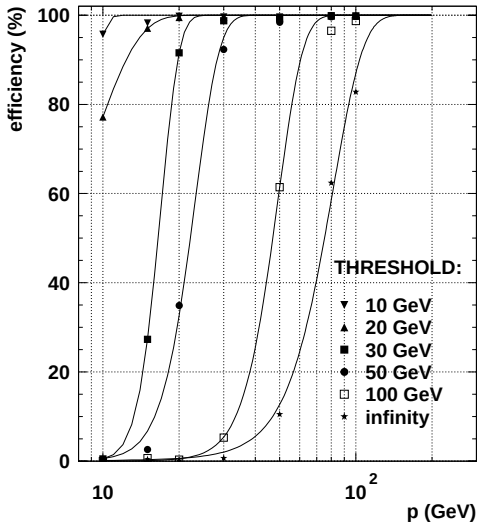

Figure 8.5: PACT efficiency vs beam momentum.

Second generation of tests was performed in 1996. A PACT test bench was build with configuration much closer to the final design. It was implemented in FPGA technology except for the Readout and Control (ROC) ASIC provided by the RD12 team. The test bench consisted of 4 boards shown schematically in Fig. 8.6. It was connected to the RPC cosmic telescope MINI in Bari. Four chambers of the telescope were used as shown in Fig. 8.7. The signals were shaped to the length of 600 ns, therefore the relative synchronisation of different input channels could not be tested. Only the synchronisation of the data pipeline with the trigger signal was checked. The signals were processed by the trigger processor with frequency of 20 MHz, i.e. half of the designed one. There were read by ROC in 3 time slices, ±1 clock cycle with respect to the PAC trigger and independently by the standard MINI readout with 600 ns window. Offline the PAC algorithm was simulated on the recorded data and compared with the PAC online response. The agreement is shown in Fig. 8.8 as a function of readout delay. It is seen that by proper delay adjustment one can achieve 100% agreement.

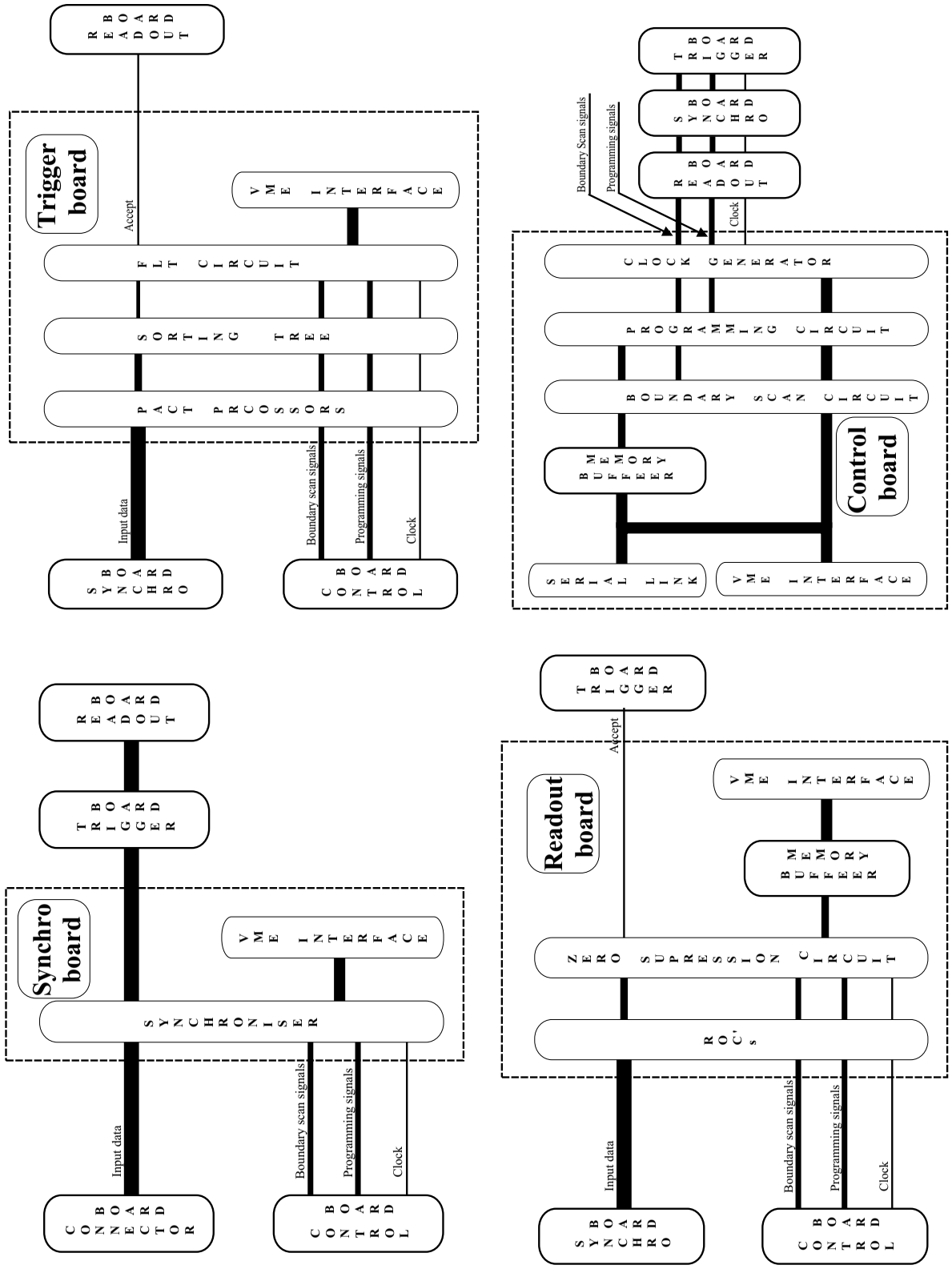

Figure 8.6: PACT test bench boards.

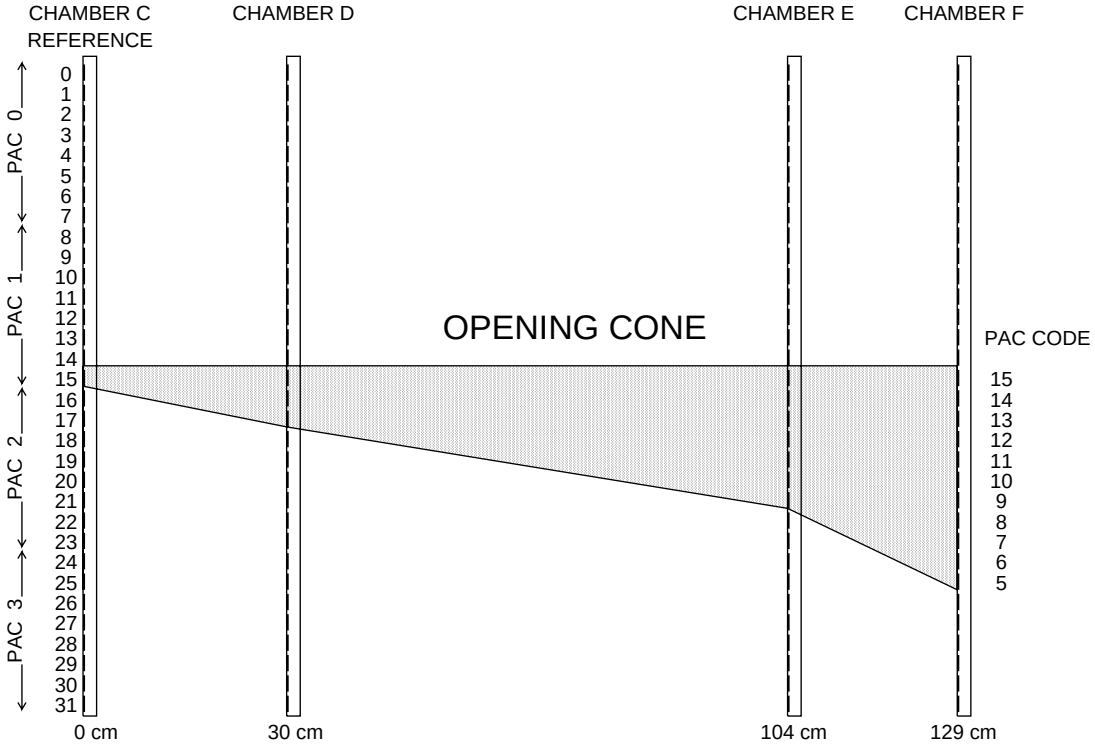

Figure 8.7: Cosmic RPC PACT test stand layout.

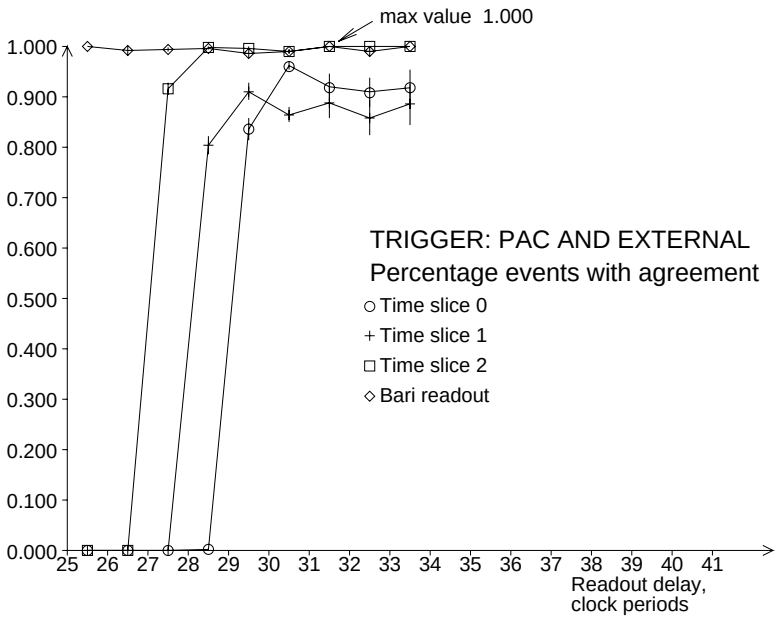

Figure 8.8: Quality of PACT prototype response.

Chapter 9

Simulated trigger performance

9.1 Simulation software

9.1.1 Event generation

For most of the study PYTHIA 5.7 [134] was used as an event generator. Wherever possible default values of parameters were preserved. Particle distribution functions were calculated according to CTEQ2L [166] parametrisation.

Minimum bias events were simulated with parameter MSEL=1 which activates the following processes having in total cross section of 55 mb:

$q_i\ q_j \rightarrow q_i\ q_j$ (where $q_i = d, u, s, c, b$)
$q_i\ \overline{q}_i \rightarrow q_i\ \overline{q}_i$
$q_i\ \overline{q}_i \rightarrow g\ g$
$q_i\ g \rightarrow q_i\ g$
$g\ g \rightarrow q_i\ \overline{q}_i$
$g\ g \rightarrow g\ g$
low p_t scattering.

This does not include diffractive and elastic scattering. For some special studies where very high rapidity region was important DTUJET 93 program was used. It includes diffractive phenomena and gives total inelastic cross section of 80.4 mb.

9.1.2 Detector simulation

Particle passed through the material of CMS detector and the detector response was simulated with CMSIM package [136]. It is based on GEANT [128] and has interfaces to PYTHIA [134] and other event generators.

For some special studies where simulation of thermal neutrons was necessary (see Sec. 5.2.4) other programs were used: FLUKA [129], GCALOR [131] and MARS [132]. They can simulate neutrons of kinetic energy well below 1 keV.

The CMSIM package is under vigorous development. Below we briefly describe its current status as it was used to obtain results presented in the next sections.

9.1.3 Geometry definition

This part is relatively well advanced and the level of details is usually adequate to the questions addressed in the next sections. E.g. muon chambers are described as composed of several material layers according to their technical designs. The biggest uncertainty is in the general layout of the barrel-endcap connection. Here, there are difficult mechanical mounts, many cables and other services, elements of the alignments system, etc. Therefore the design of this region is not yet fixed.

The precise position and shape of cryogenic chimneys connecting the magnet cryostat with helium tank are not yet known. The chimneys are not yet included in the simulation, and one can expect that they will reduce the acceptance of the muon system in the barrel.

9.1.4 Particle tracking

This task is well covered by GEANT itself. Once the geometry is defined, the user only needs to provide magnetic field map, and to set the proper cuts. The currently used field map is two-dimensional, calculated on a 10 cm grid. It is adapted to the polygonal shape of the return yoke by simple scaling and interpolation.

The set of cuts used for muon trigger studies is given in Table 9.1.

Table 9.1: GEANT cuts used in the simulation.

particle or process	GEANT param. name	far from muon chambers	close to muon chambers	inside muon chambers
γ	CUTGAM	100 MeV	10 MeV	10 keV
e	CUTELE	100 MeV	10 MeV	10 keV
n	CUTNEU	1 MeV	1 MeV	1 MeV
charged hadrons	CUTHAD	1 MeV	1 MeV	100 keV
μ	CUTMUO	10 MeV	10 MeV	100 keV
e $\rightarrow$ bremsstrahlung	BCUTE	10 MeV	10 MeV	10 MeV
$\mu \rightarrow$ bremsstrahlung	BCUTM	10 MeV	10 MeV	10 MeV
e $\rightarrow$ δ-rays	DCUTE	off	off	10 keV
$\mu \rightarrow$ δ-rays	DCUTM	off	off	10 keV
$\mu \rightarrow e^+e^-$ pair production	PPCUTM	10 MeV	10 MeV	10 MeV

9.1.5 Detector response

Phenomena inside Drift Tubes and CSC are simulated in a very detailed way. A particle ionising the gas creates electrons, which then develop cascades in the electric field of the chamber. Charge collected by electrodes gives rise to a pulse which is then shaped according to the electronics design.

In the case of RPC such level of details is not needed because the precision of the position measurement is only of the order of 1 cm and the analogue information is not needed. Thus it is sufficient to take the strip crossed by a particle as a cluster center. However, there is an effort going on to include in the simulation parametrised experimental results on the cluster size, chamber efficiency and timing resolution.

9.1.6 Trigger algorithms — current status

Drift Tube front end electronics, BTI, TRACO and Trigger Server are very precisely described in the simulation. Simulation results were checked against the test beam data taken with a chamber equipped with a BTI prototype. Very good agreement has been found.

CSC front end electronics including Anode and Cathode FEB's is simulated at the level of behavioural model. Currently the work is going on the design and simulation of the Motherboard and Port Card.

Basic algorithm of Track Finder is already coded and interfaced to the Drift Tube trigger output. Current effort concentrates on interfacing it to the CSC output, and on developing algorithms suitable for the endcap and for the barrel/endcap corner.

In the case of RPC PACT the whole chain is precisely simulated. Current work concentrates on improving algorithms in the regions of low acceptance or weak bending.

Because the simulation of the full CSC/DT/TF chain is not yet available, most of the results concerning trigger rates etc. are given for the RPC PACT only. This can be considered as the "worst case" because including the CSC/DT branch can only improve the overall trigger performance.

9.2 Geometrical acceptance and low momentum cutoff

In principle, the DT/CSC system can trigger with track segments in at least two muon stations. However, background rejection is more powerful if 3 stations are used. Momentum measurement is the best if the first or the second muon station is among them. Acceptance for these three cases is plotted in Fig. 9.1. The white area below the curves corresponds to the coincidence of 3 stations, one of them being MB1, MB2, ME1 or ME2. If we accept the coincidence of any 3 stations we gain the dotted area. Finally, coincidence of any two stations is represented by the uppermost histogram, which is everywhere above 97%.

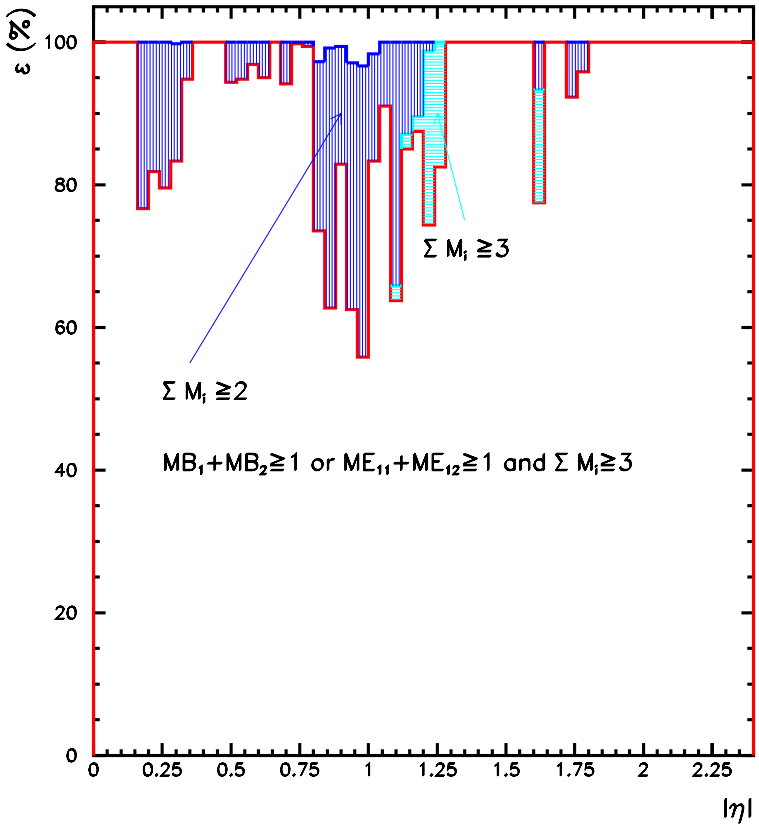

Figure 9.1: Geometrical acceptance of the DT/CSC system.

RPC PACT trigger is based on four RPC planes and it requires coincidence of at least three of them. However, four planes provide better momentum measurement. These two cases we denote 3/4 and 4/4 respectively. Fig. 9.2 shows the 3/4 acceptance in gray and 4/4 one in black. The upper plots show the local acceptance for a given η, whereas the lower ones — the acceptance averaged over trigger towers. The plots in the left column correspond to the high p_t algorithm based on one RPC plane per station which is used for muons with $p_t > 5$ GeV in the barrel and for all muons in the endcap. The plots in the right column correspond to the low p_t algorithm based on two RPC planes in the first station (denoted as MS1 and MS1′)[1] and two RPC planes in the second one (denoted as MS2 and MS2′) — this algorithm is used only in the barrel.

The acceptance in Fig. 9.2 was calculated with straight tracks in order to indicate better the origin of inefficiencies. There is a region ($|\eta| \approx 0.3$) with exceptionally low efficiency. This is due to the gap between the wheels of the CMS barrel. The gap is needed mainly for cables from the inner tracker and calorimeters. In the current design it is 15 cm wide, but the simulation was done for the previous version of the design with a 20 cm wide gap. On top of that, one should add 2×4 cm of dead RPC border. The efforts are made to reduce these numbers, but it seems that the absolute lower limit is 15+2×2 cm. The impact of the gap on the muon trigger acceptance is better seen in Fig. 9.3 The trigger acceptance (coincidence of 3 out of 4 planes) for muons with $4.5 < p_t < 5.0$ GeV is plotted for low (MS1, MS1′, MS2, MS2′) and high p_t (MS1, MS2, MS3, MS4) algorithms separately as well as for the logical OR of the two.

[1] Here we use the acronym MS for a generic Muon Station, which could be either MB or ME.

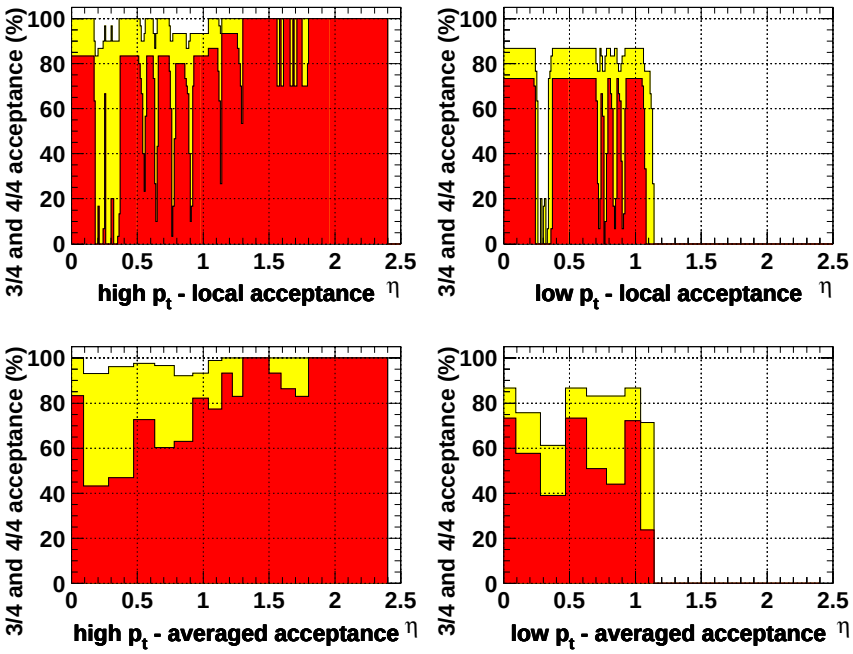

Figure 9.2: Geometrical acceptance of the RPC system.

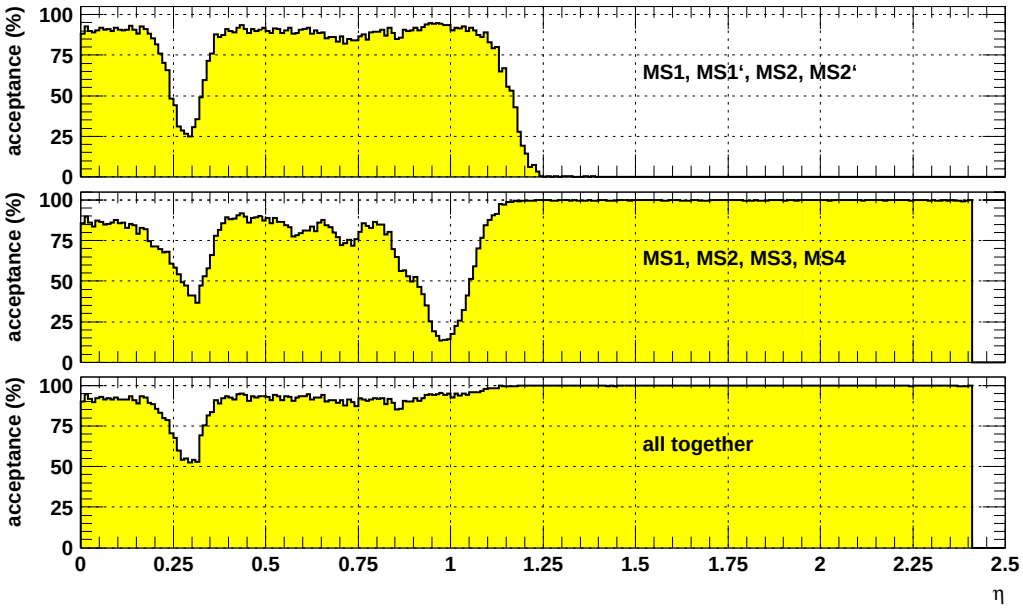

Figure 9.3: Geometrical acceptance for muons with $4.5 < p_t < 5.0$ GeV.

The minimal values of a trigger threshold p_t^{min} achievable in CMS are plotted in Fig. 9.4 as a function of $|\eta|$. The corresponding total momentum p^{min} is also plotted. The cutoff is not sharp because of Landau fluctuations of energy lost by muons. Therefore, different p_t^{min} values are obtained for different required efficiencies. Because the detector design is not yet completely frozen, one can expect some small changes in the amount of absorber. However, they should not be bigger than one nuclear interaction length λ. This is indicated in the figure as error bars.

Keeping in mind all the above mentioned uncertainties one can conclude that the lowest "triggerable" muon p_t is about 4 GeV in the barrel, and it decreases down to ∼2 GeV in the endcaps if the efficiency of 90 % is required. One can, however, reduce p_t^{min} in the barrel down to ∼3.5 GeV relaxing requirement on the efficiency down to 80 %. Relaxing it further down to 50 % allows us to trigger on muons with $p_t \approx 3.2$ GeV. This can be better seen from Fig. 9.5a.

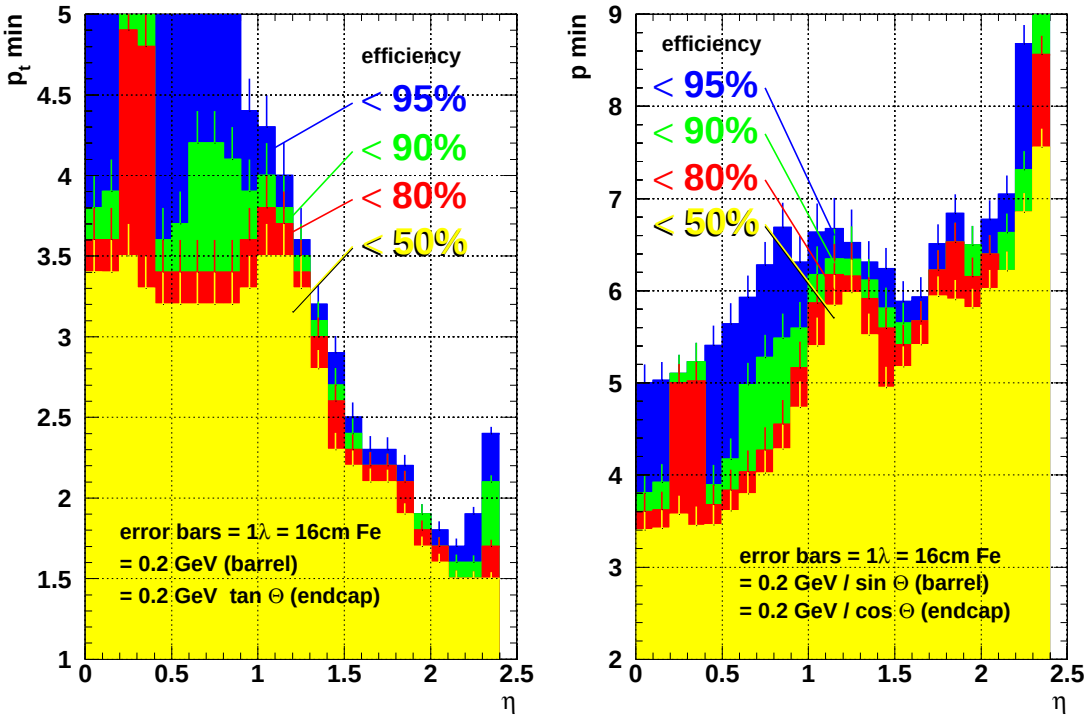

Figure 9.4: Minimal p_t and p thresholds for various efficiencies.

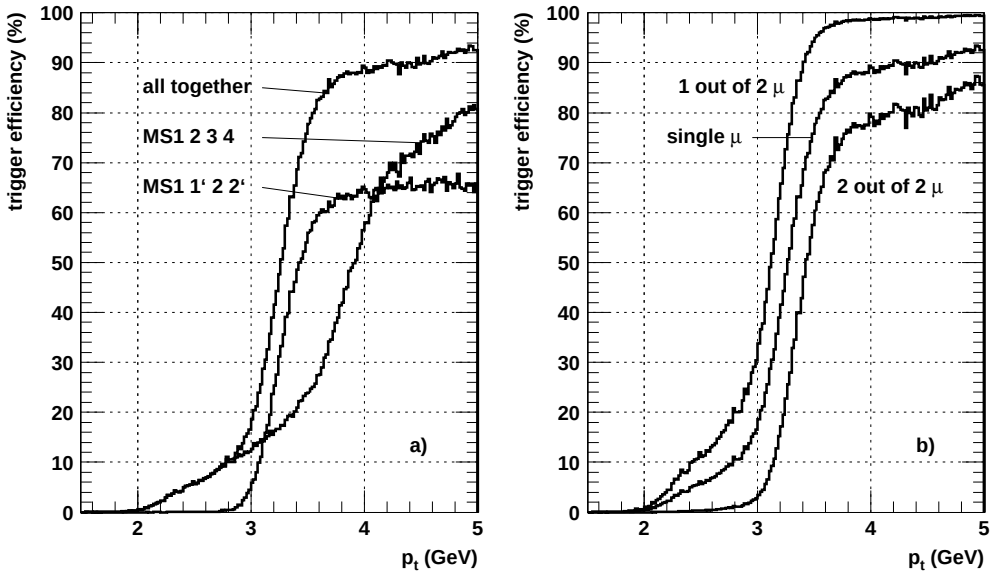

Figure 9.5: Trigger efficiency for low p_t tracks at $|\eta| < 1.5$; a) single muons, b) muon pairs.

In most of the cases we are interested in two-muon events (see Sec. 4.1). Requirement of 2 muons at the first level trigger strongly reduces the trigger rate, but also squares the single muon trigger efficiency. The result is shown as the lowest curve in Fig. 9.5b. In such a case the trigger is rather inefficient, especially at low p_t. If one can, however, trigger on one of the two muons then the inefficiency gets squared and the trigger performance becomes very good (the upper curve in Fig. 9.5b).

As an example, one can consider heavy ion physics with Pb-Pb collisions. Study of Υ production require recording of two-muon events. The two muon trigger is not very efficient, because of low momenta of the muons. It has been shown [77], however, that one can use single muon trigger because all backgrounds amount only to about 500 Hz. In the case of high luminosity p-p collisions background rates are much higher and one has to rise the single muon threshold significantly. Nevertheless such trigger is still very helpful to increase the overall trigger efficiency.

9.3 Overall performance of trigger subsystems

9.3.1 Drift Tubes

Full trigger performance can be understood only when background is taken into account. The most severe background for Drift Tubes comes from muon radiation. This is because additional particle can give shorter drift time. The effect is well visible in Fig. 9.6. As a result the measured muon position is wrong. Distribution of the error is shown in Fig. 9.7.

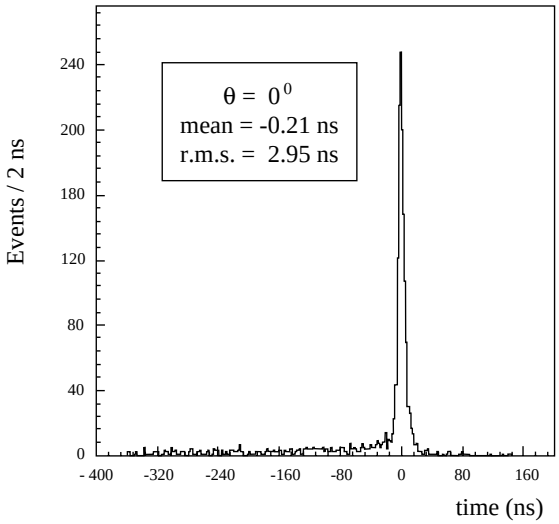

Figure 9.6: Measured time distribution of the DT meantimer for 200 GeV μ beam. The tail on the left is due to muon secondaries.

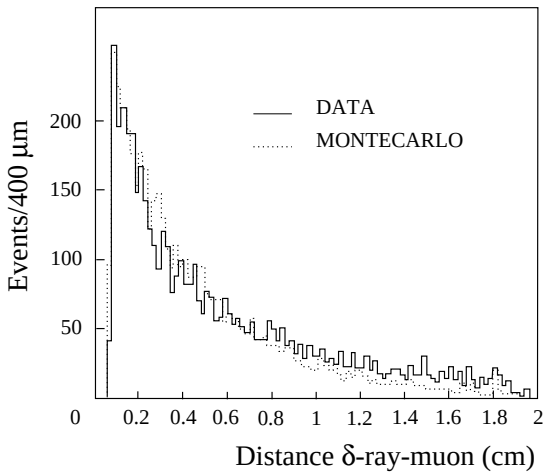

Figure 9.7: Distance between the muon track and the hit spoiled by secondaries as obtained by DT meantimer.

If more than one out of four layers in a superlayer is disturbed significantly, the track may not be found. The loss of efficiency due to this effect is seen in Fig. 9.8. Significant fall of efficiency above p_t = 200 GeV is a result of an increase of bremsstrahlung and pair production probability (see Fig. 5.14, page 49). Bunch crossing recognition efficiency (Fig. 9.9) is not affected as much, because temporal correlation of secondaries with a muon is much better than the spatial one.

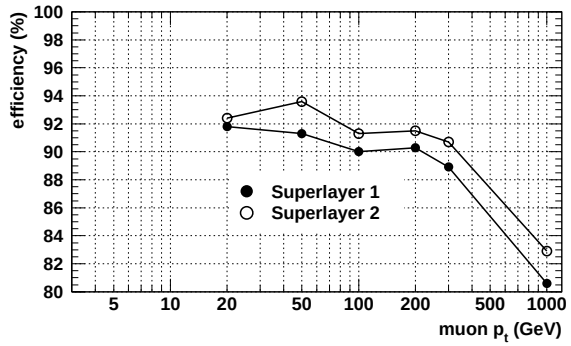

Figure 9.8: Track recognition efficiency for single superlayer (BTI simulation for station MB4).

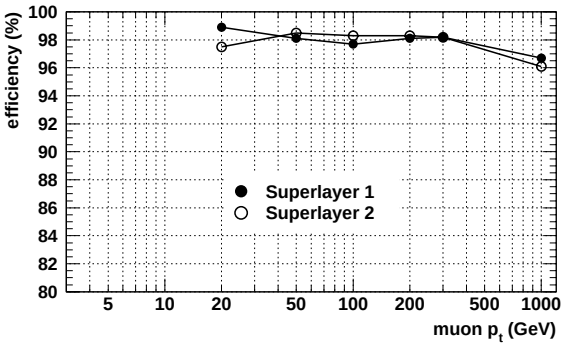

Figure 9.9: Bunch crossing recognition efficiency for single superlayer (BTI simulation for station MB4).

Bunch and track recognition efficiency on the level of one station are given in Figs 9.10-9.12. In the case of ϕ projection, where two superlayers per station are available, some single-SL efficiency losses are recovered.

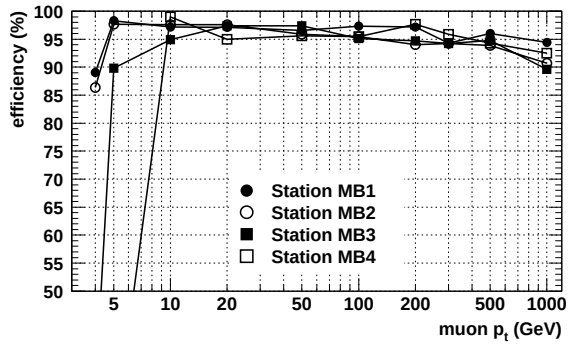

Figure 9.10: Bunch crossing recognition efficiency for one muon station (BTI+TRACO simulation).

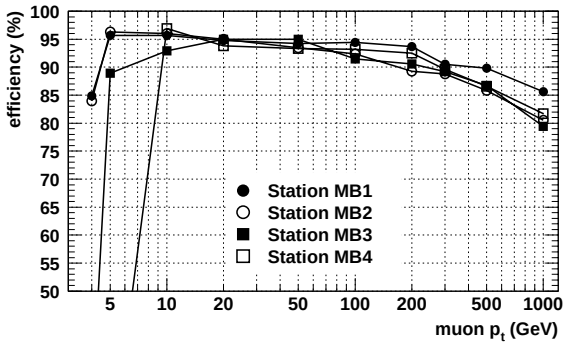

Figure 9.11: Track recognition efficiency for one muon station — ϕ projection (BTI+TRACO simulation).

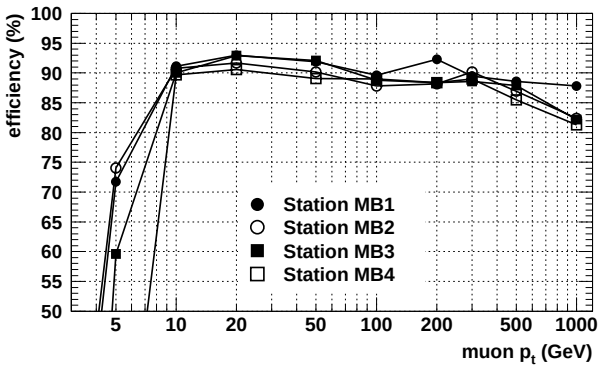

Figure 9.12: Track recognition efficiency for one muon station — η projection.

Finally, the overall efficiency of the entire Drift Tube system is shown in Figs 9.13 and 9.14. The Track Finder algorithm was not simulated explicitly, and only the presence of track segments in muon stations was required. Different trigger criteria can be used to optimise the balance between efficiency and background rejection.

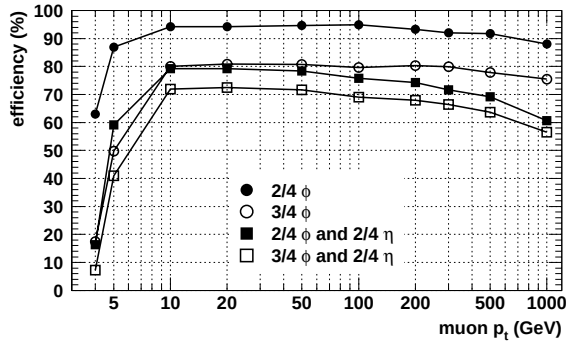

Figure 9.13: Total Drift Tube Trigger efficiency for $|\eta| < 1$. Notation "2/4 ϕ" means that at least 2 track segments out of 4 muon stations are required in the ϕ projection.

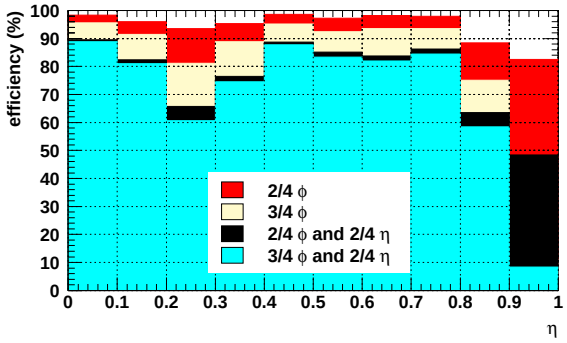

Figure 9.14: Total Drift Tube Trigger efficiency for muons of p_t = 100 GeV.

9.3.2 Cathode Strip Chambers

Cathode Strip Chambers can be also effected by muon secondaries, although the mechanism is different. Distribution of charge caused by a muon can be disturbed by nearby secondaries. Secondaries separated by more than 3-4 strips from the muon can be seen as independent tracks. These phenomena are illustrated in Figs 9.15 and 9.16 which show the number of hits caused by a single muon and the distance of secondary tracks from the muon.

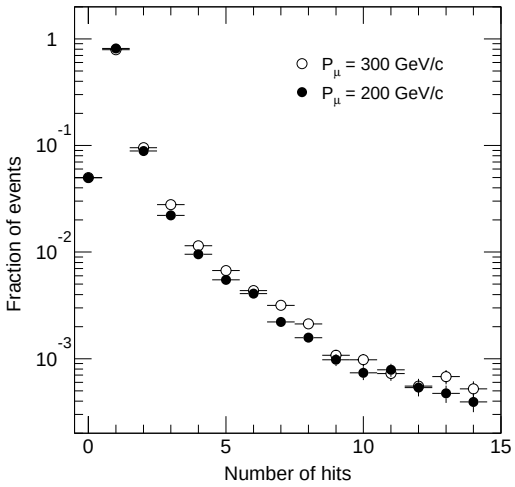

Figure 9.15: Measured distribution of number of hits per CSC layer for 200 and 300 GeV incident muons [152].

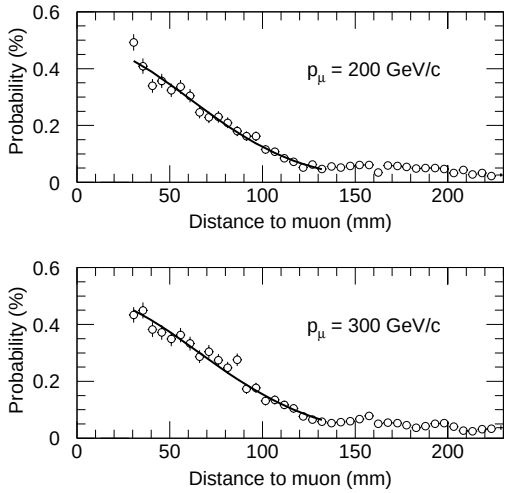

Figure 9.16: Measured (points) and simulated (lines) distance of secondary track from the muon. Track is defined as set of clusters in 4 CSC layers [152].

CSC's, being placed in the endcaps, are more than Drift Tubes exposed to uncorrelated background: electrons originating from thermal neutrons and hadrons from punchthrough and backsplashes (see Sec. 5.2). This background can produce track segments (or Local Charged Tracks — LCT) in muon chambers. The effect has been simulated in detail [45] and the results are given in Table 9.2. Even if the rate of uncorrelated electrons was 10 times higher than expected (last row in the table) the functioning of the trigger is not seriously affected.

Table 9.2: Background influence on 100 GeV muons. Symbol "e" stands for uncorrelated electrons (from neutrons), "had." — for hadrons from punchthrough and backsplashes.

	strips		wires	
	Number of CSC's with LCT's per μ	Fraction of CSC's with $\geq$2 LCT's	Number of CSC's with LCT's per μ	Fraction of CSC's with $\geq$2 LCT's
μ alone	4.1	2.1 %	4.2	5.0 %
μ + e	5.3	2.2 %	5.8	5.3 %
μ + had.	10.8	2.8 %	16.5	4.8 %
μ + e + had.	11.7	3.4 %	17.9	5.6 %
μ + 10$\times$e	11.4	4.4 %	14.9	6.9 %

9.3.3 Track Finder

An extensive simulation study has been performed in order to develop the Track Finder algorithm (see e.g. [68]). Here we present only the final result of this study, namely the efficiency curves. They are shown in Fig. 9.17 together with curves for the RPC PACT. The optimisation of the TF algorithm is not yet finished, and the results should be considered as preliminary. Especially in the endcaps and in the barrel/endcap corner, the curves represent the first iteration of the design.

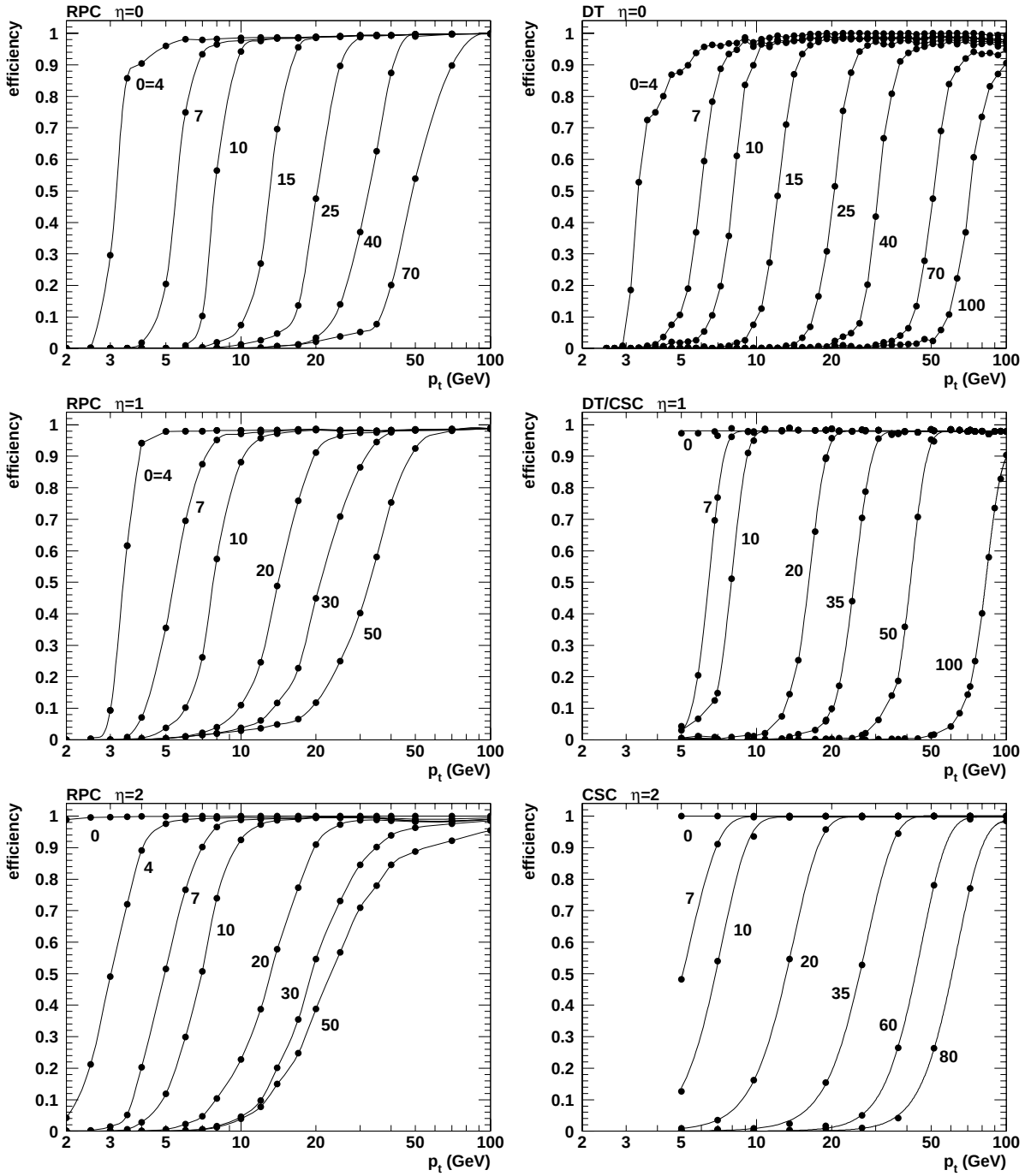

Figure 9.17: Trigger efficiency curves $\varepsilon(p_t)$ of RPC PACT and DT/CSC Track Finder in different detector regions. Trigger threshold p_t^{cut} [GeV] is indicated next to each curve. It is defined so that $\varepsilon(p_t^{cut}) = 90\,\%$. Index "0" corresponds to the lowest possible p_t^{cut}, limited only by muon energy loss; "0=4" means that the lowest possible p_t^{cut} in this region is 4 GeV. The CSC Track Finder algorithm has not yet been simulated below $p_t = 5$ GeV.

An ideal trigger should have efficiency equal to zero for muons with p_t below the threshold p_t^{cut}, and equal to 100 % above p_t^{cut}. In practice, the momentum resolution is limited by multiple scattering and energy loss fluctuations at low p_t and by detector resolution at high p_t. Because of that, the efficiency curves $\varepsilon(p_t)$ have finite slopes proportional to the momentum resolution. Efficiency curves $\varepsilon(p_t)$ of RPC PACT and DT/CSC Track Finder have been calculated for various trigger thresholds p_t cut in three detector regions: in the barrel ($\eta = 0$), in the endcap ($\eta = 2$), and in the transition region ($\eta = 1$). They are shown in Fig. 9.17. As expected, at $p_t < 20$ GeV the curves for RPC and DT/CSC are almost identical. At higher momenta one can clearly see the superior resolution of DT and CSC. The threshold adjustable trigger with good efficiency can be provided by RPC PACT up to 70 GeV in the barrel and up to 50 GeV in the rest of CMS. The DT/CSC threshold can be effectively adjusted up to 80 GeV in the endcaps, and even up to 100 GeV in the barrel.

9.3.4 Resistive Plate Chambers and Pattern Comparator Trigger

Muon secondaries

The influence of muon secondaries on the RPC performance was tested experimentally [152]. Muon beam was entering the chamber after traversing a thick iron block. Cluster size distributions were measured in two configurations: RPC placed 1 cm and 70 cm behind the iron. The results are shown in Fig. 9.18. The measured cluster size is slightly higher in the case of the 70 cm air gap. This can be explained by the fact that the secondaries produced in the iron can in this case diverge more from the original muon. The difference is, however, marginal and one can conclude that the muon secondaries do not influence significantly the RPC performance.

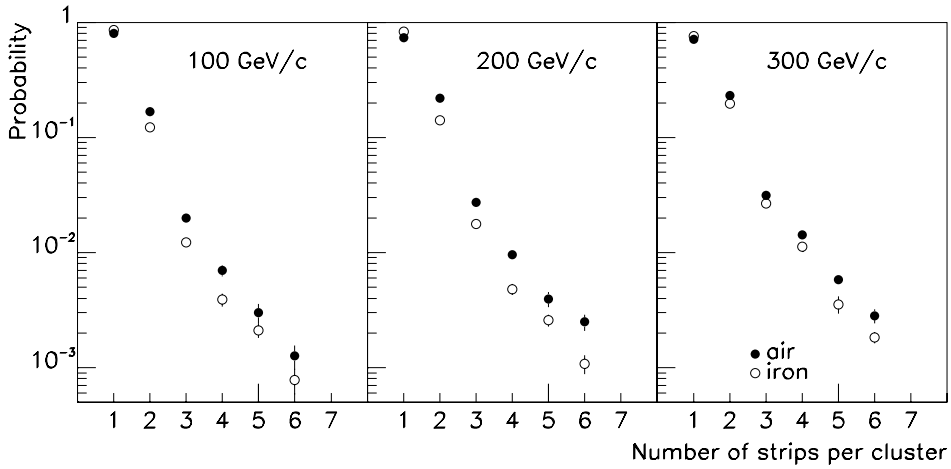

Figure 9.18: RPC cluster size distribution for different muon energies. Open circles — RPC just behind the iron, full circles — 70 cm apart. The strip width is 3 cm.

Efficiency and momentum resolution

Efficiency curves of the Pattern Comparator Trigger are presented in Fig. 9.17. They are calculated for various possible trigger thresholds defined by selecting certain set of strip patterns. It is seen that the PACT can provide relatively sharp p_t cut up to about 20 GeV. At higher p_t thresholds the performance is slowly degrading. An effective trigger cut can be provided up to 50-70 GeV but for the highest possible p_t^{cut} values the efficiency curves are rising rather slowly and one can expect high contamination of low p_t muons in the triggered sample.

This is better seen in Figures 9.19 and 9.20, where the trigger response is compared to the true muon momentum for two samples of generated events — minimum bias and z^0 decays. An ideal trigger should never underestimate the muon p_t in order to maintain high efficiency. For such a trigger, all events in Figures 9.19 and 9.20 should lie above the diagonal. One can see that with a few exceptions this is the case. On the other hand the trigger should not overestimate the muon p_t too much, in order to maintain high purity of the sample and not to blow up the output rate. This means that the events in Figures 9.19 and 9.20 should be as close to the diagonal as possible. Again this is nearly the case, with an exception of the upper right corner ($p_t^{gen} > 50$ GeV, $p_t^{rec} > 50$ GeV) of Fig. 9.20.

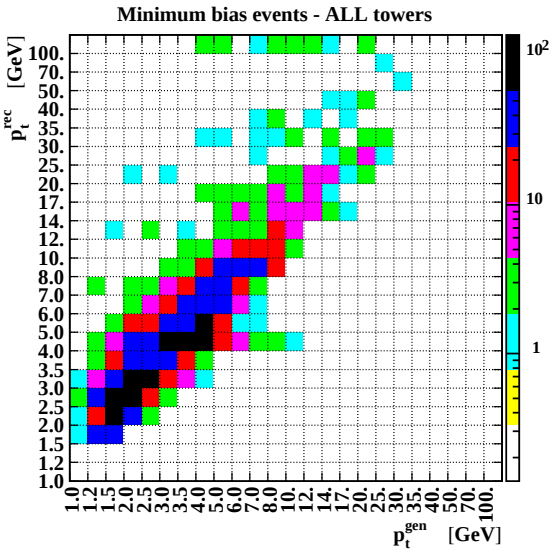

Figure 9.19: Trigger response $p_t^{reconstructed}$ vs true muon momentum $p_t^{generated}$ for min. bias events.

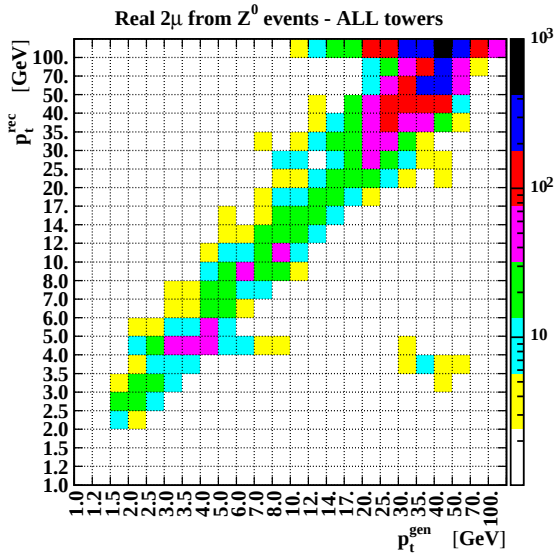

Figure 9.20: Trigger response $p_t^{reconstructed}$ vs true muon momentum $p_t^{generated}$ for Z^0 events.

Trigger rates

Single muon trigger rates due to various physics processes are shown in Fig. 9.21. The total rate is clearly dominated by minimum bias events. One can see that the trigger rate can be tuned by adjusting the threshold up to about 50 GeV. Above this value not much can be gained. This confirms the conclusion drawn from Figures 9.17 and 9.20.

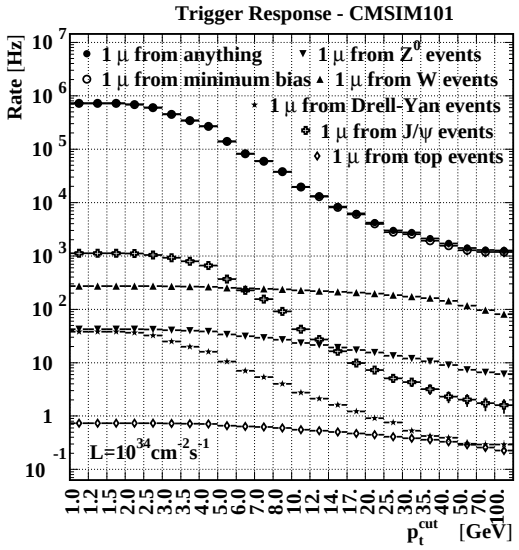

Figure 9.21: Single muon trigger rates.

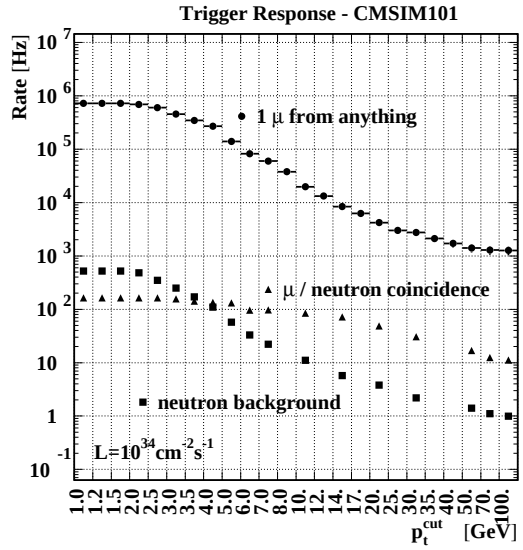

Figure 9.22: Signal and background trigger rates.

The total single muon trigger rate is compared to the rate of two kinds of background in Fig. 9.22. The one denoted as *neutron background* is caused by random coincidences of uncorrelated electrons created by thermal neutrons. The rate denoted as *μ/neutron coincidence* is due to an overlap of such an electron with a real muon. Because of the overlap the observed pattern may correspond to a higher momentum than the original one. Both

background rates are at least two orders of magnitude below the signal, which leaves us a good safety margin.

The two-muon trigger due to various physics processes is shown in Fig. 9.23. Again, it is dominated by the minimum bias rate. Its breakdown into different components is given in Fig. 9.24. The highest contribution is given by events which contain b- and c-quark semileptonic decays.

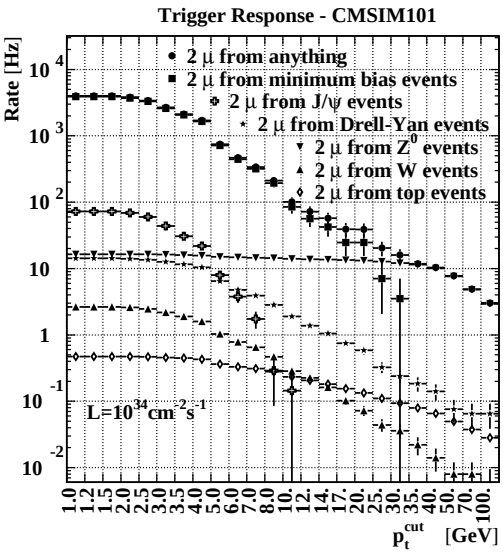

Figure 9.23: Two-muon trigger rates.

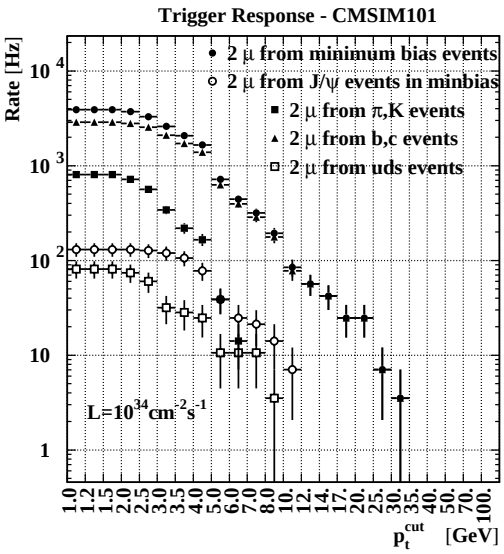

Figure 9.24: Two-muon trigger rates.

Pileup effect

Another source of background for the two-muon trigger is the pileup effect. The two muons causing the trigger might come from two different pp interactions which occurred in the same bunch crossing. Such a case we call *fake two-muon trigger*. Its rate is compared to the real two-muon rate in Figures 9.25 and 9.26. The effect is not dangerous at low luminosity, but it cannot be neglected at $\mathcal{L} = 10^{34}\mathrm{cm}^{-2}\mathrm{s}^{-1}$.

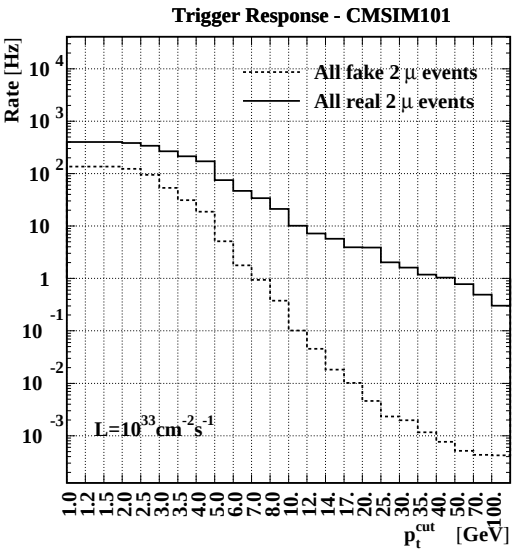

Figure 9.25: Fake two-muon trigger rates at $\mathcal{L} = 10^{33}\mathrm{cm}^{-2}\mathrm{s}^{-1}$.

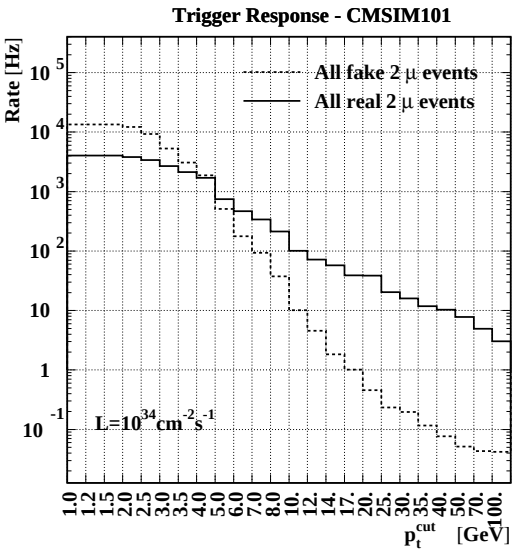

Figure 9.26: Fake two-muon trigger rates at $\mathcal{L} = 10^{34}\mathrm{cm}^{-2}\mathrm{s}^{-1}$.

Double muon resolution

The double muon resolution of the Pattern Comparator Trigger was extensively studied by simulating various physics channels [80]. In this paper we concentrate on three cases: minimum bias events, inclusive W production and J/ψ production. The angular distance between the two muons at their origin[2] is plotted in Figures 9.27-9.30. Scales on the axes correspond to the granularity of PACT (one bin = one segment processor, see page 73) which is about[3] 0.1-0.2 in η and 2.5° in ϕ.

In the case of minimum bias sample (Fig. 9.27) a significant correlation is observed. It can be explained by the jet structure of events. Even stronger correlation is seen in W events (Fig. 9.28). The muons from J/ψ (Fig. 9.29) are correlated in η but it is difficult to see any correlation in ϕ. However, if one restricts the sample to relatively high p_t particles (Fig. 9.30) a strong correlation emerges, also in ϕ. This is an important case, because higher p_t muons have better chance to be detected in the muon system. Summarising, there are important angular correlation between muons at their origin.

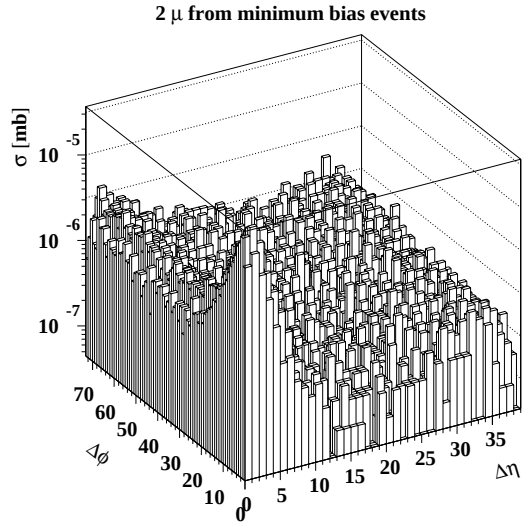

Figure 9.27: Dependence between $\Delta\eta$ and $\Delta\phi$ for minimum bias events in the case of p_t^{cut}=1 GeV.

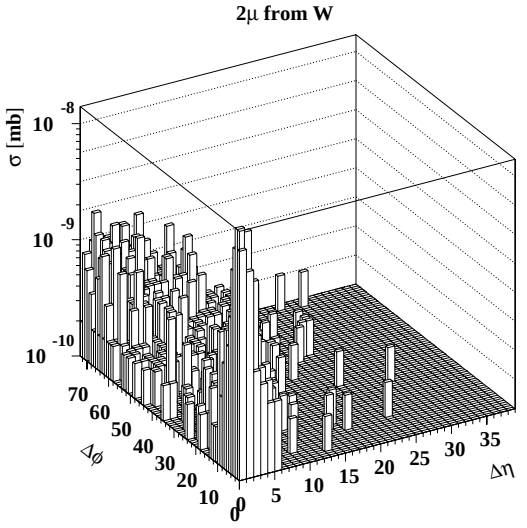

Figure 9.28: Dependence between $\Delta\eta$ and $\Delta\phi$ for W in the case of p_t^{cut}=1 GeV.

The situation might be different after muons traverse calorimeters and suffer strong bending in the magnetic field. This is discussed in Figures 9.31-9.38. Here, the muon coordinates are taken from the trigger output. One histogram bin corresponds to one segment processor of PACT. The figures with even numbers show the entire detector, whereas odd numbered ones give the zoomed view of the small distance region.

In the case of minimum bias and W events the correlation, especially in ϕ, is smeared out by the combined effect of multiple scattering, energy loss fluctuations and magnetic bending. In the J/ψ case the η correlation remains significant, whereas the ϕ orientation is completely lost, even in the high p_t sample.

The efficiency loss due to finite trigger granularity for the two-muon events can be concluded from this study. In the trigger logic there must be a provision for muons crossing boundaries of trigger segments. This may cause a side effect that sometimes one muon can be seen in two (or even more) neighbouring segments. In order to avoid a two-muon trigger in such case, one can veto 1 or 2 segments around the segment with the highest p_t candidate. The efficiency loss caused by such vetoing can be read from Figures 9.32, 9.34, 9.36, and 9.38. A summary is given in Table 9.3, including also Z^0, top, and Drell-Yan events. From this table one can conclude that the efficiency loss is rather modest and the PACT trigger granularity is adequate for the two muon physics at LHC.

[2]Muons from π and K decays, in the first approximation, continue the flight direction of their parents.
[3]The exact η segmentation is given in Fig. 6.10.

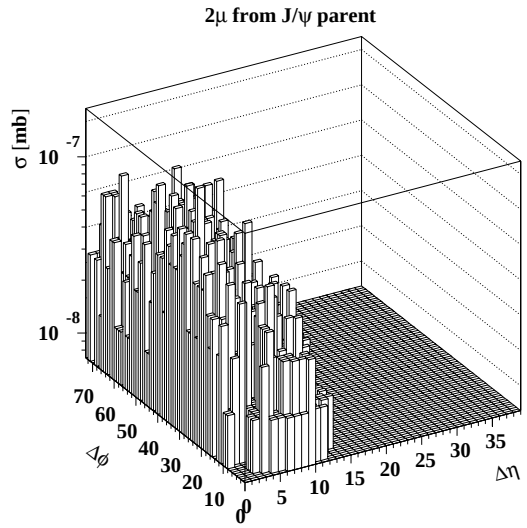

Figure 9.29: Dependence between $\Delta\eta$ and $\Delta\phi$ for J/ψ in the case of p_t^{cut}=1 GeV.

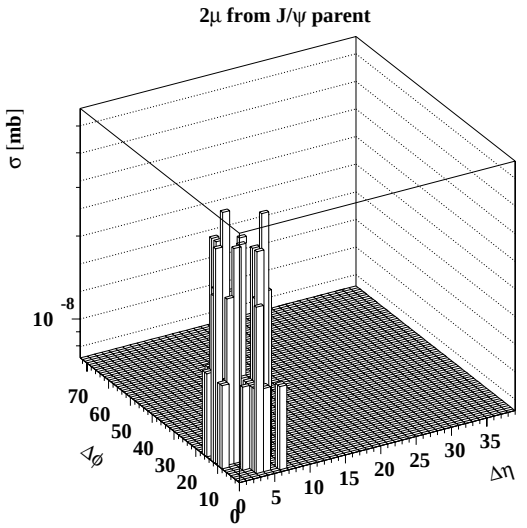

Figure 9.30: Dependence between $\Delta\eta$ and $\Delta\phi$ for J/ψ in the case of p_t^{cut}=4 GeV.

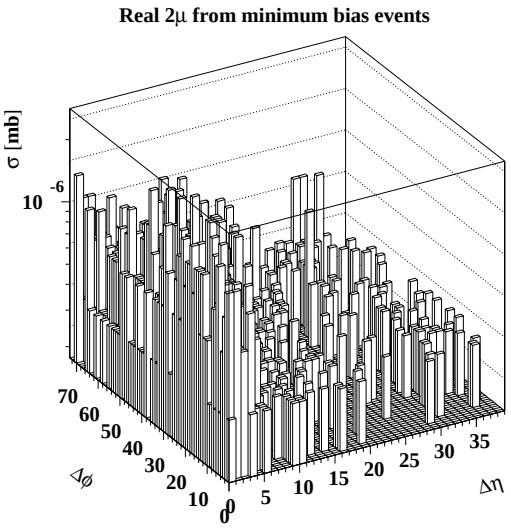

Figure 9.31: Dependence between $\Delta\eta$ and $\Delta\phi$ for muons from minimum bias events in the case of p_t^{cut}=1 GeV – full trigger response.

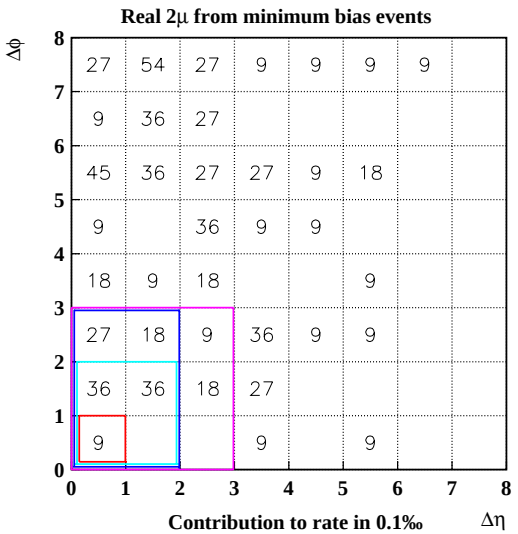

Figure 9.32: Contributions to the minimum bias rate from the region of small differences in η and ϕ for p_t^{cut}=1 GeV – full trigger response.

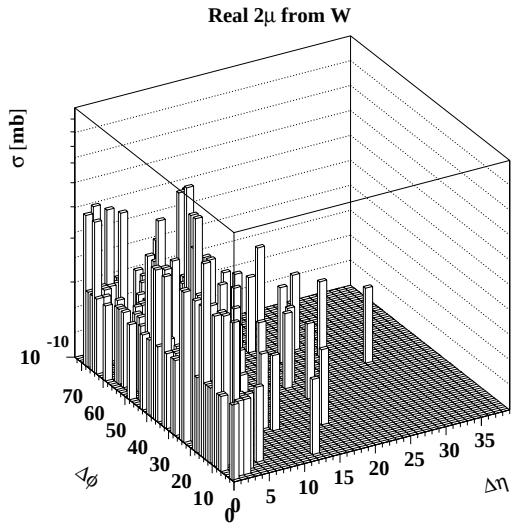

Figure 9.33: Dependence between $\Delta\eta$ and $\Delta\phi$ for muons from W in the case of p_t^{cut}=1 GeV – full trigger response.

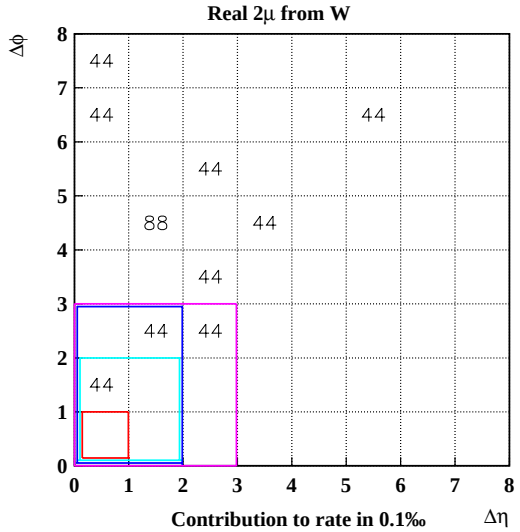

Figure 9.34: Contributions to W rate from the region of small differences in η and ϕ for p_t^{cut}=1 GeV – full trigger response.

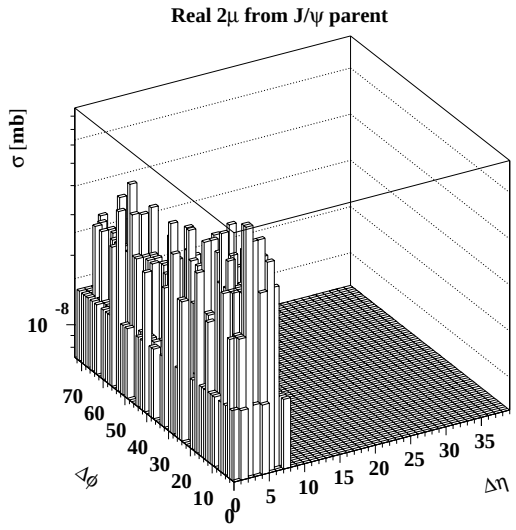

Figure 9.35: Dependence between $\Delta\eta$ and $\Delta\phi$ for muons from J/ψ in the case of p_t^{cut}=1 GeV – full trigger response.

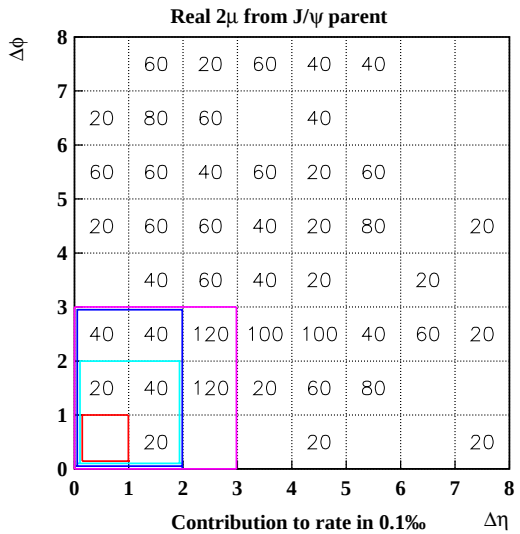

Figure 9.36: Contributions to J/ψ rate from the region of small differences in η and ϕ for p_t^{cut}=1 GeV – full trigger response.

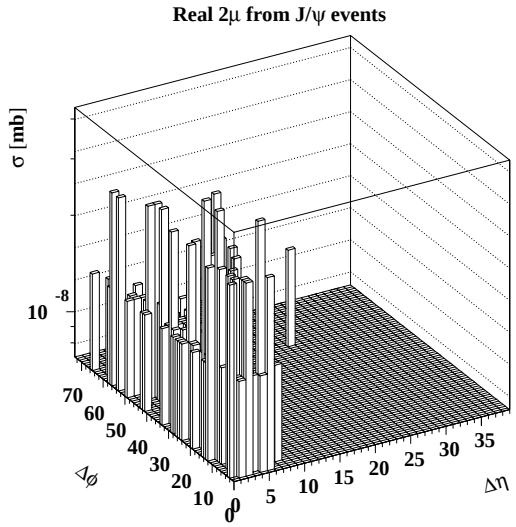

Figure 9.37: Contributions to J/ψ rate from the region of small differences in η and ϕ for p_t^{cut}=4 GeV – full trigger response.

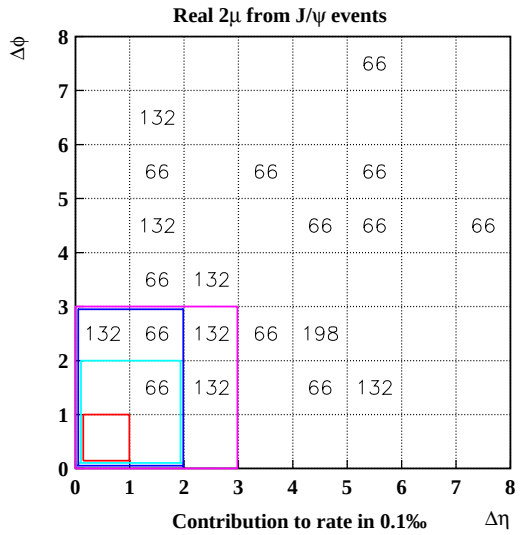

Figure 9.38: Contributions to J/ψ rate from the region of small differences in η and ϕ for p_t^{cut}=4 GeV – full trigger response.

Table 9.3: Percentage of 2 muon events lost due to the limited 2 muon resolution.

Source	$\Delta\eta < 1$ and $\Delta\phi < 1$	$\Delta\eta < 1$ and $\Delta\phi < 2$	$\Delta\eta < 2$ and $\Delta\phi < 2$
Minimum bias	0.8 %	1.3 %	1.5 %
J/ψ events (all)	0.8 %	1.6 %	4.0 %
J/ψ events ($p_t > 4$ GeV)	0.7 %	2.6 %	5.3 %
W events	0.4 %	0.9 %	1.3 %
Z^0 events	0.03 %	0.09 %	0.09 %
top events	0.2 %	0.5 %	0.8 %
Drell-Yan events	0.0 %	0.0 %	0.0 %

9.3.5 Global Muon Trigger

The main goal of the Global Muon Trigger (GMT) algorithm is to exploit complementarity of the RPC/PACT and DT/CSC/TF subsystems. Ideally, one would expect from GMT higher efficiency and stronger background suppression than from each of the two subsystems. The GMT algorithm described in Section 7.7.3 was tested in this respect by simulation. Single muons were generated with a flat distribution of $0 < \phi < 360^{\circ}$, $|\eta| < 1$, and $5 < p_t < 100$ GeV. Obtained efficiency is compared in Fig. 9.39 to the efficiency of DT and RPC. It is seen that GMT improves the efficiency significantly. Moreover, it makes it more uniform over η, ϕ, and p_t.

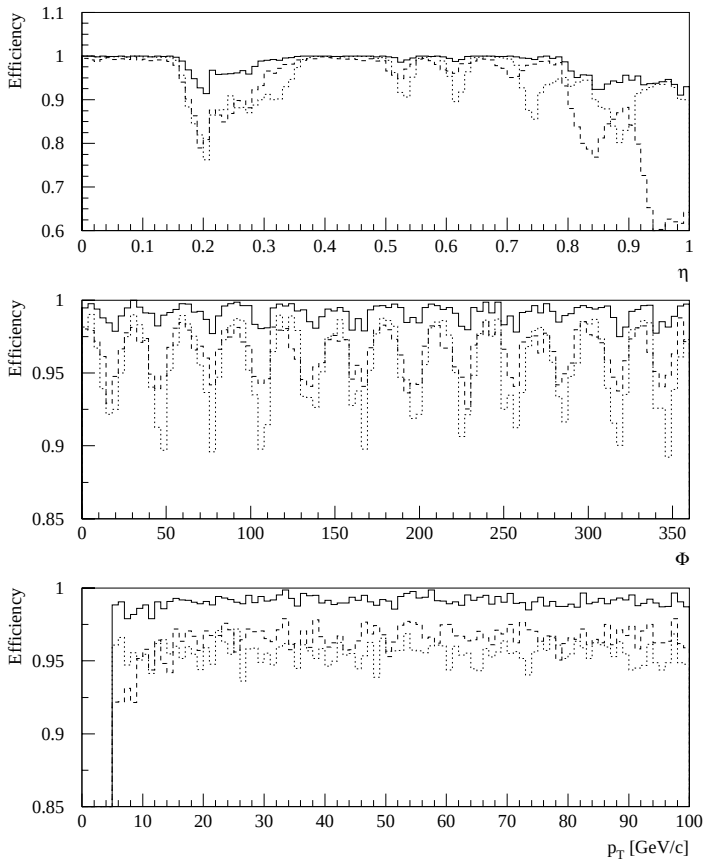

Figure 9.39: Trigger efficiencies for RPC (dotted line), Drift Tubes (dashed line) and Global Muon Trigger.

Table 9.4: Efficiency of the Global Muon Trigger tested with single muons at $|\eta| < 0.8$.

Number of muons found	0	1	>1
RPC	4.44±0.11 %	95.54±0.68 %	0.02±0.01 %
DT	5.36±0.12 %	94.41±0.68 %	0.22±0.02 %
GMT	1.04±0.05 %	98.78±0.70 %	0.18±0.02 %

The overall performance of the GMT algorithm is summarised in Table 9.4. The inefficiency is reduced from about 5% for each subsystem down to the level of 1%. In addition, the resulting number of artificially created muons (ghosts) is smaller that the sum of ghosts from the two subsystems. This proves that the algorithm performs better than a simple AND/OR combination. In the case of simple OR one would expect improvement in efficiency for the price of many ghosts. In the case of AND, ghosts would be suppressed for expense of efficiency. In the presented algorithm efficiency is significantly improved without increasing the number of ghosts. Furthermore the system is very flexible and there is a lot of room for optimisation of the algorithm.

9.4 Muon and calorimetric trigger thresholds and rates

As it was discussed in Sections 4.1 and 5.1 the CMS 2nd Level Trigger is designed to receive up to 100 kHz events. The 1st Level is assumed to deliver not more than 30 kHz in order to ensure a safety margin. This bandwidth should be divided between muon and calorimeter triggers. Rates of calorimeter triggers, i.e. one or two electrons or photons; electron from a b-quark decay; 1, 2, 3 or 4 jets; electron/photon + jet; missing transverse energy $\not{E}_t$ and total transverse energy ΣE_t, have been calculated and they are discussed in detail elsewhere [141]-[151]. The muon trigger was also simulated [2, 21, 27, 80, 84, 19] and the rates of one- and two-muon trigger were discussed in the previous section. Now, we are going to discuss combined muon-calorimeter trigger rates, namely μ-e, μ-jet, μ-$\not{E}_t$, and μ-ΣE_t.

Combined muon-calorimetric triggers have a great importance for many processes to be studied in the future pp colliders. The presence of a high energetic muon gives a very good event signature mainly due to the significant improvement in the signal/noise ratio. In case of the CMS detector in many processes it might be sufficient to use the muon trigger alone but there are processes where only a combined muon/calorimetric signature makes the study feasible. There are also several processes for which the combined signature is expected to improve the efficiency significantly since the muon requirement should allow for important reduction in calorimeter thresholds extending in this way the physics potential. These processes are listed in Table 9.5.

Table 9.5: Physics channels involving combined muon/calorimeter triggers.

physics channel	μ-e/γ	μ-jet	μ-$\not{E}_t$
$t\bar{t}$, WZ, Wγ production	+	+	+
H, h $\rightarrow$ ZZ$^{(*)}$ $\rightarrow$ $\mu\mu$ ee	+		
H, h $\rightarrow$ ZZ$^{(*)}$ $\rightarrow$ $\mu\mu$ 2jets		+	
H, h $\rightarrow$ ZZ$^{(*)}$ $\rightarrow$ $\mu\mu$ $\nu\nu$			+
H, h $\rightarrow$ WW $\rightarrow$ $\mu\nu$ 2jets		+	+
Wh, Zh, Hh $\rightarrow$ $\ell(\ell)$ $\gamma\gamma$	+		
h, A, H $\rightarrow$ $\tau\tau$ $\rightarrow$ e$\nu\nu$ $\mu\nu\nu$	+		+
h, A, H $\rightarrow$ $\tau\tau$ $\rightarrow$ $\ell\nu\nu$ had.	+	+	+
$t\bar{t}$ $\rightarrow$ H$^{\pm}$b Wb	+	+	+
H$^{\pm}$ $\rightarrow$ $\tau\nu$; W $\rightarrow$ $\ell\nu$	+	+	+
B_d^0 $\rightarrow$ J/ψ K_s^0 b_{tag} $\rightarrow$ μ or e + control channels	+		
B_d^0 $\rightarrow$ $\pi^+\pi^-$ b_{tag} $\rightarrow$ μ or e		+	
B_s^0 $\rightarrow$ $D_s\pi$ $\rightarrow$ $\varphi\pi\pi$ $\rightarrow$ KK $\pi\pi$ b_{tag} $\rightarrow$ μ or e		+	
$\tilde{g}\tilde{g}$, $\tilde{q}\tilde{q}$ $\rightarrow$ 1-4 ℓ χ_1^0 + X	+	+	+
$\tilde{\ell}\tilde{\ell}$ $\rightarrow$ 2-3 ℓ χ_1^0's	+		+
$\chi_2^0\chi_1^{\pm}$ $\rightarrow$ $\ell\ell$ χ_1^0 $\ell'\nu\chi_1^0$	+		+
leptoquarks	+	+	
technicolor ρ_T, ω_T	+		

In the case of two-object triggers at low luminosity we can afford the lowest possible muon p_t cut. It is determined by the muon energy loss in the calorimeters, and therefore varies with η. In the barrel it is $\approx$4 GeV. In the endcaps, it decreases down to $\approx$2 GeV at $|\eta| = 2.4$. More precisely one can define the threshold as:

$$
\begin{array}{lll}
p_t > 4.0\ \text{GeV} & \text{for} & |\eta| < 1.5 \\
p_t > 2.5\ \text{GeV} & \text{for} & 1.5 < |\eta| < 1.9 \\
p_t > 2.0\ \text{GeV} & \text{for} & 1.9 < |\eta| < 2.4
\end{array}
$$

At high luminosity it is convenient to set the muon threshold for two-object triggers at 4 GeV in the entire η range.

Once we fixed the muon thresholds we can plot the two-object trigger rates as a function of the threshold on the second object. This is done in Figures 9.40-9.44.

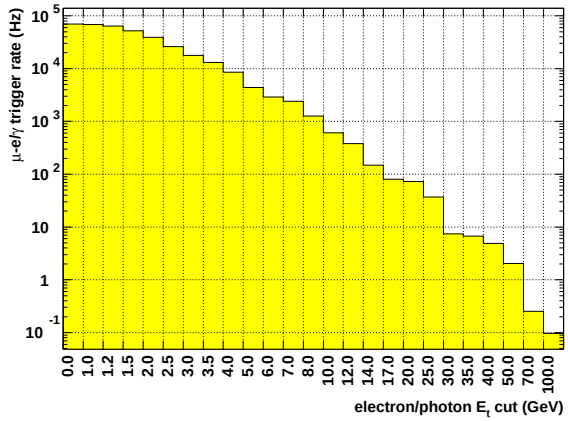

Figure 9.40: Muon-electron/photon trigger rate for $p_t^{cut}(\mu)$ = 2-4 GeV at $\mathcal{L} = 10^{33}\text{cm}^{-2}\text{s}^{-1}$.

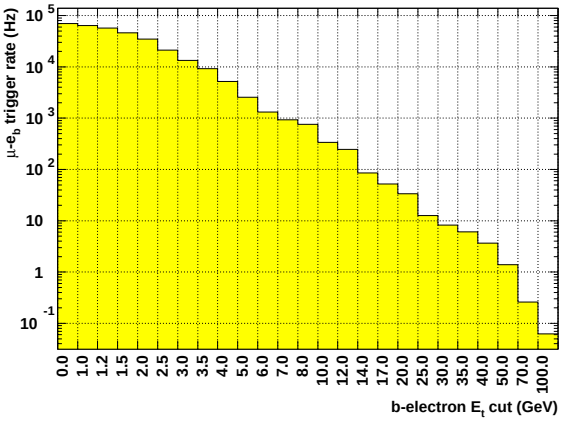

Figure 9.41: Muon-beauty electron trigger rate for $p_t^{cut}(\mu)$ = 2-4 GeV at $\mathcal{L} = 10^{33}\text{cm}^{-2}\text{s}^{-1}$.

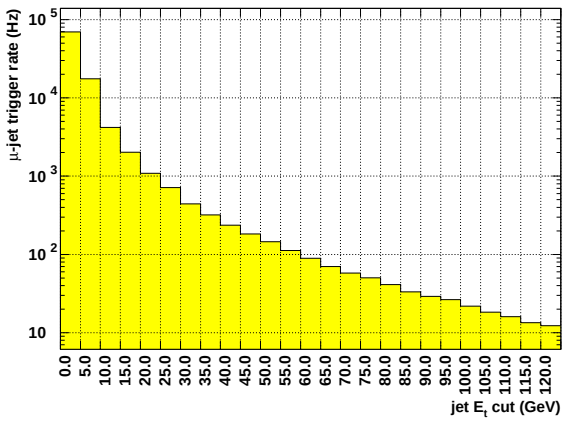

Figure 9.42: Muon-jet trigger rate for $p_t^{cut}(\mu)$ = 2-4 GeV at $\mathcal{L} = 10^{33}\text{cm}^{-2}\text{s}^{-1}$.

All the results are summarised in Table 9.6. We have chosen the thresholds to keep the total trigger rate at 30 kHz. The rates of calorimeter triggers are taken from [149].

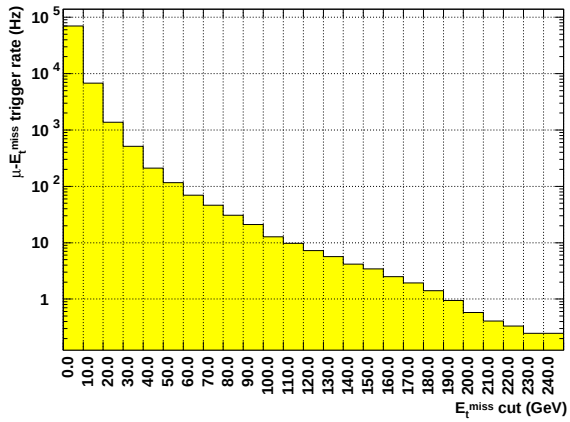

Figure 9.43: Muon-$\not\!\!E_t$ trigger rate for $p_t^{cut}(\mu) =$ 2-4 GeV at $\mathcal{L} = 10^{33}\mathrm{cm}^{-2}\mathrm{s}^{-1}$.

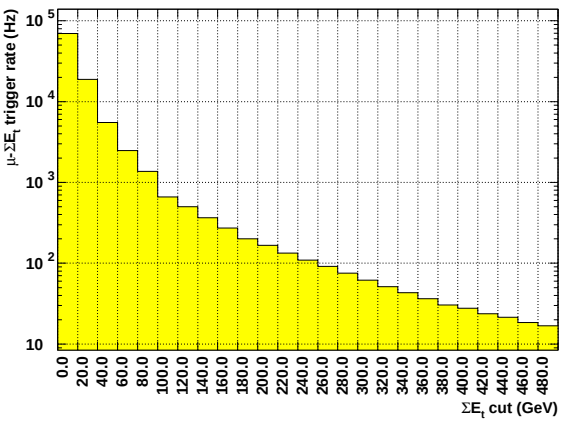

Figure 9.44: Muon-ΣE_t trigger rate for $p_t^{cut}(\mu) =$ 2-4 GeV at $\mathcal{L} = 10^{33}\mathrm{cm}^{-2}\mathrm{s}^{-1}$.

Table 9.6: Trigger rates for selected cuts.

trigger type	$\mathcal{L} = 10^{33}\mathrm{cm}^{-2}\mathrm{s}^{-1}$ thresholds (GeV)		rate (kHz) individual	rate (kHz) cumulative	$\mathcal{L} = 10^{34}\mathrm{cm}^{-2}\mathrm{s}^{-1}$ thresholds (GeV)		rate (kHz) individual	rate (kHz) cumulative
ΣE_t		150	1.04	1.04		400	0.48	0.48
$\not\!\!E_t$		40	2.11	2.82		80	1.29	1.70
e		12	10.3	12.3		25	6.84	8.34
e e		7	1.54	13.1		12	1.45	9.52
j		50	1.98	13.5		100	2.06	10.7
j j		30	1.63	13.9		60	2.17	11.6
j j j		20	1.02	14.1		30	3.16	13.3
j j j j		15	0.68	14.2		20	2.96	14.3
e j	9	15	5.98	15.2	12	50	1.35	14.9
μ		7	7.0	7.0		20	7.8	7.8
$\mu\mu$		2-4	0.5	7.3		4	1.6	9.2
μ e	2-4	7	2.4	9.2	4	8	5.5	14.4
μ e_b	2-4	4	5.2	12.8				
μ j	2-4	10	4.2	14.4	4	40	0.3	14.4
μ $\not\!\!E_t$	2-4	40	0.2	14.4	4	60	1.0	15.3
μ ΣE_t	2-4	100	0.7	14.4	4	250	0.2	15.3

Chapter 10

Organisational issues

10.1 Scale of the project

One of the biggest difficulties in the Muon Trigger Project is its large scale. The muon trigger electronics consists of a few thousand boards. It requires development of more than ten dedicated ASICs. The overall cost of the system exceeds 15 millions CHF, not counting the trigger detectors. About 100 physicists and engineers from 14 laboratories located around the world participate in the Muon Trigger Project. The time scope of the project is also extraordinary. The first trigger processor prototype was tested in 1993, i.e. 12 years before the start of LHC! Preliminary simulation study were done already in 1990. Key ingredients necessary for a success of such a big project are:

- documentation — comprehensive, kept up to date and easily accessible;
- communication between different groups — meetings, teleconferences, World Wide Web, electronic mail;
- planning — taking into account available financial and human resources, forecasting the technology and market trends;
- monitoring — milestones, reports and reviews.

The rest of this paper is devoted to those issues. Extensive list of documents related to the CMS Muon Trigger is given in a dedicated chapter. It is followed by an Appendix with the table of milestones which are important tools to monitor the project. The Appendix also contains a graphical overview of the project schedule.

10.2 Participating institutes

- Austria
  - Institut für Hochenergiephysik der OeAW, HEPHY, Vienna
- Italy
  - Università di Bari e Sezione dell' INFN, Bari
  - Università di Bologna e Sezione dell' INFN, Bologna
  - Università di Padova e Sezione dell' INFN, Padova
- Poland
  - Instytut Fizyki Doświadczalnej Uniwersytetu Warszawskiego, Warsaw
  - Instytut Problemów Jądrowych im. A.Sołtana, Warsaw
- U.S.A.
  - Massachusetts Institute of Technology, Cambridge
  - The Ohio State University, Columbus
  - University of California at Davis
  - Rice University, Houston
  - University of California at Los Angeles
  - Carnegie Mellon University, Pittsburgh
- International laboratories
  - Joint Institute for Nuclear Research, Dubna
  - European Laboratory for Particle Physics, CERN, Geneva

Recently, several institutes from Korea expressed their interest in the project.

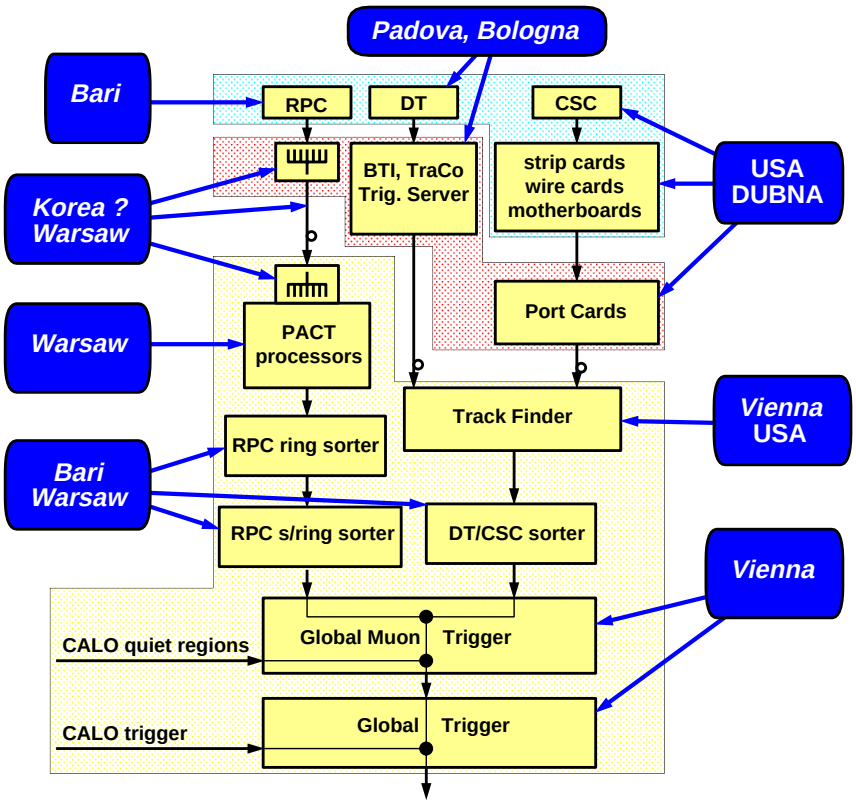

Figure 10.1: Schematic diagram of responsibilities in the Muon Trigger project.

10.3 World Wide Web services

Almost all documents related to CMS Muon Trigger are available in a computer form and their are accessible through WWW. In the documentation list we refer to them by their URL addresses. Some of the documents are catalogued as CMS notes which are available at the CMSDOC server: ⟨http://cmsdoc.cern.ch/documents.html⟩ In such a case we only refer to the note number. The list of other WWW servers of concern is given below.

General CMS WWW servers

- CMS public information CMSINFO — ⟨http://cmsinfo.cern.ch/cmsinfo⟩
- CMS internal information CMSDOC — ⟨http://cmsdoc.cern.ch/cms.html⟩

Muon Trigger — general information

- Muon Trigger documents and news — ⟨http://cmsdoc.cern.ch/mu_tr.html⟩
- Muon Trigger documentation guide — ⟨http://cmsdoc.cern.ch/doc/mu_tr/docs/MUTRGUIDE.HTML⟩
- Muon Trigger milestones — ⟨http://cmsdoc.cern.ch/doc/mu_tr/docs/MUTRIGMILESTONES⟩
- Archives of Muon Trigger transparencies by G.Wrochna — ⟨http://cmsdoc.cern.ch/~wrochna⟩

Resistive Plate Chambers (RPC) — Pattern Comparator Trigger (PACT)

- PACT WWW site at Warsaw — ⟨http://info.fuw.edu.pl/HEP/cms/docs/docs.html⟩
- RPC electronics WWW site at Bari — ⟨http://sunba2.ba.infn.it/cadel_works/attivita.html⟩
- RPC page of Bari/Pavia group — ⟨http://cmsdoc.cern.ch/user/a/acolaleo/rpc.html⟩

Drift Tubes (DT) — Bunch and Time Identifier (BTI), Track Correlator (TRACO), Trigger Server (TS)

- Padova CMS Group — ⟨http://warco.pd.infn.it/cms/cmspd.html⟩
- Bologna CMS Group — ⟨http://www.bo.infn.it/cms/⟩
- CMS page of Pierluigi Zotto — ⟨http://warco.pd.infn.it/ zotto/CMS.html⟩

Cathode Strip Chambers (CSC)

- CMS Endcap muon home page at FNAL — ⟨http://uscms.fnal.gov/uscms/Subsystems/MUON/Muon.html⟩
- CMS Endcap muon site at Wisconsin — ⟨http://lobelia.physics.wisc.edu/cms/muon/welcome–endcap.html⟩
- CMS Endcap muon site at Davis — ⟨http://ucdheg.ucdavis.edu/welcome.html⟩
- CSC Trigger Electronics page at UCLA — ⟨http://www-collider.physics.ucla.edu/cms/trigger/⟩
- CSC Trigger motherboard WWW site at Rice — ⟨http://bonner–ntserver.rice.edu/motherboard⟩

Track Finder

- Track Finder home page by T.Wildschek and A.Kluge
  — ⟨http://sungraz.cern.ch/CMS/trigger/muonTrigger/Welcome.html⟩

Trigger related general items

- Global Muon Trigger page by N.Neumeister
  — ⟨http://sungraz.cern.ch/CMS/trigger/globalMuonTrigger/Welcome.html⟩
- Global Trigger WWW page by F.Szoncso — ⟨http://wwwcn.cern.ch/∼szoncso/globaltrigger/⟩
- Trigger and Data Acquisition home page by S.Cittolin — ⟨http://cmsdoc.cern.ch/∼cittolin/⟩
- CMS Data Link page by O.Bouianov and E.Pietarinen
  — ⟨http://www.evitech.fi/∼olegb/personal/fiber_optics.html⟩
- Timing, Trigger and Control (TTC) System page by B.Taylor — ⟨http://www.cern.ch/TTC/intro.html⟩

Documentation

The list of documents related to CMS Muon Trigger is divided into subject groups. In each group the documents are listed in an antychronological order. An HTML version of this list can be found at ⟨http://cmsdoc.cern.ch/doc/mu_tr/docs/MUTRGUIDE.HTML⟩

Resistive Plate Chambers (RPC) — Pattern Comparator Trigger (PACT)

[1] *Data Compression Scheme for the data transfer from the RPCs to the Muon Trigger*, M.Ćwiok et at., paper in preparation

[2] *"Ghost Buster" for the CMS RPC based muon trigger*, A.Fengler, P.Zalewski, paper in preparation

[3] *RPC Readout System*, G.Wrochna, October 96, ⟨ftp://cmsdoc.cern.ch/doc/tridas/docs/9610/9610_wrochna1.ps.Z⟩

[4] *Parametrisation functions of the RPC based muon trigger*, M.Konecki, J.Królikowski, G.Wrochna, **CMS TN/96-104**

[5] *Update on RPC trigger performance*, M.Konecki, May 96, ⟨ftp://cmsdoc.cern.ch/doc/tridas/docs/9605_wrochna2.ps.Z⟩

[6] *RPC Trigger acceptance*, G.Wrochna, March 96, ⟨ftp://cmsdoc.cern.ch/doc/tridas/docs/9603_mutr_wrochna4.ps.Z⟩

[7] *RPC Muon Trigger Software MRPC 100-102*, M.Konecki, J.Królikowski, G.Wrochna, paper in preparation ⟨http://cmsdoc.cern.ch/∼wrochna/mrpc/mrpc.ps⟩ (draft)

[8] *Status of PAC and test bench construction*, I.M.Kudła, March 96, ⟨ftp://cmsdoc.cern.ch/doc/tridas/docs/9603_mutr_kudla.ps.Z⟩

[9] *PAC (Pattern Comparator) Trigger Processor — VLSI implementation*, (Talk given at *The Second Workshop on Electronics for LHC Experiments*, Sept. 23-27 1996, Balatonfüred, Hungary), M.Górski et al.

[10] *VHDL description of PAC, Segment Processor and Test Bench*, I.M.Kudła, ⟨http://info.fuw.edu.pl/HEP/cms/docs/PAC/vhdl.html⟩

[11] *Specifications of the PAC (trigger ASIC) for Muon RPC Trigger*, I.M.Kudła, ⟨http://info.fuw.edu.pl/HEP/cms/docs/PAC/⟩

[12] *Feasibility study of PAC trigger ASIC*, W. Kuźmicz, M. Niewczas, Z. Jaworski, ⟨ftp://cmsdoc.cern.ch/doc/tridas/docs/9511_tr_jaworski.ps.Z⟩

[13] *VLSI implementation of the RPC Pattern Comparator (PAC) ASIC for the CMS experiment — feasibility study*, W. Kuźmicz, M. Niewczas, Z. Jaworski, **CMS TN/96-003**

[14] *Status of the PACT test bench construction*, I.M.Kudła, ⟨ftp://cmsdoc.cern.ch/doc/tridas/docs/9511_tr_kudla.ps.Z⟩

[15] *The RPC System For The CMS Experiment At LHC* (Talk given at III International Workshop on Resistive Plate Chambers and Related Detectors Pavia, Italy, 11-12 Oct. 1995), G.Wrochna, **CMS TN/95-182**

[16] *Trigger Electronics for Muon RPC Chambers in CMS* (Talk given at *The First Workshop on Electronics for LHC Experiments*, Sept. 11-15 1995, Lisbon), M.Górski et al., **CMS TN/95-138**

[17] *Proposal of guidelines for RPC design and R&D*
⟨http://cmsdoc.cern.ch/doc/mu_tr/docs/RPC_GUIDELINES⟩

[18] *RPC geometry and Muon Trigger acceptance*, M.Konecki, J.Królikowski, I.Kudła, G.Wrochna, **CMS TN/95-120**

[19] *Clusters in RPC and Muon Trigger performance*, M.Górski et al., **CMS TN/95-107**

[20] *Long term operations with RPCs: status report and future tests for CMS*, G.Iaselli, **CMS TN/95-016**

[21] *Muon Trigger Rates*, Á.Csilling, M.Konecki, J.Królikowski, G.Wrochna, **CMS TN/94-282**

[22] *Pattern Comparator Trigger (PACT) for the Muon System of the CMS Experiment*, M.Andlinger et al., **CMS TN/94-281**, **CERN-PPE/94-227**, Nuclear Instruments and Methods **A 370** (1996) 389

[23] *Simulation of the CMS Muon Trigger System*, C.-E.Wulz et al., **CMS TN/94-174**

[24] *Estimation of the RPC Muon Trigger rates due to neutral particles*, M.Huhtinen, G.Wrochna, **CMS TN/94-138**

[25] *RPC based CMS Muon Trigger - progress report*, H.Czyrkowski et al., **CMS TN/93-111**

[26] *RPC based Muon Trigger for the CMS detector at LHC*, G. Wrochna, **CMS TN/93-080**

[27] *Simulation study of the RPC based Single Muon Trigger for CMS*, M.Konecki, J.Królikowski, G.Wrochna, **CMS TN/92-039**

Drift Tubes (DT) — Bunch and Time Identifier (BTI), Track Correlator (TRACO), Trigger Server (TS)

[28] *TRACO — Barrel muon track correlator*, A.Sancho, June 97,
⟨http://cmsdoc.cern.ch/∼wsmith/TRACO697.pdf⟩

[29] *DTBX trigger server simulation*, S.Marcellini, June 97,
⟨http://cmsdoc.cern.ch/∼wsmith/ts_june97.pdf⟩

[30] *Review of the performance of a FPGA prototype of a Front-End Trigger device for CMS Muon Barrel Chambers*, P.Zotto, October 96,
⟨ftp://cmsdoc.cern.ch/doc/tridas/docs/9610/BTI_FPGA.ps.Z⟩

[31] *Track Correlator for the CMS Muon Barrel Chamber Trigger System*, A.J.Sancho, October 96,
⟨ftp://cmsdoc.cern.ch/doc/tridas/docs/9610/traco1810.ps.Z⟩

[32] *Track-Segment Sorting in the Trigger Server of a Barrel Muon-Station in CMS*, I.D'Antone et al., **CMS TN/96-078**

[33] *Beam Test of a FPGA Prototype of a Front-end Trigger Device for Muon barrel Chambers*, M. De Giorgi, A. De Min, I.Lippi, R.Martinelli, P.Zotto, **CMS TN/96-002**

[34] *Design and Simulation of the Trigger Electronics for the CMS Muon Barrel Chambers* (Talk given at *The First Workshop on Electronics for LHC Experiments*, Sept. 11-15 1995, Lisbon), M. De Giorgi et al.

[35] *Design and simulation of the Muon Barrel Chamber Trigger of CMS*, M.De Giorgi et al., **CMS TN/95-001**

[36] *Further studies on a DTBX prototype for the CMS Muon Detector at LHC*, F.Gasparini et al., Nucl. Instr. and Meth. **A360** (1995) 507-511

[37] *Performance of a DTBX prototype*, F.Gasparini et al., Nucl. Instr. and Meth. **A344** (1994) 137

[38] *Bunch crossing identification at LHC using a mean-timer technique*, F.Gasparini et al., Nucl. Instr. and Meth. **A336** (1993) 91

[39] *A possible scheme for a first level muon trigger with bunch crossing identification at LHC*, F. Gasparini, P. Zotto, **CMS TN/92-018**

Cathode Strip Chambers (CSC)

[40] *Status of the CSC trigger*, P.Padley, June 97, ⟨ftp://bonner-ntserver.rice.edu/cms/emu/padova.pdf⟩

[41] *Baseline for CSC-based Endcap Muon Trigger, v 2.6*, J.Hauser, July 96, ⟨ftp://hepsun0.physics.ucla.edu/pub/cms/csc_tn_95_013_v2p6.ps⟩

[42] *Status of the CSC trigger*, J.Hauser,
October 96: ⟨ftp://cmsdoc.cern.ch/doc/tridas/docs/9610/9610_hauser.ps.Z⟩
August 96: ⟨ftp://hepsun0.physics.ucla.edu/pub/cms/csc_trig_status_8_30_96.ps⟩
April 96: ⟨ftp://hepsun0.physics.ucla.edu/pub/cms/csc_trig_status.ps⟩
February 96: ⟨ftp://hepsun0.physics.ucla.edu/pub/cms/CSC_Trigger_Status_Report.html⟩
November 95: ⟨ftp://cmsdoc.cern.ch/doc/tridas/docs/9511_tr_hauser.ps.Z⟩

[43] *Comparator and strip LCT circuitry*, J.Kubic, ⟨ftp://hepsun0.physics.ucla.edu/pub/cms/kubic/comparator/⟩

[44] *Front-end electronics for the cathode strip readout of the CMS endcap muon system*, (Talk given at the Second Workshop on Electronics for LHC Experiments, Sept. 23-27 1996, Balatonfüred, Hungary), R.E.Breedon et al., **CMS CR/1996-008**

[45] *Background LCT rates by CSC type using the forward muon triger simulation in CMSIM*, R.E.Breedon et al., **CMS TN/96-070**

[46] *CSC layout and trigger segmentation*, G.Wrochna, October 96, ⟨ftp://cmsdoc.cern.ch/doc/tridas/docs/9610/9610_wrochna3.ps.Z⟩

[47] *LCT design status report*, J.Kubic, August 96, ⟨ftp://hepsun0.physics.ucla.edu/pub/cms/kubic/fermi896_transps/⟩

[48] *CSC strip trigger rates*, J.Hauser, ⟨http://cmsdoc.cern.ch/doc/mu_tr/news/00018⟩

[49] *CSC LCT rate due to background*, R.Breedon, Yu.Fisyak, W.Ko, J.Rowe, ⟨http://cmsdoc.cern.ch/doc/mu_tr/news/00016⟩

[50] *CSC Trigger Simulation in CMSIM 100*, J.Rowe, **CMS TN/96-069**

[51] *CSC Trigger Simulation in CMSIM 100*, J.Rowe, TRIDAS meeting, FNAL, 3 May 1996 ⟨http://ucdheg.ucdavis.edu/ rowe/csc_trig/csc_trig.html⟩

[52] *Study of the background in the CMS Endcap Cathode Strip Chambers*, R.Breedon, *Workshop on LHC Backgrounds*, CERN, 22 March 1996, ⟨http://ucdheg.ucdavis.edu/ breedon/bkgd/bkgd.html⟩

[53] *CSC trigger: Dubna activities*, V.Karjavin, March 96, ⟨ftp://cmsdoc.cern.ch/doc/tridas/docs/9603_mutr_karjavin.ps.Z⟩

[54] *CMS Modeling of Electron Signal for The Forward CSC*, L.S.Durkin, **CMS TN/95-194**

[55] *Design of a Stereo CSC Front-End Trigger*, D.Acosta, **CMS TN/95-193**

[56] *Bunch Crossing Identification Study on MF1 Prototype Beam Test Experimental Data*, A.Chvyrov et al., **CMS TN/95-161**

[57] *Study of Algorithms for Muon Trigger with MF1 Prototype '95 Test Beam Data*, A.Chvyrov et al., **CMS TN/95-160**

[58] *Development of a Switched Capacitor Array ASIC for the CMS Forward Muon Chamber Readout*, R.Breedon, **CMS TN/95-132**

[59] *Study of the T0 Cathode Strip Chamber Prototype at FNAL*, N.Bondar et al., **CMS TN/95-131**

[60] *Baseline for CSC-based Endcap Muon Trigger*, J.Hauser, **CMS TN/95-013**

[61] *Momentum Resolution Required for the Level 1 Muon Trigger*, J.Hauser, **CMS TN/94-261**

[62] *A Model for the Forward Muon Trigger Primitives*, J.Rowe, paper in preparation

[63] *Electromagnetic secondaries in the detection of high energy muons*, C.Albajar et all, **CERN-PPE / 94-204**, Nucl. Instr. and Meth. **A364** (1995) 473

[64] *Position and Timing Resolution of Interpolating Cathode Strip Chambers in a Test Beam*, M.Mohammadi et al., **CMS TN/94-243**

[65] *Digital cathode strip chambers*, A.Korytov, G.Mitselmakher, **CMS TN/94-213**

[66] *Analysis of valid hit patterns in cathode strip chambers*, A.Korytov, **CMS TN/94-212**

[67] *CMS Endcap muon home page*, ⟨http://www.hep.net/us–cms/uscms/Subsystems/MUON/Muon.html⟩

Track Finder

[68] *Track finder simulation*, T.Wildschek, June 97, ⟨http://sungraz.cern.ch/CMS/trigger/muonTrigger/Slides/TrgMtg_Jun97.ps⟩

[69] *Track Finding Processor in the DTBX Based CMS Barrel Muon Trigger*, (Talk given at *The Second Workshop on Electronics for LHC Experiments*, Sept. 23-27 1996, Balatonfüred, Hungary), A.Kluge, T.Wildschek

[70] *Track-Segment Sorting in the Trigger Server of a Barrel Muon-Station in CMS*, A.Kluge, T.Wildschek, **CMS TN/96-078**

[71] *Status of milestone D330: Track Finder test bench*, T.Wildschek, October 96, ⟨ftp://cmsdoc.cern.ch/doc/tridas/docs/9610/TrgMtg_Oct96.ps.Z⟩

[72] *Status of the DT/CSC Track Finder simulation*, T.Wildschek, March 96, ⟨ftp://cmsdoc.cern.ch/doc/tridas/docs/9603_mutr_wildschek.ps.Z⟩

[73] *Track Finding Processor in the DTBX Based CMS Barrel Muon Trigger* (Talk given at *The First Workshop on Electronics for LHC Experiments*, Sept. 11-15 1995, Lisbon), A.Kluge, T.Wildschek, **CMS CR/1996-007**

Muon Sorter

[74] *The Sorting Processor — an update*, A.Ranieri, October 96, ⟨http://sunba2.ba.infn.it/cadel_works/sorter.ps⟩

[75] *The Sorting Processor Project*, G. De Robertis, A.Ranieri, I.M.Kudła, G.Wrochna, **CMS TN/95-028**

Muon Trigger — common items

[76] *Muon Trigger Milestones*,
⟨http://cmsdoc.cern.ch/doc/mu_tr/docs/MUTRIGMILESTONES⟩

[77] *Muon Trigger for heavy ion physics*, G.Wrochna, **CMS NOTE 1997/089**.

[78] *Data Acquisition for heavy ion physics*, G.Wrochna, **CMS IN 1997/032**.

[79] *Overview of the CMS muon trigger system*, (Talk given at the Second Workshop on Electronics for LHC Experiments, Sept. 23-27 1996, Balatonfüred, Hungary), G.Wrochna, **CMS CR 1996/004**.

[80] *Double Muon Trigger Rates in CMS Experiment*, A.Fengler, PHD Thesis, Warsaw University, 1996.
⟨http://cmsdoc.cern.ch/∼fengler/trig2mu.ps.Z⟩,
related transparencies (June 96): ⟨ftp://cmsdoc.cern.ch/doc/tridas/docs/9606_mtp_fengler.ps.Z⟩

[81] *Trigger in the barrel/endcap corner*, G.Wrochna, June 96,
⟨ftp://cmsdoc.cern.ch/doc/tridas/docs/9606_mtp_wrochna.ps.Z⟩

[82] *Isolated muon trigger*, C.Albajar, May 96,
⟨ftp://cmsdoc.cern.ch/doc/tridas/docs/9605_wrochna4.ps.Z⟩

[83] *CMS Muon Trigger — Preliminary specifications of the baseline trigger algorithms*, **CMS TN/96-060**.

[84] *Muon rates in UA1, D0, CDF and CMS predicted by PYTHIA 5.7*, M.Ćwiok, G.Wrochna, **CMS TN/95-150**

[85] *Muon Trigger Model — block diagrams*, G.Wrochna, May 95,
⟨http://cmsdoc.cern.ch/doc/mu_tr/docs/MUTRIGMODEL⟩

[86] *Complementarity of the Two Components in the CMS Muon Trigger System*, W.Smith, G.Wrochna, **CMS TN/95-014**

[87] *Proposal of Unified Criteria for Muon Trigger Studies*, G.Wrochna, **CMS TN/94-200**

[88] *CMS Muon Trigger in Transparencies*, I.M.Kudła, E.Radermacher, G.Wrochna, **CMS TN/94-154**

[89] *The muon system of the CMS detector at LHC*, G.Wrochna, Nucl. Instr. and Meth. **A344** (1994) 98

[90] *What is the trigger rate due to cosmic muons in CMS? — answer for the LHCC Referees*,
W.Smith, G.Wrochna,
⟨http://cmsdoc.cern.ch/doc/mu_tr/docs/REFER_COSM⟩

[91] *Muon Trigger momentum scale — a proposal*, G.Wrochna,
⟨http://cmsdoc.cern.ch/doc/mu_tr/docs/PT_SCALE⟩

Trigger related general items

[92] *CMS Global Trigger*, N.Neumeister, A.Taurok, C.-E.Wulz, F.Szoncso, **CMS NOTE/1997-009**

[93] *Specifications of the prototype trigger synchronization Tx/Rx circuits*, J.Varela, **CMS IN/1997-009**

[94] *A method for synchronization of the trigger data*, J.Varela, **CMS TN/96-011**,
transparencies (October 96): ⟨http://cmsdoc.cern.ch/∼varela/Slides/sync_trigger_slides.ps⟩

[95] *CMS Data Link*, O.Bouianov, E.Pietarinen,
⟨http://www.evitech.fi/∼olegb/personal/fiber_optics.html⟩

[96] *TTC for CMS CSC and RPC muon systems*, G.Wrochna,
⟨http://cmsdoc.cern.ch/∼wrochna/GW_talks/ttc_rpc_csc.ps⟩

[97] *Combined muon/calorimeter trigger rates*, J.Pliszka, G.Wrochna, ⟨http://cmsdoc.cern.ch/∼wrochna/tmp/emu.ps⟩

[98] *Front End Logical Model in CMS*, S.Cittolin, J.F Gillot, A.Racz, **CMS TN/96-015**

[99] *Front End Driver in CMS DAQ*, S.Cittolin et al., **CMS TN/95-020**

[100] *The CMS First Level Trigger Latency — WWW page*, A.Kluge, ⟨http://cmsdoc.cern.ch/∼akluge/latency.html⟩

[101] *CMS Level 1 Trigger Latency*, A.Kluge, W.Smith, **CMS TN/96-033**

[102] *Trigger Efficiency Measurement in CMS*, J.Varela, ⟨http://cmsdoc.cern.ch/doc/tridas/docs/trig_eff_meas.ps⟩

[103] *A contribution for the Trigger Strategy of CMS*, C.Laurenço, J.Varela, **CMS TN/95-025**

[104] *Answers for the LHCC referees concerning the CMS Trigger Bandwidth*, S.Cittolin, W.H.Smith, P.Sphicas, ⟨http://cmsdoc.cern.ch/doc/tridas/docs/BANDREF⟩

[105] *CMS Trigger System Engineering*, W.Smith, ⟨http://cmsdoc.cern.ch/doc/tridas/docs/ELECTRAN⟩

[106] *CMS Trigger, Timing and Control Requirements*, W.Smith, ⟨http://cmsdoc.cern.ch/doc/tridas/docs/TTCTRAN⟩

[107] *Timing, Trigger and Control (TTC) System*, B.Taylor, ⟨http://www.cern.ch/TTC/intro.html⟩

Background sources

[108] *Simulation of background in the muon stations*, M.Huhtinen, CMS Internal Note in preparation.

[109] *Report from CMS Radiation Working Group*, M.Huhtinen, talk given at the CMS Collaboration Meeting, Aachen, 11 December 1996.

[110] *Punchthrough in the barrel muon stations with and without the Tail Catcher*, G.Wrochna, **CMS IN/96-011**

[111] *Muons at LHC. Part 2: Arcs and Interaction Regions*, N.V.Mokhov, **CMS TN/96-089**

[112] *Evaluation of the CMS Muon Endcap Shielding*, Y.Fisyak, **CMS TN/96-076**

[113] *Workshop on LHC backgrounds*, CERN, 22 March 1996, transparencies can be obtained from Luisa Passardi (EST), ⟨luisa.passardi@macmail.cern.ch⟩

[114] *Accelerator Related Background in the CMS Detector at LHC*, A.I.Drozhdin, M.Huhtinen, N.V.Mokhov, **CMS TN/96-056**

[115] *Muon system background simulation of the CMS TP-baseline design*, R.Breedon, Y.Fisyak, **CMS TN/96-035**

[116] *Comments on the simulation of background for the CMS muon system*, Y.Fisyak, R.Breedon, **CMS TN/96-019**

[117] *Background muons generated in the CMS detector area by the beam losses in the LHC*, I.Azhgirey, V.Talanov, A.Uzunian, **CMS TN/95-202**

[118] *Radiation Environment Simulations for the CMS Detector* (Talk given at the *2nd Workshop on Simulating Accelerator Radiation Environments SARE2*, 9-11th Oct. 1995, CERN), M.Huhtinen, **CMS TN/95-198**

[119] *Background muons generated by the beam halo losses in the Straight Section*, I.Azhgirey, V.Talanov, A.Uzunian, **CMS TN/95-102**

[120] *Preliminary estimations of muon fluences on CMS muon chambers due to proton losses on LHC Straight Section 5*, I.Azhgirey, V.Talanov, A.Uzunian, **CMS TN/95-053**

[121] *Background electrons track length distribution in CSC*, I.Azhgirey, A. Uzunian, **CMS TN/94-267**

[122] *CMS Muon system radiation background shielding*, I.Azhgirey, A. Uzunian, **CMS TN/94-266**

[123] *Muon chambers occupancy in the Low-Energy background fields*, I.Azhgirey, A. Uzunian, **CMS TN/94-265**

[124] *Neutron and Photon Fluxes and Shielding Alternatives for the CMS Detector at LHC*, M.Huhtinen, P.A.Arnio, **CMS TN/94-241**

[125] *Neutron and gamma backgrounds in GEM and CMS Muon System*, Y.Fisyak, K. McFarlane, G.Mitselmakher, **CMS TN/94-147**

[126] *Radiation problems at LHC experiments — I: Neutral particle background*, M.Huhtinen, P.A.Arnio, **CMS TN/94-135**

[127] *A Study of Charged Particle Rates and Muon Backgrounds in the CMS Muon Chambers*, D.Chrisman, Th. Moers, **CMS TN/93-106**

Other documents quoted in this paper

Generic software

[128] *GEANT — Detector Description and Simulation Tool*, CERN Program Library Long Writeup **W5013**

[129] *FLUKA user's guide*, P.A.Aarnio et al., Technical Report **TIS-RP-190**, CERN, 1987, 1990
FLUKA92, A.Fassò, A.Ferrari, J.Ranft, P.R.Sala, G.R.Stevenson, J.M.Zazula, *Proceedings of the Workshop on Simulating Accelerator Radiation Environments*, Santa Fe, USA, 11-15 January 1993

[130] *GHEISHA — Simulation of hadronic showers, physics and applications*, H.C.Fesefeldt, Technical Report **PITHA 85-02**, III Physikalisches Institut, RWTH Aachen Physikzentrum, 5100 Aachen, Germany, September 1985.

[131] *GCALOR — The GEANT-CALOR Interface*, C.Zeitnitz, T.A.Gabriel, procedeengs of *International Conference on Monte Carlo Simulation in High Energy and Nuclear Physics*, Tallahassee, 1993
The GEANT-CALOR interface and benchmark calculations of ZEUS test calorimeters, C.Zeitnitz, T.A.Gabriel, Nuclear Instruments and Methods **A 349** (1994) 106

[132] *The MARS Code System User's Guide*, N.V.Mokhov, **Fermilab-FN-628** (1995)
Passage of High-Energy Particles through Matter, A.N.Kalinovskii, N.V.Mokhov, Yu.P.Nikitin, AIP, NY (1989)

[133] *DTUJET*, J.Ranft et al., *Multiparticle Dynamics*, Seewinkel, Austria, 1986
J.Ranft et al., **UL-92-7**, **UL-HEP-93-01**
DTUJET-93: Sampling Inelastic Proton-Proton and Antiproton-Proton Collisions According to the Two-component Dual Parton Model, P.Aurenche et al., *Computer Physics Commun.* **83** (1994) 107

[134] *PYTHIA 5.7 and JETSET 7.4 Physics and Manual*, T.Sjöstrand, **CERN-TH.7112/93**, **LU TP 95-20**
T.Sjöstrand, *Computer Physics Commun.* **82** (1994) 74

[135] *ISAJET*, F.Paige and S.Protopopescu, in *Supercollider Physics*, p.41, ed. D.Soper (world Scientific, 1986)
H.Baer, F.Paige, S.Protopopescu and X.Tata, in *Proceedings of the Workshop on Physics at Current Accelerators and Supercolliders*, ed. J.Hewett, A.White and D.Zeppenfeld, (Argonne National Laboratory, 1993).

[136] *CMS Simulation Package CMSIM — Users' Guide and Reference Manual*,
⟨http://cmsdoc.cern.ch/cmsim/cmsim.html⟩

Muon chambers

[137] *Experimental Tests of the Q2 Drift Tubes Prototype Chamber for the CMS Muon Barrel*, E. Conti et al., **CMS NOTE/1997-019**.

[138] *Tests of Cathode Strip Chamber Prototypes*, Yu. Bonushkin et al., **CMS NOTE/1997-078**
Fabrication and Test of the Full-Scale P3 Prototype of the ME1/1 CSC, Y. Ershov et al., **CMS IN/1997-003**.

[139] *Recents Results and Developments on Double Gap RPC for the CMS*, A. Colaleo, **CMS CR/1997-013**.

Calorimeter Trigger study

[140] *A study of the 1st level tau trigger*, A.Nikitenko, J.Varela, **CMS TN/95-195**
A Proposal for Update of CMS Level-1 Calorimeter Regional Trigger Implementation, S.Dasu, M.Jaworski, J.Lackey, W.H.Smith, **CMS IN/1997-011**

[141] **CMS TN/94-219**, Ph. Busson, J. Varela, *Calorimeter Trigger in CMS Algorithm studies I*.

[142] **CMS TN/95-027**, C. Lourenco, J. Varela, *A fine granularity calorimeter trigger for CMS*.

[143] **CMS TN/95-143**, J. Varela, *Requirements for a fine grained calorimeter trigger*,
presented at the *First Workshop on Electronics for LHC Experiments*, Lisbon, 11-15 September 1995.

[144] **CMS TN/95-197**, C. Lourenco, A. Nikitenko, J.Varela,
A low p_t 1st level single electron trigger for beauty studies in CMS.

[145] **CMS TN/96-021**, R. Nobrega, J. Varela,
The CMS electron/photon trigger: simulation study with CMSIM data.

[146] **CMS TN/94-285**, S. Dasu, J. Lackey, W.H. Smith, W. Temple,
CMS Level 1 Calorimeter Trigger Performance Studies.

[147] **CMS TN/95-111**, S. Dasu, J. Lackey, W.H. Smith, W. Temple,
CMS Missing Transverse Energy Trigger Studies.

[148] **CMS TN/95-112**, S. Dasu, J. Lackey, W.H. Smith, W. Temple,
New Algorithms for CMS Electron/Photon Trigger — Use of Fine Grain Calorimeter Data.

[149] **CMS TN/95-183**, S. Dasu, J. Lackey, W.H. Smith, W. Temple,
CMS Level 1 Calorimeter Trigger Performance on Technical Proposal Physics.

[150] **CMS TN/96-066**, S. Dasu, W.H. Smith, *CMS Level-1 Jet Trigger Study*.

[151] S. Dasu, C. Lourenco, A. Nikitenko, R. Nobrega, W.H. Smith, J. Varela,
Simulation of the CMS Level-1 Calorimeter Trigger,
presented at the *VI International Conference on Calorimetry in High Energy Physics*, Frascati, Italy, June 1996.

Experiments in general

[152] *Status Report of the RD5 Experiment*, **CERN/DRDC 91-53**, January 13, 1992
Status Report of the RD5 Experiment, **CERN/DRDC 93-49**, January 5, 1994
M. Aalste et al, *Zeitschrift für Physics* **C 60** (1993) 1
C. Albajar et al, *Nucl. Instr. Meth.* **A 364** (1995) 473
C. Albajar et al, *Measurement of Momentum and Angular Distributions of Punchthrough Muons at RD5 Experiment*, to be published in *Zeitschrift für Physics*

[153] *RD5 '92 Trigger System*, G.Wrochna, **RD5 TN/92-08**
RD5 '93 Trigger System, G.Wrochna, **RD5 TN/93-14**

[154] *ATLAS Technical Proposal*, **CERN/LHCC 94-43**, December 1994

[155] *The Compact Muon Solenoid – Letter of Intent*, **CERN/LHCC 92-3**, October 1992

[156] *The Compact Muon Solenoid – Technical Proposal*, **CERN/LHCC 94-38**, December 1994

Others

[157] *Searches for new particles at present colliders*, P.Janot, talk given at the *International Europhysics Conference on High Energy Physics*, 19-26 August 1997, Jerusalem, Israel.

[158] *Weakly-Coupled Higgs Bosons and Precision Electroweak Physics*, H.E.Haber, et al., proceedings of the workshop *New Directions for High Energy Physics*, June 25 - July 12, 1996, Snowmass, Colorado.

[159] *Supersymmetry Prospects at an Upgraded Fermilab Tevatron Collider*, S.Mrenna, et al., proceedings of the workshop *New Directions for High Energy Physics*, June 25 - July 12, 1996, Snowmass, Colorado.

[160] *SUSY studies in CMS*, D.Denegri, proceedings of the *LHCC SUSY Workshop*, October 29-30, 1996, CERN, Geneva.

[161] *Extended Gauge Sectors at Future Colliders*, T.G.Rizzo, proceedings of the workshop *New Directions for High Energy Physics*, June 25 - July 12, 1996, Snowmass, Colorado.

[162] *Search Limits for Extra Neutral Gauge Bosons at High Energy Lepton Colliders*, S.Godfrey, proceedings of the workshop *New Directions for High Energy Physics*, June 25 - July 12, 1996, Snowmass, Colorado.

[163] *Expected SM/SUSY Higgs observability in CMS*, R.Kinnunen and D.Denegri, **CMS NOTE 1997/057**,

[164] *Detection of Sleptons in CMS, Mass Reach*, D.Denegri, L.Rurua and N.Stepanov, **CMS TN/96-059**,

[165] *Sensitivity to Sparticle Masses and Model Parameters in Direct $\tilde{\chi}_1^{\pm}\tilde{\chi}_2^0$ Production*, I.Iashvili, A.Kharchilava and C.Racca, **CMS NOTE 1997/069**,

[166] J.Botts et al., Phys. Lett. **B304** (1993) 159
CTEQ — The Coordinated Theoretical-Experimental Project on QCD,
⟨http://www.phys.psu.edu/∼cteq/⟩

Appendix A

Milestones and schedule

GENERAL TRIGGER AND DATA ACQUISITION MILESTONES 1996-97

D11 — ***November 1996 (All)***
Trigger and data acquisition requirements review and Preliminary design review

The physics performance requirements will be finalized. The interface requirements to the front end electronics will be finalized. The rate requirements for the trigger and data acquisition levels will be finalized. The preliminary conceptual design of all components will be reviewed to determine if the designs meet the requirements.

D12 — ***November 1997 (All)***
Trigger and data acquisition Intermediate Design Review

The designs of the trigger and data acquisition systems will be reviewed as to whether they meet the requirements established in D11. The technical progress towards completion of the designs will be reviewed. The plan to complete design, write the technical design report, and begin production will be reviewed.

MUON TRIGGER MILESTONES 1996-97

D300 — ***November 1996 (Warsaw)***
Review of test benches with FPGA prototypes of PAC and synchro/readout chips

The test bench of the Pattern Comparator Trigger for RPC will consist of 4 cards: synchronisation, trigger, readout, and control. They will be equipped with FPGA versions of the Pattern Comparator (PAC) chip and the synchronisation module. The RD6 ROC ASIC will be used for the readout. The primary purpose is to test the system aspects of the complete muon trigger setup. The setup will be equipped with boundary scan, which will be used for testing and programming. The modular structure of the test bench will allow for changes from FPGA's to ASIC's once the latter are available (D350).

D310 — ***November 1996 (Bari)***
Review of FPGA prototype tests of the muon sorter ASIC

The muon sorter selects 4 highest momentum muons in the entire muon trigger system. It is a tree-like structure of sorter chips, each one selecting 4 out of 8 muons. FPGA versions of this chip will be tested in the test bench (D300).

D320 — *November 1996 (Padova)*
Review of FPGA prototype tests of the meantimer ASIC

Three meantimer prototypes in a FPGA reduced version, mounted on a 6U VME card, have been tested on H2 beam in summer '95. Detailed analysis of their performance will be completed

D330 — *November 1996 (Vienna)*
Review of FPGA prototype tests of the Track Finder ASIC's

The hardware implementation of the track finder is going to be tested using a FPGA prototype system. In the first testing phase the chamber electronics will not be available, thus the track finder prototype will be evaluated in a prototype test bench. This test bench will deliver simulated physics data to the FPGA prototype.

D340 — *November 1996 (UCLA[1], MIT[2], CERN)*
Delivery of prototypes of comparator tree and pattern finding chips for cathode strip chamber trigger

The CSC chamber strip preamp/fast shaper ASICs plus strip comparator tree ASICs plus strip pattern-finding FPGAs will be connected to 16 strip x 6 layers of a CSC prototype chamber and tested for efficiency and spatial resolution.

D341 — *December 1997 (Dubna)*
Prototype tests of center cluster and pattern finding chips for MF1/1 trigger

Cathode front end electronics based on Minsk ASICs (amp./shaper, fast shaper/Discr.) will be available in May 97. They will be mounted on the P3 prototype of MF1/1 together with center cluster and pattern finding FPGAs prototypes.

D350 — *June 1997 (Warsaw, Bari)*
Delivery of first presamples of PAC, synchro/readout and sorter ASICs

These ASIC's will have full functionality but the size (number of channels) may be smaller than in the final versions. They will replace corresponding FPGA prototypes and the RD6 ROC ASIC in the test bench (D30 and D31). The technology for the prototype ASICs will be 0.7 μm, whereas the final version is planned to be 0.35 μm.

D360 — *June 1997 (UCLA, CMU[3], OSU[4])*
Delivery of prototypes of wire pattern-finding and bunch i.d. chips for CSC trigger

The CSC wire preamp/discriminator ASICs plus wire pattern-finding/bunch i.d. FPGAs will be connected to 16 strips x 6 layers of a CSC prototype chamber and tested for efficiency, and time resolution.

D361 — *December 1997 (Dubna)*
Prototype tests of wire bunch i.d. and pattern finding chips for MF1/1 trigger

Anode front end electronics based on Minsk ASICs (preamp./shaper, discr.) will be available in May 97. It will be mounted on the P3 prototype of MF1/1 together with wire pattern finding and BX identification FPGA prototypes.

[1] University of California at Los Angeles
[2] Massachusetts Institute of Technology, Cambridge
[3] Carnegie Mellon University, Pittsburgh
[4] The Ohio State University, Columbus

D370 — ***November 1997 (UCLA, UCD, OSU)***
Delivery of first presamples of ASICs for strip and wire LCT generation for CSC trigger

The strip pattern-finding and wire pattern-finding/bunch i.d. trigger chips will be implemented in ASICs with intended performance close to final design specifications.

D380 — ***November 1997 (UCLA, UCD, OSU, Dubna)***
Review of prototype design of motherboard circuits for CSC trigger

Motherboard circuits will receive and correlate wire and strip trigger information and pass stub information on to the Track Finder (see D330) over an optical fiber.

D390 — ***November 1997 (Padova)***
Delivery of meantimer and correlator final chips for full trigger test (=M16)

The final meantimer and correlator chips will be mounted on 128 channel Trigger Boards connected to MB97 chamber (end '97 milestone). Trigger Boards will be mounted in a 9U VME crate with a dedicated backplane, along with a Control Board, to test the full chain of chamber triggering devices.

MUON TRIGGER MILESTONES 1998

Numbering convention:

30x — RPC PACT
32x — Drift Tubes
33x — Track Finder
34x — CSC strip electronics (comparators, etc.)
36x — CSC wire LCT
37x — CSC strip LCT
38x — CSC Motherboard, Port Card, system tests

D303 — ***December 1998 (Warsaw, Bari)***
Review of test bench with prototypes of PAC and Sorter ASICs

The test bench of the Pattern Comparator Trigger for RPC consists of 4 cards: synchronisation, trigger, readout, and control. They will be equipped with Pattern Comparator (PAC) and Muon Sorter ASICs. The primary purpose is to test the system aspects of the complete muon trigger setup. The setup will be equipped with boundary scan, which will be used for testing and programming.

D322 — ***February 1998 (Padova, Bologna)***
Delivery of Trigger Board prototype with BTI, TC and TS ASICs

Trigger Board prototype for 128 channels will be equipped with Bunch and Track Identifier (BTI), Track Correlator (TraCo) and Trigger Server (TS) ASICs, to be tested with Drift Tube prototype MB96.

D331 — ***1998 (Vienna)***
Track Finder milestone(s) — not yet defined

D343 — ***June 1998 (US)***
Delivery of pre-production comparator ASICs

D362 — ***September 1998 (US)***
Delivery of 2nd version anode LCT FPGAs and PC board

D363 — ***December 1998 (Dubna)***
Test of 2nd version anode LCT FPGAs and PC board with ME1/1 CSC prototype

D364 — ***November 1998 (US)***
Delivery of presample anode LCT ASICs

D371 — ***April 1998 (US)***
Delivery of 2nd version strip LCT FPGAs and PC board

D372 — ***July 1998 (Dubna)***
Test of 2nd version strip LCT FPGAs and PC board with ME1/1 CSC prototype

D373 — ***November 1998 (US)***
Delivery of presample strip LCT ASICs

D381 — ***May 1998 (US)***
Delivery of prototype motherboard trigger circuits and PC board

D382 — ***August 1998 (Dubna)***
Test of prototype motherboard trigger circuits and PC board with ME1/1 CSC prototype

D383 — ***November 1998 (US)***
Delivery of Port Card design document

D384 — ***December 1998 (US)***
Chamber LCT system test (strip, anode, motherboard triggers)

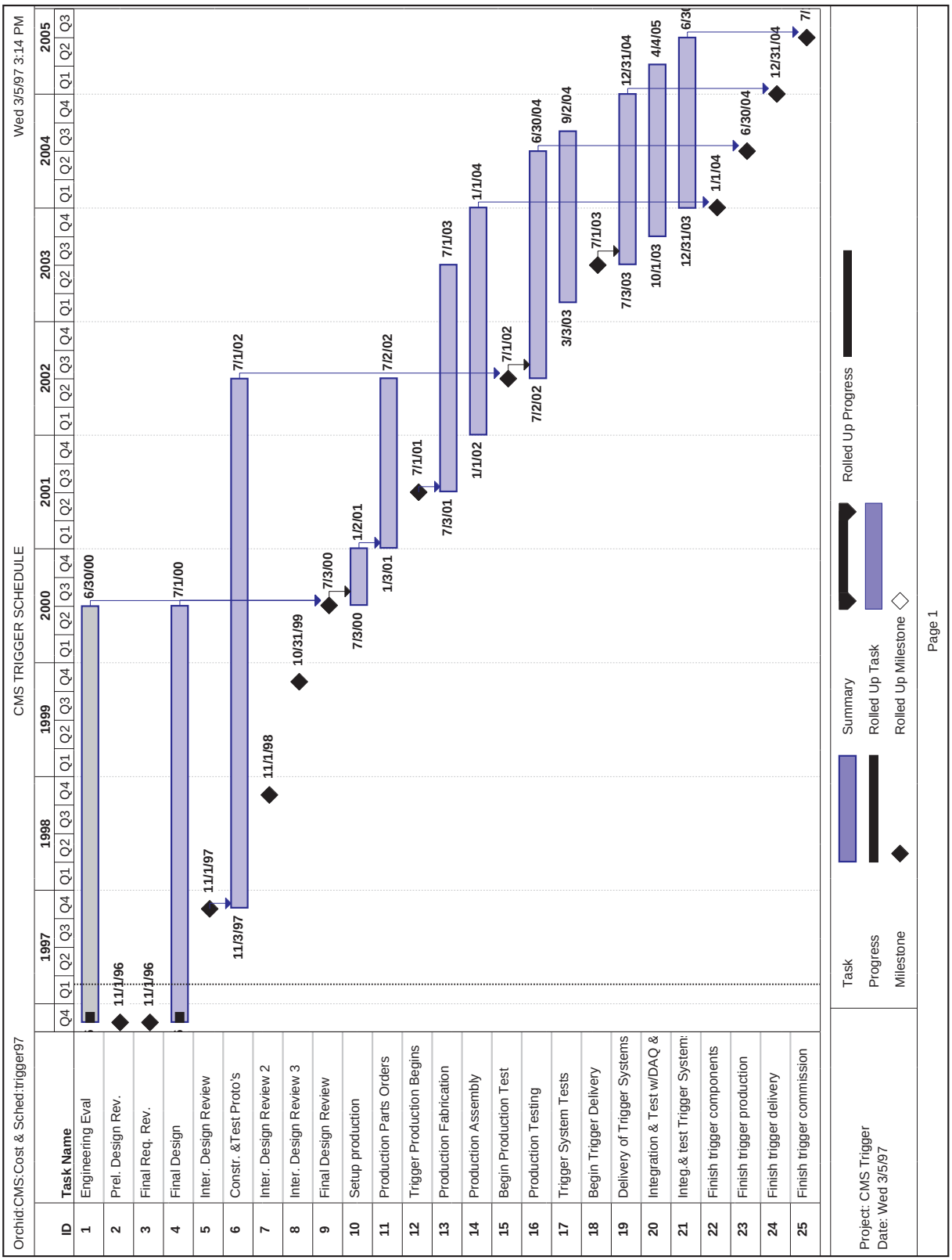

Figure A.1: CMS Trigger schedule.

Appendix B

Momentum scale

Because Muon Trigger has to select the highest p_t muons, the information about p_t has to be exchanged between its various components. The important question is how precise this information should be, i.e. how many bits are needed to code it.

Selecting of highest p_t muons is time consuming. Number of logical operations strongly depends on the number of bits to be sorted. This limits the precision one can afford. On the other hand fine p_t scale is needed to tune trigger rates. One step on the scale should not change the trigger rate too dramatically. Ideally, increasing p_t by one bin should decrease the trigger rate by a given, not too large factor. Since the muon p_t spectra are falling down exponentially, the logarithmic scale would be appropriate. What is proposed below is an approximately logarithmic scale with rounded values in order to make it more convenient for human beings.

Proposed 5-bit p_t scale is given in Table B.1. Muon sign is carried by the 6th bit. Exact logarithmic scale is given in column 2. An average ratio of rates corresponding to two neighbouring bins (i.e. the accuracy of rate tuning) is 1.53. In case of "rounded" scale, given in the third column, the ratio varies from 1.41 to 1.78 (column 5). The difference between "exact" and "rounded" p_t is $\pm$4% (column 4).

Several codes are reserved for some special cases. Code 0 means "no muon in this part of the detector". Another example would be "the chamber full of hits", when one cannot exclude that there was no muon, but its momentum estimation is impossible.

Table B.1: Proposed p_t scale for trigger.

code	exact p_t	rounded p_t	Δ	rate factor
0	"no muon"			
1	reserved			
2	reserved			
3	reserved			
4	2.03	2.0	–2%	
5	2.42	2.5	3%	1.78
6	2.89	3.0	4%	1.60
7	3.46	3.5	1%	1.49
8	4.12	4.0	–3%	1.41
9	4.92	5.0	2%	1.78
10	5.88	6.0	2%	1.60
11	7.02	7.0	0%	1.49
12	8.38	8.0	–4%	1.41
13	10.00	10.0	0%	1.78
14	11.94	12.0	1%	1.60
15	14.25	14.0	–2%	1.49

code	exact p_t	rounded p_t	Δ	rate factor
16	17.01	17.0	0%	1.65
17	20.31	20.0	–2%	1.52
18	24.24	25.0	3%	1.78
19	28.94	30.0	4%	1.60
20	34.55	35.0	1%	1.49
21	41.25	40.0	–3%	1.41
22	49.24	50.0	2%	1.78
23	58.78	60.0	2%	1.60
24	70.17	70.0	0%	1.49
25	83.77	80.0	–4%	1.41
26	100.00	100.0	0%	1.78
27	119.38	120.0	1%	1.60
28	142.51	140.0	–2%	1.49
29	reserved			
30	reserved			
31	reserved			

Appendix C

Useful numbers and formulae

1 barn	1 mb	1 pb	1 fb	
1	10^{-3}	10^{-12}	10^{-15}	barns
10^{-24}	10^{-27}	10^{-36}	10^{-39}	cm^2

Rate [MHz] = σ [mb] $\cdot$ $\mathcal{L}$ $[10^{33}\mathrm{cm}^{-2}\mathrm{s}^{-1}]$

1 LHC running year: $\approx$ 1/3 of calendar year $\approx 10^7$ s

Luminosity integrated over 1 year:

$$\int(\mathcal{L} = 10^{33}\mathrm{cm}^{-2}\mathrm{s}^{-1}) = 10^4\mathrm{pb}^{-1} = 10\ \mathrm{fb}^{-1}$$

$$\int(\mathcal{L} = 10^{34}\mathrm{cm}^{-2}\mathrm{s}^{-1}) = 10^5\mathrm{pb}^{-1} = 100\ \mathrm{fb}^{-1}$$

Inelastic pp cross section at $\sqrt{s} = 14$ TeV: $\quad \sigma_{pp}^{inel} = 55$ mb

Average number of pp collisions per bunch crossing: $\quad \bar{n}_{\mathcal{L}=10^{33}\mathrm{cm}^{-2}\mathrm{s}^{-1}} = 1.38, \quad \bar{n}_{\mathcal{L}=10^{34}\mathrm{cm}^{-2}\mathrm{s}^{-1}} = 13.8$

Number of pp collisions per bunch crossing n follows Poisson distribution: $\quad P_n = \frac{\bar{n}^n e^{\bar{n}}}{n!}$

However, in the case of triggered events one should count the collision which caused the trigger separately, i.e. one should expect $n + 1$ collisions superimposed.

Nuclear interaction length λ = 16.8 cm Fe = 15.1 cm Cu
Average muon energy loss in iron (muon energy = 1-100 GeV) $\approx$ 0.25 GeV / $\lambda \approx$ 1.5 GeV / m

---

Radiation length X_0 = 1.76 cm Fe = 1.43 cm Cu

Multiple scattering: $\quad \theta_0 = \frac{13.6\ \mathrm{MeV}}{\beta cp}\sqrt{\frac{x}{X_0}}\left(1 + 0.038\ln\frac{x}{X_0}\right)$

angle: $\theta_{plane}^{rms} = \theta_0$, $\quad$ position: $y^{rms} = \frac{x}{\sqrt{3}}\theta_0$, $\quad$ saggita: $s^{rms} = \frac{x}{4\sqrt{3}}\theta_0$

Bending in a magnetic field: $\quad p_t[\mathrm{GeV}] = 0.3 \cdot B[\mathrm{T}] \cdot R[\mathrm{m}]$

Appendix D

Dictionary of acronyms

ASIC Application Specific Integrated Circuit
ATLAS A ToroidaL AparatuS
AU Assignment Unit
BTI Bunch and Track Identifier
b.x. bunch crossing
CAN Control Area Network
CMS Compact Muon Solenoid
CR Conference Report
CSC Cathode Strip Chambers
DAQ Data AcQuisition
DAS Data Acquisition System
DEMUX DEMUltipleXer
DPM Dual Port Memory
DT Drift Tubes
DTBX Drift Tubes with Bunch X-sing capability
ECAL Electromagnetic CALorimeter
EM ElectroMagnetic
ERS Extrapolation Result Selector
EU Extrapolation Unit
FE Front End
FEB Front End Board
FEBC Front End Board Control
FEC Front End Chip
FED Front End Driver
FPGA Field Programmable Gate Array
GMT Global Muon Trigger
HCAL Hadronic CALorimeter
HF Hadronic Forward calorimeter
HV High Voltage
LB Link Board
LCT Local Charged Track
LHC Large Hadron Collider
LI Local Isolation
LMUX Link MUltipleXer
LOI Letter Of Intent
LV1 1-st Level Trigger
LV2 2-nd Level Trigger
MB Muon Barrel
ME Muon Endcap (=MF)
MF Muon Forward
MIP Minimum Ionising Particle
MS Muon Station
MSGC Micro-Strip Gas Chambers
MSSM Minimal Supersymmetric Standard Model
MTD Monitored Drift Tubes
NLC Next Linear Collider
NNLC Next to Next Linear Collider
QCD Quantum Chromo-Dynamics
PAC PAttern Comparator
PACT PAttern Comparator Trigger
PCB Printed Circuit Board
RB Readout Board
RDPM Readout Dual Port Memory
ROC ReadOut and Control
ROI Region Of Interest
RPC Resistive Plate Chambers
Rx Receiver
SC Super-Conductive
SER SERialiser
SL Super-Layer
SM Standard Model
STS Single Track Selector
SU Synchronisation Unit
SUSY Super-Symmetry
TCL Track Cancellation Logic
TDR Technical Design Report
TF Track Finder
TGC Thin Gap Chambers
TN Technical Note
TP Technical Proposal
TRACAL TRAcking CALorimeter
TRACO TRAck COrrelator
TB Trigger Board
TRIDAS TRIgger and Data Acquisition System
TS Trigger Server
TSEL Track SELector
TSL Track Segment Linker
TR Track Router
TTC Timing, Trigger and Control
Tx Transmitter
URL Uniform Resource Locator
VHDL VHSIC Hardware Description Language
VHSIC Very High Speed Integrated Circuit
VLHC Very Large Hadron Collider
VLSI Very Large Scale Integration
VME Versa Module Eurocard